Analysis of Four-component Seafloor Seismic Data for Seismic Anisotropy

by

Jianxin Yuan

Thesis submitted for the degree of Doctor of Philosophy

Department of Geology and Geophysics

University of Edinburgh

2001

Abstract

Interest in converted waves (C-waves) has been growing significantly in recent years due to the advent of four-component (4C) ocean-bottom-cable (OBC) seismic recordings. This has changed the way geophysicists obtain fluid and lithology information about hydrocarbon reservoirs through joint P- and converted-wave analysis. Since 4C OBC surveys use conventional air-gun sources, which generate P-waves only, the shear-waves recorded by the 4C sensors on the ocean bottom are mode-converted shear-waves. The main focus of this thesis is to find ways to process and understand these mode-converted shear-waves in the presence of seismic anisotropy which is common in marine sediments. To this end, I examine and model the data characteristics of 4C seismic data, review the basic theory of converted-wave processing, develop new kinematic theories for converted-waves propagating in anisotropic, inhomogeneous media, and apply these new methods to field 4C data. I focus on two types of anisotropy: transverse isotropy with either a vertical (TIV) or horizontal (TIH) axis of symmetry.

As an emerging technology, the characteristics of 4C seismic data have not been fully understood, and there are many acquisition related problems yet to be solved. The characteristics of 4C seafloor data have been studied by field data analysis and by synthetic modelling. I have found: 1) the water-column reverberations in the vertical geophone are much weaker than those in the hydrophone, because of the different sensor responses to the source- and receiver-side multiples; 2) the presence

of a low shear-wave velocity gradient in the seabed prohibits P-to-S conversion, and this implies that most shear-waves recorded in 4C data are converted at deep reflectors; 3) due to current sensor design, there is a shear-wave energy leakage from the inline horizontal geophone to the vertical geophone, resulting in geophone coupling problem. I have also studied the problem of sensor orientation and presented geophone orientation algorithms for both gimballed and non-gimballed geophone systems.

The presence of TIV (or polar anisotropy) has a significant influence on converted-wave processing in terms of both the conversion-point offset and moveout. There is no accurate analytical equation for calculating the conversion point offset in layered TIV media. Furthermore, the existing moveout equations for anisotropy are restricted to near-offsets. To overcome these problems, I have developed new analytical equations for both the conversion point offsets and converted-wave moveout. These equations are accurate up to intermediate-to-far offsets. The equations for the conversion-point offset are derived by the Taylor series expansion method, and those for converted-wave moveout are derived by both the Taylor-expansion method and by a double-square-root (DSR) approach. The Taylor series expansion can be used for parameter estimation and moveout correction, and the DSR equation for anisotropic pre-stack time migration. It is also observed that anisotropy has a stronger influence on conversion point offset than on moveout, and this is explained by the derived analytical equations. New parameters and are introduced to quantify the influence of TIV anisotropy on pure and converted shear-waves, respectively, at far offsets. Methods for estimating anisotropic parameters are also presented and tested on both synthetic and field data using converted-waves.

For TIH (or azimuthal anisotropy), a 2C rotation analysis has been implemented and tested on 2D synthetic and field data for determining the direction of the symmetry axis. Although the 2C rotation analysis requires normal incident shear-wave

data, the synthetic analysis shows that it is generally acceptable to use post-stack data instead. However, the presence of both TIV and TIH anisotropy, giving rise to orthorhombic anisotropy, can make the 2C rotation analysis less reliable. A modelling analysis is also performed for 3D data. In a 3D azimuthal gather, there is a polarity reversal in the transverse component corresponding to the direction of the symmetry axis, and this is independent of offset and TIV anisotropy. The phenomenon can be used for identification of fracture direction.

An integrated study of both P- and converted-waves is carried using the new methods. The data are from the North Sea (Courtesy of Shell Expro), and are of excellent quality. The study reveals the presence of strong TIV but very weak TIH anisotropy in the area. The integrated analysis has validated the new methods.

Acknowledgement

Years ago, when I first moved into a new country to begin my PhD study in Edinburgh, Scotland, I was so lucky to have an extremely helpful supervisor, Dr Xiang-Yang Li. His help has been with me through years not only as a guide in my academic study, but also as a close friend in my personal life. The numerous discussions, even argument with him, have been a constant source of idea-inspiration. This thesis is partly a fruit of his extensive review and corrections. During my spare time, my wife and I enjoyed a lot of wonderful parties in his house near the King's Building campus. A million thanks to him and his family.

I also would like to thank my other two supervisors, Professors Anton Ziolkowski and Stuart Crampin. My knowledge about field data has been benefited a lot from discussion with Anton. Without Anton, it would have been impossible to finished the thesis in due time, especially after I began my career in oil industry. Stuart Crampin's insurmountable knowledge helped me to gain understanding of seismic anisotropy through many discussions.

I would cordially like to thank my friends in the British Geological Survey (BGS), Enru Liu and Hengchang Dai, for frequent discuss and some happytime together. I also thank David Kerridge of the BGS, and Roger Scrutton in the department, for their administrative work. I thank my fellow students, Peter Hassen, Yi-Jie Liu, Hejie Wang, Jun Yan in BGS for a lot of good laughs as well as serious discussions.

My PhD study was sponsored by the Project *Processing Three-component Seafloor*

Seismic Data of the department, and the Edinburgh Anisotropy Project (EAP) of the BGS. Thanks to all the sponsors of the projects. Particularly, I would like to thank Shell Expro UK and Floris Strijbos for providing a field 4C OBC data for testing my theory.

Finally, dearest thanks to my wife, Yanghua Xiang, for her patience during countless evenings and weekends which I spent on the thesis. Alas, this thesis is also to my baby daughter, Rachel, who is just a few months old.

Contents

Notations and conventions

All the mathematical variables and other abbreviations that are used throughout the thesis are explained here. They are arranged by chapters in the order of their appearance.

General

Symbol	Meaning
TIV	transverse isotropy with a vertical axis of symmetry
TIH	transverse isotropy with a horizontal axis of symmetry
4C	four-component (three-component geophone plus a hydrophone)
OBC	ocean-bottom cable
CCP	common-conversion-point
ACCP	asymptotic common-conversion-point
CMP	common-middle-point
NMO	normal moveout
DMO	dip moveout
C-wave	P-SV converted shear waves at the reflection point
DSR	double-square-root
RMS	root-mean-square

Chapter 2

Symbol	Meaning	Unit
t_c	traveltime (moveout) of converted wave	s
x	source-to-receiver offset	m
z	reflector depth	m
x_c	conversion point offset	m
V_p	P-wave velocity (isotropic)	m/s
V_s	S-wave velocity (isotropic)	m/s
γ	velocity ratio V_p/V_s	
V_c	converted-wave stacking velocity (isotropic)	m/s
s	source coordinate	m
r	receiver coordinate	m
x_b	coordinate of CCP bin	m
w	CCP bin width	m
τ	two-way traveltime of DMO trajectory	s
h	half source-to-receiver offset	m
t_n	NMO corrected time	s
t_{c0}	two-way vertical traveltime of converted wave	s
t_{c0i}	interval two-way vertical traveltime of converted wave	s
V_{mig}	post-stack migration velocity of converted wave	m/s
V_a	average velocity of converted wave	m/s
v_{pi}	interval P-wave velocity (isotropic)	m/s
v_{si}	interval S-wave velocity (isotropic)	m/s

Chapter 3

Symbol	Meaning	Unit
Z	Z-transform	
$S(Z)$	Z-transform of source-side water-column reveberations	
$H(Z)$	Z-transform of receiver-side water-column reveberations (hydrophone)	
$G(Z)$	Z-transform of receiver-side water-column reveberations (geophone)	
K_r	seafloor reflectivity	

Chapter 4

Symbol	Meaning	Unit
$\mathbf{D}(t)$	vector displacements of three-component geophone (after geophone orientation)	
$\mathbf{D}_r(t)$	vector displacements of three-component geophone (before geophone orientation)	
x, y and z	inline, crossline and vertical components of $\mathbf{D}(t)$	
a_1, a_2 and a_3	inline, crossline and vertical components of $\mathbf{D}_r(t)$	
$\mathbf{R}_y$	rotation matrix about the y-axis	
$S(t)$	source wavelet	
$\lambda(t)$	wave progatation function in the water	
T_{pp}	P-P transmission coefficient just below the seafloor	
T_{ps}	P-S transmission coefficient just below the seafloor	
θ_{pp}	P-P transmission angle just below the seafloor	

θ_{ps}	P-S transmission angle just below the seafloor	
α, β and ϕ	three Euler's rotation angles	

Chapter 5

Symbol	Meaning	Unit
x_c	converstion point offset	m
x	source-to-receiver offset	m
z	reflector depth	m
C_0, C_2 and C_3	coefficients of conversion point approximation using reflector depth z	
V_p	P-wave velocity (isotropic)	m/s
V_s	S-wave velocity (isotropic)	m/s
γ	velocity ratio V_p/V_s	
t_c	traveltime (moveout) of converted wave	s
t_{c0}	two-way vertical traveltime of converted waves	s
V_c	short-spead NMO velocity of converted wave in single-layered medium	m/s
A_4 and A_5	coefficients of converted wave moveout approximation by modified Taylor series expansion	
V_{p0}	vertical average P-wave velocity in layered media	m/s
v_{pi}	interval P-wave velocity of the ith layer	m/s
t_{p0}	one-way vertical travel time of P-wave	s
Δt_{p0i}	P-wave one-wave vertical travel time in the ith layer	s

V_{s0}	average S-wave velocity in layered media	m/s
v_{si}	interval S-wave velocity in layered media	m/s
t_{s0}	one-way vertical travel time of S-wave	s
Δt_{s0i}	S-wave one-way vertical travel time in the ith layer	s
Δz_i	thickness of the ith layer	m
γ_0	vertical velocity ratio V_{p0}/V_{s0}	
V_{p2}	short-spead NMO velocity of P-wave	m/s
V_{s2}	short-spead NMO velocity of S-wave	m/s
γ_2	NMO velocity ratio V_{p2}/V_{s2}	
V_{p4}	fourth-order velocity of P-wave	m/s
V_{s4}	fourth-order velocity of S-wave	m/s
c_0, c_2 and c_3	coefficients of conversion point approximation using vertical travel time t_{c0}	
γ_{eff}	effective velocity ratio γ_2^2/γ_0	
V_{c2}	short-spead NMO velocity of converted wave	m/s
Δt_{c0i}	two-way converted-wave vertical traveltime in the ith layer	s

Chapter 6

Symbol	Meaning	Unit
$\mathbf{C}$	elastic constant matrix	
C_{ij}	elastic constant	g/(ms^2)
ε	Thomsen parameter $(C_{11} - C_{33})/2C_{33}$	
γ'	Thomsen parameter $(C_{66} - C_{44})/2C_{44}$	

δ	Thomsen parameter $\frac{(C_{13}+C_{44})^2-(C_{33}-C_{44})^2}{2C_{33}(C_{33}-C_{44})}$	
ρ	density	g/m^3
V_{p0}	vertical velocity of P-wave	m/s
V_{s0}	vertical velocity of S-wave	m/s
γ_0	vertical velocity ratio V_{p0}/V_{s0}	
V_{p2}	short-spread NMO velocity of P-wave	m/s
V_{s2}	short-spread NMO velocity of S-wave	m/s
σ	deritive anisotropy parameter $\sigma = \gamma_0^2(\varepsilon - \delta)$	
η	deritive anisotropy parameter $\eta = \frac{\varepsilon-\delta}{1+2\delta}$	
V_{ph}	horizontal velocity of P-wave	m/s
V_{c2}	short-spead NMO velocity of converted wave	m/s
v_{p2i}	interval NMO velocity of P-wave in the ith layer	m/s
v_{p0i}	interval vertical velocity of P-wave in the ith layer	m/s
Δt_{p0i}	inverval one-way vertical travel time of P-wave in the ith layer	s
t_{p0}	one-way vertical travel time of P-wave in layered media	s
v_{s2i}	interval NMO velocity of S-wave in the ith layer	m/s
v_{s0i}	interval vertical velocity of S-wave in the ith layer	m/s
Δt_{s0i}	inverval one-way vertical travel time of S-wave in the ith layer	s
t_{s0}	one-way vertical travel time of S-wave in layered media	s
t_p	one-way P-wave traveltime	s
ζ	deritive anisotropy parameter $\zeta = \gamma_{eff}^2 \eta$	
ε_i	interval ε in the ith layer	

δ_i	interval δ in the ith layer	
σ_i	interval σ in the ith layer	
η_i	interval η in the ith layer	
ζ_i	interval ζ in the ith layer	
η_{eff}	effective η in layered TIV media	
ζ_{eff}	effective ζ in layered TIV media	
χ	anisotropy paramter for converted wave moveout at far offset	
χ_{eff}	effective χ in layered TIV media	

Chapter 7

Symbol	Meaning	Unit
$R(t)$	radial component	
$T(t)$	transverse component	
$S_1(t)$	fast S-wave	
$S_2(t)$	slow S-wave	
Δt	time delay between the fast and slow S-waves	s
θ	fracture strike from survey line	
$N_R(t)$	noise in the radial component	
$N_T(t)$	noise in the transverse component	
ω	angular frequency	s^{-1}
$F(\theta, \Delta t)$	objective funtion for 2C rotation analysis	

Chapter 1

Introduction

1.1 Seismic anisotropy and four-component seafloor seismic

Seismic anisotropy, the variation of seismic velocity with the direction in which it is measured or with wave polarization, has been identified in the upper Earth crust for decades (Crampin, 1966; Crampin, 1981). There are many types of seismic anisotropy. Transverse isotropy, orthorhombic anisotropy and monoclinic anisotropy (Sheriff and Geldart, 1995), are among those most often discussed in the geophysical literature. This thesis will focus on transverse isotropy and its effects on the seismic data acquired from the seafloor. Transverse isotropy is the most simple anisotropy, and is very common in marine sediments (Thomsen, 1986). Transverse isotropy has one symmetry axis, and the elastic properties are the same (isotropic) in any direction perpendicular to the symmetry axis. Two important types of transverse isotropy are observed: that with a vertical symmetry axis (TIV or polar anisotropy) (Postma, 1955; Backus, 1962), and that with a horizontal axis (TIH or azimuthal anisotropy)(Crampin *et al.*, 1986). TIV is often found in shaly sediments, or sedi-

ments with thin layers. TIH is often found in vertically fractured rocks.

The importance of seismic anisotropy for the oil industry has been recognized since its first observation in hydrocarbon reservoirs in 1986 (Crampin *et al.*, 1986; Alford, 1986; Lynn and Thomsen, 1986). As shear-waves are often more sensitive to seismic anisotropy than *P*- waves (Krey and Helbig, 1956; Crampin and Radovich, 1982; Winterstein, 1990), most of seismic anisotropy related research has been focused on shear-waves, particularly the pure shear-wave mode. Not until very recently have *P*-wave data become popular due to their wide availability (Sena, 1991; Mallick *et al.*, 1998; Li, 1999).

Since 1994, the industry has shown a growing interest in acquiring shear-waves in the marine environment (Berg *et al.*, 1994), as shear-waves have the ability to provide information about the internal structure of a reservoir including fracture density and orientation, which it is difficult or impossible to obtain with *P*-waves (Crampin, 1985; Crampin and Lovell, 1991; Li, 1997). The new acquisition technique is implemented by implanting four-component (4C) sensors into the seabed while still using conventional airgun sources, which can only generate compressional waves in the water. Thus the recorded shear-wave seismic data are made of various converted waves, with different types of raypaths. The 4C sensor includes one hydrophone, one vertical geophone, one inline horizontal geophone and one crossline horizontal geophone. Time-lapse 4C sea-floor seismic surveys have also been acquired for monitoring hydrocarbon migration.

1.2 History of seafloor seismics

Although the 4C seafloor seismic survey came into the limelight of the oil industry just a few years ago, its early application can be traced back more than half a century. Since the late 1940s, Halliburton Geophysical Services have been developing

the ocean-bottom-cable (OBC) method for offshore seismic exploration (Barr, 1997). Although this was the earliest method of marine seismic exploration, it was largely replaced with towed streamer methods between the early 1960s and the mid-1980s. Since then, OBC was only used in shallow waters where streamers could not be towed.

Since the late 1980s, ocean-bottom cable has become more popular. In many well-explored offshore regions of the world, the proliferation of producing platforms has made it difficult, if not impossible, to acquire seismic data safely using towed streamers. For these mature areas, tightly-spaced 3D surveys are usually required. The OBC is obviously an attractive solution to this dilemma, since it permits very complicated geometries. For example, it permits planting geophones very close to platforms or other obstacles. The high level of repeatability of OBC acquisitions is also suitable for monitoring the fluid migration and changes of gas-oil and oil-water contacts (Beasley *et al.*, 1996).

However, like the towed streamer survey, OBC data are often contaminated by reverberations in the water column. In 1989, Barr and Sanders described a dual-sensor OBC technology, which combined hydrophones and vertical geophones to record both pressure and vertical velocity fields. After careful scaling, and by combining hydrophone and vertical geophone seismic data, the water column reverberations can be suppressed (Dragoset and Barr, 1994). The concept is based on White's composite detector (White, 1965) including a hydrophone and a geophone for sensing sound waves that arrive from a solid (up-going waves) and from a liquid (down-going waves). The response of down-going waves on a hydrophone have opposite polarity to that on a geophone, while the up-going waves have same response both on the geophone and the hydrophone. The calibration of geophone and hydrophone can be performed using the reflection coefficients at the seafloor (Barr and Sanders, 1989), calibration shots (Barr, 1997), or autocorrelation analysis

(Dragoset and Barr, 1994).

The interest in marine 4C acquisition was greatly increased in 1994 by Berg *et al.* (1994), who used converted shear-waves for imaging through a gas cloud. In the marine environment, most shear wave study is based on mode converted waves, as it is hard and expensive to deploy shear wave sources on the seafloor to acquire pure-mode shear waves free of mode conversion. The earliest marine shear wave experiment using converted waves was by Tatham and Stoffa (1976) in the U.S. Gulf Coast near the Alabama-Florida border, where the high velocity seafloor can generate strong mode converted shear waves. The survey was made by conventional towed streamers. The *P*- waves generated by the air-gun sources were converted to shear waves at the seafloor, then reflected back at the reflectors and converted to *P*-waves again at the seafloor, and finally recorded by the hydrophones near the sea surface. This kind of converted shear wave has a symmetric raypath and can be processed using conventional techniques. Although this experiment shows the potential ability of shear waves with regard to reservoir description, the method can not be widely used, since the seafloor velocity is not sufficiently high for effective mode conversion in most offshore areas.

The 4C seismic survey technology is an extension from dual-sensor OBC to four-component by adding two horizontal geophones to sense shear motion directly from the seafloor. Following the publication of Berg *et al.* (1994), the technology has gained wide acceptance as a potentially valuable tool for reservoir characterization and monitoring (Thomsen *et al.*, 1997; MacLeod *et al.*, 1999). The benefits from 4C seismic survey include:

1. good quality shear-wave data;

2. flexible acquisition geometry;

3. that in most cases the seafloor data have significantly better quality than the

hydrophone data acquired by towed streamers (Barr, 1997);

4. wide azimuthal coverage;

5. good repeatability, which is essential for reservoir monitoring (Beasley *et al.*, 1996).

1.3 4C seismic survey

4C seismic acquisition is a hybrid marine and land seismic data acquisition. It often employs a stationary array of 4C sensors on the seafloor, and a conventional marine seismic source, particularly an array of airguns, towed by a shooting vessel. It is thus common to have two vessels for a 4C seafloor acquisition: a shooting vessel towing the airgun array, and a recording vessel which stays above the receiver array (Figure 1.1). When the required shooting coverage has finished, the receiver array can be moved to a new location. Additional vessels may be required to retrieve and lay the receiver array.

Since 4C seafloor seismics is a very new technology, there are many methods and instruments, developed by different major geophysical contractors, to accomplish this acquisition operation. While the airgun source is industry standard equipment, the differences among the seafloor acquisitions lie in the designs of the receiver array. There are four fundamentally different acquisition systems used in the industry today to acquire the seafloor seismic data: three different cable-based systems, and one node-based system (Caldwell, 1999).

Among the three cable-based systems, the first design is based on the conventional OBC technology by adding two horizontal geophones to the original dual-sensor (vertical geophone plus hydrophone) package. The sensors may be attached to the outside of the cable, or may be enclosed in a molded plastic cylinder. The

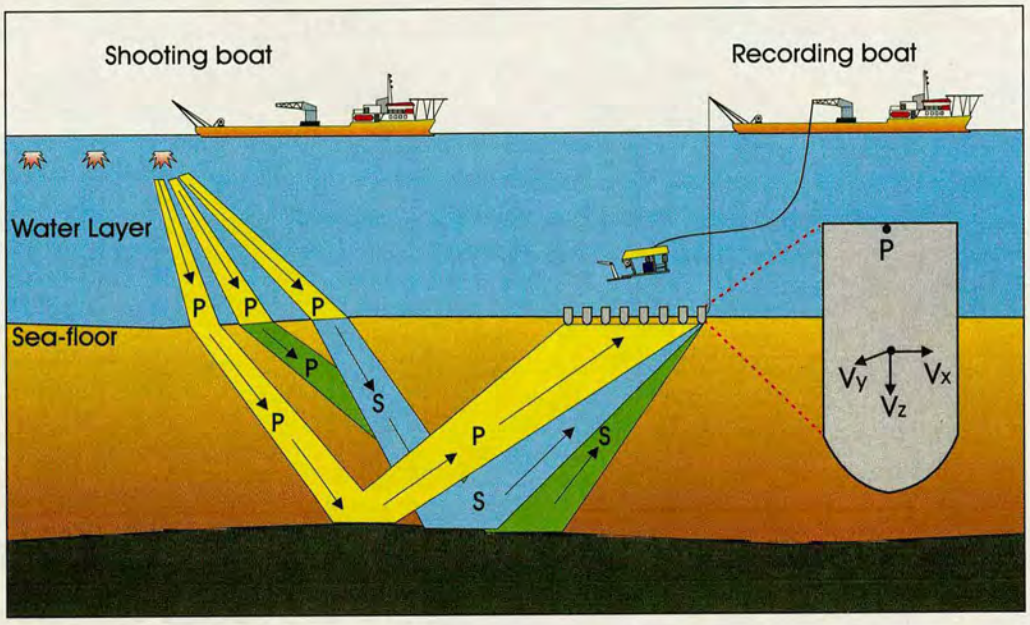

Figure 1.1: Configuration of 4C seafloor acquisition (courtesy of Companie Générale de Géophysique, CGG).

second design is based on logging technology, where sled-like structures contain the sensors, and are dropped into the seafloor (Berteussen *et al.*, 1997). The third one is based on streamer technology in which the sensors are placed inside a fluid-filled cable. The sensors used in all these systems can be different as well. Figure 1.2a shows an example of gimballed seafloor geophones used by the cable-based systems.

The node-based systems are used by Companie Générale de Géophysique (CGG) (Pettenati-Auziere *et al.*, 1997). The systems are direct derivatives from the original SUMIC (subsea seismic) system (Berg *et al.*, 1994; Caldwell, 1999). The system consists of multiple arrays of nodes either cylindrical (Figure 1.2b) or hemispherical in shape. The nodes are planted into the seafloor by means of a remotely operated vehicle (Figure 1.1).

In the data acquisition stage, three basic problems have to be addressed:

1. positioning of the sensors - While the position of shooting vessel is determined

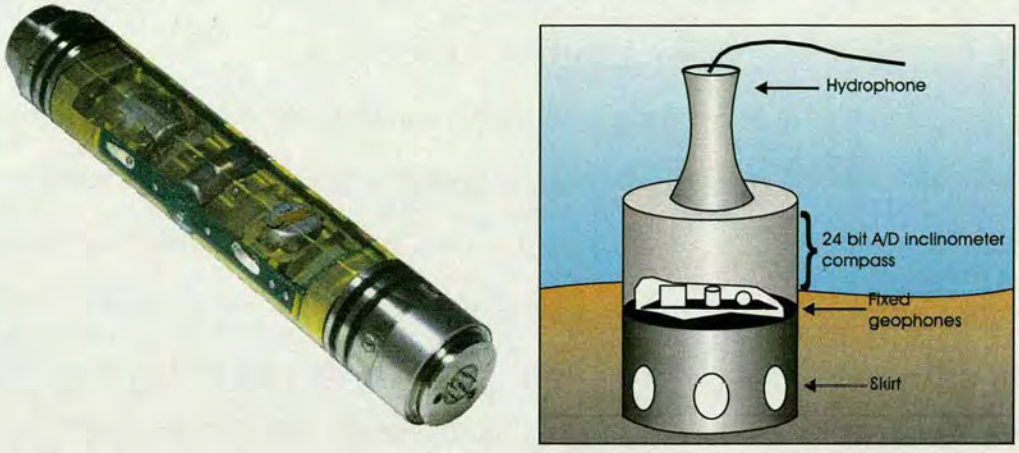

(a) (b)

Figure 1.2: Four-component geophones. (a) Gimballed seafloor geophones (hydrophone is not included, courtesy of Geo Space Corporation); (b) a seafloor geophone node (courtesy of Companie Générale de Géophysique).

by GPS (Global Positioning System), the positions of receivers are either determined by first breaks (Barr, 1997; Bole *et al.*, 1999) or by the remote operated vehicle (Pettenati-Auziere *et al.*, 1997).

2. orientation of geophones - Most of the cable-based systems use gimballed geophones, while CGG's node-based system uses non-gimballed geophones, which are calibrated by compass and inclinometer readings (Figure 1.2b)

3. coupling of the geophones - The cable-based systems achieve a good coupling by the pure weight of the cable or by keeping it under tension, and coupling of CGG's node system is achieved by carefully planting the nodes into the seafloor, involving either a diver or a remote operated vehicle.

Nowadays, the positioning problem is handled with acceptable precision. However orientation and coupling remain the main obstacle in the data acquisition stage. Some algorithms have been proposed to correct the effect of geophone mis-

orientation and poor coupling in the processing stage (Yuan *et al.*, 1997; Gaiser, 1998; Li and Yuan, 1999c; Li *et al.*, 1999).

These different implementations of acquisition systems often give rise to different data quality, due to different system designs and methods of deployment. More data analysis and research are required in this area before the standardization of technology is possible. Marine multicomponent acquisition is 3-5 times more expensive than a conventional towed streamer, which is to be expected in the current stage of the development of the technology (Caldwell, 1999). The cost surely will decrease when the survey becomes a conventional practice.

1.4 Objectives and outline of the thesis

This thesis deals with a range of fundamental issues in the processing of 4C seismic data, such as 1) where the conversion takes place, 2) how to perform standard processing in isotropic media and 3) how to handle anisotropy. As a relatively new technology, these basic issues are not really fully understood. For example, in the early 4C survey conducted by Berg *et al.* (1994), the conversion is assumed at the seabed, which was, in fact, the common assumption at the time (Caldwell, 1999). Note that if the conversion happens at the seabed, the raypath is symmetric with regard to the seabed, and processing is made relatively easy. Subsequent industrial practice reveals that most of the conversions happen at the reflectors, and the converted-wave raypath is asymmetric. This requires a different processing methodology, since the imaging point of a converted-wave depends on the P- and S-wave velocity ratio, which is a physical parameter of the subsurface media. Consequently, a proper imaging of the subsurface cannot be formed without careful consideration of this parameter. This is fundamentally different from pure mode propagation with a symmetric raypath, where physical characterization of the media may follow imag-

ing. The situation is further complicated by the discovery of polar anisotropy in the marine sediments and the fact that the converted shear waves are very sensitive to anisotropy (Thomsen, 1999). The main objective of this thesis is to achieve some new understanding of these issues through both theoretical studies and real data analysis. The layout of the thesis is as follows:

Chapter 2 gives an overview of the standard processing technology with regard to the 4C data in the absence of anisotropy, particularly the converted wave processing on the assumption that *P-S* conversion takes place at a deep reflector with an asymmetric raypath. It includes common-conversion-point (CCP) binning, converted-wave velocity analysis and non-hyperbolic NMO, DMO and migration.

Chapter 3 investigates the wavefield characteristics, such as water-column reverberations and *P-S* wave conversion, observed in 4C data, and discusses their implications for data processing. These characteristics are not only identified, but also explained both from theory and from synthetic modelling. Issues related to geophone coupling and orientation are discussed in Chapter 4. A robust algorithm for determining the geophone orientation is also presented in Chapter 4.

Chapters 5 and 6 focus on the moveout signature and parameter estimation in layered isotropic and anisotropic media. The anisotropy studied is TIV, and new approximations for the conversion point offset in layered isotropic and anisotropic media are presented. Both Taylor series expansion and double-square-root (DSR) equations for *PS*-wave moveout are derived, for the purpose of parameter estimation and processing. The theory is applied to both the synthetic data and the field data.

Chapter 7 illustrates how to handle TIH (azimuthal anisotropy) using 4C data. TIH is diagnosed by shear-wave splitting, and a robust method for analyzing the polarization and time delays of the split shear waves is presented. The analysis is based on both 2D and 3D data.

Finally, one complete case study is presented in Chapter 8 for verifying the

methodology presented in the previous chapters.

1.5 Datasets used

1.5.1 Synthetic data

Synthetic data used in Chapter 2 are generated by **Seismic Unix** routine `susynlvcw`, which is a Kirchhoff synthetic modelling for converted waves in media with linear velocity changes (Alfaraj, 1993) in depth.

The modelling studies in Chapters 3, 4 and 7 are based on the full-wave modelling package ANISEIS (Taylor, 1991).

The synthetic datasets used in Chapters 5 and 6 are created by ray tracing through a horizontally multi-layered medium either for the isotropic or anisotropic case. The main concern is about the kinematic information, such as traveltimes of various wave types and conversion point offsets of *P-S* waves.

1.5.2 Guillemot, The North Sea

In November 1996, Shell Exploration and Production (UK) acquired four lines of 4-component seismic data in the North Sea. The dataset comprises 3 km full fold data recorded by the early prototype drop-drag cable from Geco-Prakla, Schlumberger Ltd. The dataset has since been donated to the Project *Processing Four-component Seafloor Seismic Data* of the Department of Geology and Geophysics of The University of Edinburgh. The Processing of the inline and crossline shooting of the survey is presented in Chapter 8, while its data characteristics are analyzed in Chapters 3 and 4.

1.6 Software used

Processing of synthetic and field datasets in this thesis was performed by **Seismic Unix**. on a Sun Ultra 2 workstation with operating system Solaris 2.6. **Seismic Unix** is a free available scientific research environment developed by Center for Wave Phenomena (CWP), Colorado School of Mines. Some multi-component processing routines, such as three-component geophone orientation, CCP binning, converted wave NMO and DMO, and converted wave velocity analysis, are written by the author for Seismic Unix in C. Most of the seismic diagrams displayed in this thesis are plotted by Seismic Unix's graphics routines, by the Generic Mapping Tools (GMT) (Wessel and Smith, 1995) and Xfig. All text processing is done with LaTeX and LyX.

Chapter 2

Overview of 4C seismic data processing

The 4C seismic survey has only recently become a practical tool for oil and gas exploration. Many processing techniques related to this new data type are evolving rapidly. However, some basic concepts about how to process mode converted waves were well established more than a decade ago (Tessmer and Behle, 1988; Harrison, 1992). The objective of this chapter is to review the existing processing techniques, understand the limits of these techniques and present improved standard techniques for converted wave processing.

2.1 Introduction

Here, I give a brief introduction to conventional processing of 4C seismic data, on the assumption that P-waves are mainly recorded by hydrophones and vertical geophones, and mode converted shear waves are recorded by two horizontal geophones. It is also assumed that P-S conversions occur at the reflectors. These assumptions are valid for most cases as indicated by Caldwell (1999).

A conventional 4C data processing scheme consists of three basic stages: 1) preprocessing; 2) P- wave processing and 3) converted-wave processing. A typical processing flowchart is shown in Figure 2.1. Other non-conventional processing techniques, such as AVO analysis and anisotropic pre-stack migration, which are topics alone by themselves, are beyond the scope of this thesis.

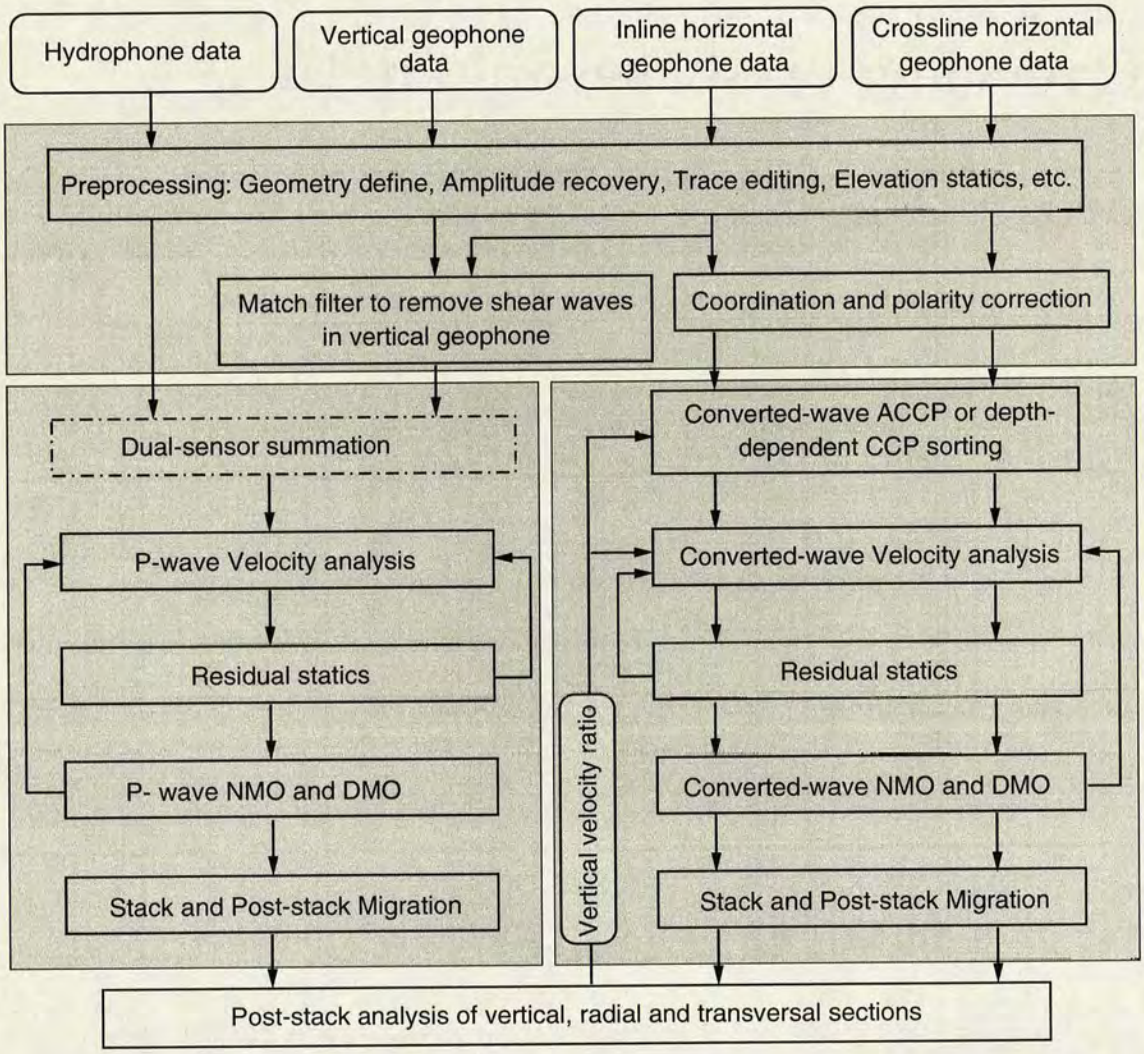

Figure 2.1: The flowchart of 4C data processing. Some iterations are often necessary. Three gray rectangles indicate the three processing stages respectively: 1) preprocessing; 2) P-wave processing and 3) converted-wave processing.

2.1.1 Preprocessing of 4C seismic data

Preprocessing of the four components (hydrophone, vertical geophone, and two horizontal geophones) includes geometry define, true amplitude recovery, trace editing, and elevation datumming.

The true amplitude recovery can be performed by spherical geometric corrections for P- and converted waves, using their respective moveout velocities. Harrison (1992) pointed out that converted wave geometric spreading can be approximately compensated for by using its moveout velocity function and total two-way time, which is similar to that of P-waves.

The datumming, bringing shots and receivers to the same plane, can be achieved by a vertical time shift for shallow water or by wave-equation datumming (Beasley and Lynn, 1992; Bevc, 1995) for medium water depth or deep water (Zhu *et al.*, 1999).

Due to the problem of the present acquisition implementation, the vertical geophone data are often contaminated by shear wave energy leaked either from inline horizontal motion (Yuan *et al.*, 1998) or from crossline horizontal motion (Gaiser, 1998), depending on cable designs. The shear wave energy in the vertical geophone can jeopardize the imaging quality of the P-wave. If the leakage is from the inline horizontal phone, a match filter should be used to remove it from the vertical geophone data (Yuan *et al.*, 1998). If the leakage is from the crossline horizontal phone, a deconvolution approach (Gaiser, 1998) can be applied. These issues will be investigated in more detail in Chapters 3 and 4.

As a vector wave field, shear waves in the two horizontal geophones have specific problems at the preprocessing stage. Firstly, the polarity of seismic events in the inline horizontal geophone reverses across the positive and negative offsets, which needs to be corrected at the preprocessing stage. If the survey area is azimuthally

anisotropic, the polarity in the crossline horizontal geophone will also reverse itself. Furthermore, the signal-to-noise ratio of the crossline component is normally worse than that of the inline horizontal component. Secondly, the inline and crossline geophone data should be rotated into radial and transversal components, if the receiver locations are deviated from the shooting lines. Thirdly, if the three component geophones are mis-orientated, an orientation and rotation procedure (Li and Yuan, 1999c; Li *et al.*, 1999) is required. Chapter 4 discusses the orientation problem in more detail.

In the early development stage of 4C seismic exploration, it was generally believed that a wavefield separation procedure to separate the P- and S-waves must be applied in the preprocessing stage (Amundsen and Reitan, 1995a). Because conventional seismic processing and interpretation prefer to deal with scalar wavefields, it seems natural to decompose seafloor vector measurements into scalar P- and S-wavefields. However, most 4C seismic experiments today reveal that this step is unnecessary (Granli *et al.*, 1999) or does not have significant influence on the following processing. This is because of the presence of low velocity layers near the seafloor, which cause waves to propagate nearly vertically in shallow sediments and separates the waves naturally in the geophone components (see section 3.2). However, wavefield separation may be necessary for areas where a high-velocity seafloor exists (Tatham and Goolsbee, 1984).

2.1.2 *P*-wave processing

The P-wave processing of 4C seismic data is similar to the conventional case. Normal processing techniques, like hyperbolic velocity analysis, residual statics, NMO and DMO stacks, post-stack migration, are also applicable to 4C P-wave processing.

One difference from the conventional processing is the combination of hydrophone

and vertical geophone data for removing or attenuating water-column multiples. Many studies (Barr and Sanders, 1989; Dragoset and Barr, 1994; Soubaras, 1998) have demonstrated the effectiveness of this procedure. However, the success of this procedure is dependent on the sea-floor reflectivity and the acquisition systems deployed. In areas with sea-floor reflectivity higher than 0.3 where an arrayed acquisition system is used during acquisition, the multiples (source- and receiver-side water-column reverberations) in the vertical geophone component are often insignificant. As a result, the summation of vertical geophone and hydrophone signals can often degrade the data, as shown in section 3.1.

2.1.3 Converted wave processing

At the present stage of 4C seafloor seismic acquisition, only airgun sources, which are generally just a few meters below the sea surface, are used. As the airgun source only generates compressional waves propagating in the water, the shear waves recorded from the horizontal sensors are inevitably mode-converted waves. In early years, (Berg *et al.*, 1994), there was a misunderstanding about where the effective *P*- to *S*- conversion takes place. Berg *et al.* (1994) initially processed their data assuming that the conversion took place at the seafloor so that the converted-waves had symmetric ray paths with regard to the seafloor, and conventional *P*- wave processing tools could be used. Today, it is generally accepted that the conversion is actually taking place at the deep reflectors (Yuan *et al.*, 1998; Zhu *et al.*, 1999), as shown in Figure 1.1: This implies that the converted-waves have an asymmetric raypath. Consequently the data processing procedures should be modified accordingly (Figure 2.1). Thomsen (1999) referred to the shear waves generated by this type of conversion as *C*-waves.

Note that in some cases, the seafloor can become a dominant source of mode-

converted energy (Tatham and Goolsbee, 1984). Before processing of shear wave data, evidence should be collected to identify the type of conversion, as shown section 3.2.

Since most marine shear waves acquired today are waves converted from the deep reflectors, the converted-wave processing techniques in this thesis are based on the asymmetric ray path with a down-going P-wave leg and an up-going S-wave leg. In the following sections, I discuss the present processing techniques, such as converted-wave binning, velocity analysis, NMO, DMO and migration of converted waves in isotropic media. I discuss their limitations and some possible improvements. More advanced techniques are presented in Chapter 5 for layered isotropic media, in Chapter 6 for layered TIV media (transverse isotropy with vertical symmetry axis), and in Chapter 7 for layered TIH media (transverse isotropy with horizontal symmetry axis).

2.2 Geometry of converted waves

It is commonly known that the raypath of a mode-converted wave from a reflector is asymmetric, even for the simplest isotropic homogeneous case. As shown in Figure 2.2, a P-wave takes off from the source, impinges onto a reflector where it is converted at point CP, then travels back as an S-wave to the receiver. The traveltime can be written as:

$$t_c = \frac{1}{V_p}\sqrt{x_c^2 + z^2} + \frac{1}{V_s}\sqrt{(x - x_c)^2 + z^2}, \tag{2.1}$$

where V_p and V_s are P- and S- wave velocities, respectively, x is the source-receiver offset, x_c is the conversion point offset from the source point, and z is the reflector depth.

The accurate determination of the conversion-point has been discussed by many authors (Tessmer and Behle, 1988; Zhang and Robinson, 1992). Tessmer and Behle

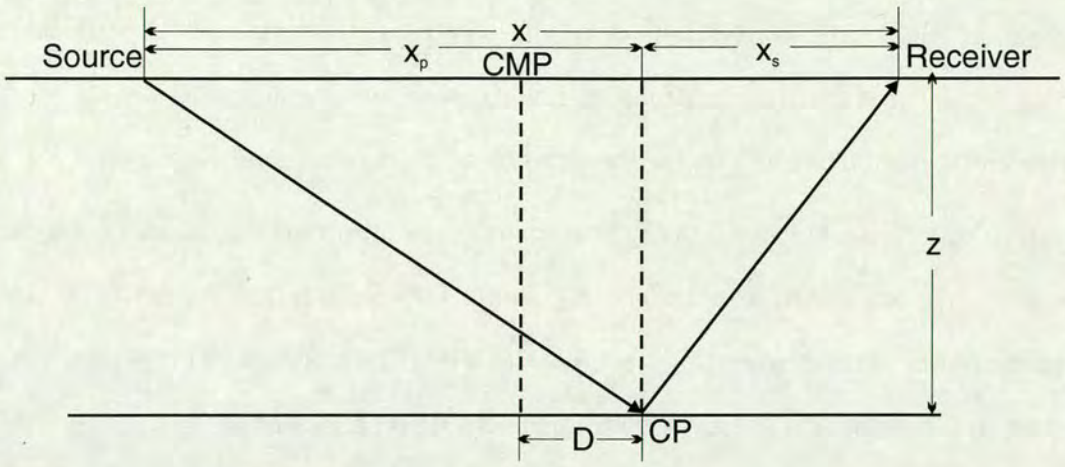

Figure 2.2: The ray-path of a *P-SV* converted wave.

gave an analytic solution, by finding the roots of the fourth-order polynomial equation

$$D^4 + (z^2 - \frac{x^2}{2})D^2 - z^2 mxD + \frac{1}{16}(x^4 + 4x^2z^2) = 0, \tag{2.2}$$

where D is the distance between the midpoint and the conversion point (Figure 2.2), and

$$m = \frac{(V_p/V_s)^2 + 1}{(V_p/V_s)^2 - 1}.$$

From equation (2.2), it is clear that the conversion-point offset is a function of the velocity ratio, the reflector depth, and the source-receiver offset.

Zhang and Robinson (1992) gave a numerical approach for determining the conversion-point offset by the iterative equation

$$x_c^{(new)} = \frac{\sqrt{\gamma^2 + (x_c^{(old)}/z)^2(\gamma^2 - 1)}}{1 + \sqrt{\gamma^2 + (x_c^{(old)}/z)^2(\gamma^2 - 1)}}x, \tag{2.3}$$

where γ is the velocity ratio of V_p to V_s. This iterative method converges very quickly. For example, if we determine the precision to

$$\Delta = \left|1 - \frac{x_c^{(old)}}{x_c^{(new)}}\right| = 0.0001,$$

then in most cases, the conversion-point offset can be determined with sufficient accuracy after three to five iterations. I find that on an average workstation, the iterative method is 60%-110% faster than the root-finding method of equation (2.2).

Despite this, the exact solution of the conversion-point offset, which involves a lot of square-root calculation, is still relatively computationally intensive; not even the computing power of modern computers makes this less of a problem. Therefore, some approximations, based on Taylor-series expansion, are commonly used in converted-wave processing.

If the source-receiver offset is much smaller than the reflector depth, x_c can be approximated by the first-order Taylor expansion as (Fromm *et al.*, 1985)

$$x_c \approx \frac{\gamma}{1+\gamma} x. \tag{2.4}$$

Equation(2.4) is often referred to as the asymptotic approximation, because it represents the asymptote to the conversion-point trajectory in the limit of small offset-to-depth ratio. It is also interesting to note that the asymptotic approximation is a natural result of the iteration method given by equation (2.3) when offset-to-depth ratio x/z becomes zero.

Figure 2.3 shows how this asymptotic approximation is related to the exact solutions. Note that the horizontal axis is the offset-to-depth ratio x/z. As the offset-to-depth ratio decreases, the asymptotic approximation is much closer to the exact solutions, but for shallow reflectors or larger offsets, this approximation may introduce large errors. When x/z is larger than 3.0, the relative errors given by the asymptotic approximation exceed 15%.

To improve the accuracy, Thomsen (1999) gave a new approximation based on a modified two-term Taylor expansion for both single-layered and multi-layered isotropic media. This is discussed in Chapter 5, and its anisotropic counterpart

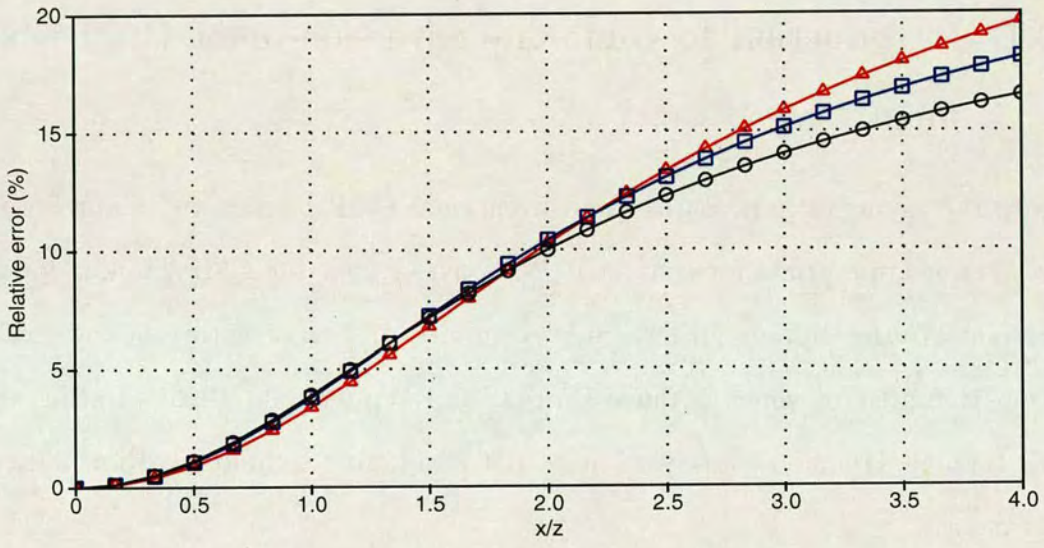

Figure 2.3: Relative errors of conversion-point offsets x_c under the asymptotic approximation in an isotropic homogeneous medium. The relative errors are calculated by $\left(x_c^{(exact)} - x_c^{(approximation)}\right)/x$. The three curves are for different velocity ratios V_p/V_s of 2.0 (triangle marks), 2.5 (square marks) and 3.0 (circle marks), respectively.

is presented in Chapter 6.

Conversion point position has at least two fundamental applications in data processing: converted-wave binning and moveout correction. Although the asymptotic approximation introduces a large error for large x/z, it is still the preferred algorithm for common-conversion-point (CCP) binning at the initial processing stages.

2.3 Converted-wave binning

2.3.1 Introduction to common-conversion-point (CCP) binning

Due to the asymmetric raypath, the conventional CMP binning technique for *P-P* waves is not appropriate for converted *P-S* waves. Applying CMP binning for *P-S* waves smears the dipping structures horizontally, and all structure in the stacked section is shifted by some distance (Frasier and Winterstein, 1990). Rather than CMP binning, common-conversion-point (CCP) binning techniques are usually applied instead.

A few CCP binning methods have been published in the literature, including asymptotic binning (Tessmer and Behle, 1988; Frasier and Winterstein, 1990), depth-dependent trace binning (Tessmer *et al.*, 1990), depth-variant CCP mapping (Eaton *et al.*, 1990; Stewart, 1991), and converted-wave dip moveout (DMO) binning (Harrison, 1992; Alfaraj, 1993).

The asymptotic trace binning is a simple approximation using equation (2.4), and commonly used in the early processing stages. However, this approximate method causes mispositioning of conversion points and loss of spatial resolution at the shallow reflectors.

Depth-dependent trace binning attempts to solve this problem by focusing the

stack to a given depth or layer. For other depths or layers it causes some mispositioning of conversion points, but it is more accurate than asymptotic binning. A full stack section can be constructed from several stack sections corresponding to different reflectors. Obviously, this will introduce more man hours in data processing.

Eaton *et al.* (1990) and Stewart (1991) introduced a depth-variant mapping technique as a substitute binning method for converted waves. Strictly speaking, the depth-variant CCP mapping is not a trace binning method; it is actually a partial migration procedure with a zero integral aperture (Harrison, 1992; Thomsen, 1999). It maps every time sample into an appropriate CCP position on the assumption of a horizontally layered medium.

Like *P*-wave DMO, its counterpart for converted-waves is also a partial migration to remove the effect of dipping reflectors. However, the trajectory of converted wave DMO is no longer symmetric. The lowest point of its DMO trajectory is at the conversion point of zero dip. Thus the DMO procedure for converted wave is also a CCP mapping. Furthermore, a zero aperture DMO is equivalent to a depth-variant mapping (Harrison, 1992).

2.3.2 CCP binning periodicity

The asymmetry of the *P*-*S* ray-path also introduces a further problem which has not been encountered in *P*-*P* wave processing: the binning periodicity of the fold (Eaton and Lawton, 1992), when asymptotic CCP (or abbreviated as ACCP) binning or depth-dependent trace binning is used. The fold in CCP gathers often changes periodically rather than remaining constant, even for a perfectly regular acquisition geometry. Note that partial migration binning methods, such as depth-variant mapping and converted wave DMO, do not suffer from CCP binning periodicity.

Here is a simple example to show the ACCP binning periodicity. Consider an

ideal survey geometry with shooting interval Δs twice the receiver interval Δr and 60 receiver channels. Figures 2.4a and 2.4b show the ACCP fold for velocity ratios

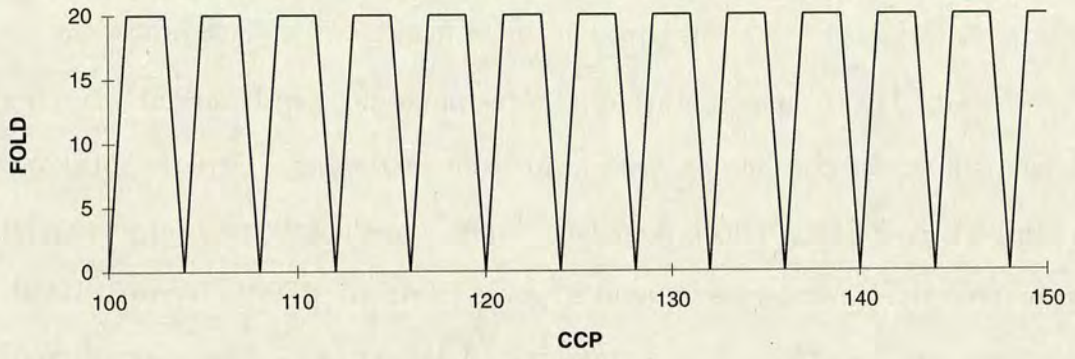

(a)

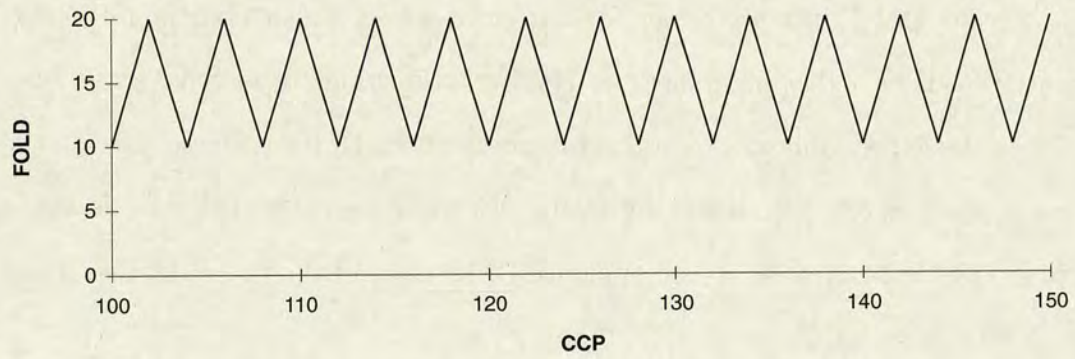

(b)

Figure 2.4: Theoretical fold pattern for CCP binning using (a) $V_p/V_s = 2.0$ and (b) $V_p/V_s = 1.95$. $\Delta s = 2\Delta r$, and the number of receiver channels is 60.

V_p/V_s, 2.0 and 1.95, respectively. For $V_p/V_s = 2.0$, the periodic fold sequence is 0, 20, 20 and 20, and for $V_p/V_s = 1.95$, the sequence is 10, 15, 20 and 15. By changing the V_p/V_s ratio slightly, the fold sequences are changed dramatically, while the overall oscillatory nature of ACCP binning remains.

The reason is quite simple: the interval between two conversion points is, in general, greater than the actual CCP or CMP binning interval. Eaton and Lawton (1992) suggested that satisfactory results can be obtained by letting the CCP binning

width be twice CCP binning interval (at loss of some lateral resolution). However, I find that this does not help much in eliminating the effect caused by fold periodicity (as shown in Figures 2.5a and 2.5b).

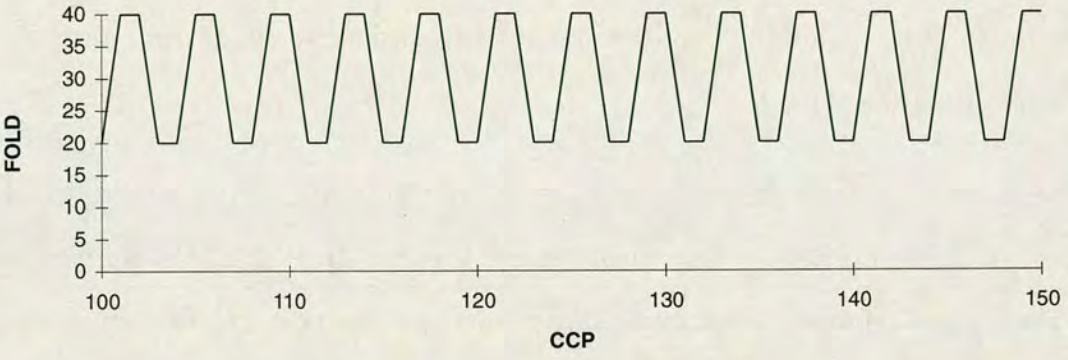

(a)

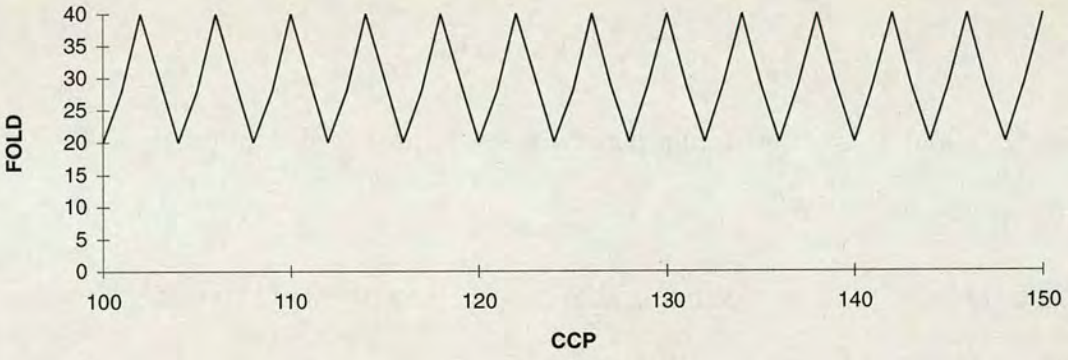

(b)

Figure 2.5: Theoretical fold pattern for CCP binning using (a) $V_p/V_s = 2.0$ and (b) $V_p/V_s = 1.95$. The CCP binning width is twice the CCP binning interval as suggested by Eaton and Lawton (1992). The geometry information is same as in Figure 2.4.

Eaton and Lawton (1992) also suggested that certain considerations at the acquisition stage should be made to avoid empty CCP bins. $\Delta s/\Delta r$ should be chosen so that it is not an integer multiple of the anticipated V_p/V_s ratio, since this leads to empty CCP bins when conventional trace binning is employed. However, this is clearly very restrictive and difficult to implement during the acquisition stage. Be-

fore the data acquisition, one is unlikely to obtain exact V_p/V_s information, which is very sensitive to the fold pattern. For a *P-P* survey, the shot interval is usually an integer multiple of the receiver interval. It is very impractical to design different survey geometries for *P-S* and *P-P* acquisitions because the *P-S* surveys are incorporated with *P-P* surveys by a multi-component recording system at same time for both land or marine surveys.

Therefore, it is more desirable to gain an understanding of the intrinsic fold patterns that are imposed by the acquisition and binning algorithms. For simplicity, here I use the asymptotic approximation to calculate the positions of conversion-points. By modifying equation (2.4), one can get

$$x_c^{'} = s + \frac{r - s}{1 + V_s/V_p} \tag{2.5}$$

where $x_c^{'}$, s and r are the in-line coordinates of the conversion point, shot and receiver group, respectively.

From equation (2.5), in a common shot gather, the interval distance between two conversion-points $\Delta x_c^{'}$ can be written as

$$\Delta x_c^{'} = \frac{1}{1 + V_s/V_p} \Delta r. \tag{2.6}$$

Setting $V_p = V_s$, equation (2.6) yields $\Delta x_c^{'} = \Delta r/2 = \Delta x_b$, which is the common bin width for *P-P* or *S-S* seismic trace gathering. On the other hands, setting $V_s = 0$ leads to the selection of bin width chosen by Eaton and Lawton. In general, the conversion-point interval is somewhat larger than the CCP bin interval. A larger conversion-point interval means that there are some empty CCP bins in a single shot if every trace is collected into only one closest bin. Of course, gathering traces from the whole dataset with many different shots alleviates the effect of empty CCP bins

in a single shot, and helps to allocate traces as equally as possible to the CCP bins. However, it does not always work for all situations, and often still causes the serious problem of fold periodicity. To solve this problem, the basic binning strategy should enable every CCP bin in every shot to get a unique seismic trace, which could be helpful to eliminate or at least minimize the fold periodicity. To achieve this, the best choice implied by equation (2.6) is to select the conversion-point interval for bin width as

$$w = \Delta x_c^{'} = \frac{1}{1 + V_s/V_p} \Delta r \tag{2.7}$$

while keeping the CCP bin interval the same as the CDP bin interval in *P-P* processing. When the conversion-point lies exactly on the edge of CCP bin, in order to get unique trace for each bin, special care should be taken to insure that only the traces on the left or right edge of CCP bins are gathered. The relation between the bin coordinate x_b and the conversion-point coordinate is

$$x_b - \frac{w}{2} \leq x_c^{'} < x_b + \frac{w}{2}$$

or

$$x_b - \frac{w}{2} < x_c^{'} \leq x_b + \frac{w}{2}. \tag{2.8}$$

Figures 2.6a and 2.6b show the fold of CCP by using this binning strategy for both V_p/V_s ratio of 2.0 and 1.95 respectively. It is clear that the fold is nearly constant at 20. The effects of fold periodicity and sensitivity to velocity ratio are both suppressed.

It should be pointed out that when the bin width is wider than the bin interval, we have overlapping bins, and some seismic traces are gathered twice, reducing lateral resolution. But this loss of the lateral resolution is small compared with the *P-S* Fresnel radius, which is usually larger than one hundred meters for the

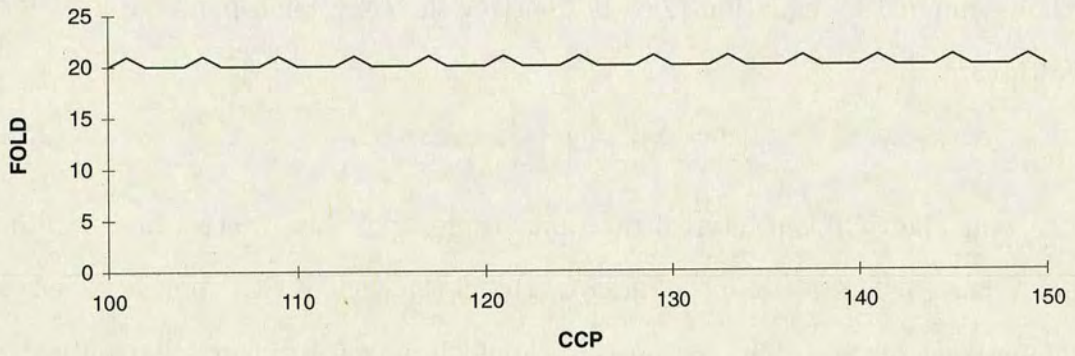

(a)

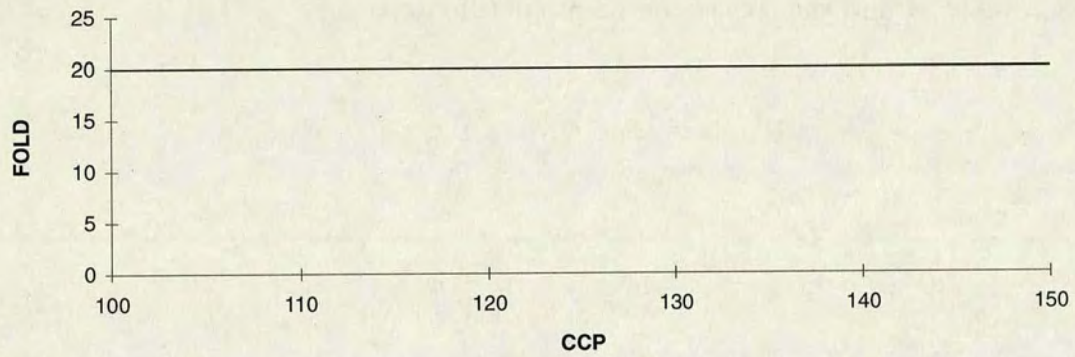

(b)

Figure 2.6: Theoretical fold pattern for CCP binning using (a) $V_p/V_s = 2.0$ and (b) $V_p/V_s = 1.95$. CCP bin size w is $\frac{1}{1+V_s/V_p}\Delta r$. Geometry information is the same as that in Figure 2.4.

P-S converted wave with a dominant frequency from 20 Hz to 40 Hz (Eaton *et al.*, 1991). Because the bin width calculated using equation (2.7) is smaller than Δr, the resolution loss is also smaller than that resulting from using twice the CCP interval as the bin width.

Moreover, the CCP binning periodicity is a problem only for 2D or 3D surveys which use only inline shooting. For a 3D survey with crossline (patch) shooting, CCP binning periodicity vanishes due to wide azimuthal coverage. However, for 3D survey with inline (swath) shooting, CCP binning periodicity may still exists due to limited azimuthal coverage. The binning strategy discussed here can still be applicable in the data processing.

2.4 Converted wave velocity analysis and NMO

The most commonly used converted wave velocity analysis today is based on the hyperbolic moveout equation of short spread (Tessmer and Behle, 1988; Harrison, 1992; Thomsen, 1999). Velocity analysis and NMO are key steps in conventional seismic data processing. Here I give a brief discussion of the methodology.

Tessmer and Behle (1988) show that the moveout curves of converted waves of short spread are hyperbolae given by

$$t_c^2 = t_{c0}^2 + \frac{x^2}{V_c^2} \tag{2.9}$$

where t_{c0} is the two-way converted-wave vertical travel time. V_c is converted wave moveout velocity defined by

$$V_c^2 = V_p V_s. \tag{2.10}$$

Equation (2.9) is the first-order Taylor expansion of equation (2.1) in a homogeneous and isotropic medium. Thus, after the converted-wave data are binned into CCP

gathers, a conventional hyperbolic velocity analysis and NMO stacking procedure, similar to those used with P-waves can be applied to the data. This procedure, together with the ACCP binning procedure, is regarded as standard, and is commonly used to produce an initial velocity field and stacked section during the early processing stages. Like ACCP binning, hyperbolic velocity analysis is also limited. Chapter 5 discusses the issues of limitations and accuracy in more detail and an improved method is also given and tested on synthetic and field data.

2.5 Converted wave DMO

So far the discussion has been based on a horizontally-layered model. In the presence of dipping layers, it is desirable to perform dip moveout (DMO) before the final stack, in order to reduce the reflection point dispersal and to preserve energy of the dipping events which is essential for post-stack migration (Judson *et al.*, 1978). There are three primary different implementations of DMO used today for P-P waves: 1) integral or Kirchhoff summation (Deregowski and Rocca, 1981); 2) Fourier-transform DMO by Hale (1984) and 3) dip decomposition method by Jakubowicz (1990).

With converted waves, besides the usual correction for dipping events like P-P waves, the DMO procedure can also be used to perform CCP binning, as I pointed out in section 2.3. This is because the reflection point is no longer at the midpoint even for horizontal layers. The travel time of the converted wave DMO trajectory in a homogeneous and isotropic medium, was obtained by Harrison (1992) as

$$\tau^2 = \frac{h^2 - x^2}{V_p^2 (h - x) + V_s^2 (h + x)} \left[\frac{V_p^2 (h - x_c) + V_s^2 (h + x_c)}{h^2 - x_c^2} t_n^2 + (x - x_c) \left(V_p^2 - V_s^2 \right) \left(\frac{V_p + V_s}{V_p V_s} \right)^2 \right] \tag{2.11}$$

where τ is the two-way travel time in the DMO trajectory, t_n is the NMO-corrected

time, x is the offset from source to conversion point with dip, x_c is the offset from source to conversion point for zero dip, and h is half the source-to-receiver offset. Harrison's implementation of DMO was based on Kirchhoff summation, which gives good results with integral aperture less than 30°, but produces artifacts of integral aliasing (Hale, 1991) when the integral aperture is greater than 40°.

Alfaraj (1993) also gave a DMO algorithm based on the modified Fourier-transform method of (Hale, 1984). The method does not suffer from the integral artifacts of Harrison's technique, but its DMO travel time trajectory is an approximation, which deviates seriously when the offset-to-depth ratio is large. More seriously, it does not allow the velocity and velocity ratio to change vertically.

To overcome this difficulty, we applied Jakubowicz's (1990) dip decomposition method to converted waves. For a given NMO-corrected time, the horizontal shifts are calculated for a given ray parameter using equation (2.11). The implementation is in the common-offset domain. Figure 2.7 shows an example of the DMO impulse response for a common offset gather. The offset is 1000 meters, the P-wave velocity is 2500m/s and the velocity ratio γ is 2.5. Note that the curved line indicates the conversion points at the zero dip. A series of zero-phase Ricker wavelets with primary frequency of 20 Hertz is used to test the DMO operator. It can be seen that all the travel time, amplitude and phase are all correctly calculated. All the DMO-corrected traces are summed to form a single trace in order to check whether there is any amplitude or phase distortion. The summed trace reproduces the input impulse very well.

2.6 Post-stack migration

Once a stacked section is obtained after NMO and DMO processing, a natural step is to perform a post-stack migration to the section, in order to collapse the diffractions

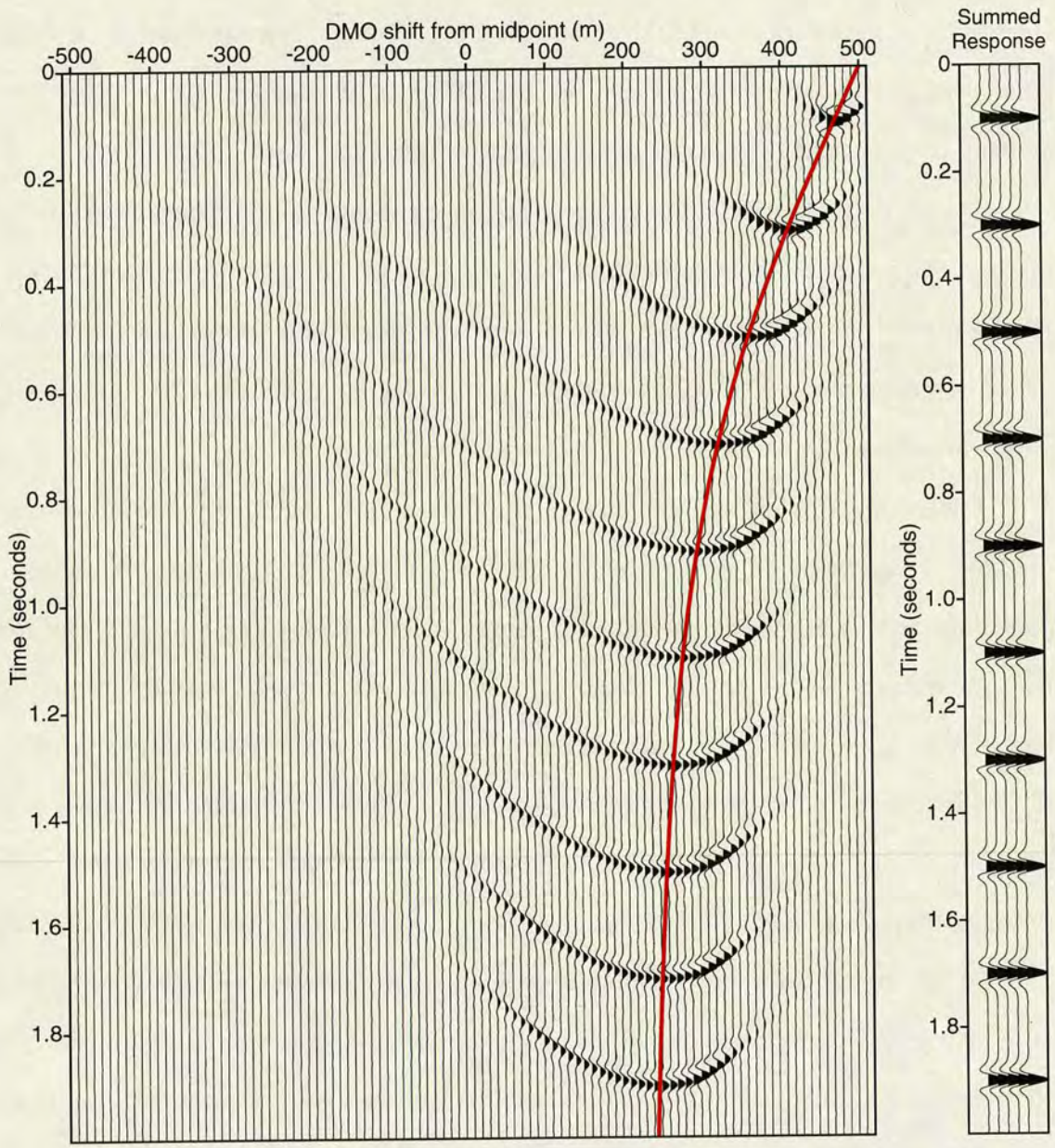

Figure 2.7: Converted wave DMO by dip decomposition method. The input data are a series of zero-phase Ricker wavelet located at the midpoint at the given times. The offset is 1000 meters, $V_p = 2500\text{m/s}$ and $\gamma = 2.5$. The summed response is the summation of all DMO corrected traces. The curved line is the trajectory of the conversion points at zero dip.

and to migrate the dipping events to the proper position. Harrison (1992) has shown that, by ignoring the fourth-order and higher terms, the travel time of the diffraction curve is hyperbolic:

$$t^2 = t_0^2 + \frac{4x^2}{V_{mig}^2} + o(x^4) \tag{2.12}$$

where V_{mig} is the migration velocity. For converted waves, the migration velocity can be obtained by

$$V_{mig} = 2\sqrt{\frac{\left(\sum_{i=1}^{n} \frac{V_{pi}^2 V_{si}}{V_{pi}+V_{si}} \Delta t_{c0i}\right)\left(\sum_{i=1}^{n} \frac{V_{pi} V_{si}^2}{V_{pi}+V_{si}} \Delta t_{c0i}\right)}{t_{c0} \sum_{i=1}^{n} V_{pi} V_{si} \Delta t_{c0i}}} \tag{2.13}$$

where Δt_{c0i} is the two-way vertical travel time of the converted waves. For a homogeneous and isotropic medium, equation (2.13) reduces to

$$V_{mig} = \frac{2V_p V_s}{V_p + V_s} = V_a$$

where V_a is the average velocity of the converted wave. Note that the post-stack migration velocity of the converted wave is different from the hyperbolic moveout velocity in equations (2.10) and (5.19). In normal practice, the migration velocity V_{mig} is 6-11% slower than the moveout velocity V_{c2} (Harrison, 1992).

The hyperbolic nature of equation (2.12) also means that the conventional post-stack migration procedure can be used for the converted waves, if a proper converted-wave migration velocity is used.

2.7 Synthetic data tests

A synthetic dataset is generated by the Seismic Unix modelling routine, `susynlvcw`, which carries out a Kirchhoff synthetic modelling for converted waves in a linear velocity medium. The model consists of two flat reflectors and a reflector with a

45° fault plane as shown in Figure 2.8. A constant P-wave velocity of 2500 m/s and

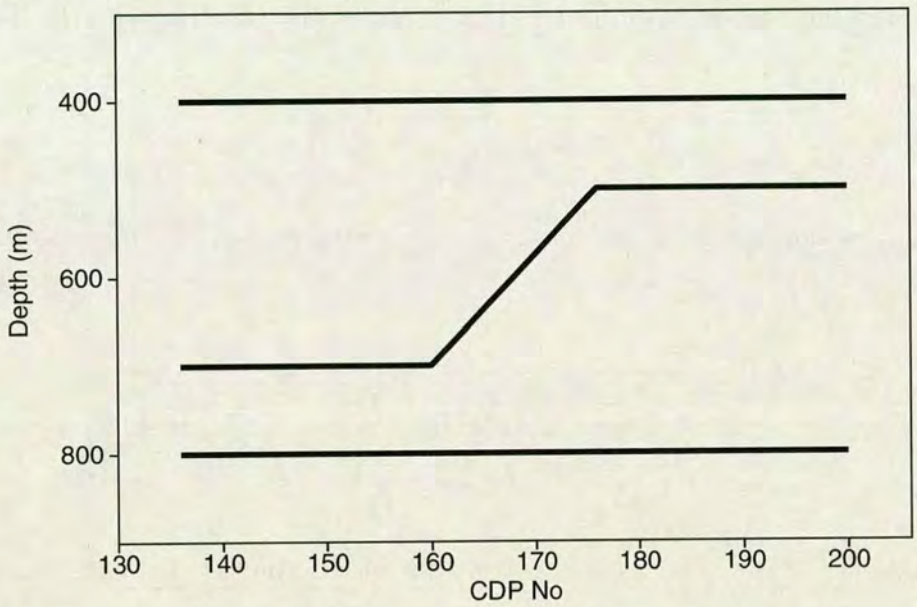

Figure 2.8: Schematic diagram of the synthetic modelling. Shot and receiver intervals are 25 meters, and CDP interval is 12.5 meters.

velocity ratio of 2.5 are used. The shot and receiver intervals are 25 meters, and the CDP interval is 12.5 meters. A zero-phase Ricker wavelet with primary frequency of 20 hertz and frequency band of 0-60 hertz is used.

Figure 2.9a shows a receiver gather at CDP location 168. As `susynlvcw` is a Kirchhoff-based modelling program, the amplitude is not correct. For example, there is no polarity reversal at the near offset. Apart from this, the modelling is adequate for imaging purposes, since it has accurate reflection and diffraction trajectories.

The synthetic data are processed first by NMO correction. The accurate travel time equation (2.1) is used (Figure 2.9b). Then three CCP binning methods are used before the stack, including ACCP binning, true CCP binning and converted-wave DMO binning. It can be see from Figure 2.9c that DMO mapping does not produce any artifacts, and preserves both reflections and diffractions very well. Comparing with Figure 2.9b, the reflection points are moved toward the receiver by the DMO operation. If the survey line is not a dip line, the situation is more complicated and

true 3D DMO is required which is beyond the context of this study.

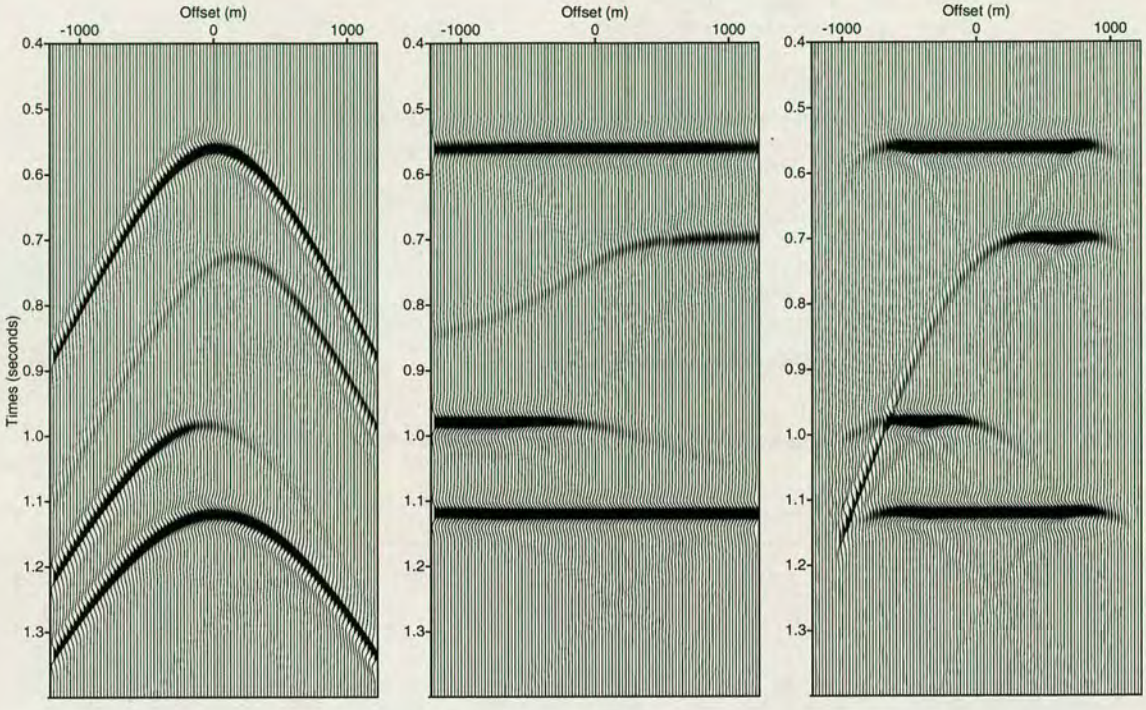

Figure 2.9: Synthetic receiver gathers with receiver location at about CDP 168 (Figure 2.12). (a) unprocessed data; (b) NMO-corrected data using equation (2.1) and (c) DMO-corrected data.

An *f-k* post-stack migration (Stolt, 1978) is performed on the stacked sections to compare the effect of different binning techniques. It can be seen from Figure 2.10 that ACCP can introduce some lateral smearing at the end of the reflector. It is worse for the shallow reflectors. The lateral smearing can be reduced by application of true CCP binning (Figure 2.11). However, the dipping reflection generated by the ACCP binning method appears to be much clearer than that arising from the true CCP binning. This is because the asymptotic approximation can reduce the CCP dispersal for arrivals converted from positive-dip reflectors (Harrison, 1992). If DMO binning is used, the dipping reflector is preserved very well compared with the other two methods, and the lateral smearing disappears as well (Figure 2.12).

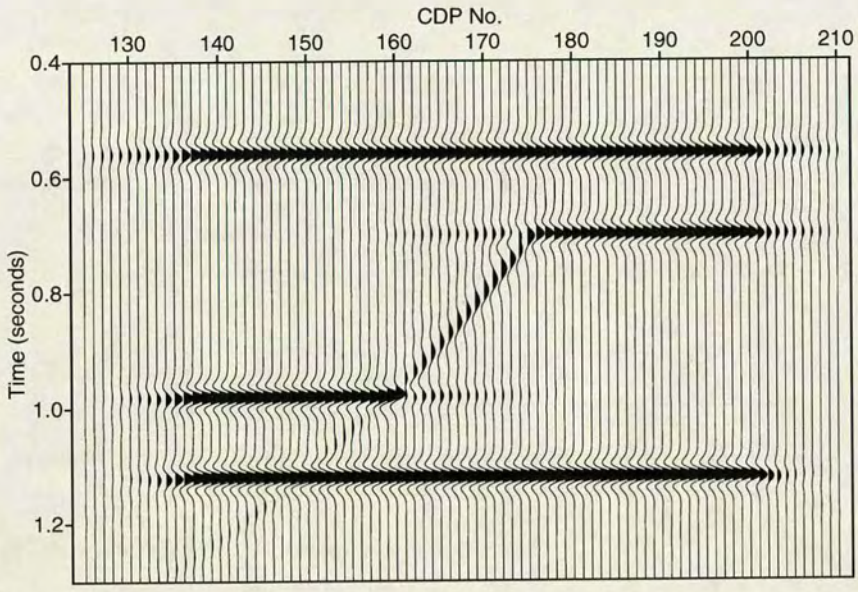

Figure 2.10: Migration section using ACCP binning.

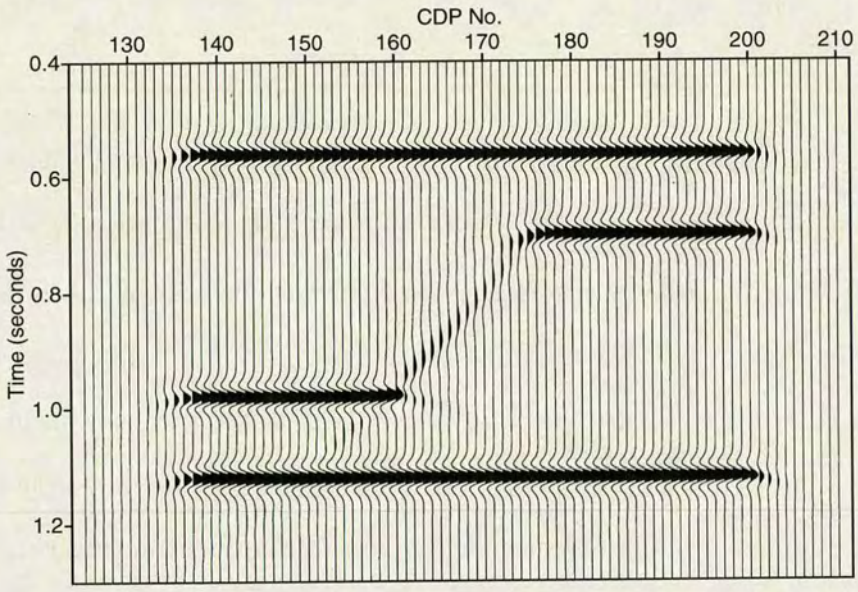

Figure 2.11: Migration section using true CCP binning.

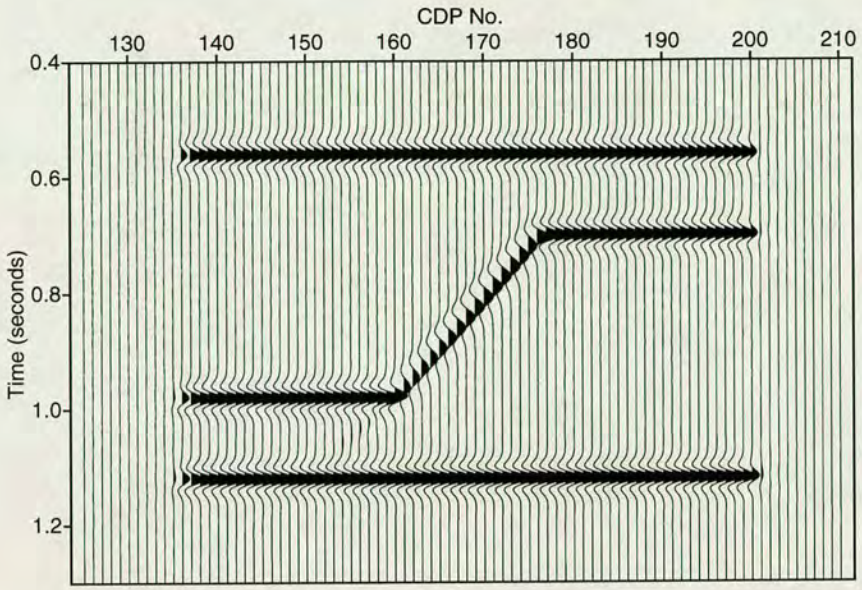

Figure 2.12: Migration section using converted-wave DMO binning.

2.8 Discussion and conclusions

I have given an overview of 4C seafloor seismic data processing, including preprocessing of 4C data, *P*-wave and converted-wave processing. The focus of the discussion has been on the processing of converted waves with asymmetric raypath i.e. the conversion takes place at the deep reflector. The conventional converted-wave processing includes CCP binning, velocity analysis, DMO and post-stack migration. These processing procedures can be implemented either for 2D or 3D. However, the problems may rise in presence of lateral velocity variations. Time processing, such as DMO or even prestack time migration, can not handle the situation very well. Satisfactory solution can be honored through prestack depth migration (Yilmaz, 2001; Herrenschmidt *et al.*, 2001).

In summary, asymptotic binning combined with hyperbolic velocity analysis can be used to generate an initial stack section, which is good for the estimation of processing parameters. To overcome CCP binning periodicity, an improved binning strategy has been given. However, asymptotic binning can introduce lateral smear-

ing for the shallow events. Better images can be obtained through DMO binning. Although true CCP binning can reduce the lateral smearing, it cannot image the dipping events properly, which makes it less desirable in the presence of structure.

Chapter 3

4C Data characteristics and modelling studies

This chapter shows some special wavefield characteristics observed in 4C seafloor data from the Guillemot field in the North Sea (courtesy of Shell Expro), explains the physical reasons behind these phenomena with modelling studies, and discusses their implications for data processing.

The following three issues are addressed:

1. water-column reverberations in the hydrophone and vertical geophone components.

2. where does the *P-S* mode conversion take place?

3. shear-wave energy in the vertical geophone.

Figure 3.1 shows a shot gather at FFID 510, and Figure 3.2 shows a receiver gather at CHAN 2. For comparison, the data are displayed both with and without automatic gain control (AGC). The inline horizontal component has very high amplitudes compared with the vertical component. To correlate the events in the horizontal

and vertical components, a time scaling factor of 2 is used, which corresponds to a V_p/V_s ratio of 3, assuming that the main energy on the horizontal component is the *P-S* wave converted at the deep reflector (see section 3.2). The true amplitude of the crossline horizontal component is small. The overall quality of the data is very good.

3.1 Water-column reverberations

One purpose of a 4C survey is to acquire both hydrophone (pressure) and vertical geophone (particle velocity) data for suppressing water-column reverberation. This is achieved by combining the pressure and particle velocity data using a calibration factor associated with the water-bottom reflection coefficient (Barr and Sanders, 1989). According to Barr and Sanders (1989), and Dragoset and Barr (1994), the method has been widely used.

However, the successful application of the method is dependent on the characteristics of the recorded wavefields. Figure 3.3, after Barr and Sanders (1989) illustrates the basic characteristics required for a successful combination of hydrophone and geophone data. It can be seen that the receiver ghost causes a negative trough at 61ms in the hydrophone data, and a positive peak in the vertical geophone data. The opposite notches and peaks are shown in the amplitude spectra. After combination, the receiver ghost has been removed.

However, we find that our field data exhibit different characteristics from above in the hydrophone and vertical geophone data. The basic characteristics shown in Figure 3.3 are not clear in our data. The autocorrelogram of the hydrophone data (Figure 3.4a) shows clearly the negative trough at a lag of 118 milliseconds, representing the negative-polarity receiver ghost associated with each primary reflection. The second multiple is also shown at a lag of 236 milliseconds. However, the cor-

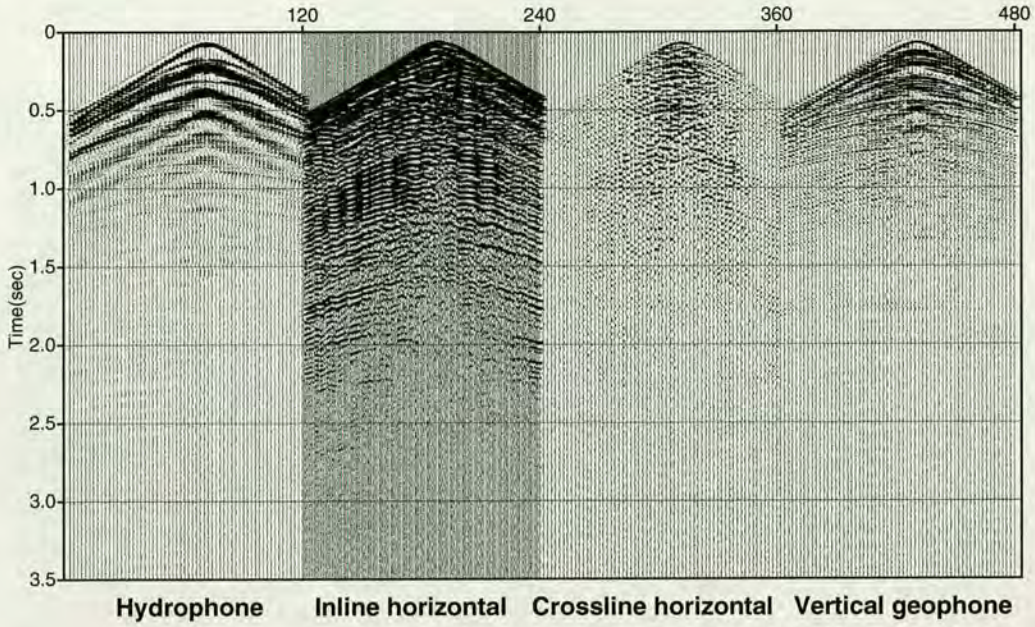

(a)

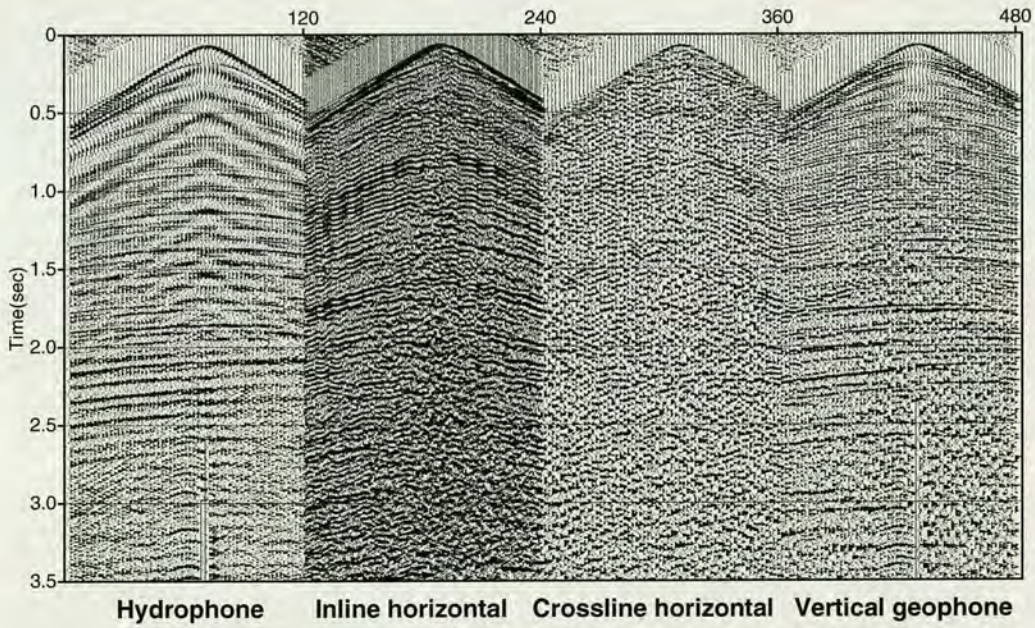

(b)

Figure 3.1: Shot gathers (a) without and (b) with AGC at FFID 510. AGC gate is 500 milliseconds. The four panels of data are from hydrophone, inline geophone component, crossline geophone component and vertical geophone component. The values of the hydrophone data have been scaled down by a factor of 30 to the level of that of the vertical geophone for display purposes. Note that the inline horizontal component is spatially more densely sampled. The channel interval for inline horizontal component is only half of the interval for other components. Details of the acquisition geometry are documented in Chapter 8.

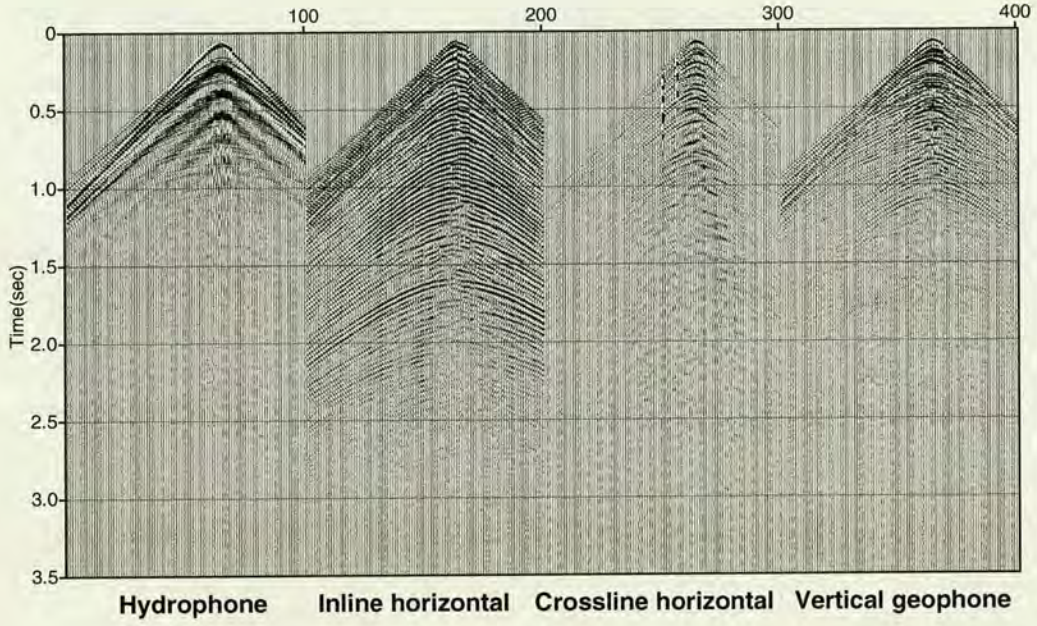

(a)

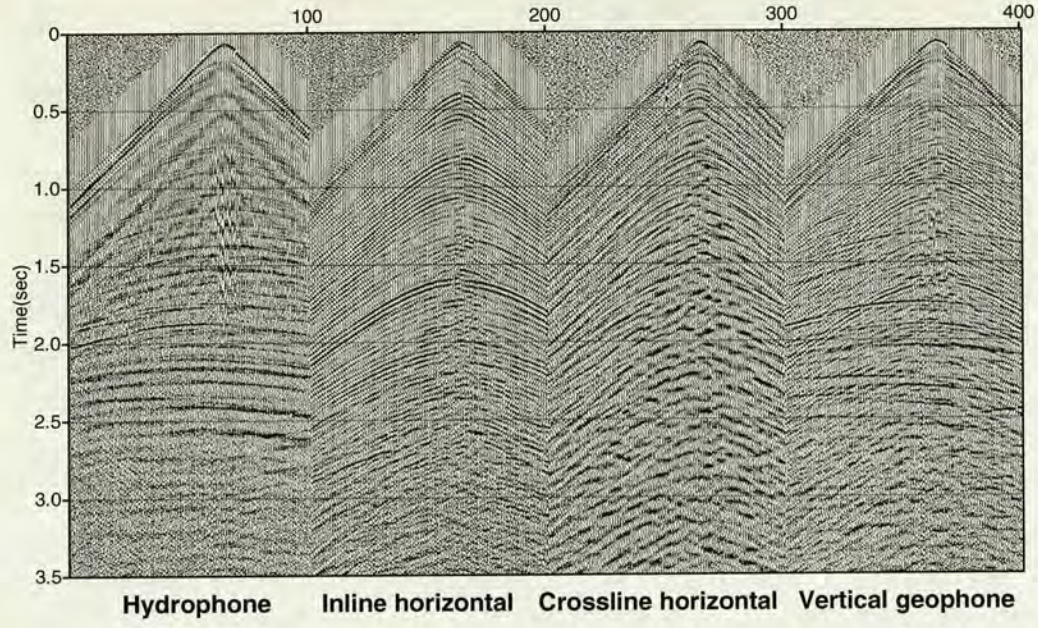

(b)

Figure 3.2: Receiver gathers (a) without and (b) with AGC at CHAN 2. AGC gate is 500 milliseconds. The FFID range is from 450 to 650.

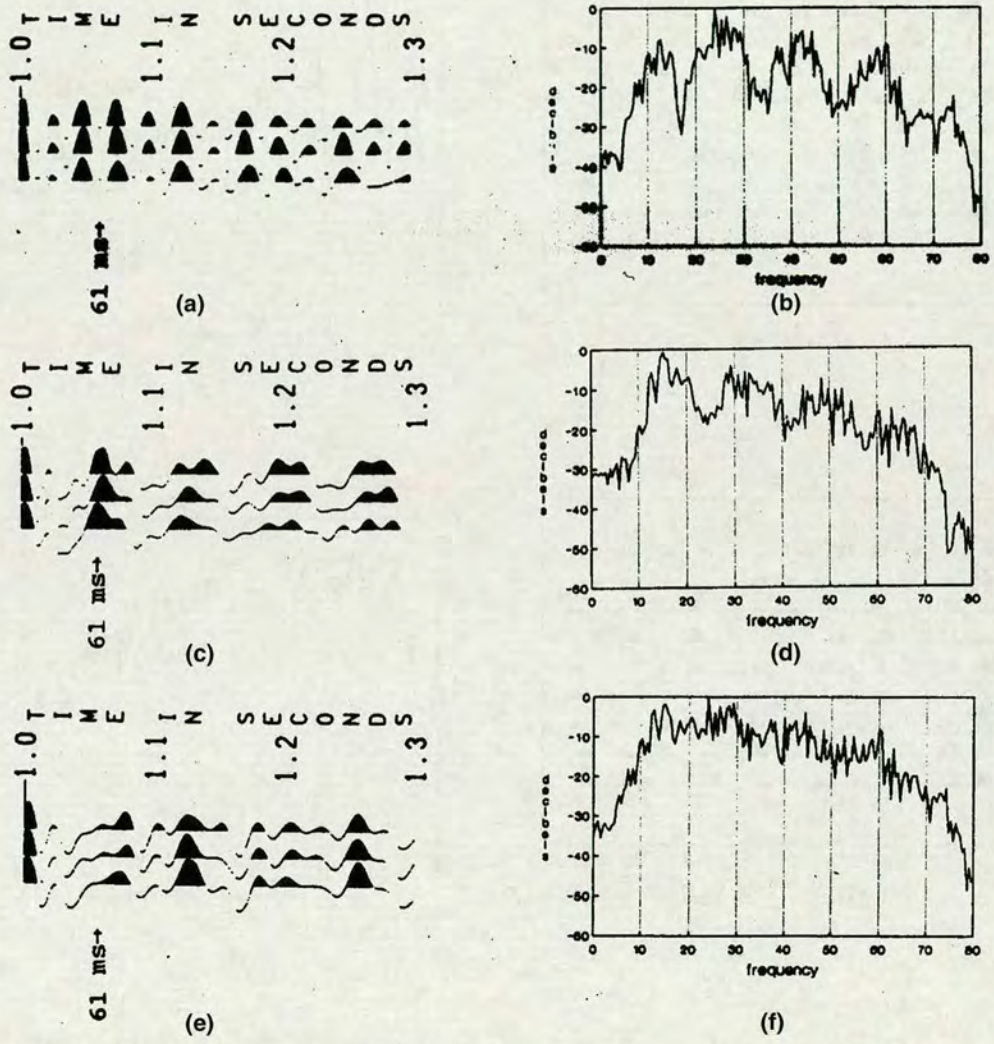

Figure 3.3: The autocorrelograms and average spectra (after Barr and Sanders 1989). (a), (c), (e) are the autocorrelograms of the hydrophone, vertical geophone and the combined data, respectively. (b), (d), (f) are the corresponding average spectra of the data, respectively. The receiver ghost, caused by a 150-feet water layer, is clear at 61ms. Frequency notches are shown in the average spectra.

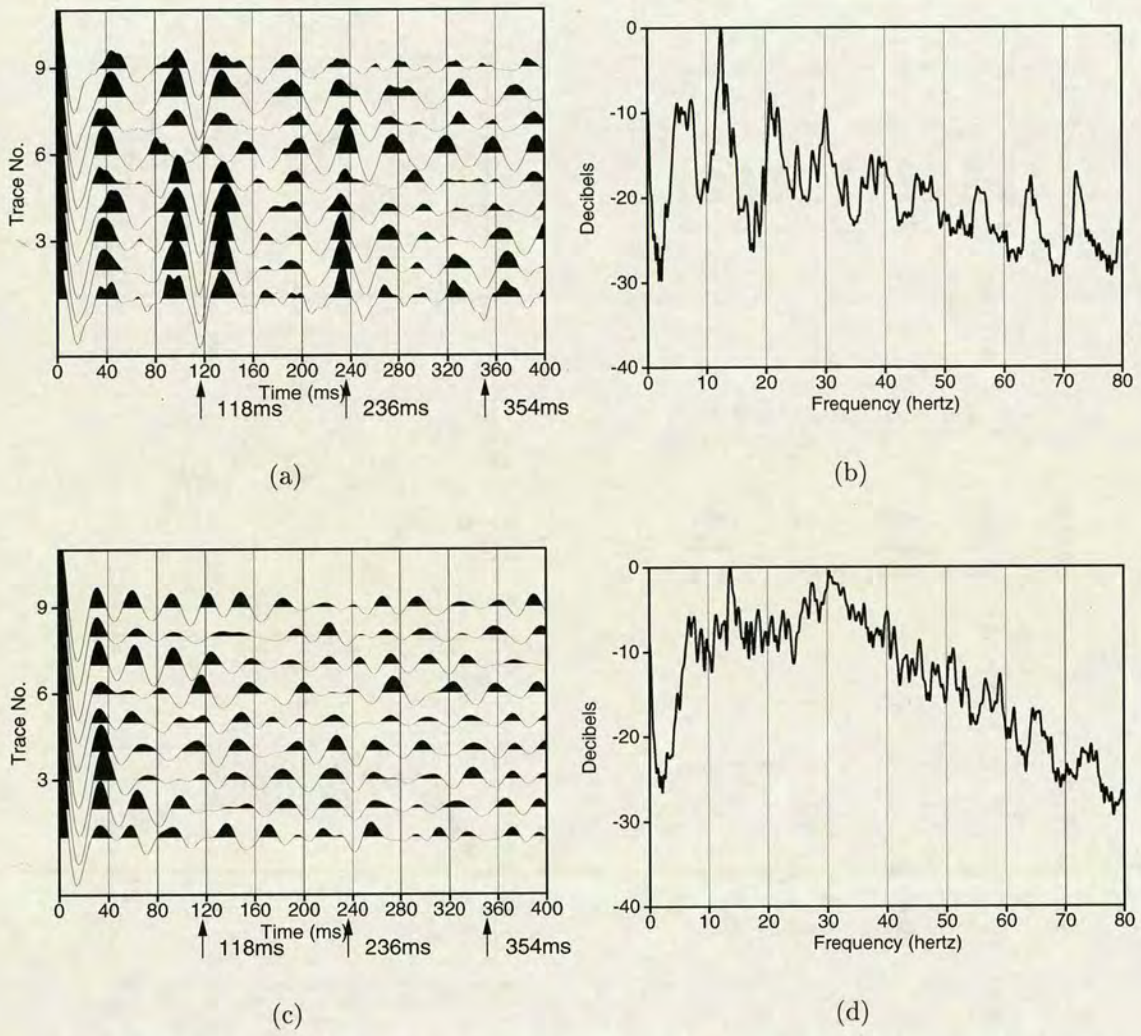

Figure 3.4: The autocorrelograms and average spectra of the Guillemot data. (a) and (c) are the autocorrelograms of the hydrophone and vertical geophone data, respectively. (b) and (d) are the average spectra of the hydrophone and vertical geophone data, respectively. The receiver ghost is expected at about 118 milliseconds, as indicated by the arrow, because water depth is 89 metres. The data are processed by applying true amplitude recovery, first break muting for all the diagrams, while a 10-20-100-120 bandpass filter is used before the autocorrelation to remove the low-frequency reverberations in the hydrophone component (Figure 3.1).

responding positive polarity peak in the autocorrelogram of the vertical geophone data (Figure 3.4c) is ambiguous. This is also true for the amplitude spectra. For 89 metres water depth, the notches caused by the receiver ghost should appear in the amplitude spectrum with a frequency of 8.4 Hz. Theoretically, if the amplitude spectrum of source signal is white, a notch in the pressure (hydrophone) spectrum corresponds to a peak in the velocity (geophone) spectrum, and vice versa. Again, this is not the case for our data. From Figure 3.4b, we can see that the hydrophone data show the periodic amplitude variation as predicted by the theory, but the geophone data have an amplitude spectrum (Figure 3.4d) similar to that of the combined data in Figure 3.3. This implies that the energy of the receiver ghost in the geophone data is very weak, if it exists, and can be ignored.

What happens then to the vertical geophone data? As we know, the water-column reverberation must be there. Next, I try to explain this through the analysis of both the source-side and receiver-side reverberations, and to verify the results using full-wave modelling.

Figure 3.5a shows the source-side reverberations in a water layer with a horizontal

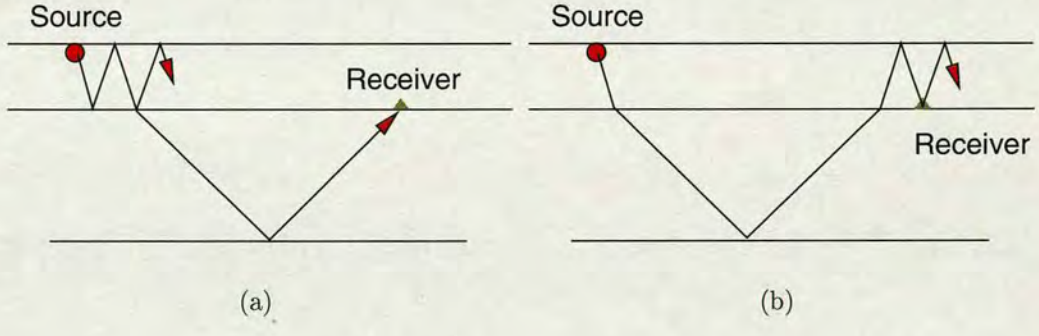

Figure 3.5: (a) Source-side and (b) receiver-side water-column reverberations.

seafloor. The incident P-wave travels down and is reflected up, then down and up

again, and so on. It can be represented by a Z-transform as

$$S(Z) = 1 - K_r Z + K_r^2 Z^2 - K_r^3 Z^3 + \cdots \tag{3.1}$$

where K_r is the seafloor reflectivity. The first term is the primary arrival, then the first multiple, and so on.

Similarly, Figure 3.5b shows the receiver-side reverberations. After the primary arrival, the multiples are bounced between the sea surface and the seafloor. The receiver-side hydrophone and geophone responses were given by Barr and Sanders in 1989 as

$$H(Z) = 1 - (1 + K_r)Z + (1 + K_r)K_r Z^2 - (1 + K_r)K_r^2 Z^3 + \cdots \tag{3.2}$$

$$G(Z) = 1 + (1 - K_r)Z - (1 - K_r)K_r Z^2 + (1 - K_r)K_r^2 Z^3 - \cdots \tag{3.3}$$

where $H(Z)$ is the hydrophone response, and $G(Z)$ is geophone response. Note that the coefficient of the first multiple in the hydrophone is $-(1 + K_r)$, while for geophone it is $1 - K_r$.

The total responses of the hydrophone and geophone can be calculated with equations (3.2), (3.3) and (3.1). This gives

$$H(Z)S(Z) = 1 - (1 + 2K_r)Z + (2 + 3K_r)K_r Z^2 - (3 + 4K_r)K_r^2 Z^3 + \cdots \tag{3.4}$$

$$G(Z)S(Z) = 1 + (1 - 2K_r)Z - (2 - 3K_r)K_r Z^2 + (3 - 4K_r)K_r^2 Z^3 - \cdots \tag{3.5}$$

Thus the first multiple response is $-(1 + 2K_r)$ for the hydrophone, and $1 - 2K_r$ for the geophone. This means that, compared with the hydrophone, the multiple in the geophone is much weaker if the seafloor reflectivity is larger than 0.3. If the seafloor reflectivity is near 0.5, the first multiple term will vanish. Comparing the

theory with the real data results, as shown in Figure 3.4. We find that the seafloor reflectivity in the survey area is likely to be close to 0.3 or higher.

This explanation is verified by full-wave synthetic modelling. The velocity model is constructed from stacking velocity analysis (see Chapter 8). Figure 3.6a shows the velocity model for the shallow layers. The synthetic record is generated by full

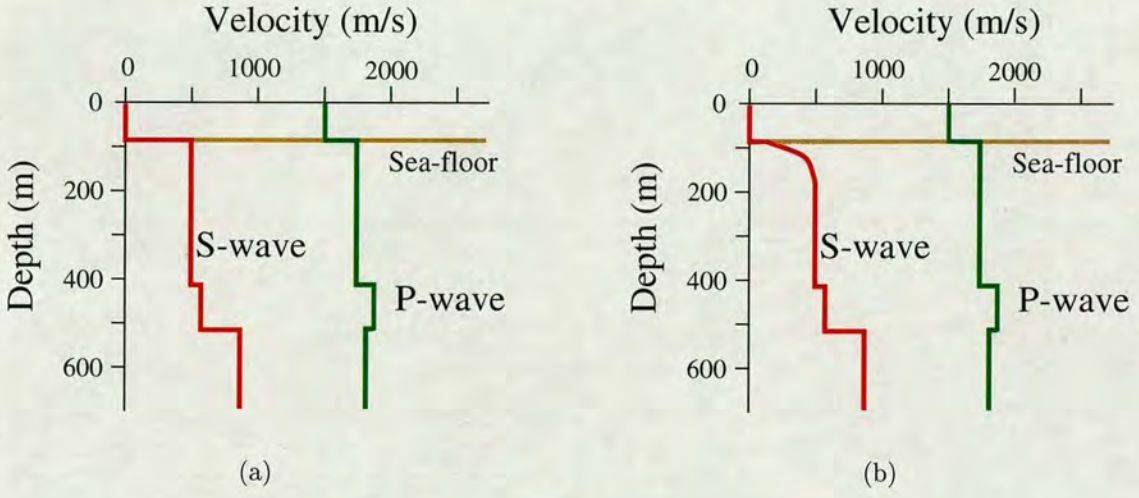

Figure 3.6: Models (shallow layers) (a) without and (b) with shear velocity gradient, corresponding to the synthetic record in Figures 3.7 and 3.10, respectively. The shear velocity gradient is from 100 m/s to 500 m/s in a depth of 90 meters. The density of 2.2 g/cm^3 is used for all the layers except water.

wavefield modelling software ANISEIS (Taylor, 1991) (Figure 3.7). We plot the autocorrelograms and average spectra of both hydrophone and vertical geophone data in Figure 3.8. In the model, the reflectivity of the seafloor is about 0.435. As expected, the hydrophone data show strong multiples at a time interval of 120 milliseconds, while they are almost invisible in the vertical geophone.

Thus, if the reflectivity of seafloor is larger than 0.3 or higher, and the seafloor is nearly flat, the multiple in the geophone data will be very weak and negligible due to the cancelling effect of both source-side and receiver-side reverberations in the geophone component. This "absence" of multiples in the vertical geophone component indicates that it is not necessary to sum the hydrophone and geophone data

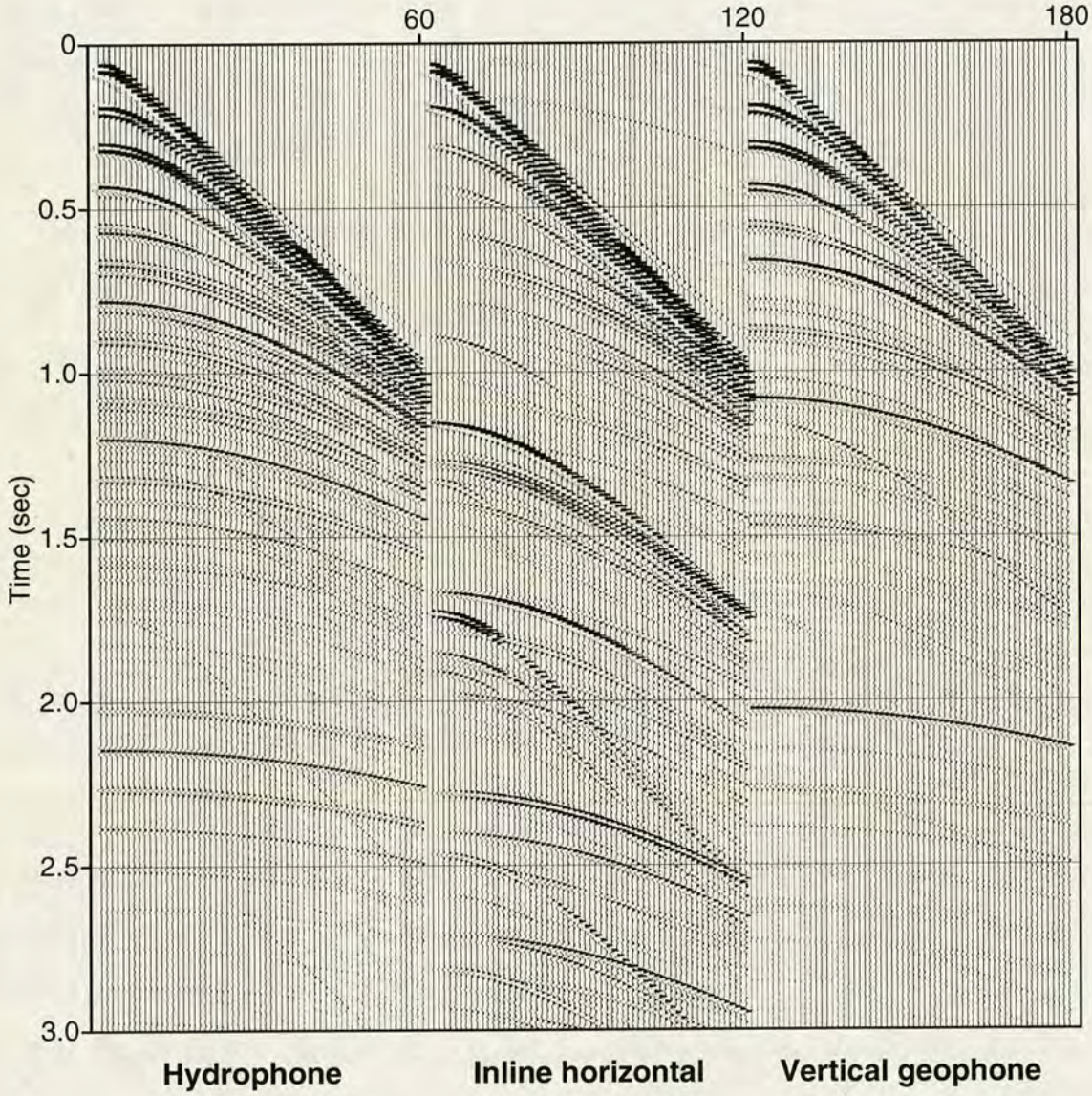

Figure 3.7: Synthetic modelling for analysing water-column reverberations using the model in Figure 3.6a without shear velocity gradient. It is generated by ANISEIS (Taylor, 1991) for water depth of 90 meters. The trace spacing is 25 meters.

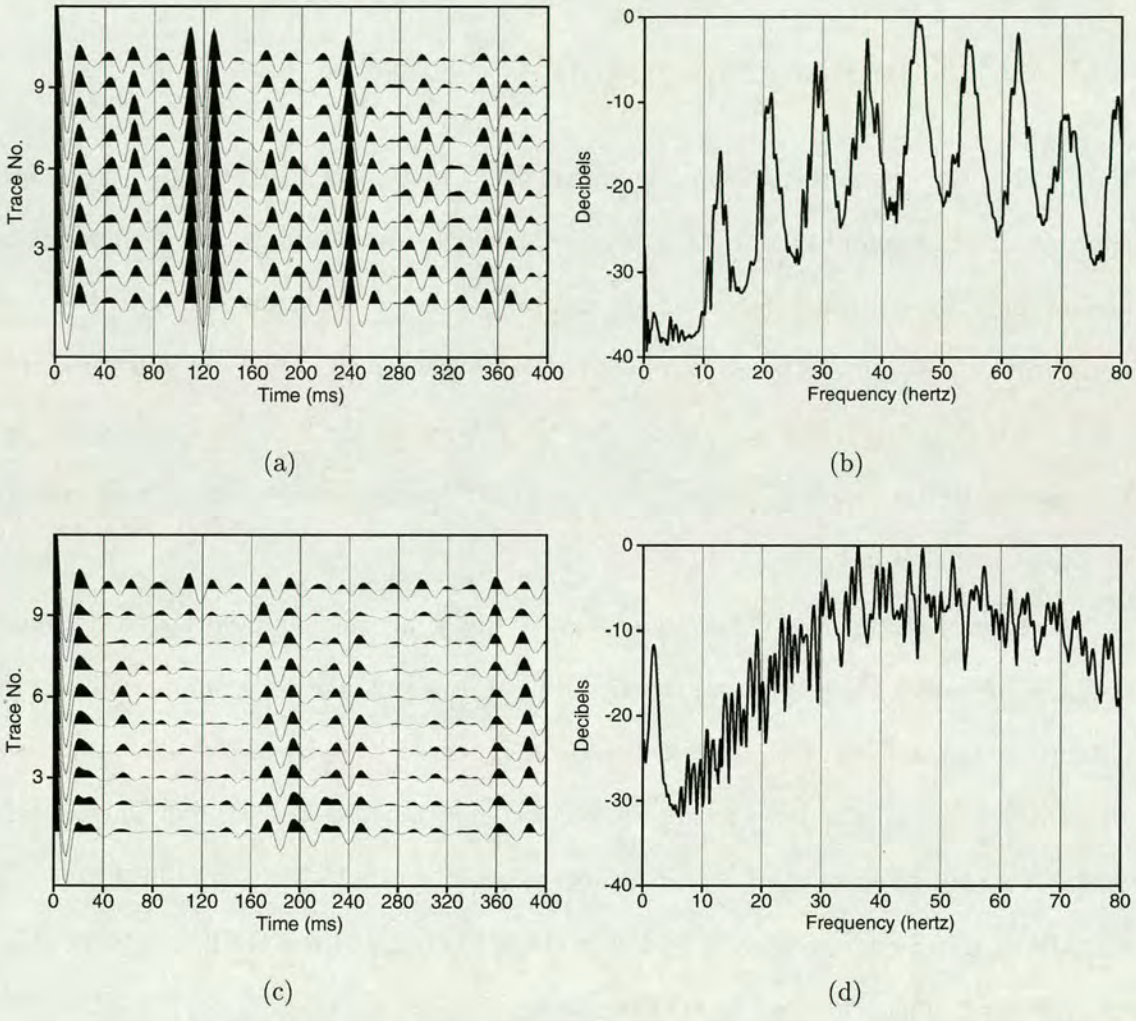

Figure 3.8: The autocorrelograms and average spectra from the synthetic record (Figure 3.7). (a) and (c) are the autocorrelograms of hydrophone and vertical geophone data, respectively. (b) and (d) are the average spectra of hydrophone and vertical geophone data, respectively. The receiver ghost is expected at about 120 milliseconds, as water depth is 90 metres.

if the reflectivity of the seafloor is high. The desired result can be produced by processing the geophone data only. On the other hand, an improper summation of the hydrophone and vertical data can pollute the data.

3.2 *P-S* mode conversion

Here I discuss where the *P-S* mode conversion takes place, an essential point for the design of the appropriate data processing flow. As we know, the seafloor is a strong reflector and the *P-S* conversion can take place at either the seafloor (Tatham and Stoffa, 1976), or at the deep reflector(Berteussen *et al.*, 1997), as illustrated by Figure 1.1, or both. If the conversion is at the reflectors, the *P-S* converted wave (or C-wave in the terminology of by Thomsen (1999)) processing techniques discussed in Chapter 2 should be applied.

In the early days of 4C seafloor survey, it was generally believed that the mode conversion was at the seafloor. It turned out to be a mistake. The mode conversion should be at the deep reflectors, as has been observed in most of the 4C surveys so far. However, it is still dangerous to process the data using an asymmetric ray path without a proper account of where the conversion occurs (Thomsen, 1999).

After careful examination, I find that the conversion in the Guillemot data is at the reflector. There are two lines of evidence.

First, in the shot gathers (Figure 3.1), the events in the vertical geophone and hydrophone components are continuous, while the wobbly effects in the inline and crossline horizontal components show a shear wave static problem. These static shifts are not caused by the elevation of the receivers and the sources, as the water breaks have good alignment for all four components. They are static shifts caused by shear wave velocity variations in the near sea-bottom sediments. In the common receiver domain (Figure 3.2), these static shifts disappear. This indicates that these

shifts are mainly due to receiver statics and one-way *S*- wave ray paths from the reflectors, as the *P*- wave statics are small.

Secondly, the non-hyperbolic moveout characteristic in the horizontal component also confirms that the conversion takes place at the reflectors. As we know, the *P-S-S* type of shear waves, converted at the seafloor, should exhibit hyperbolic travel time when the water layer is not very deep. Figure 3.9a shows CCP gather 1100 before normal moveout correction. Figure 3.9b shows the same gather after conventional hyperbolic moveout correction. The overcorrection at far offsets is evident for the events shallower than 3.0s, especially for the events at 1.6s and 2.2s. Using the non-hyperbolic travel time for *P-S* converted waves, the overcorrection can be extensively compensated (Figure 3.9c).

These two pieces of evidence clearly show that the *P-S* conversion in these data takes place at the deep reflector. The physical reason behind this phenomenon is that the *P*- wave, generated by the airgun source, cannot generate effective mode conversion at the seafloor if the shear velocity at the seabed is too low, as reported by some *in situ* experiments (Theilen *et al.*, 1997). Again, I will use full-wave modelling to verify this. I calculate full-wave synthetics for the two models in Figure 3.6, of which one has a high velocity seafloor and the other has a low-to-high shear-wave gradient.

If the shear velocity of the seafloor is high, as shown by Figure 3.6a which is 500 m/s, both types of mode conversion can be seen in the inline horizontal geophone on the synthetic seismogram (Figure 3.7). By using a shear velocity gradient at the seafloor (Figure 3.6b), the mode conversion at the seafloor can be substantially suppressed (Figure 3.10) .

Comparing Figures 3.7 and 3.10 also reveals a few other interesting characteristics which are worthy of note:

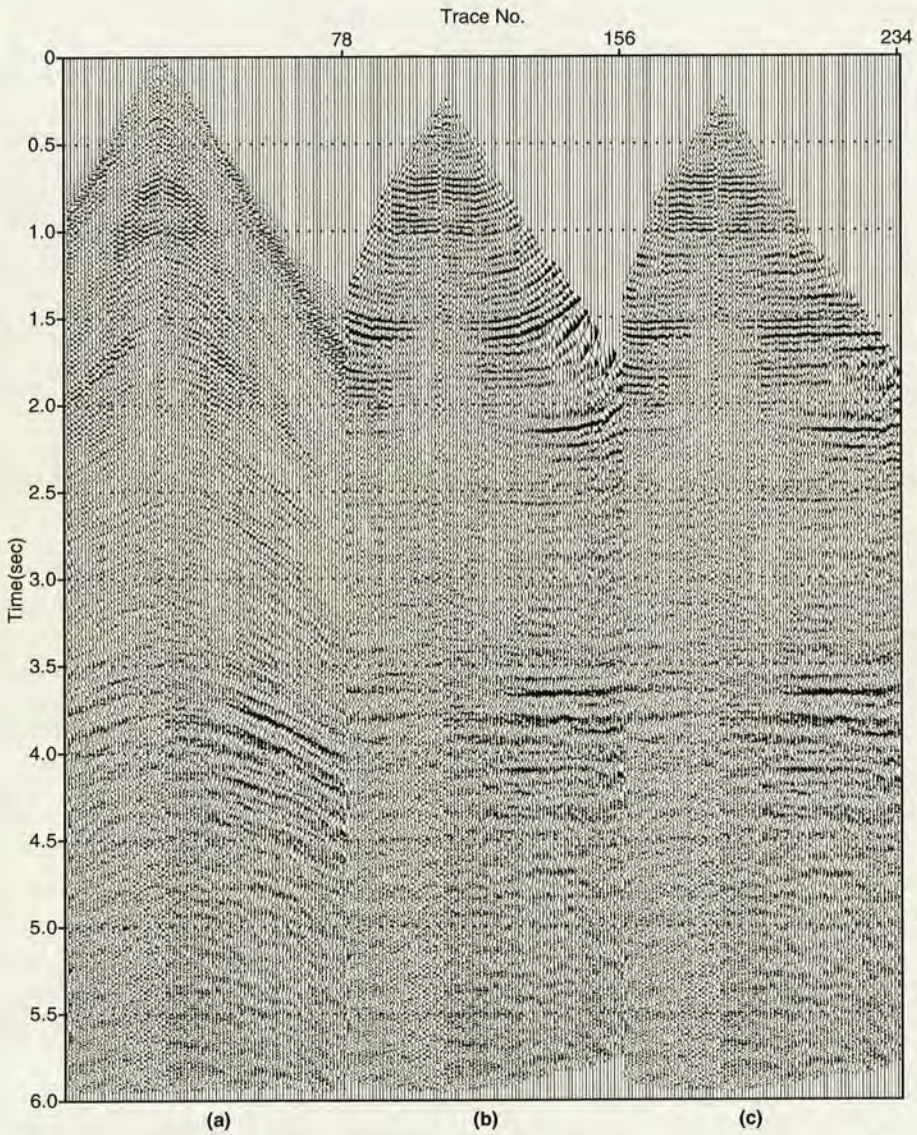

Figure 3.9: Comparison of hyperbolic and non-hyperbolic NMO correction at CCP 1100. (a) before NMO; (b) after hyperbolic NMO; and (c) after non-hyperbolic NMO. A muting gate has been applied to both hyperbolic and non-hyperbolic NMO. The hyperbolic NMO causes over-correction of events before 3.0s, while the non-hyperbolic NMO corrects all events reasonably well. The maximum offset if 2500 meters.

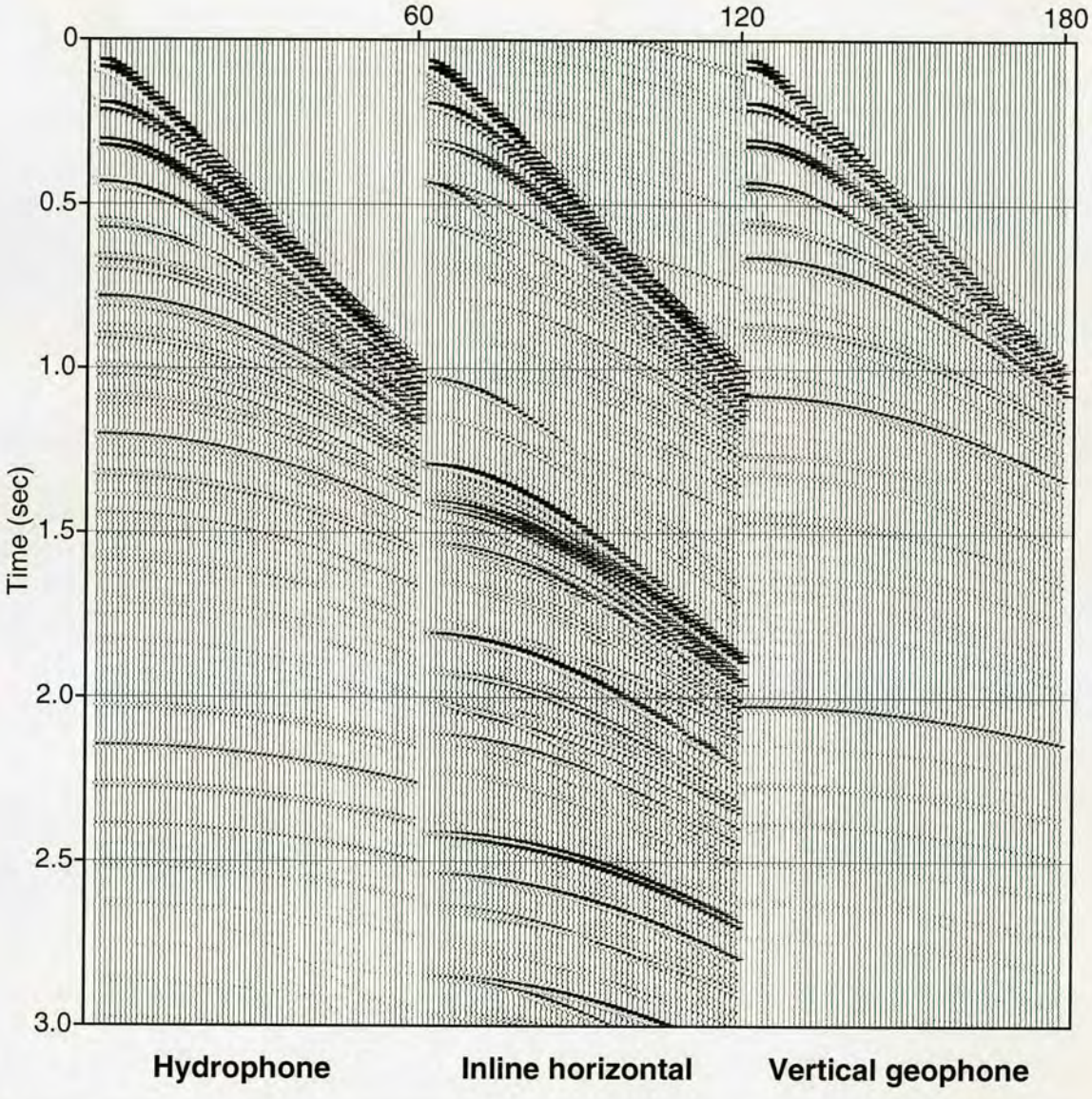

Figure 3.10: Synthetic modelling for analysing water-column reverberations using model in Figure 3.6b with shear velocity gradient. It is generated by ANISEIS (Taylor, 1991) for water depth of 90 meters. The trace spacing is 25 meters.

1. In the presence of a shear velocity gradient, shear energy is suppressed in the vertical geophone, due to its propagation angle being nearly vertical.

2. Mode conversions at seafloor (at 1.7 seconds and 2.4 seconds in the hydrophone data, Figure 3.7) show the feasibility of acquiring shear waves with a towed streamer survey when seafloor shear velocity is high, as was demonstrated by (Tatham and Stoffa, 1976).

3. Low shear velocity at the seafloor leads to a relatively high amplitude in the inline horizontal component (Figure 3.10), which is also shown by field data (Figures 3.1a and 3.2a).

4. The P-wave can have strong influence in the horizontal geophone at early times.

The above synthetic modelling demonstrates that the seafloor *PS* conversion is controlled by the near sea-bottom shear-wave velocity gradient. Probably the earliest research on this topic was done by Kim and Seriff (1992) for towed streamer surveys. They showed that if the shear-wave vlocity at the seafloor is about 1500 ft/s (462 m/s), the amplitude of the *PSSP* events (by down-going *P-S* and up-going *S-P* conversions at the seafloor) is comparable with that of typical *PPPP* events. If the shear-wave velocity at the seafloor is below 500 ft/s (154 m/s), the *PSSP* events are about 30db weaker and probably not visible. These observations hold true for a seafloor survey as is shown by the synthetic modelling.

3.3 Shear waves in vertical geophones

Theoretically, when both *P*- and shear-waves strike the seafloor at non-normal incident angles, both vertical and horizontal geophone components should record these

waves (Figure 3.7). However, if the shear wave velocity of the seafloor is low, only the P-wave can give an effective contribution to the vertical geophone (Figure 3.10). In the Guillemot data, careful examination of the receiver gathers (Fig 3.2) shows that only the vertical geophone recorded both P- and S- waves (Fig 3.2d), and there is no evidence of P- waves present in the horizontal component. Furthermore, the energy of shear waves in the vertical geophones varies with the receiver locations as shown by Figure 3.11. One explanation to this may be that the vertical geophone is

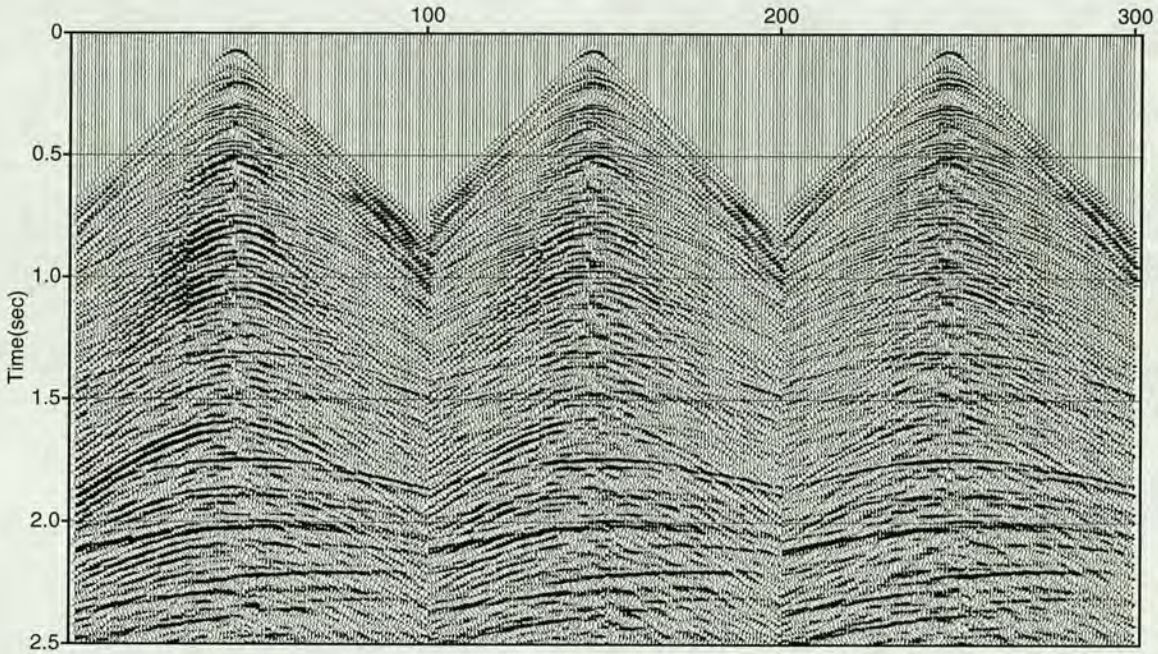

Figure 3.11: Shear wave energy variation in three successive receiver channels in the vertical geophone. True amplitude recovery is applied.

not completely vertical. However, the polarization analysis of the water break (see Chapter 4) has shown that this is not the cause. Other explanations have to be sought.

Figure 3.12 shows the f-k spectra for four components. Note that the transformation time is from 0 - 3.0s, with the water break muted. Comparing Figure 3.12a, the hydrophone spectrum, with Figure 3.12b, the inline horizontal geophone spectrum, shows that the hydrophone recorded mostly P-waves, as expected, whilst the

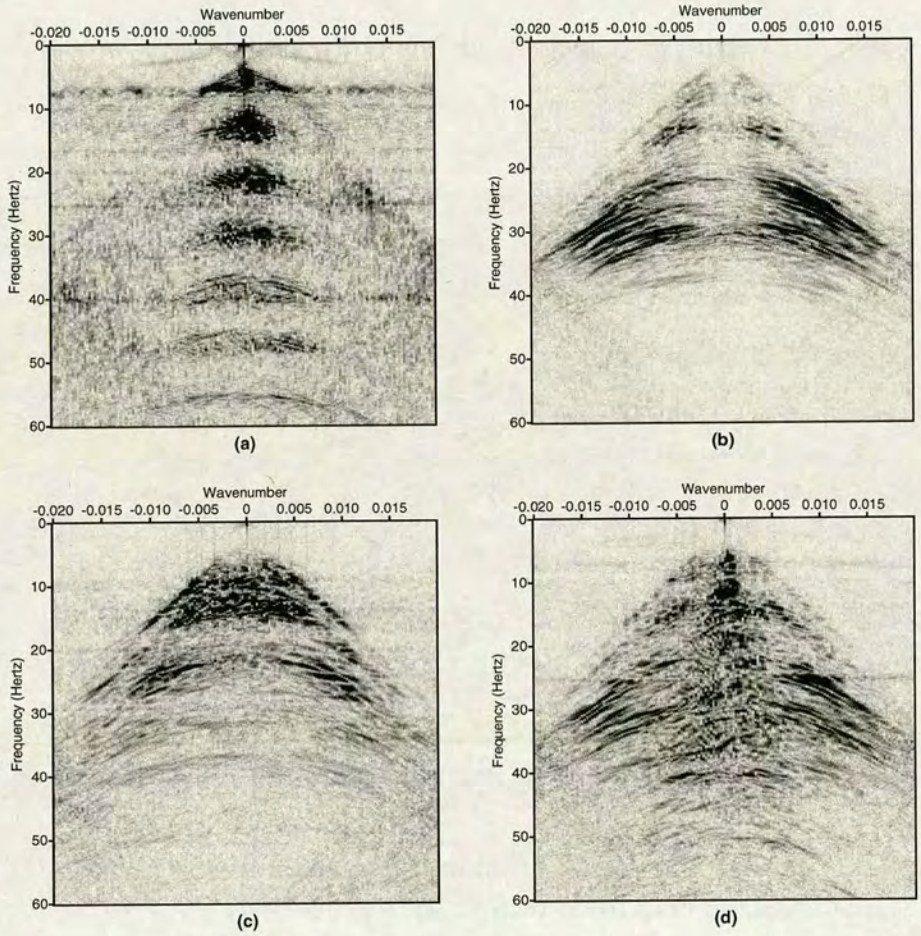

Figure 3.12: *f-k* spectra of the 4C records in Figure 3.2. Note that the transformation time is from 0 - 3.0s, with water break muted. (a) Hydrophone; (b) inline horizontal geophone; (c) crossline horizontal geophone and (d) vertical geophone. The unit of wavenumber is $(\text{metre})^{-1}$.

inline horizontal geophone recorded mainly S- waves, with very little, if any, P-wave energy. However, the vertical geophone, as shown in Figure 3.12d, clearly recorded both P- and shear waves.

As we know, the P-wave velocity in the seafloor sediments is often equal to or slightly above the acoustic velocity of the water (Dunn *et al.*, 1986), and the S-wave velocity is very low (Theilen *et al.*, 1997). Thus one could expect little shear wave energy in the vertical geophone, because the angle of approach should be nearly vertical.

This characteristic has been studied by (Gaiser, 1998). Based on consideration of different acquisition technologies, especially the cable type, he concluded that the the shear wave energy in the vertical phone in the data he analyzed is energy leaked from the crossline horizontal geophone, due to the poor geophone isolation.

To examine why shear-waves are present in the vertical component of the Guillemot data, I calculate the crosscorrelations of the inline and crossline horizontal geophone data with the vertical geophone data (Figure 3.13). There is a clear correlation between the shear-waves in the inline horizontal geophone and those in the vertical geophone (Figure 3.13a) In contrast, there is very little correlation between waves in the crossline and vertical geophone data (Figure 3.13b). Thus, contrary to Gaiser (1998)'s geometry, should there be a leakage from the horizontal components to the vertical component, the leakage would come from the inline rather than the crossline horizontal component.

For the purpose of seismic data processing, this shear wave energy in the vertical geophone is regarded as undesired signals for P- wave imaging. Normally, An f-k dip filter can be applied. However, the f-k filter introduces artificial effects like wormy appearances. Moreover, in the presence of dipping structure, f-k filter has limitations for separating P- and S-waves.

Since we understand that shear-wave energy may come from the horizontal com-

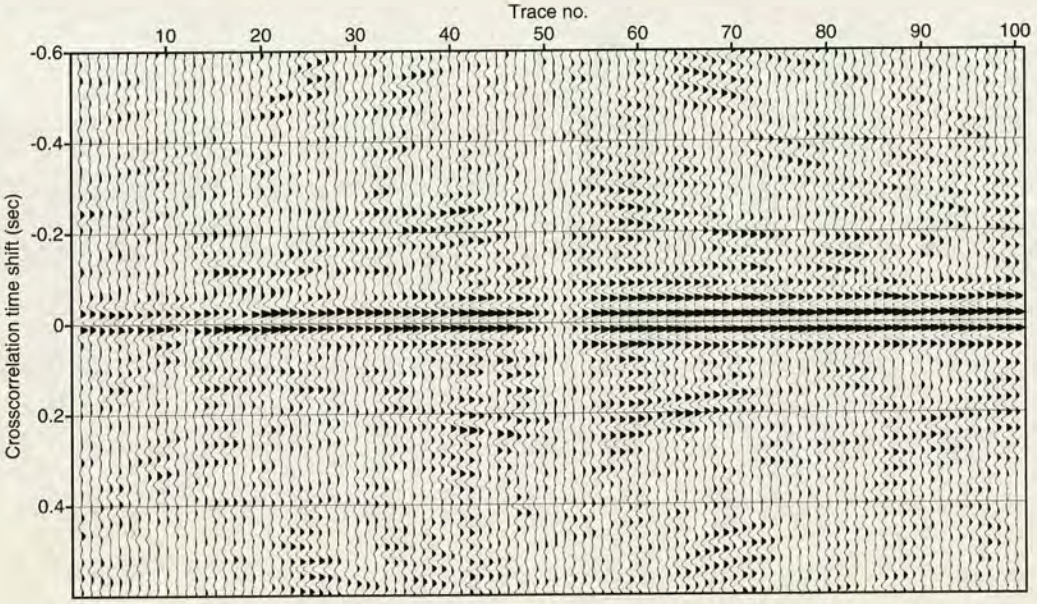

(a)

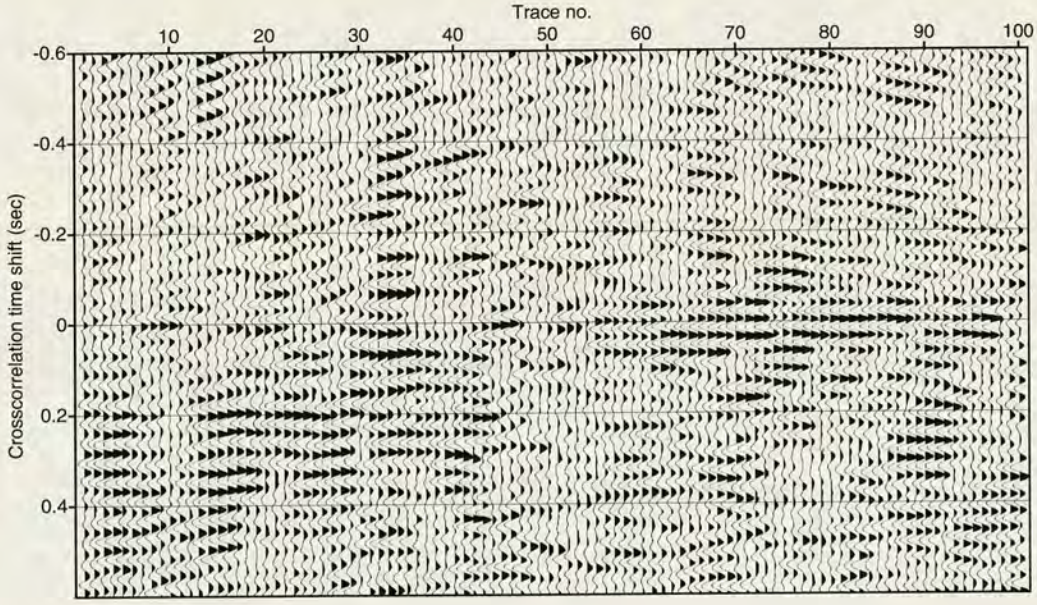

(b)

Figure 3.13: Crosscorrelograms of the (a) inline and (b) crossline horizontal geophone data with the vertical geophone data. True amplitude recovery and water break muting are applied.

ponent, we design a match filter to remove it using the horizontal geophone data as the reference data. The match factor is determined by the crosscorrelation of two components, and a constant time shift is applied as well if there is a time delay in correlation.

Figure 3.14 shows the result of the match filter. It can be seen that most of the shear wave energy has been removed from the vertical geophone.

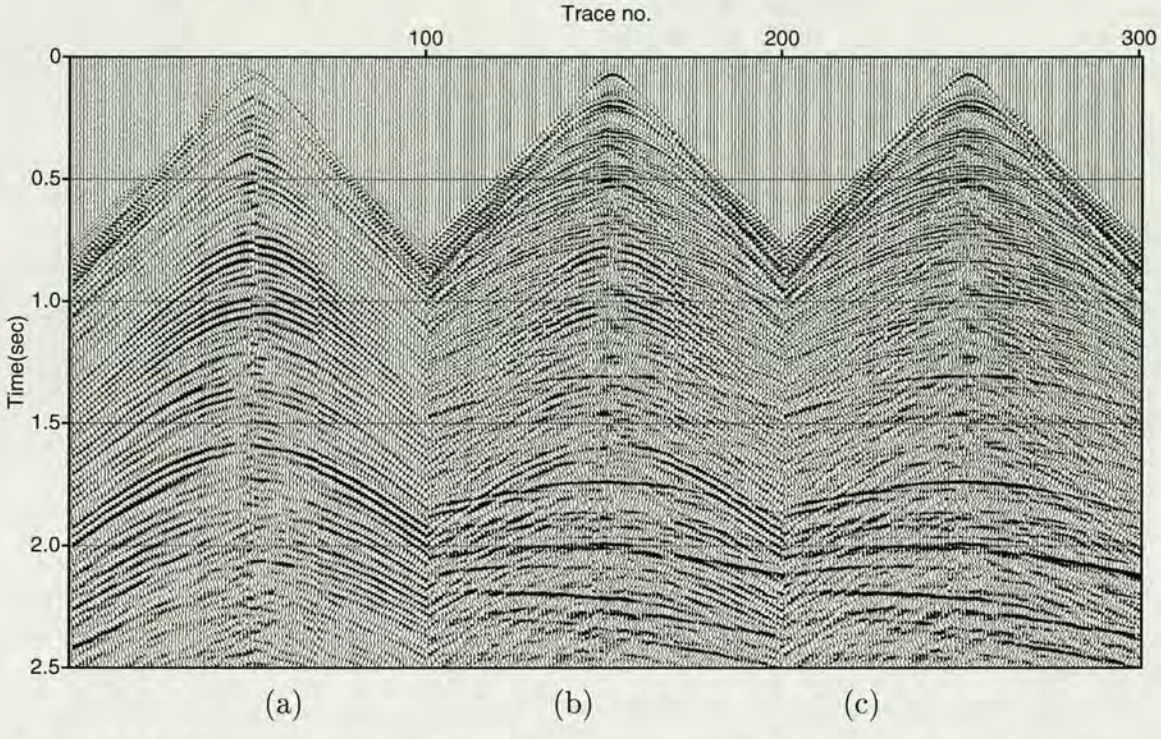

Figure 3.14: Match filter for attenuating shear waves in the vertical geophone data. (a) inline horizontal geophone, (b) vertical geophone and (c) vertical geophone after applying the match filter.

3.4 Discussion

I have discussed several issues related to the data characteristics of the 4C data using both quantitative analysis and full-wave modelling. These include summation of hydrophone and geophone data, type of conversion and geophone coupling. In the early development stages of the 4C technology, there were a lot of misconceptions

of the 4C data. It is important to correct these misconceptions and understand the data characteristics. Here I discuss two additional issues, which are also important for a better understanding of the 4C data and for achieving better imaging.

3.4.1 "Hard seafloor"

A commonly used expression of the marine geophysics is *hard seafloor* or *hard seabed.* In this thesis, I will avoid the words like *hard* or *soft*, as they are inaccurate for describing the property of the seafloor.

The meaning of *hard seafloor* can refer to high reflectivity, which is the case in our field data when dealing with the water-column reverberation. The reflectivity is governed by the *P*- wave acoustic impedance. In our data, the seafloor reflectivity should be 0.3 and above.

However, an alternative meaning refers to the ability to generate an effective mode conversion, which is not the case in our data. The mode conversion at the sea bottom is mainly influenced by the shear wave velocity of the seafloor. If the seafloor shear-wave velocity is below 500 ft/s (154 m/s), the mode conversion at the seafloor is probably invisible (Kim and Seriff, 1992).

3.4.2 Multiples in the horizontal geophones

Up to now, all the published literature on removal of water-column reverberations aims at the hydrophone and vertical geophone data. However, shear wave data in the horizontal geophones can also be contaminated by the reverberations. As I mentioned in section 3.1, although the receiver-side reverberation is very weak, due to the fact the double mode conversion is required, the source-side reverberation is still as strong as the *P*- wave. Of course, the reverberations cannot be as strong as those in the hydrophone data.

Figure 3.15 shows the autocorrelograms and average spectra of the inline horizontal geophone for both the real and the synthetic data. In the field data, the indication of reverberation is not very clear in the autocorrelogram (Figure 3.15a) because of the limited bandwidth of the shear waves, but it is quite clear from its average spectrum (Figure 3.15b). The synthetic modelling (Figures 3.15c and 3.15d) confirms this observation as well.

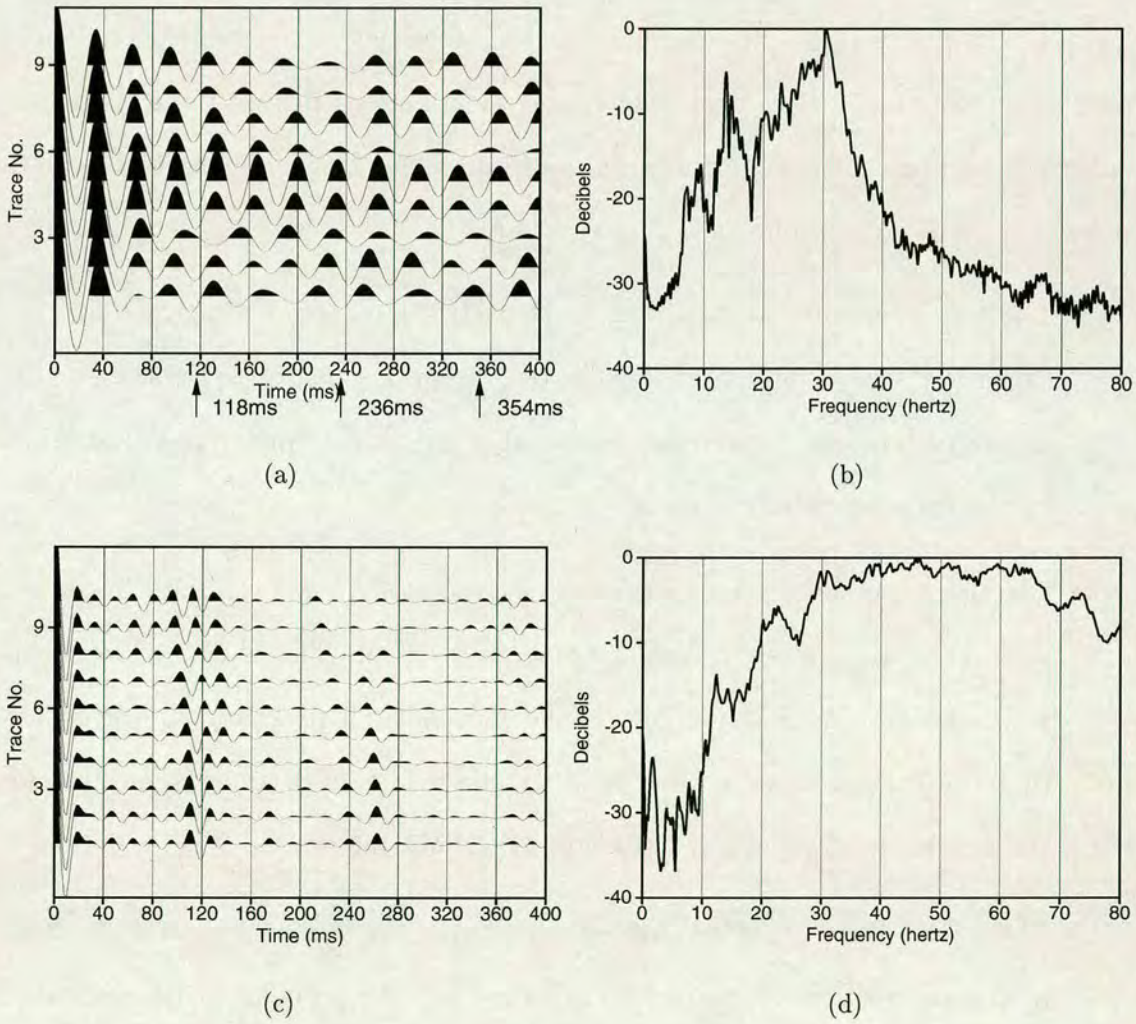

Figure 3.15: The autocorrelograms and average spectra of the inline horizontal geophone. (a) and (c) are the autocorrelograms of field (Figure 3.1) and synthetic data (Figure 3.10), respectively. (b) and (d) are the average spectra of field and synthetic, respectively.

The technology of summation of hydrophone and geophone data cannot be used for removal of the multiples in the horizontal components, and the conventional deconvolution can not effectively collapse the reverberations into the original wavelet for water depths greater than about 10 meters (Barr, 1997). This issue may become significant when a high quality imaging of shear waves is required.

3.5 Conclusions

So far I have analyzed the data characteristics of 4C seismic data using the Guillemot data as an example. I have explained the physical reasons behind these characteristics with numerical modelling, and have also discussed their implications for data processing. The conclusions for this chapter are:

- The water-column reverberations in the vertical geophone are very weak, because the source- and receiver-side reverberations cancel each other in the geophone response and reinforce each other in the hydrophone response, when the seafloor reflectivity is high.

- The shear-wave energy in the horizontal geophones comes from the *P-S* conversion at the deep reflectors, instead of at the seafloor. This is verified by shear-wave static shifts and non-hyperbolic moveout. This characteristic means that the converted wave processing technique should be used to account for the asymmetric raypath and the non-hyperbolic moveout.

- There is an energy leakage of shear-waves from the inline horizontal geophone to the the vertical geophone, due to the coupling problem in the gimballed geophone system, and the energy leakage varies with geophone locations. To compensate for this leakage, a match filter is designed and applied to the vertical geophone data, yielding satisfactory results.

Chapter 4

Geophone orientation

The analysis of shear wave energy in the vertical geophone in Chapter 3 has demonstrated that there may be a geophone coupling problem. This chapter continues to investigate 4C acquisition issues. Here I examine the geophone orientation which is another important issue during data acquisition and preprocessing. I aim to derive processing algorithms for determining the geophone orientation for both gimballed and non-gimballed geophone systems. I also apply these algorithms to the Guillemot data to examine the geophone orientation and associated coupling issues.

4.1 Introduction

Compared with the dual-sensor OBC recording, 4C OBC recording has proved to be more expensive due to increasing costs in cable manufacture, deployment, and data processing, and also more difficult to acquire due to the considerations for the coupling and orientation of the horizontal geophones.

As discussed in Chapter 1, there are currently various types of acquisition systems for recording 4C seismic data at the seafloor. These include node-based systems with individually-planted sensors, and cable-based systems with either externally

clamped sensor packages, or internally hard-wired sensor groups. Meunier *et al.* (1998) evaluated some of these systems using field tests. Sensors planted by a diver or by a remote operated vehicle often yield good control of coupling and orientation (Pettenati-Auziere *et al.*, 1997). However poor coupling may sometimes arise if re-planting of the sensor is required, which loosens the mud surrounding the node (James Martin, personal communication).

For the cable system with externally-clamped sensor packages, the coupling of the inline geophone is often good, but that of the crossline geophone is often poor and results in leakage of energy to the vertical. Gaiser (1998) examined this coupling problem in more detail and presented a method to filter out the crossline contamination. Furthermore, the converted shear waves are often of low signal-to-noise (S/N) ratio, compared with the *P*-waves, and the system appears to be more suitable for dual-sensor summation (MacLeod *et al.*, 1999). For the cable system with internally hard-wired sensor groups, high quality shear-wave data have been acquired (Figure 3.2), and the coupling of both horizontal phones with the seafloor appears to be better compared with the external sensor packages. However, a leakage of energy from the *inline* geophone to the vertical has been observed as discussed in Chapter 3, and the cause of this will be investigated further here.

This chapter focuses on the geophone orientation and coupling related to the cable system with internally hard-wired sensor groups. For this, processing algorithms are developed to determine the geophone orientation in 4C data both for quality control and for data processing in case of any geophone mis-orientation. The algorithms are based on the polarization of the water break recorded by the geophones on the seafloor, and can be applied for 4C systems in which all three geophone orientations may initially be unknown. I will first examine the effects of varying seafloor properties on the polarization of the water break, and then present the processing algorithms for both gimballed and non-gimballed geophones, followed

by synthetic tests and real data analysis.

4.2 Characteristics of the water break

Consider a 4C geometry with three-component orthogonal geophones on the solid seafloor. $\mathbf{D}(t)$ or $\mathbf{D}_r(t)$ represents the vector displacements at the recording position generated by the air gun,

$$\mathbf{D}(t) = \begin{bmatrix} x(t) \\ y(t) \\ z(t) \end{bmatrix} \quad \text{or} \quad \mathbf{D}_r(t) = \begin{bmatrix} a_1(t) \\ a_2(t) \\ a_3(t) \end{bmatrix}. \tag{4.1}$$

If the geophone is aligned perfectly, x is the inline (parallel to the propagation plane and pointing from the source to receiver), y is the crossline direction (perpendicular to the propagation plane), and z points vertical downwards, forming a right-handed coordinate system; if the geophone is out of alignment, a_1, a_2 and a_3 are the three-orthogonal axes.

To begin with, it is important to examine the effects of varying seafloor properties on the polarization of the water break recorded on the seafloor. Consider two cases: a homogeneous seafloor and a seafloor with a velocity gradient. The seafloor is often a composite of soft sedimentary rocks and the shear-wave velocity changes dramatically near the seafloor (Theilen *et al.*, 1997).

For a horizontal seafloor, the displacements of the water break can be expressed in the oriented coordinate system as

$$\mathbf{D}(t) = \begin{bmatrix} x(t) \\ y(t) \\ z(t) \end{bmatrix} = \mathbf{R}_y(\theta_{pp}) \begin{bmatrix} 0 \\ 0 \\ S(t) * \lambda(t) T_{pp} \end{bmatrix} + \mathbf{R}_y(\theta_{ps}) \begin{bmatrix} S(t) * \lambda(t) T_{ps} \\ 0 \\ 0 \end{bmatrix}, \quad (4.2)$$

where $\mathbf{R}_y$ is the rotation matrix about the y-axis,

$$\mathbf{R}_y(\theta) = \begin{bmatrix} \cos\theta & 0 & -\sin\theta \\ 0 & 1 & 0 \\ \sin\theta & 0 & \cos\theta \end{bmatrix}.$$

$S(t)$ is the source wavelet, $\lambda(t)$ is the wave propagation function in the water, T_{pp}, T_{ps}, θ_{pp} and θ_{ps} are the P-P and P-S transmission coefficients and angles, respectively, when the water break impinges upon the seafloor. These transmission coefficients and angles are dependent on the velocities of the seafloor. As a result, the polarization direction of the water break does not point to the source. Changes in the velocities of seafloor will induce different behaviour of the polarizations of the water break. Full-wave synthetics are used to illustrate these effects.

As in the last chapter, I construct three synthetic models as shown in Figure 4.1: a consolidated seafloor with high seismic velocities, the same consolidated seafloor but with very low shear velocities and an un-consolidated sea-floor with a velocity gradient. The calculated polarizations of the water breaks with different incidence angles are shown in Table 4.1 for these three models. The synthetic data are generated by ANISEIS (Taylor, 1991). Note that the water velocity here is 1500m/s.

As shown in Table 4.1, it can be seen that the polarization directions of the water breaks are dependent on their incident angles and the P- and S-wave velocities of the

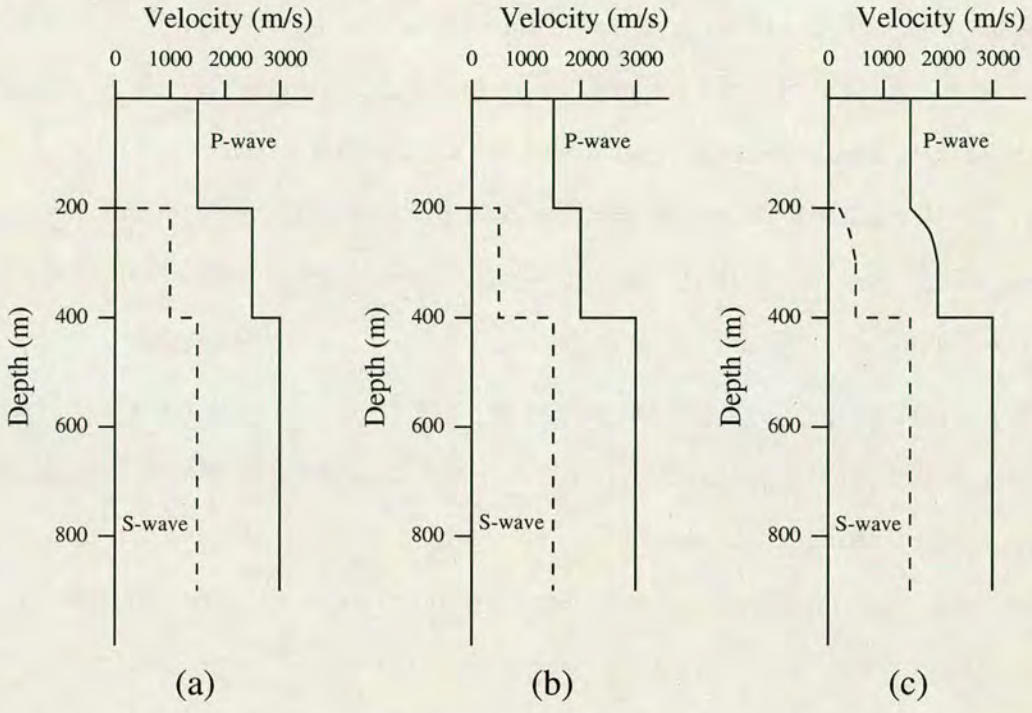

Figure 4.1: Models for water break polarization analysis: (a) a high-velocity seafloor (b) a low-velocity seafloor and (c) a seafloor with a velocity gradient. The solid-lines are P-wave velocities, and the dashed-lines are S-wave velocities.

Table 4.1: Polarization diagrams of the water breaks in the vertical plane $(x - z)$ recorded on the seafloor. (a), (b) and (c) correspond to the models in Figures 4.1a, 4.1b, and 4.1c, respectively.

Incident angles	0°	5°	10°	20°	40°	60°
(a) $v_p = 2500$m/s, $v_s = 1000$m/s						
polarization angles	0°	1.40°	2.95°	7.50°	35.6°	−51.2°
(b) $v_p = 2000$m/s, $v_s = 500$m/s						
polarization angles	0°	3.29°	6.68°	14.8°	42.9°	−82.2°
(c) $v_p = 1500 - 2000$m/s, $v_s = 50 - 500$m/s						
polarization angles	0°	4.32°	8.57°	17.5°	36.0°	56.9°

seafloor. For a high-velocity seafloor (Table 4.1a), the polarization direction of the water break are significantly deviated from the incident direction, and the deviation increases with incidence angle and with velocity. For a low-velocity seafloor (Table 4.1b), the deviation between the incident and the recorded polarization direction is significantly reduced. In both cases, the water breaks are linearly polarized before the critical angle, and the critical angle increases as the seafloor velocities decrease.

For a velocity gradient, on the assumption of an elastic seafloor whose density, P- and S-wave velocities increase with depth, I can use a series of fine layers to simulate the gradient. As shown in Table 4.1c, the polarization directions of the water breaks are mainly determined by the properties of the medium immediately below the seafloor, and the effects are similar to those of a low-velocity seafloor. When the S-wave velocity of the seafloor is very low, and P-wave velocity is near to the water velocity, the polarization angles are near to the corresponding incident angles, and the polarizations are very linear.

4.3 Processing algorithms

Here I consider two cases. In the first case, the geophone is gimballed within the cable, so that one of the axes (assuming a_3-axis) is always vertical. In this case, we need to determine the orientation of the two horizontal geophones (a_1 and a_2, Figure 4.2). In the second case, a non-gimballed geophone system is assumed and it is needed to determine all three geophone orientations. All the algorithms are derived based on polarization analysis, of which some basic concepts are enclosed in the Appendix A.

Note that if a dual-gimballed system is used, or if a gimballed crossline-geophone system is deployed on a horizontal seabed, all three orientations are known. In such cases, the processing algorithms may be used for quality control. If a gimballed

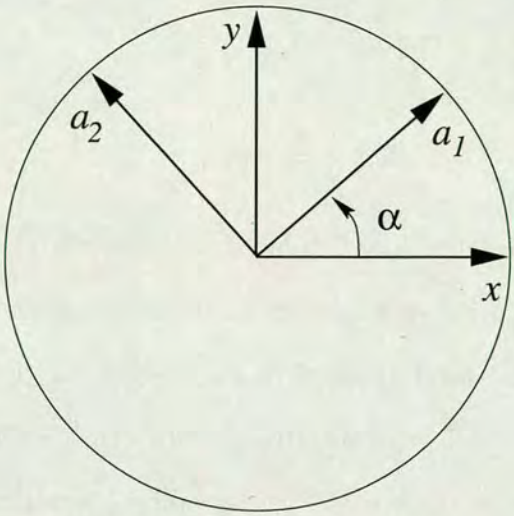

Figure 4.2: Coordinate system for a gimballed vertical geophone system. The z-axis pointing away from the origin, $x - y$ is the inline and crossline horizontal components, and $a_1 - a_2$ is the recording geophone system which is mis-oriented α degrees. The convention for definition of positive angle is that in a right-handed coordinate system, looking towards the origin, measured counter-clockwise.

crossline-geophone system is deployed on dipping seabed with the cable twisted, all three orientations will be unknown and this can be treated in the same way as in the non-gimballed case.

4.3.1 Gimballed vertical geophone system

In this case, assuming the a_1-axis is oriented α degrees from the x-axis (the inline direction, Figure 4.2), the recorded displacement of the water break in the horizontal plane may be written as,

$$\mathbf{D}(t) = \begin{bmatrix} a_1(t) \\ a_2(t) \end{bmatrix} = \mathbf{R}(\alpha) \begin{bmatrix} S(t) * \lambda(t) \sin\theta \\ 0 \end{bmatrix} \tag{4.3}$$

where $\mathbf{R}$ is 2x2 rotation matrix as defined in equation (A-4) in the appendix. Equation (4.3) shows that rotation $\mathbf{R}(\alpha)$ will rotate vector $[a_1(t),\ a_2(t)]^T$ into its principal polarization axes. Thus comparing equation (4.3) with equation (A-3) in the ap-

pendix gives

$$\alpha = -\phi_{a_1 a_2}, \tag{4.4}$$

where $\phi_{a_1 a_2}$ is the polarization direction of vector $[a_1(t),\ a_2(t)]^T$ given by equation (A-2) in the appendix. Equation (4.3) also shows that the determination of the geophone orientation relies on the minimization of the energy on the crossline component. In an ideal case, which is free of interferences of other waves, there should be no crossline energy of the water break if the geophone is aligned within the vertical plane containing the polarization vector (the sagittal plane). Thus, the procedures for determining the geophone orientation for the gimballed geophone system are:

1. from the source-receiver geometry, calculate the water break arrival times using water velocity, and carefully define water break window length;

2. solve for the orientation angle α using (4.4);

3. rotate the horizontal components by angle α, and check the crossline component for quality control.

4.3.2 Non-gimballed geophone system

In this case, as none of the three geophone orientations is known, one has to consider polarization vectors in the three-dimensional space, and use three-dimensional rotation matrices. Again the rotation convention is in a right-handed coordinate system, looking away from the origin and rotating clockwise. Figure 4.3 shows the geometry and coordinate system for a non-gimballed system.

Consider that the water break propagates within plane $(x - z)$ with angle θ, and that the polarization vector is recorded by the un-oriented three-component geophone system $(a_1 - a_2 - a_3)$ (Figure 4.3). The problem is to determine the

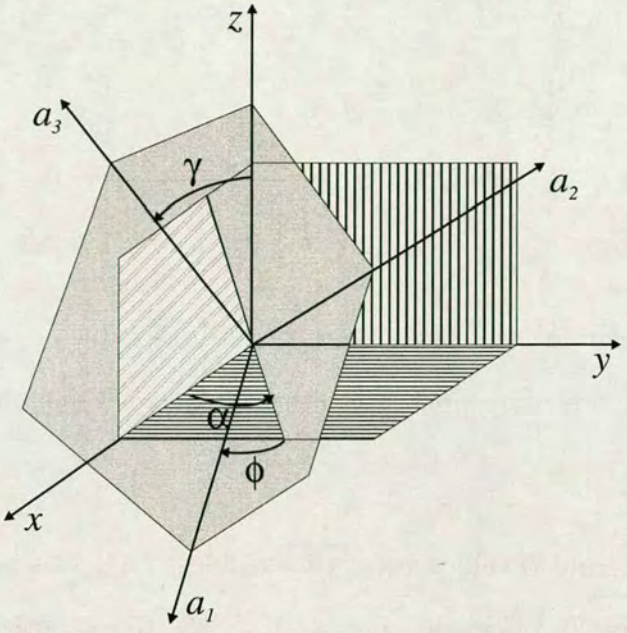

Figure 4.3: Euler's rotation and definition of Euler angles.

direction of the recording geophones and re-orient them into the coordinate system $(x-y-z)$. The recorded displacement of the water break $\mathbf{D}_r(t)$ can be obtained by rotating $\mathbf{D}(t)$ of equation (4.2) from the oriented system to the acquisition system using three Euler's rotations. Denoting the Euler angles as α (about z-axis), β (about new y- axis) and ϕ (about a_3-axis), one has

$$\mathbf{D}_r(t) = \begin{bmatrix} a_1(t) \\ a_2(t) \\ a_3(t) \end{bmatrix} = \mathbf{R}_{a_3}(\phi)\mathbf{R}_y(\beta)\mathbf{R}_z(\alpha)\mathbf{D}(t) = \mathbf{R}_{a_3}(\phi)\mathbf{R}_y(\beta)\mathbf{R}_z(\alpha) \begin{bmatrix} x(t) \\ y(t) \\ z(t) \end{bmatrix}, \tag{4.5}$$

where $\mathbf{R}_{a_3}$, $\mathbf{R}_y$ and $\mathbf{R}_z$ are three-dimensional rotations about the a_3-, new y- (after rotation about z-axis) and z-axis:

$$\mathbf{R}_{a_3}(\phi) = \mathbf{R}_z(\phi) = \begin{bmatrix} \cos\phi & \sin\phi & 0 \\ -\sin\phi & \cos\phi & 0 \\ 0 & 0 & 1 \end{bmatrix}; \quad \mathbf{R}_y(\beta) = \begin{bmatrix} \cos\beta & 0 & -\sin\beta \\ 0 & 1 & 0 \\ \sin\beta & 0 & \cos\beta \end{bmatrix}.$$

When angle β is near to zero, three Euler's rotations reduce to one rotation about z-axis with angle $\phi + \alpha$ corresponding to the gimballed- geophone case.

With known P- and S-velocities of the seafloor, $\mathbf{D}(t)$ can be predicted with a normalization factor $S(t)$ [see equation (4.2)]. Thus, from traces within the critical angle of the water break, angles α, β, and ϕ can be determined from equation (4.5) using some optimization methods. However, it is difficult to obtain the seafloor velocities precisely, and these velocities may vary from one site to another, due to change of seafloor sediments and depth (Theilen *et al.*, 1997). Furthermore, as indicated by our polarization analysis of the water break (Table 4.1), the polarization angles of the water breaks are mainly determined by the properties immediately below the seafloor surface. This makes it more complicated to obtain the proper seafloor velocities. Therefore, an alternative solution has to be found.

Consider that a common receiver gather often contains a number of traces with incidence angles varying from vertical to near horizontal. Thus a two-stage method is proposed. First, by selecting those vertically or near-vertically incident traces within a common receiver gather, angles ϕ and β can be determined; then all the traces in this gather are rotated by these two angles, and finally angle α can be determined by other non-vertically incident traces . To begin with, letting θ=0 and noting equation (4.2), equation (4.5) becomes

$$\begin{bmatrix} a_1(t) \\ a_2(t) \\ a_3(t) \end{bmatrix} = \mathbf{R}_{a_3}(\phi)\mathbf{R}_y(\beta)\mathbf{R}_z(\alpha) \begin{bmatrix} 0 \\ 0 \\ S(t) * \lambda(t)T_{pp} \end{bmatrix}, \tag{4.6}$$

which yields,

$$\begin{bmatrix} a_1(t) \\ a_2(t) \end{bmatrix} = \mathbf{R}(\phi) \begin{bmatrix} -\sin\beta \\ 0 \end{bmatrix} S(t) * \lambda(t)T_{pp}, \text{ and } \phi = \phi_{a_1a_2}\ , \tag{4.7}$$

where $\phi_{a_1a_2}$ is the polarization direction of vector $[a_1(t),\, a_2(t)]^T$ given by equation (A-2). With angle ϕ determined, the common receiver gather can be rotated to minimize the energy on the a_2-axis. Applying this rotation to equation (4.6), the rotated displacement vector for those vertically, or near vertically incident traces can be written as,

$$\begin{bmatrix} a_1'(t) \\ a_2'(t) \\ a_3(t) \end{bmatrix} = \mathbf{R}_{a_3}^T(\phi) \begin{bmatrix} a_1(t) \\ a_2(t) \\ a_3(t) \end{bmatrix} = \mathbf{R}_y(\beta)\mathbf{R}_z(\alpha) \begin{bmatrix} 0 \\ 0 \\ S(t) * \lambda(t)T_{pp} \end{bmatrix}, \tag{4.8}$$

which yields

$$\begin{bmatrix} a_1'(t) \\ a_3(t) \end{bmatrix} = \begin{bmatrix} a_1(t)\cos\phi - a_2(t)\sin\phi \\ a_3(t) \end{bmatrix} = \mathbf{R}_y(\beta) \begin{bmatrix} 0 \\ S(t) * \lambda(t)T_{pp} \end{bmatrix}, \text{ and } \beta = \frac{\pi}{2} - \phi_{a_1'a_3}. \tag{4.9}$$

where the prime indicates the new coordinate after rotation of $\mathbf{R}_{a_3}^T(\phi)$.

Based on this, a two-stage algorithm is introduced to determine the orientation of a non-gimballed three-component geophone dropped, or planted in the seafloor. In the first stage, I determine angles ϕ and β from the vertically and near-vertically incident traces of a common receiver gather and apply these rotations to equation

(4.5) for all traces within the common receiver gather. This will align the a_3-axis along the z-axis, and the case is reduced to a gimballed- geophone case. Then the azimuthal angle α can be determined from the horizontal components in a similar way to the gimballed system using equation (4.4).

To sum up, the procedures for determining the geophone orientations for a non-gimballed geophone system are:

1. carefully select the vertically and near-vertically incident traces and window the water break free of interferences of other arrivals on the a_1- and a_2-components;

2. solve for the orientation angle ϕ using (4.7), and angle β using equation (4.9);

3. rotate the common receiver gather using equation (4.5), and check the two horizontal components of the near-vertically incident traces for quality control;

4. now follow the procedure for the gimballed geophone system to determine azimuthal angle α, and note that this has to be performed on the non-vertically incident traces.

Note that the above procedure can also be used to determine the three orientations in the case of a gimballed crossline-geophone system deployed at a dipping seabed with the cable twisted. In this case, although one of the axes remains horizontal, its azimuth is unknown, and all the three orientations still need to be determined.

4.4 Testing with synthetic data

For testing, the above processing algorithm for the non-gimballed geophone system is applied to a full-wave synthetic three-component data computed by the reflectivity method using ANISEIS (Taylor, 1991) for the isotropic model in Figure 4.1b. I

test the algorithm for three cases with different noise levels: (1) free of noise, (2) 10% Gaussian noise, and (3) 25% Gaussian noise. Figure 4.4 a shows the noise-free

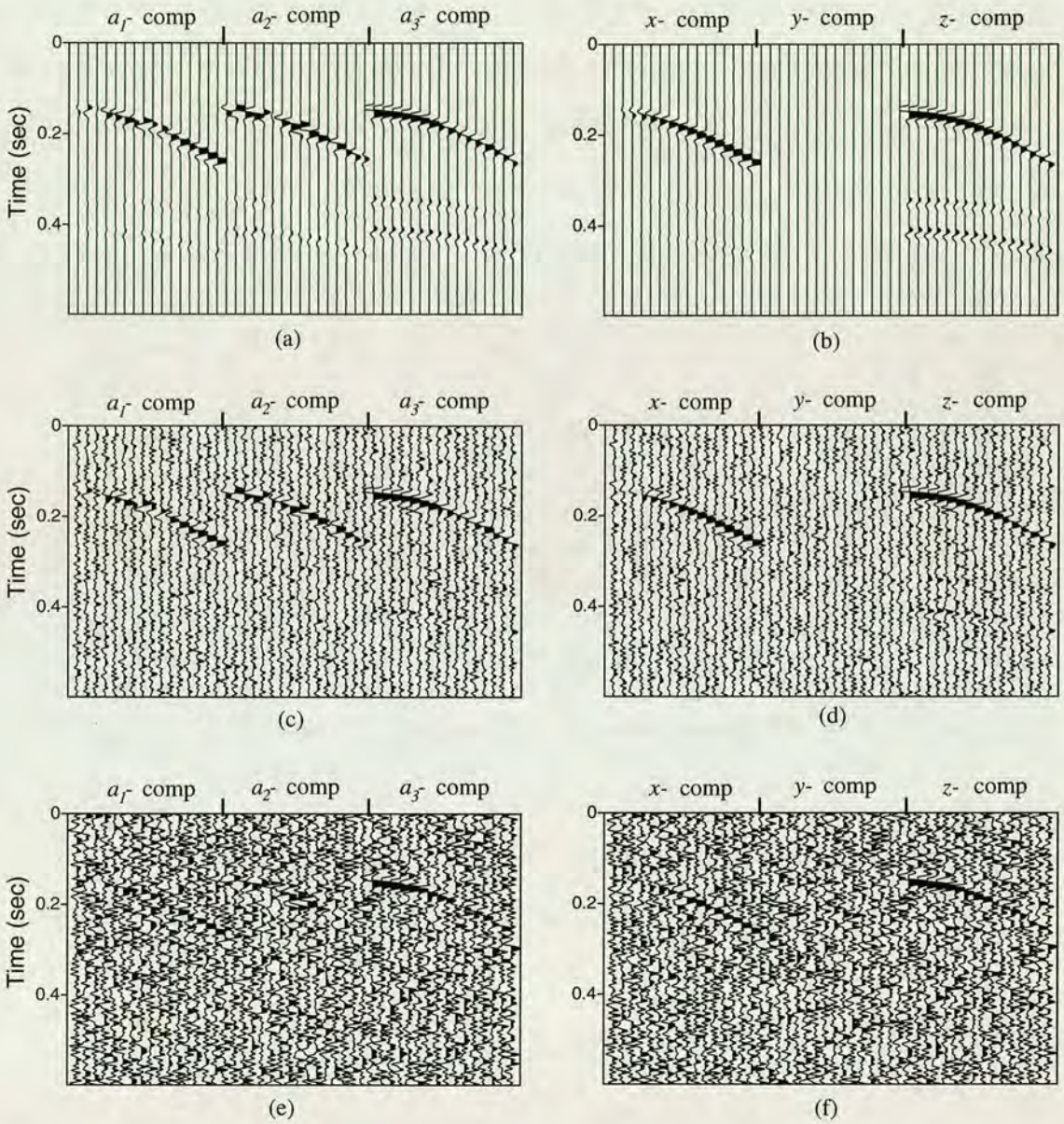

Figure 4.4: Synthetic data (generated by ANISEIS) analysis. (a) Noise-free synthetic records for a non-gimballed system with designed mis-orientations. (c) and (e) Same as (a) but with 10% and 25% Gaussian noise added, respectively. (b), (d) and (f) Processed results by the two-stage algorithm.

synthetic shot records with designed geophone mis-orientations. The corresponding processed results are shown in Figure 4.4b, and the energy on the crossline compo-

nent is completely eliminated as desired. Figures 4.4c and 4.4d show the synthetic data and the processed results for 10% noise. Figures 4.4e and 4.4f show the corresponding data and results for extremely high noise (25%). In both cases of noise tests, the algorithm yields sufficiently accurate results. There is almost no coherent energy on the rotated crossline (y) components, and the continuity of events on the inline (x) components is improved (Figures 4.4d and 4.4f). Figure 4.5 compares the

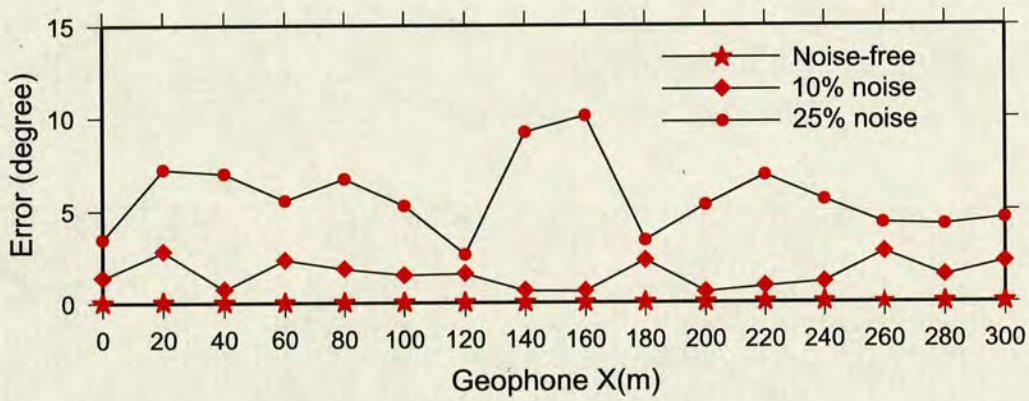

Figure 4.5: Error analysis. Vertical axis shows the maximum deviation between the re-oriented coordinate system and the designed coordinate system. The star-line is for noise-free data, the diamond-line for 10% Gaussian noise, and the circle-line for 25% Gaussian noise.

difference between estimated and designed geophone orientation for all the three cases using the two-stage algorithm. For noise-free data, the errors in the estimated geophone orientation are negligible. For data with 10% Gaussian noise, the errors are well within 5°. The error increases with noise level as shown by the circle-line in Figure 4.5.

4.5 Field data analysis

Here the two-stage algorithm is applied to field data from Guillemot, the North Sea, provided by Shell Exploration (Figure 3.2a). Although the data were acquired by a gimballed geophone system, the algorithm is used to check the geophone orientation

and coupling.

In Figure 3.2b, there is very strong shear-wave energy in the vertical (z) component, even for near-vertical propagating waves, as discussed in the previous chapter. There are two possible reasons for this. Firstly, the vertical geophone may be tilted, and secondly there may be a coupling problem in the geophone system. Here I investigate whether the vertical geophone is tilted or not. For this, I analyze the polarization diagrams (PDs) of the water break, and apply the two-stage algorithm to calculate the geophone orientation.

Figure 4.6 shows the windowed water break for polarization analysis. Table 4.2

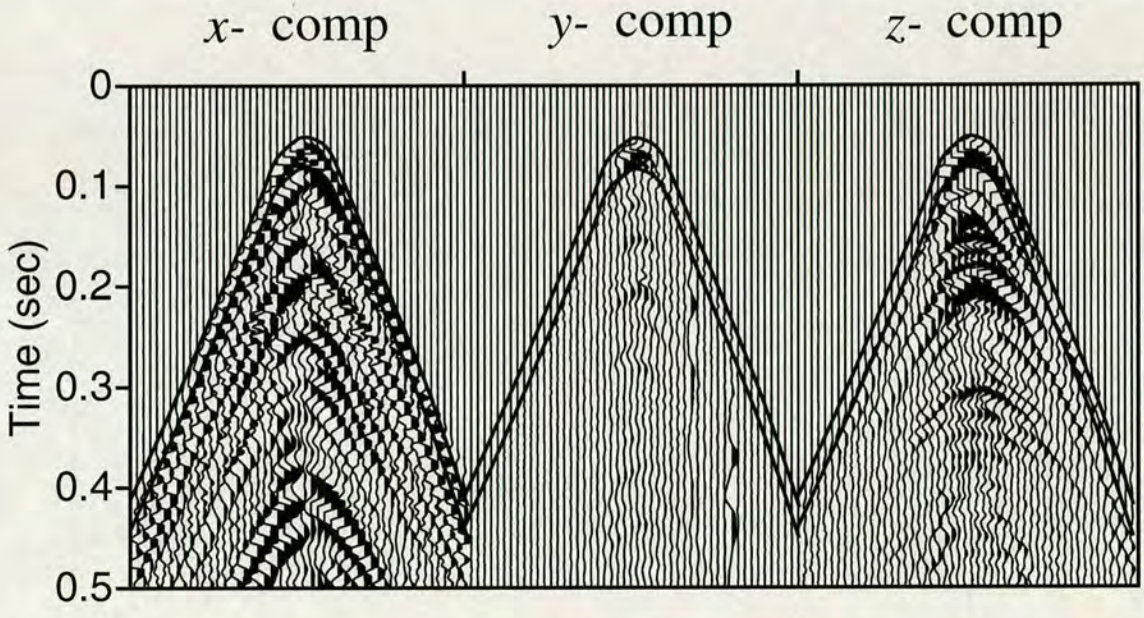

Figure 4.6: A window section of Figure 3.2a, showing the water break. Only the three-geophone components are displayed. A single gain is applied to show the relative amplitudes among the components. The two lines over the water break mark the time window for polarization analysis.

shows the polarization diagrams (PDs) of the water break for selected geophones in the sagittal ($x - z$) plane and in the horizontal ($x - y$) plane. For near vertical propagations in the ($x - z$) plane, the deviation of the polarization direction from the vertical axis is very small (Table 4.2a), indicating that the vertical axis is true vertical. For non-vertical propagations in the ($x - y$) plane, the azimuthal deviation

Table 4.2: Polarization diagrams of water break at the seafloor from the data in Figure 4.6: (a) sagittal $x-z$ plane, and (b) horizontal $x-y$ plane.

Incident angles	$-4.7°$	$13.9°$	$27.9°$	$39.5°$	$48.2°$	$59.6°$
(a) $x-z$ polarization	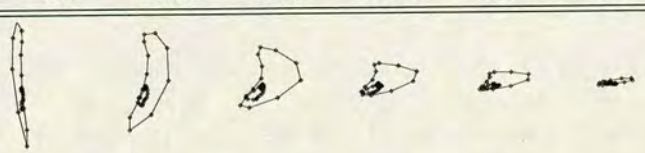					
polarization angles	$-3.5°$	$12.4°$	$37.4°$	$66.0°$	$77.0°$	$83.3°$
(b) $x-y$ polarization	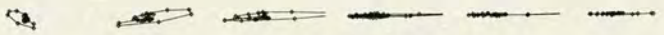					
polarization angles	$-37.4°$	$8.6°$	$2.1°$	$0.73°$	$0.15°$	$0.05°$

of the polarization direction from the inline axis is very small (Table 4.2b), indicating that the horizontal axes are also oriented satisfactorily. Applying the two-stage method to the whole data reveals that the vertical deviation (angle β) is within 5° (star-line, Figure 4.7), and that the azimuthal mis-orientation is also within a similar

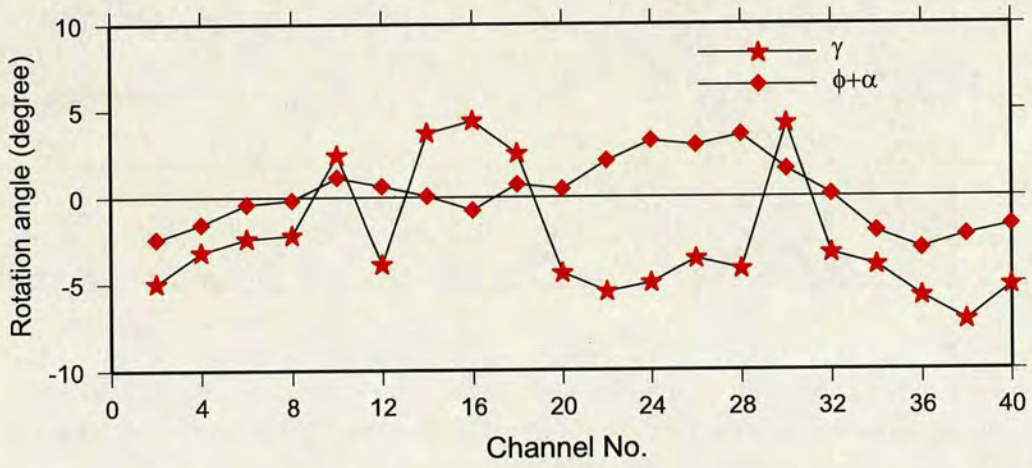

Figure 4.7: Geophone orientations determined from Figure 4.6 using the two-stage method, for different geophone locations. The star-line is the Euler angle β. As β is very small, the other two Euler angles reduce to $\phi+\alpha$ (diamond-line).

range (diamond-line, Figure 4.7). Thus the strong shear-wave energy in the vertical component is not caused by geophone mis-orientation. Note that although a 5° error is often acceptable for exploration purposes, higher accuracy may be required

in some time-lapse surveys for reservoir monitoring. In such cases, the determination of geophone orientation using first arrivals is no longer appropriate and other non-seismic methods may have to be used. For example, the four-component node system (see Chapter 1) is orientated by the bulit-in compass and inclinometer (Pettenati-Auziere *et al.*, 1997).

Also note that to perform the above polarization analysis, careful selection of the analysis window is essential. The window should contain the water break only, and be free from the interference of other wave types. When there is a clean arrival, the window should be sufficiently large to cover at least one cycle of the waveform in order to obtain consistent estimations. If there are interferences from refracted waves, smaller windows may be used. In three-component VSPs, window lengths as small as 5-10ms were used for similar polarization analysis (Gaiser *et al.*, 1984), which may be suitable for a high frequency VSP data. However, such tiny windows are not recommended for 4C seafloor data, as the results can be unstable. In our example, a clean water-break can be identified as marked in Figure 4.6, and the average time window is 50 ms.

4.6 Discussion

Based on the polarization of the water break on the seafloor, processing algorithms have been derived for determining the geophone orientations for the gimballed and non-gimballed geophone systems and tested with synthetic and real data. Compensating for sensor coupling and orientation correction is not new and there have been many theoretical and practical works published on the subject for three-component VSP applications (Hardage, 1983; DiSiena *et al.*, 1984; Esmersoy, 1984). These include sensor design, effects of surrounding media, tool resonance, survey design, polarization analysis and orientation corrections. Although the practical application

is different, some of the basic principles may still be applicable in 4C seafloor acquisition. So far we have mainly focused on the processing algorithms for analyzing geophone coupling and orientation. Here it is necessary to give a brief discussion on the other issues.

4.6.1 Sensor design

Sensor design is critical to good coupling. The key is to make the sensor small and light while still able to maintain maximum contact with the surrounding media. In surface seismic, this is achieved by the use of spike-planted geophones, whilst in VSP experiments by the use of a locking mechanism which clamps the geophone firmly to the borehole wall. The cable system with external sensor packages currently available resembles the VSP design. The sensor packages are sunk into the mud due to their weight, like the clamping mechanism, for achieving firm contact with the solid seafloor. As a result, this cable design suffers a similar coupling problem to its VSP counterpart, that is, the crossline component is often poorly coupled compared with the vertical and inline components (Gaiser, 1998).

4.6.2 Resonance

Resonance in the sensor packages is another source of noise which affects data quality. Beydoun (1984) showed that if a sensor has a very small bounding contact (poorly coupled) with a soft formation, the sensor can have a resonance point as low as 35 Hz, and this is not unusual in VSP surveys. Because the crossline sensor usually has less bounding contact with the surrounding media compared with the vertical and inline sensors, and also the seabed sediments are usually much softer than the borehole wall, it is thus not surprising if the resonance point of the crossline sensor falls well below the 35 Hz mark. This may explain some of the ringy signals recorded

in the crossline component of the external sensor packages.

As shown in Figure 3.2, high quality shear-wave signals can be recorded using internal sensor groups within the cable, and there is certainly an improvement in sensor coupling. This may be explained in two ways. Firstly, a cable sunk into the mud generally has better overall bounding contact with the surrounding media than the external sensor packages. Secondly, the use of a sensor group enhances the signal, increases the overall bounding contact with the surroundings and may effectively cancel out some noise resonances from individual sensors. However, the leakage from the inline component to the vertical (Figure 3.2) is likely to be due to a mechanical fault associated with the design of the cable system, particularly with the gimballed geophone mechanism.

4.6.3 Cable and survey design

The current cable-based systems have all employed a gimballed geophone mechanism. Although gimballed phones have been successful in dual-sensor acquisition (Barr *et al.*, 1996), for a gimballed three-component geophone, a good coupling of the horizontal phones is difficult to achieve (Samson *et al.*, 1995). Firstly, as we all know, it is intrinsically difficult to achieve a good coupling of the crossline geophone to the formation. Secondly, the gimballed mechanism often introduces leakages between the components, as demonstrated in this study. In contrast, a non-gimballed system may simplify the design of the sensor package and results in good coupling and no leakage (Meunier *et al.*, 1997). The use of non-gimballed geophones is a subject which may be worth pursuing in future seafloor experiments, and the algorithms presented here could have potential applications in such experiments.

Survey design and water depth also affects the solution to coupling and orientation correction. To achieve quality coupling of the three-component gimballed

system and reliable determination of the geophone orientation requires careful acquisition design which may involve changing the layout of the survey (Brink *et al.*, 1996). An alternative method involves either planted, or trench-buried geophones, which are clearly more expensive. In a deep water environment, water velocity may change with depth as temperature varies. The data redundancy in shots for a range of azimuths and offsets will help in reducing the uncertainty in orientation estimation. Analysis of near-offset traces is sometimes unstable because of noise, whilst for far offset traces the refracted arrival is most often the first arrival. In such case, analysis of the orientation and coupling may be carried for the refracted arrival, or even for some good reflection events from the subsurface (Kristiansen, 1998), and the same methodology applies. Different cable deployment methods (dragged, dropped, or trenched) may also affect the coupling and hence the orientation. Dragged cable acquisition is relatively efficient but may degrade the coupling and orientation for sensors at the side near to the boat, whilst trenched cable acquisition is often very expensive. The drag-dropped cable seems to be a good compromise in between.

4.7 Conclusions

I have developed a two-stage method for determining the three geophone orientations in a 4C seafloor seismic survey. The method utilizes the polarization of the water break at near (at the first stage) and far (at the second stage) offset traces. Applications to synthetic data show that tool orientations can be estimated with sufficient accuracy for very strong noise compared with the water break energy. To check the geophone orientation and coupling for quality control, the algorithm is applied to field data from the North Sea acquired by a gimballed geophone system. The processing results show that the mis-orientation of the geophones in the field data is within $\pm 5°$, and that there is a leakage problem between the horizontal and

vertical geophones. This leakage resulted in substantial shear-wave energy being recorded on the vertical geophone.

Chapter 5

Converted-wave analysis in layered isotropic media

5.1 Introduction

Shear waves which are converted at deep reflectors have asymmetric raypaths and require a processing flow which is different from that for conventional P-waves. The general processing procedure for converted waves has been discussed in Chapter 2, and includes CCP binning, dip moveout and post-stack migration. In this Chapter, I focus on the traveltime analysis of the converted waves in layered isotropic media. The effect of anisotropy on converted waves will be discussed in Chapter 6.

5.2 Converted wave in a single-layered medium

5.2.1 Calculation of the conversion-point offset

Exact solutions of the conversion-point offset, such as equations (2.2) and (2.3), are only valid for a single-layered medium. Furthermore, they do not reveal any analytical insight into the parameter dependencies. This gap is often filled by the use

of analytical approximations. The early approximation was based on the asymptotic equation (2.4). The accuracy of this approximation is very limited, and it introduces a large error even for a moderate offset-to-depth ratio less than 1.0 (see Figure 2.3).

Thomsen (1999) gave a more accurate approximation based on the higher-order Taylor expansion. The conversion-point offset x_c is a function of velocity ratio γ and offset-to-depth ratio x/z (Thomsen, 1999),

$$x_c \approx x\left[C_0 + C_2\frac{(x/z)^2}{1+C_3\,(x/z)^2}\right] \tag{5.1}$$

where

$$C_0 = \frac{\gamma}{1+\gamma},\quad C_2 = \frac{\gamma}{2}\frac{(\gamma-1)}{(\gamma+1)^3}$$

$$\text{and}\quad C_3 = C_2/\,(1-C_0)\,.$$

Note that equation (5.1) is a modified Taylor series expansion. The denominator in the second term ensures that the equation is asymptotically correct at the limit of $x/z \to \infty$, where the conversion point x_c is close to x.

As shown in Figure 5.1, the new approximation (5.1) is more accurate than the asymptotic equation (Figure 2.3). For a velocity ratio of 2.0, the approximation is very accurate up to offset-to-depth ratio of 2.0. Despite this, the error still increases with the velocity ratio and the offset-to-depth ratio, giving rise to severe limitations for imaging shallow structures.

5.2.2 Traveltime approximations

In a similar manner to the conversion-point offset, analytical approximations for calculating the converted-wave traveltime are widely used. The early approximation

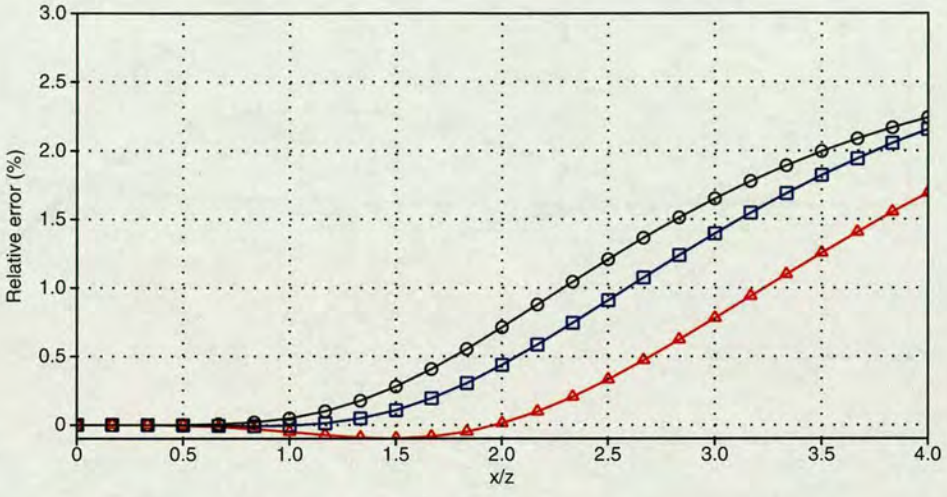

Figure 5.1: Relative errors of conversion-point offset x_c using equation (5.1) in an isotropic homogeneous medium. The relative errors are calculated by $\left|x_c^{(exact)} - x_c^{(approximation)}\right| / x$. The three curves are for different velocity ratios V_p/V_s of 2.0 (triangles), 2.5 (squares) and 3.0 (circles), respectively.

is the hyperbolic traveltime equation of Tessmer and Behle (1988) (see equation 2.9).

In Figure 5.2, the line with square marks shows the accuracy of hyperbolic equation (2.9). The P-wave velocity is 2500 m/s, velocity ratio is 2.5 and reflector depth is 1000 meters. It can be seen that it is only accurate when offset-to-depth ratio is below 0.7 if the criterion is one sampling point, which is about 2ms in field survey practice nowadays. The error is more or less independent of the velocities, but increases with the velocity ratio.

The converted-wave moveout is inherently non-hyperbolic due to the asymmetry of the ray path, and a hyperbolic assumption introduces serious error in moveout analysis. In order to improve this, a three-term Taylor series expansion was given (Tsvankin and Thomsen, 1994; Thomsen, 1999) as

$$t_c^2 = t_{c0}^2 + \frac{x^2}{V_c^2} + \frac{A_4 x^4}{1 + A_5 x^2} \tag{5.2}$$

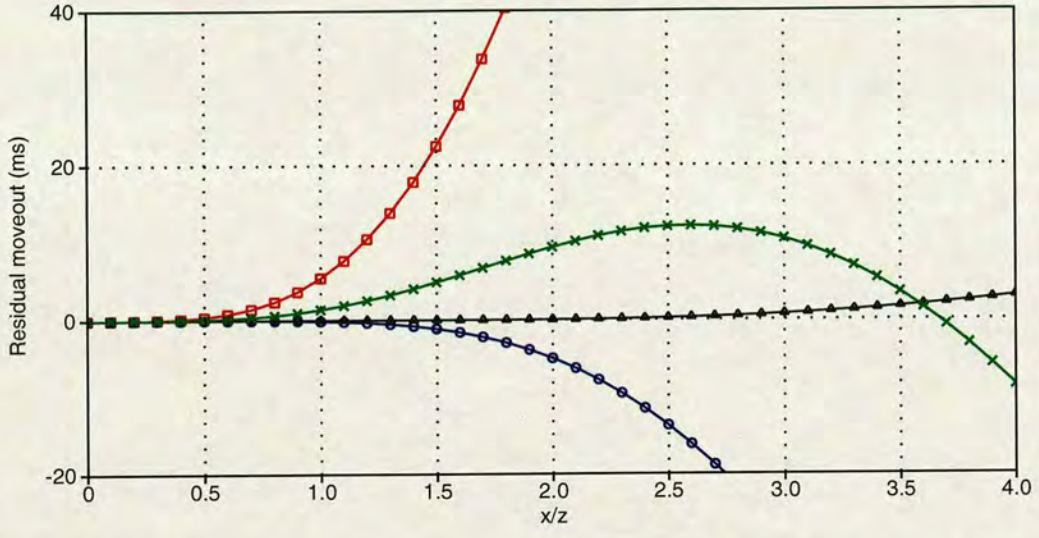

Figure 5.2: The accuracy of approximations about converted wave moveout in a homogeneous isotropic media. V_p=2500m/s and γ=2.5, and z=1000m. The vertical axis is the residual moveout to the exact traveltime. Four approximations are used: (a) hyperbolic equation (2.9) (squares), (b) three-term Taylor series (crosses) with incorrect coefficient A_4 given by Thomsen (1999) in equation (5.6); (c) three-term Taylor series (circles) with correct coefficient A_4 given by equation (5.3) and (d) DSR equation (5.5) (triangles).

where

$$A_4 = \frac{-(\gamma-1)^2}{4\gamma t_{c0}^2 V_c^4} \quad \text{and} \tag{5.3}$$

$$A_5 = \frac{-A_4 V_c^2}{1 - V_c^2/V_p^2}. \tag{5.4}$$

A_4 and A_5 are quartic terms. Note that equation (5.2) is a modified Taylor expansion. The introduction of the A_5 term is to ensure that the moveout of converted wave at far offset is quadratic to offset with P-wave velocity (Thomsen, 1999).

There is some improvement in equation (5.2) over hyperbolic equation (2.9) as can be seen from the line with circle marks in Figure 5.2. In general, the three-term Taylor expansion can be accurate up to offset-to-depth ratio of 1.5.

Equation (5.2) reveals that near offset moveout is determined by the converted wave moveout velocity V_c, and the influence of γ only shows in quartic terms or higher.

As we know, for *P-P* or *S-S* wave moveouts, the quartic or higher terms are used to compensate for layering or anisotropic effects. However, for converted waves, the quartic terms in equation (5.2) are mainly used to compensate for the effects of the asymmetric raypath. An alternative to the Taylor series expansion is to use the double-square-root (DSR) equation (2.1), which can be rewritten in the form with respect to two-way vertical traveltime t_{c0} as

$$t_c = \sqrt{\left(\frac{t_{c0}}{1+\gamma}\right)^2 + \frac{x_c^2}{\gamma V_c^2}} + \sqrt{\left(\frac{\gamma t_{c0}}{1+\gamma}\right)^2 + \frac{\gamma\,(x-x_c)^2}{V_c^2}}, \tag{5.5}$$

where x_c can be either calculated exactly from equations (2.2) or (2.3), or (5.1). The triangle-marked line in Figure 5.2 shows the accuracy of equation (5.5). Note that conversion point offset x_c is calculated by equation (5.1). If exact solutions are used, there should be no error in moveout calculation.

It is interesting to point out that the original coefficient A_4 in equation (5.2) given by Thomsen (1999) was not correct. It had the form as

$$A_4 = \frac{-(\gamma-1)^2}{4\,(1+\gamma)\,t_{c0}^2 V_c^4}. \tag{5.6}$$

The difference lies in the denominator. The error also exists in its extension to the multi-layered medium. The traveltime calculated by this incorrect coefficient can only be accurate up to offset-to-depth ratio of 1.0 as shown by the cross-marked line in Figure 5.2. In the following discussion, I only use Taylor series expansion with the correct coefficients.

5.3 Converted wave in multi-layered media

5.3.1 Definition of terminology

Before I begin to discuss the propagation of converted waves in multi-layered media, I first give a brief introduction to some basic terms commonly used in converted wave processing. Consider, for example, a multi-layered medium with n layers, each layer has parameters (z_i, V_{pi}, V_{si}), where z_i, V_{pi} and V_{si} are the layer thickness, interval P- and S-wave velocities, respectively, in the ith layer. The following terms can be defined:

1. average velocities $\bar{V}_p$ and $\bar{V}_s$ as

$$\bar{V}_p = \frac{\sum_{i=1}^{n} V_{pi}\Delta t_{p0i}}{\sum_{i=1}^{n} \Delta t_{p0i}} \text{ and } \bar{V}_s = \frac{\sum_{i=1}^{n} V_{si}\Delta t_{s0i}}{\sum_{i=1}^{n} \Delta t_{s0i}} \tag{5.7}$$

   where Δt_{p0i} and Δt_{s0i} are the vertical one-way or two-way traveltime, in ith layer;

2. average velocity ratio

$$\gamma_0 = \bar{V}_p/\bar{V}_s = \frac{t_{s0}}{t_{p0}} \tag{5.8}$$

   where t_{p0} and t_{s0} are the total vertical one-way or two-way traveltime of P-P and S-S waves, respectively, and $t_{p0} = \sum_{i=1}^{n} \Delta t_{p0i}$, $t_{s0} = \sum_{i=1}^{n} \Delta t_{s0i}$;

3. RMS (root-mean-square) velocities V_{p2} and V_{s2} as

$$V_{p2} = \sqrt{\frac{\sum_{i=1}^{n} V_{pi}^2\Delta t_{p0i}}{\sum_{i=1}^{n} \Delta t_{p0i}}} \text{ and } V_{s2} = \sqrt{\frac{\sum_{i=1}^{n} V_{si}^2\Delta t_{s0i}}{\sum_{i=1}^{n} \Delta t_{s0i}}}; \tag{5.9}$$

4. and RMS velocity ratio

$$\gamma_2 = V_{p2}/V_{s2}; \tag{5.10}$$

5. fourth-order velocities V_{p4} and V_{s4} as

$$V_{p4} = \sqrt[4]{\frac{\sum_{i=1}^{n} V_{pi}^4 \Delta t_{p0i}}{\sum_{i=1}^{n} \Delta t_{p0i}}} \text{ and } V_{s4} = \sqrt[4]{\frac{\sum_{i=1}^{n} V_{si}^4 \Delta t_{s0i}}{\sum_{i=1}^{n} \Delta t_{s0i}}}. \tag{5.11}$$

5.3.2 Conversion point offset

When converted waves travel in a horizontally multi-layered medium, there is no exact analytic solution to where the *P-S* conversion occurs, and travel-time curves become more complicated. Therefore, a proper approximation is required.

First, I extend three-term Taylor series expansion (5.1) for conversion point offset into layered medium. In equation (5.1), the x_c is expressed as a function of reflector depth. In reflection surveys, the reflector depth is often unknown. Thus the preferred conversion point equation should be expressed in terms of reflection time t_c instead of depth z. Following the modified Taylor expansion form given by Thomsen (1999), the conversion point offset x_c can be generalized as

$$x_c \approx x \left[c_0 + c_2 \frac{x^2}{1 + c_3 x^2} \right]. \tag{5.12}$$

The general forms of coefficients c_0 and c_2 for layered anisotropic media, are derived in Appendix D. For the layered isotropic case, they are given as

$$c_0 = \frac{\gamma_{eff}}{1 + \gamma_{eff}} \tag{5.13}$$

$$c_2 = \frac{V_{p4}^4 V_{s2}^2 - V_{p2}^2 V_{s4}^4}{\left(V_{p2}^2 t_{p0} + V_{s2}^2 t_{s0} \right)^4} t_{p0} t_{s0}, \tag{5.14}$$

and

$$c_3 = c_2 / \left(1 - c_0 \right).$$

γ_{eff} is the effective velocity ratio defined by Thomsen (1999) as

$$\gamma_{eff} = \gamma_2^2/\gamma_0. \tag{5.15}$$

Note that the coefficient c_2 is different from that given by Thomsen using simple depth-to-time scaling. Only when using further approximations

$$V_{p4} \approx V_{p2} \tag{5.16}$$

and

$$V_{s4} \approx V_{s2}, \tag{5.17}$$

can the coefficient c_2 take the same form given by Thomsen as

$$c_2 = \frac{\gamma_{eff}}{2\gamma_0 t_{c0}^2 V_{c2}^2} \frac{(\gamma_{eff}\gamma_0 - 1)(1+\gamma_0)}{(1+\gamma_{eff})^3}, \tag{5.18}$$

where V_{c2} is the short spread moveout velocity of converted wave in layered medium, isotropic or anisotropic. If the medium velocity function does not change dramatically, the differences between V_{p4} and V_{p2} and between V_{s4} and V_{s2} are not very large, and equation (5.18) is a very good approximation to equation (5.14).

The accuracy of equation (5.12) is tested by synthetic modelling. Table 5.1 shows the modelling parameters, including five isotropic layers with velocity ratio

Layer No.	V_{pi} (m/s)	γ_i	V_{si} (m/s)	Δz_i (m)
1	2000	3.0	666.7	400
2	2300	2.6	884.6	400
3	2500	2.3	1087.0	400
4	2600	2.1	1238.1	400
5	2700	2.0	1350.0	400

Table 5.1: Modelling parameters to examine the accuracy of traveltime analysis in isotropic media.

range from 3 to 2. In order to show the accuracy of conversion point calculation in a multi-layered medium, only conversion point errors from the second to fifth reflectors are shown in Figures 5.3 and 5.4. The lines with circles are calculated using c_2 from exact equation (5.14), and the lines with squares from Thomsen's approximation by equation (5.18). It can be seen that the difference between the two approximations is rather small. The approximation with exact c_2 term is slightly better at near offsets. Both approximations can be accurate up to offset-to-depth ratio of 2. Although Thomsen's approximation is slightly worse, it has advantage of not using independent parameters V_{p4} and V_{s4}. Therefore, in practice, Thomsen's approximation can be used as a good approximation for real data processing.

5.3.3 Traveltime

All three approximations for converted-wave traveltime in the single-layer medium discussed in section 5.2.2 [hyperbolic equation (2.9), three-term Taylor series equation (5.2) and DSR equation (5.5)] can be extended to multi-layered media.

First let us begin with the hyperbolic approximation. Equation (2.9) is the first order Taylor expansion of equation (2.1) in a homogeneous and isotropic medium. In a more realistic layered isotropic medium, t_c takes the same form as equation (2.9), while V_c is replaced by RMS (root-mean-square) velocity V_{c2} (2 in the subscript stands for RMS) as

$$V_{c2}^2 = \frac{\sum_{i=1}^{n} V_{pi} V_{si} \Delta t_{c0i}}{\sum_{i=1}^{n} \Delta t_{c0i}}. \tag{5.19}$$

It is easy to derive the relation between the converted wave moveout velocity V_{c2} and the other two moveout velocities, P-P and S-S RMS velocities V_{p2} and V_{s2}.

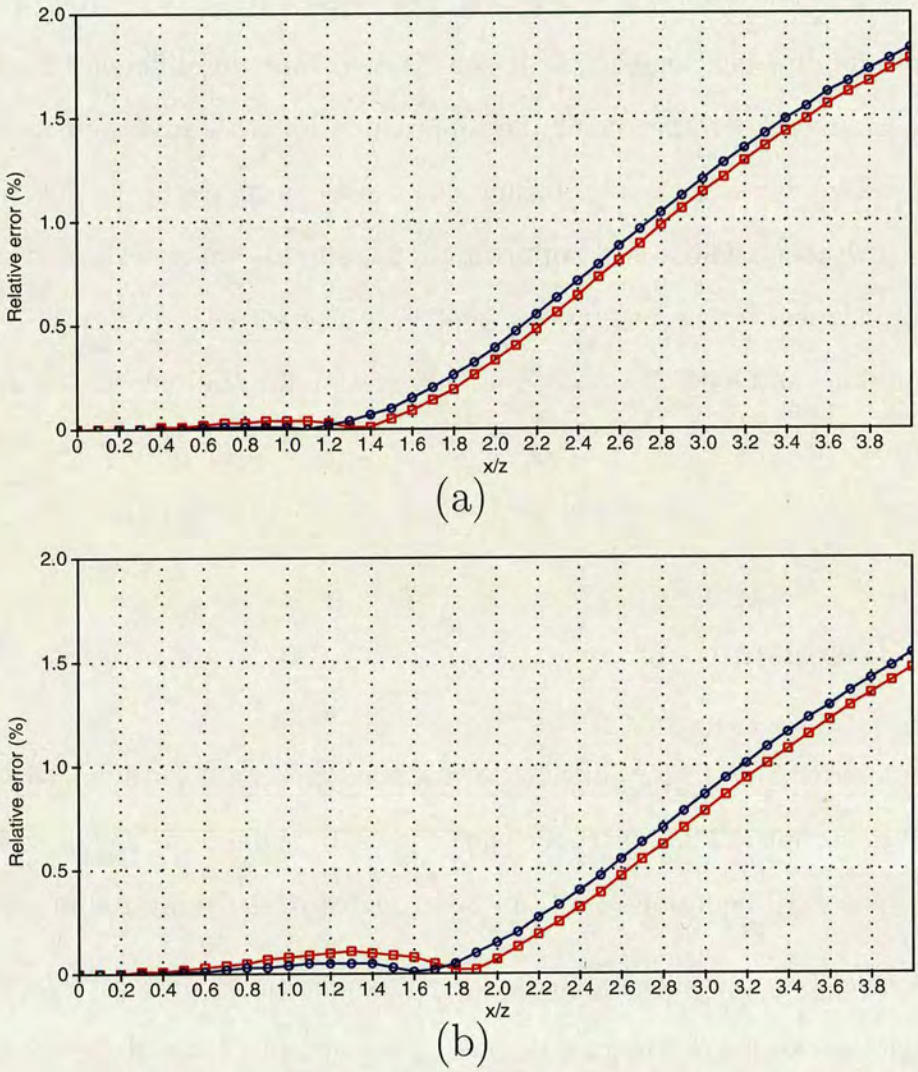

Figure 5.3: . Accuracy of conversion point approximations for the (a) second and (b) third reflectors in the multi-layered media in Table 5.1. The conversion points are approximated by equation (5.12) with coefficient c_2 calculated by equation (5.14) shown by lines with circle marks, and with coefficient c_2 calculated by equation (5.18) shown by lines with square marks.

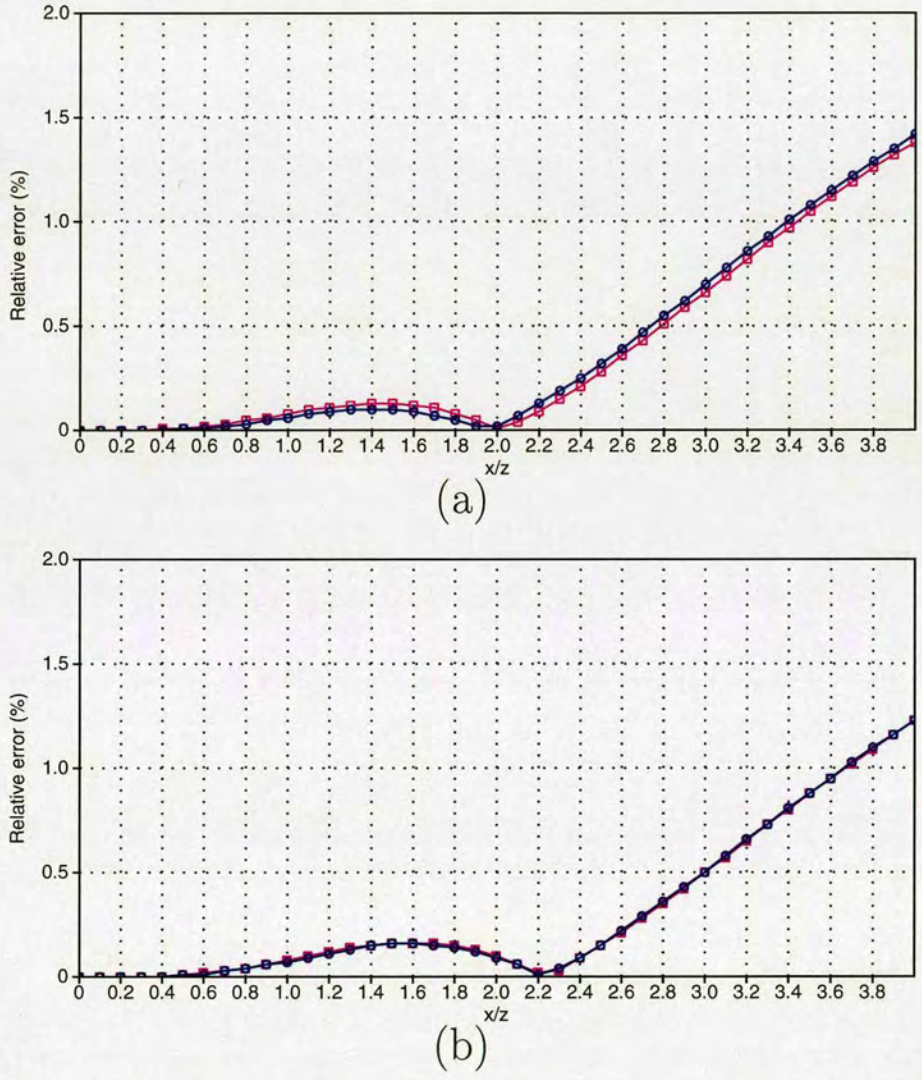

Figure 5.4: . The same as Figure 5.3 but for the (a) fourth and (b) fifth reflectors.

From equation (5.19),

$$V_{c2}^2 = \frac{\sum_{i=1}^n V_{pi} V_{si} \Delta t_{c0i}}{\sum_{i=1}^n \Delta t_{c0i}} = \frac{\sum_{i=1}^n V_{pi} V_{si} \Delta t_{p0i} + \sum_{i=1}^n V_{pi} V_{si} \Delta t_{s0i}}{\sum_{i=1}^n \Delta t_{c0i}}.$$

Because of the simple relation $V_{pi}\Delta t_{p0i} = V_{si}\Delta t_{s0i} = \Delta z$, we have

$$V_{c2}^2 = \frac{\sum_{i=1}^n V_{pi}^2 \Delta t_{p0i} + \sum_{i=1}^n V_{si}^2 \Delta t_{s0i}}{\sum_{i=1}^n \Delta t_{c0i}}. \tag{5.20}$$

Substituting (5.8), (5.9), (5.10) and (5.15) into (5.20), with $t_{c0} = \sum \Delta t_{c0i} = t_{p0} + t_{s0}$, V_{c2} can be obtained as

$$V_{c2}^2 = \frac{V_{p2}^2}{1+\gamma_0} + \frac{V_{s2}^2}{1+1/\gamma_0} = \frac{V_{p2}^2}{1+\gamma_0}\left(1 + \frac{1}{\gamma_{eff}}\right). \tag{5.21}$$

Secondly, I discuss the three-term Taylor expansion of converted wave traveltime in a multi-layered medium. The approximation has the same form as that of equation (5.2) for the single-layered medium. The term A_4 in the three-term Taylor series equation (5.2) has the form (Tsvankin and Thomsen, 1994)

$$A_4 = \frac{(1+\gamma_0) V_{c2}^4 - V_{p4}^4 - \gamma_0 V_{s4}^4}{4(1+\gamma_0) t_{c0}^2 V_{c2}^8}. \tag{5.22}$$

Using the same velocity approximations (5.16) and (5.17) as those for conversion point position, A_4 can take a simplified form as

$$A_4 = \frac{-(\gamma_2^2 - 1)^2}{4(1+\gamma_{eff})^2 \gamma_0 t_{c0}^2 V_{c2}^4} \tag{5.23}$$

The accuracy of the hyperbolic and the three-term Taylor series expansions have been checked by synthetic modelling. The model parameters are the same as those used for conversion point analysis (Table 5.1). Figure 5.5 shows the comparison of

traveltime approximation. As expected, the hyperbolic approximation can only be accurate to offset-to-depth ratio of 0.7 as shown by curves marked with squares. This result is consistent for all four reflectors in Figure 5.5. The accuracy can be improved with the three-term Taylor expansion. With an accurate A_4 coefficient, the approximation can be accurate up to offset-to-depth ratio of 1.7, and with an approximate A_4 coefficient, it is accurate up to 1.5. It can be seen that the accuracy of the three-term Taylor expansion is not consistent among the four reflectors.

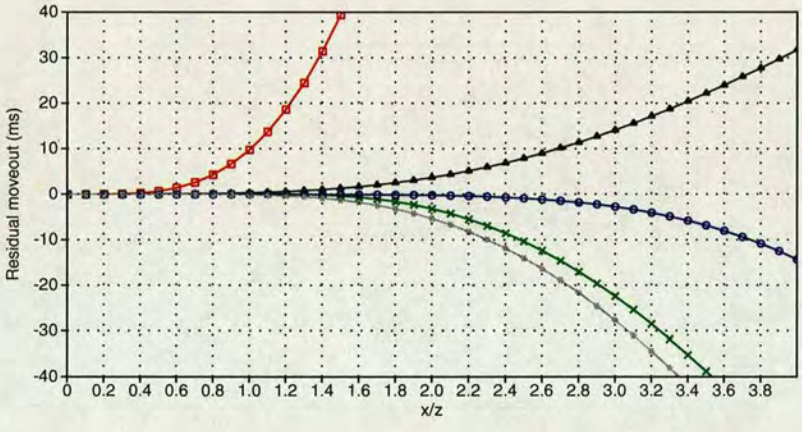

(a)

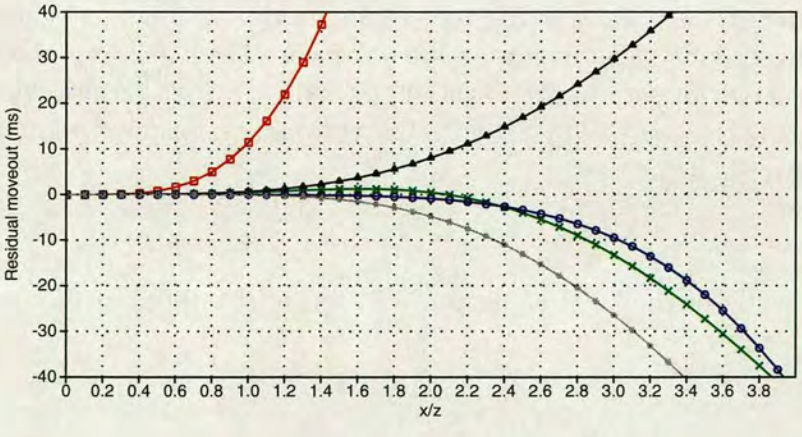

(b)

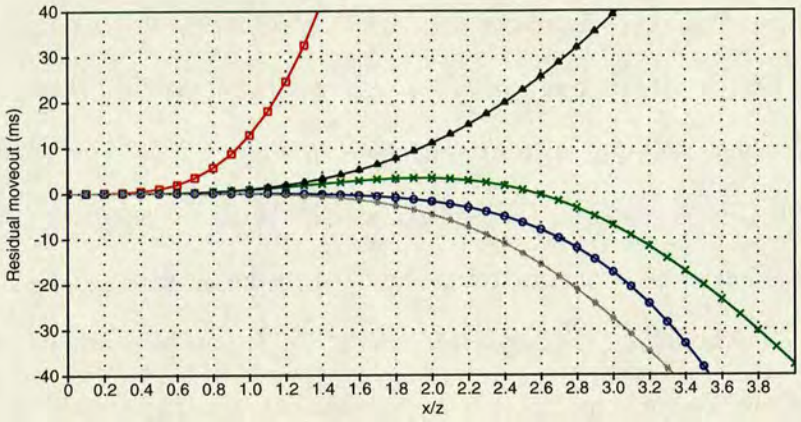

(c)

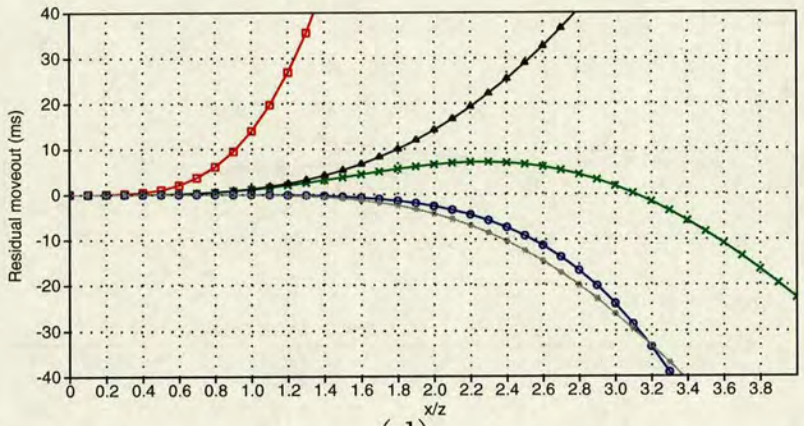

(d)

Figure 5.5: The accuracy of approximations about converted wave moveout in layered media. The model parameters are listed in Table 5.1. The four sub-figures are traveltime error from (a) the second , (b) the third, (c) the fourth and (d) the fifth reflectors, respectively. The vertical axis is the residual moveout to the exact traveltime from ray tracing. The five approximations are used: (1) hyperbolic (squares), (2) three-term Taylor series with exact A_4 (stars), (3) three-term Taylor series with approximate A_4 (crosses), (4) DSR with fourth-order terms (circles) and (5) without fourth-order term (triangles).

The extension of the DSR equation (5.5) to multi-layered medium can be given as

$$t_c = \sqrt{\left(\frac{t_{c0}}{1+\gamma_0}\right)^2 + \frac{x_c^2}{V_{p2}^2}} + \sqrt{\left(\frac{\gamma_0 t_{c0}}{1+\gamma_0}\right)^2 + \frac{(x-x_c)^2}{V_{s2}^2}}, \tag{5.24}$$

where

$$V_{p2}^2 = \frac{(1+\gamma_0)\,\gamma_{eff}}{(1+\gamma_{eff})} V_{c2}^2$$

and

$$V_{s2}^2 = \frac{(1+\gamma_0)}{(1+\gamma_{eff})\,\gamma_0} V_{c2}^2.$$

If $\gamma_0 = \gamma_2 = \gamma_{eff}$, equation (5.24) reduces to the homogeneous and isotropic case of equation (5.5). Compared with the three-term Taylor series equation (5.2), the accuracy of the DSR equation in a multi-layered medium can hold up to x/z =1.4, which is slightly less accurate than the modified three-term Taylor series. The residual moveouts are mainly from layering effects. Like *P-P* and *S-S* reflections (Hake *et al.*, 1984), the moveout of converted waves at large offsets can be approximated using higher-order Taylor terms. However, these terms should be added to *P*- and *S*- reflection legs, respectively. For example, by including the fourth-order terms, equation (5.24) can be given as

$$t_c = \sqrt{\left(\frac{t_{c0}}{1+\gamma_0}\right)^2 + \frac{x_c^2}{V_{p2}^2} + A_{p4} x_c^4} + \sqrt{\left(\frac{\gamma_0 t_{c0}}{1+\gamma_0}\right)^2 + \frac{(x-x_c)^2}{V_{s2}^2} + A_{s4}\,(x-x_s)^4} \quad (5.25)$$

where

$$A_{p4} = \frac{(1+\gamma_0)^2 \left(V_{p2}^4 - V_{p4}^4\right)}{4 V_{p2}^8 t_{c0}^2}$$

and

$$A_{s4} = \frac{(1+\gamma_0)^2 \left(V_{s2}^4 - V_{s4}^4\right)}{4 \gamma_0^2 V_{s2}^8 t_{c0}^2}$$

By considering the fourth-order terms, equation (5.25) can be accurate up to x/z=2.0 as shown by the circle-marked line in Figure 5.5. However, equation (5.25) introduces two new parameters V_{p4} and V_{s4}, which make it inappropriate for the purpose of velocity analysis. Only after the velocity functions are available, can the two parameters be calculated and be used for moveout corrections.

5.4 Accuracy of hyperbolic moveout velocity analysis

The most commonly used converted wave velocity analysis today is based on the hyperbolic moveout equation of a short spread (Tessmer and Behle, 1988; Harrison, 1992; Thomsen, 1999).

Because of the hyperbolic nature of equation (2.9), this implies that the conventional velocity analysis (Taner and Koehler, 1969) can be performed to determine the velocity function. However, as traveltime curves of converted waves are non-hyperbolic even for a homogeneous and isotropic medium, as shown by equation (2.1), and are strongly influenced by the velocity ratio of the medium, a critical question is: How accurate can velocity analysis be using the conventional hyperbolic approach? The answer is that the conventional hyperbolic velocity analysis cannot provide the velocity or velocity ratio function with enough confidence.

A synthetic example has been made to investigate this problem. The modelling parameters are the same as those used in Table 5.1. A Ricker wavelet with 15 Hz primary frequency is used. As there is no interest in amplitude information, a ray tracing algorithm is used to generate the converted wave seismogram as shown by Figure 5.6.

Semblance velocity analysis is performed using the Seismic Unix routine `suvelan` based on the conventional hyperbolic moveout. Figures 5.7a and 5.7b show the results for different offset-to-depth ratios. The picked velocities V_{c2}^* are listed in Table 5.2.

When the offset-to-depth ratio is about 1, the picked velocities V_{c2}^* have about 3% errors compared with the exact V_{c2} calculated from Table 5.1. When the offset-to-depth ratio increases to a more realistic 1.5, which is very common in modern surveys, the errors can increase to more than 5%. If offset-to-depth increases, larger

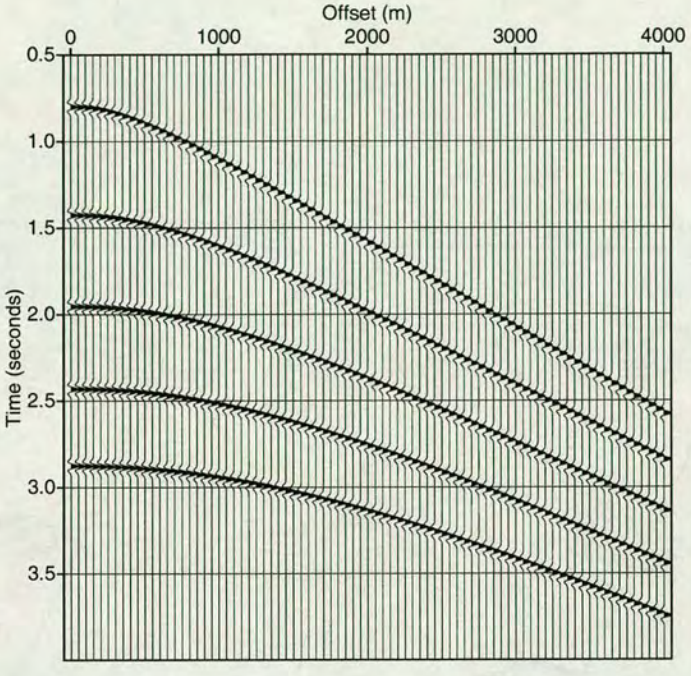

Figure 5.6: Ray tracing seismogram of converted waves using model in Table 5.1.

Reflector No.	Exact	when $x/z = 1$		when $x/z = 1.5$	
	V_{c2}(m/s)	V_{c2}^* (m/s)	$(V_{c2}^* - V_{c2})/V_{c2}$	V_{c2}^* (m/s)	$(V_{c2}^* - V_{c2})/V_{c2}$
1	1154	1198	3.8%	1209	4.8%
2	1281	1323	3.3%	1352	5.5%
3	1389	1429	2.9%	1461	5.2%
4	1478	1518	2.7%	1541	4.3%
5	1552	1589	2.4%	1619	4.3%

Table 5.2: Comparison of picked velocities V_{c2}^* from Figures 5.7a and 5.7b with the exact V_{c2} calculated from Table 5.1.

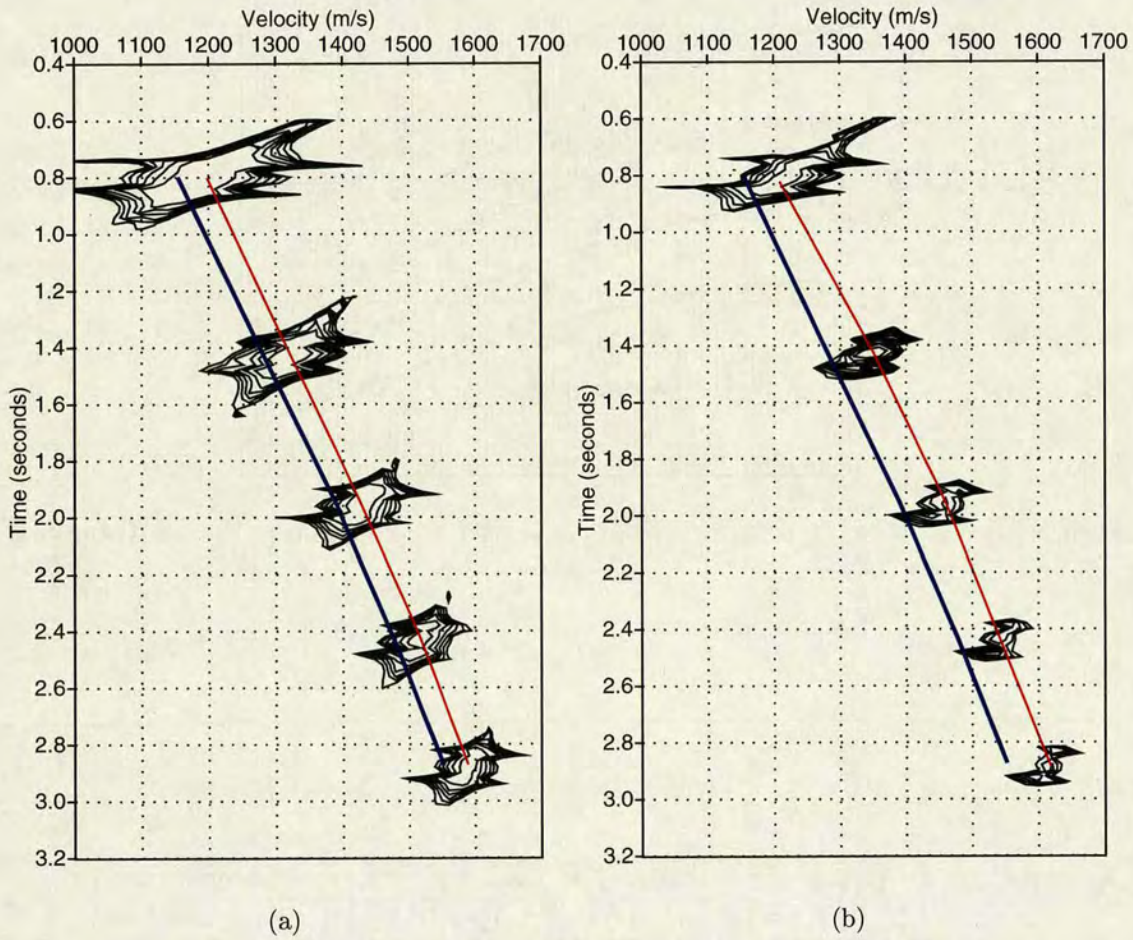

Figure 5.7: Conventional semblance hyperbolic velocity analysis of Figure 5.6 for two offset-to-depth ratios: (a) $x/z = 1.0$; (b) $x/z = 1.5$. The thick line is the exact V_c calculated from the model, whilst the thin line is the picked V_c^*.

errors are expected. For a fixed offset-to-depth ratio, the errors of the estimated pick velocities also increase with increasing velocity ratios.

The systematic error of V_{c2}^* has nothing to do with the picking mistakes. It is caused by the non-hyperbolic moveout at the non-zero offset, as the semblance analysis is the best fit of the reflection trajectory instead of hyperbolic asymptote at the zero offset.

Figures 5.7a and 5.7b also show that the resolutions of the velocity spectra are dependent on the offsets used. A shorter offset range may have smaller non-hyperbolic effect, but inevitably resolution for velocity picking is also reduced.

In Figure 5.6, the amplitude of the converted waves has not been calculated. In a more realistic case, when the amplitude of the converted wave is near zero at near offset, the error of the picked V_{c2}^* can be even bigger, when more energy at larger offset with non-hyperbolic behaviour contributes to the semblance velocity analysis.

As far as CCP binning is concerned, in layered isotropic or anisotropic media, the asymptotic conversion point is determined by the effective velocity ratio γ_{eff} (Thomsen, 1999). He suggested that it can be obtained by converting V_{c2} to γ_{eff}. By inverting equation (5.21), γ_{eff} can be obtained as

$$\gamma_{eff} = \frac{V_{p2}^2}{(1+\gamma_0)\, V_{c2}^2 - V_{p2}^2}. \tag{5.26}$$

Normally, V_{p2} can be determined quite precisely from P-wave data when the signal-to-noise ratio is not too low, and γ_0 can be obtained from correlation of P- and S-wave sections (Li and Yuan, 1999a; Thomsen, 1999). However, if there are some errors in the estimated V_{c2}, they will propagate to the estimation of γ_{eff}.

Let us consider how a small variation in V_{c2} can affect the estimation of γ_{eff} by

keeping V_{p2} and γ_0 constant. Differentiating equation (5.26) with regard to V_{c2} gives

$$\frac{\Delta\gamma_{eff}}{\gamma_{eff}} = -2\gamma_{eff}\,(1+\gamma_0)\,\frac{V_{c2}^2}{V_{p2}^2}\frac{\Delta V_c}{V_c}, \tag{5.27}$$

and substituting equation (5.21) into (5.27) gives

$$\frac{\Delta\gamma_{eff}}{\gamma_{eff}} = -2\,(1+\gamma_{eff})\,\frac{\Delta V_c}{V_c}. \tag{5.28}$$

In 4C seafloor data, γ_0 normally varies between 2.0 and 3.0, or higher. Thus, from the above equation, one can see that a small error in V_c will be propagated 6-7 times into the estimated γ_{eff}. Figure 5.8 shows that the errors in estimated V_{c2}

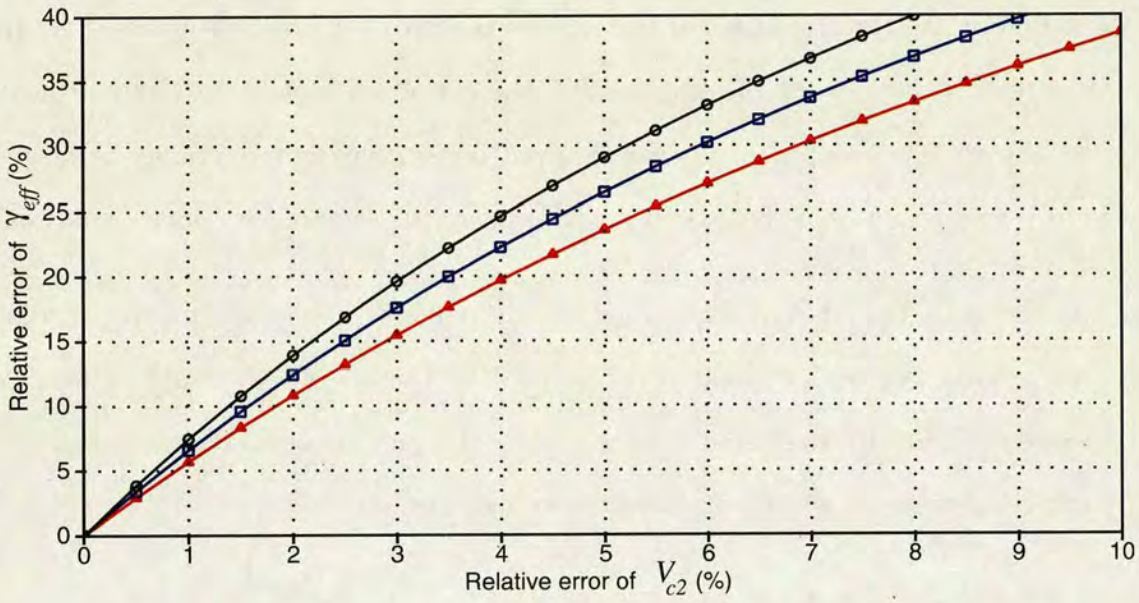

Figure 5.8: Error propagation from estimated V_{c2} to γ_{eff}. Three curves are indicated for different velocity ratios V_p/V_s 2.0 (triangles), 2.5 (squares) and 3.0 (circles), respectively.

will be amplified when converted to γ_{eff}, for different velocity ratios. Here isotropic homogeneous models with velocity ratios of 2, 2.5 and 3 are used. It can seen that only 3% of error in V_{c2} will result in 15%-20% error in the estimated γ_{eff} when average velocity ratio ranges from 2 to 3.

5.5 Moveout sensitivity to velocity ratio

The moveouts of converted waves at near offsets are determined by converted wave moveout velocity V_{c2}, and hyperbolic moveout can be accurate up to offset-to-depth ratio of 0.7. Thus conventional hyperbolic velocity analysis has to be done within this offset range.

However, typical acquisition design violates this criterion everywhere, and converted wave energy at near offsets is very weak. Thus velocity analysis inevitably involves seismic data with offsets at least up to offset-to-depth ratio of 1.0, where moveout is no longer hyperbolic, and larger velocity inversion errors are expected. The moveouts at this offset range are jointly influenced by V_{c2} and γ. It is necessary to analyse the moveout sensitivity to velocity ratio according to different offset-to-depth ratio range.

The analysis is based on a single-layered model with V_c of 1500m/s and two-way converted wave vertical traveltime of 1.5 seconds. Figure 5.9 shows the residual moveouts with different velocity ratios ranging from 2.0 to 3.0, compared with the moveouts with velocity ratio of 2.5. It can be seen that converted wave moveout is not sensitive to velocity ratio change up to an offset-to-depth ratio of 1.0, and large departures of the curves occur beyond an offset-to-depth ratio of 1.5.

5.6 Non-hyperbolic velocity analysis

The above study shows that moveouts of converted waves are relatively insensitive to the velocity ratio when x/z is less than 1.0. This means that, if a background velocity ratio is given, the converted wave moveout velocity analysis can be performed over a relatively large offset range, and a more accurate estimated V_c is expected.

Figure 5.10 shows semblance velocity V_c analysis for two different offset-to-depth

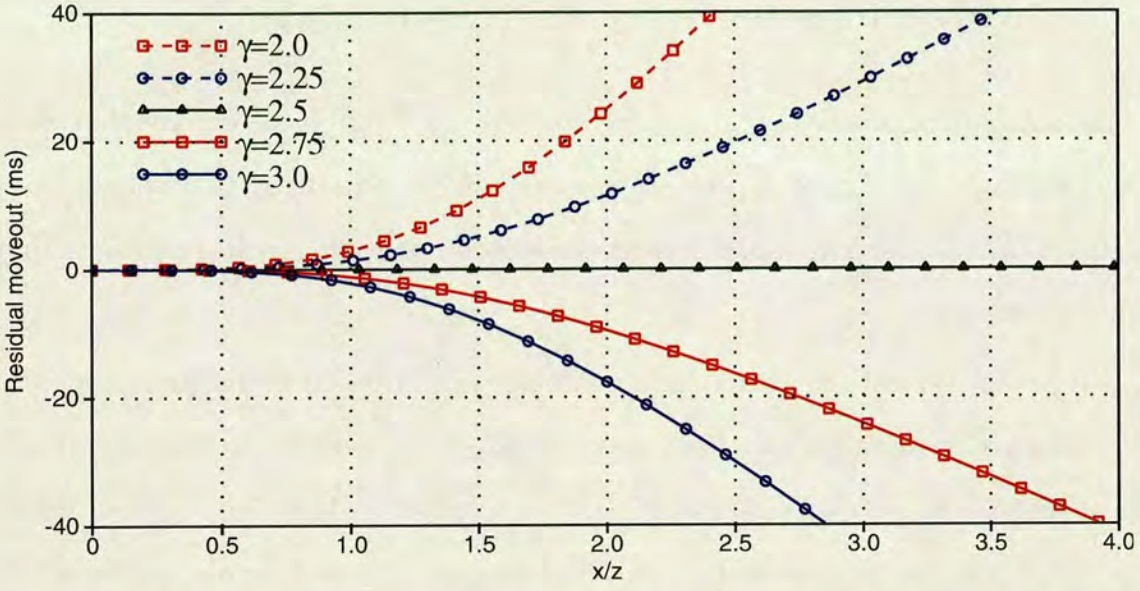

Figure 5.9: Analysis of sensitivity of moveout to velocity ratio. V_c=1500m/s, t_{c0}=1.5 seconds. The residual moveouts are difference of moveouts using γ=2.5 with those using other five velocity ratios from 2.0 to 3.0.

ratios 1.0 and 1.5. The synthetic data used in the semblance analysis are the same as that in Figure 5.6. The average and moveout velocity ratios in the model vary from 3.0 at the top to about 2.4 at the base. A background velocity ratio of 2.5 is used for the whole velocity analysis. The thick lines are the expected V_{c2} calculated from the modelling parameters listed in Table 5.1, and the thin lines are the picked values. It can be seen that the picked values agree very well with the exact values. The difference is well within 1%, which is inside the human picking error. It is also noticeable that by increasing the offset range, the resolution of the velocity spectra is also increased. However, the offset-to-depth range should be limited to 1.5, as γ influences converted wave trajectory massively beyond this range (Figure 5.9).

To check the influence of background velocity ratio on the V_c estimation, a velocity ratio of 3.0 is used in Figure 5.11. Comparing Figures 5.10 and 5.11, it can be seen that 20% velocity ratio change does not affect V_c scanning results very much. Further numerical tests show similar results. The insensitivity of converted wave

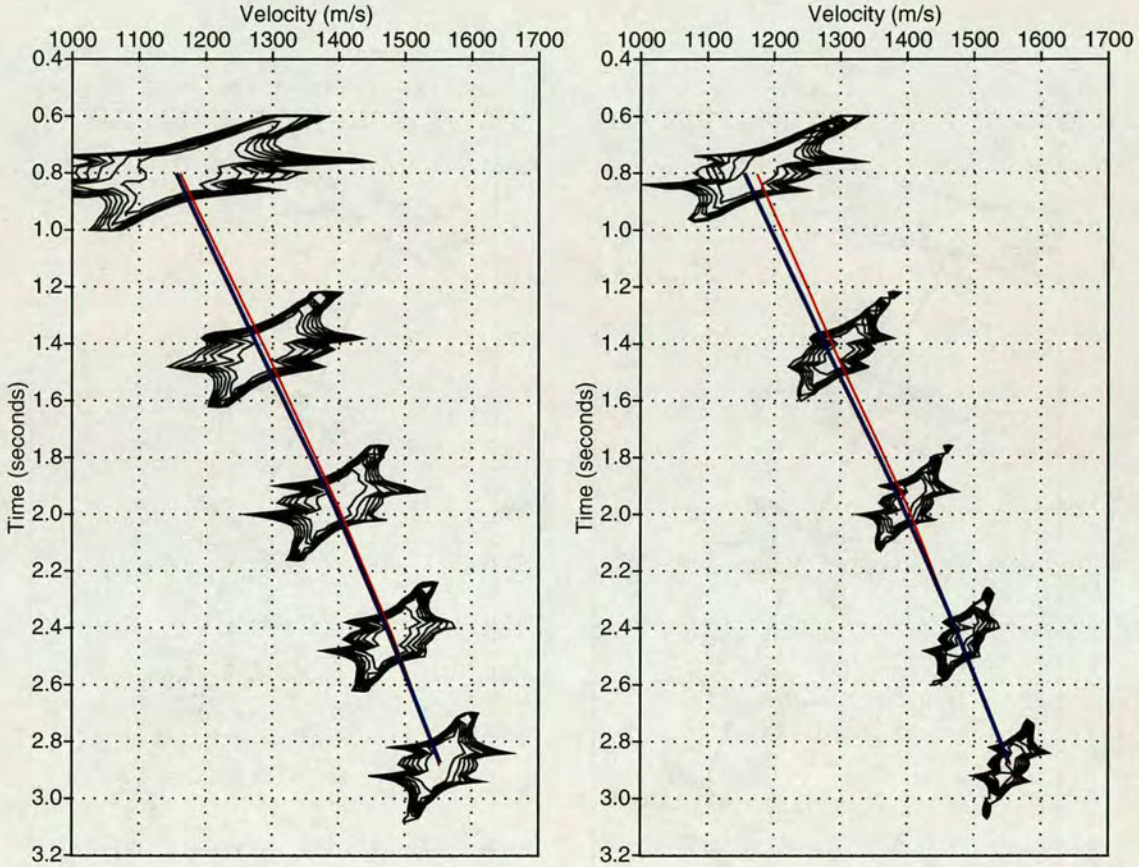

Figure 5.10: Semblance velocity analysis of Figure 5.6 for two offset-to-depth ratios: (a) $x/z = 1.0$; (b) $x/z = 2.5$. The non-hyperbolic DSR equation (5.5) is used. The background velocity ratio is 2.5. The thick line is the exact V_c calculated from the model, whilst the thin line is the picked V_c^*.

trajectory to velocity ratio means that for velocity V_c analysis purposes, detailed knowledge of the velocity ratio is not necessary. Differences between the moveout and average velocity ratio can be ignored. Thus the homogeneous and isotropic equation, the three-term Taylor series expansion (5.2) and the DSR equation (5.5), have sufficient accuracy for V_c analysis.

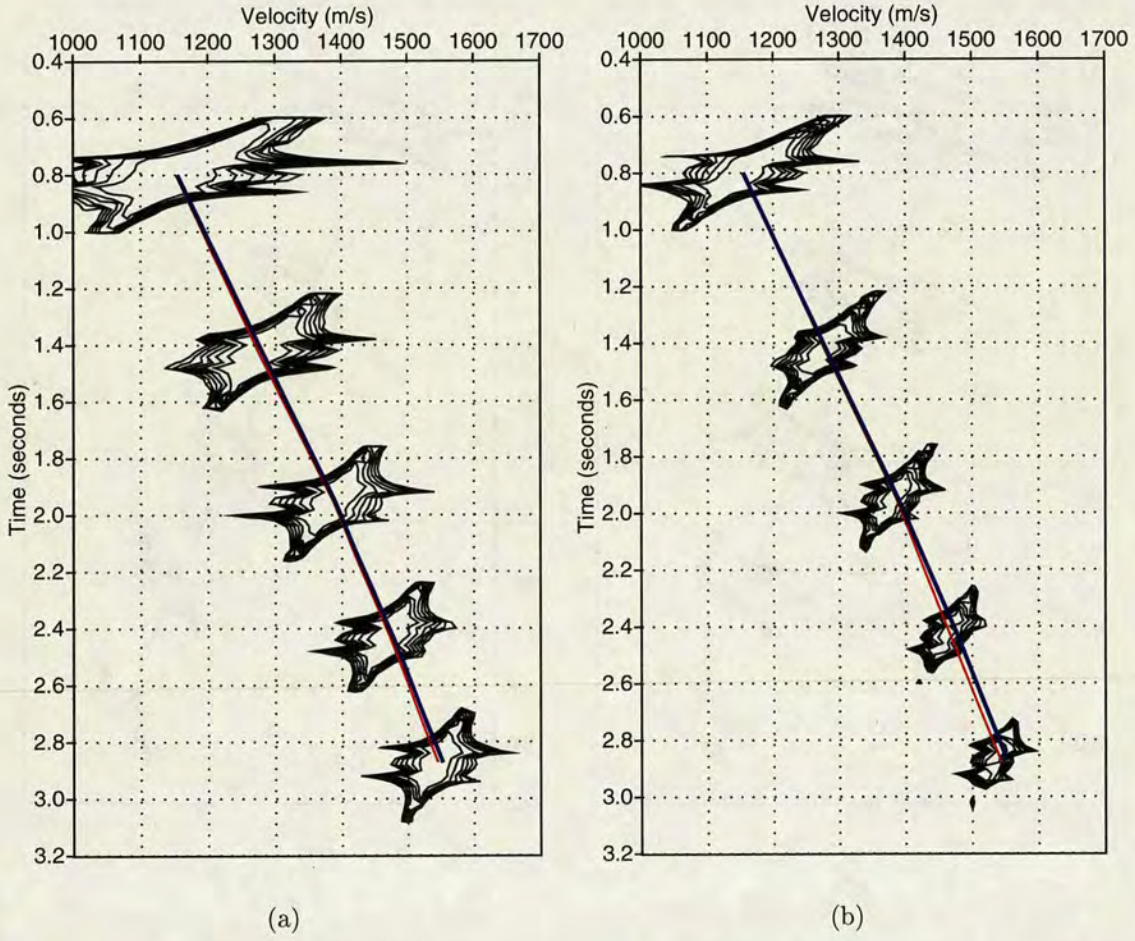

Figure 5.11: Semblance velocity analysis of Figure 5.6 for two offset-to-depth ratios: (a) $x/z = 1.0$; (b) $x/z = 2.5$. The non-hyperbolic DSR equation (5.5) is used. The background velocity ratio is 3.0. The thick line is the exact V_c calculated from the model, whilst the thin line is the picked V_c^*.

In these synthetic tests, constant background gammas are used to demonstrate that Vc analysis is relatively insensitive to background gamma. However, comparing Figures 5.10 and 5.11, the different gammas do have small influence on V_c analysis.

In practice, some initial velocity ratios as function of time or depth should be used for V_c analysis. This is particularly important if there is strong gradient in the velocity ratio.

5.7 Converted wave moveout correction

As discussed above, the moveout of a converted wave in vertically inhomogeneous media can be approximated by three parameters: near-offset moveout velocity V_{c2}, effective velocity ratio γ_{eff} and average velocity ratio γ_0. V_c can be obtained from converted velocity analysis as discussed above, and γ_{eff} can be determined from equation (5.26) with V_{p2} determined from P-P velocity analysis. The calculation of γ_{eff} also depends on the average velocity ratio γ_0, which is critical in converted wave processing. However, the average velocity can not be inverted from the converted wave moveout in vertically inhomogeneous isotropic or anisotropic media (see Chapter 6). It only can be determined from correlating P-P and P-S corresponding events as

$$\gamma_0 = \frac{2t_{c0}}{t_{pp0}} - 1, \tag{5.29}$$

where t_{c0} and t_{pp0} are P-S and P-P two-way vertical travel times. The correlation can be done when stack sections have some identifiable geological features like faults, anticlines or synclines (see Chapter 8), but it may be difficult if all the reflectors are flat. The correlation can only be done at a coarse scale, and is difficult on a finer scale. Fortunately the coarse scale correlation is good enough for velocity determination(Thomsen, 1999).

Once these three velocity functions are available, the converted wave moveout can be corrected using different approximation methods. Here, I check the accuracy of these approximations. The synthetic seismograms for velocity analysis (Table 5.1 and Figure 5.6) are used here.

1. Hyperbolic approximation - The hyperbolic equation (2.9) is the simplest method, which does not require other velocity ratio information. It is still being widely used especially at brute stack stage. However, it can only be accurate up to offset-to-depth ratio of 0.7. Beyond this range, large over-corrections are expected (Figure 5.12a).

2. Three-term Taylor series expansion - Figure 5.12b shows the NMO results from the three-term Taylor equation (5.2). It can be seen that it can be accurate up to an offset-to-depth ratio of 1.5.

3. DSR equation without vertical inhomogeneous correction - Moveout correction performed using DSR equation (5.24) is accurate up to an offset-to-depth ratio of 1.4, which is comparable with the result of the three-term Taylor series expansion.

4. DSR equation with vertical inhomogeneous correction (5.25)- When converted wave velocity and velocity ratio functions are given, the corresponding *P-P* and *S-S* moveout velocity functions can be easily derived from equation (5.21). Thus the interval velocities can be obtained from Dix-type inversion, and the fourth-order velocity V_{p4} and V_{s4} can be calculated. Using these two velocity functions, the accuracy of moveout correction can be achieved beyond offset-to-depth ratio of 2.0 (Figure 5.12d). At far offsets, there are undercorrections for the second reflector above offset 2000m, and for the third reflector above offset 3000m. From the model in Table 5.1, the reflector depth for the second reflector is 800m, and that for the third reflector is 1200m. Hence the offset-to-depth ratio is beyond 2.5, where equation (5.25) is no longer accurate. In practical data processing, these undercorrections should be muted.

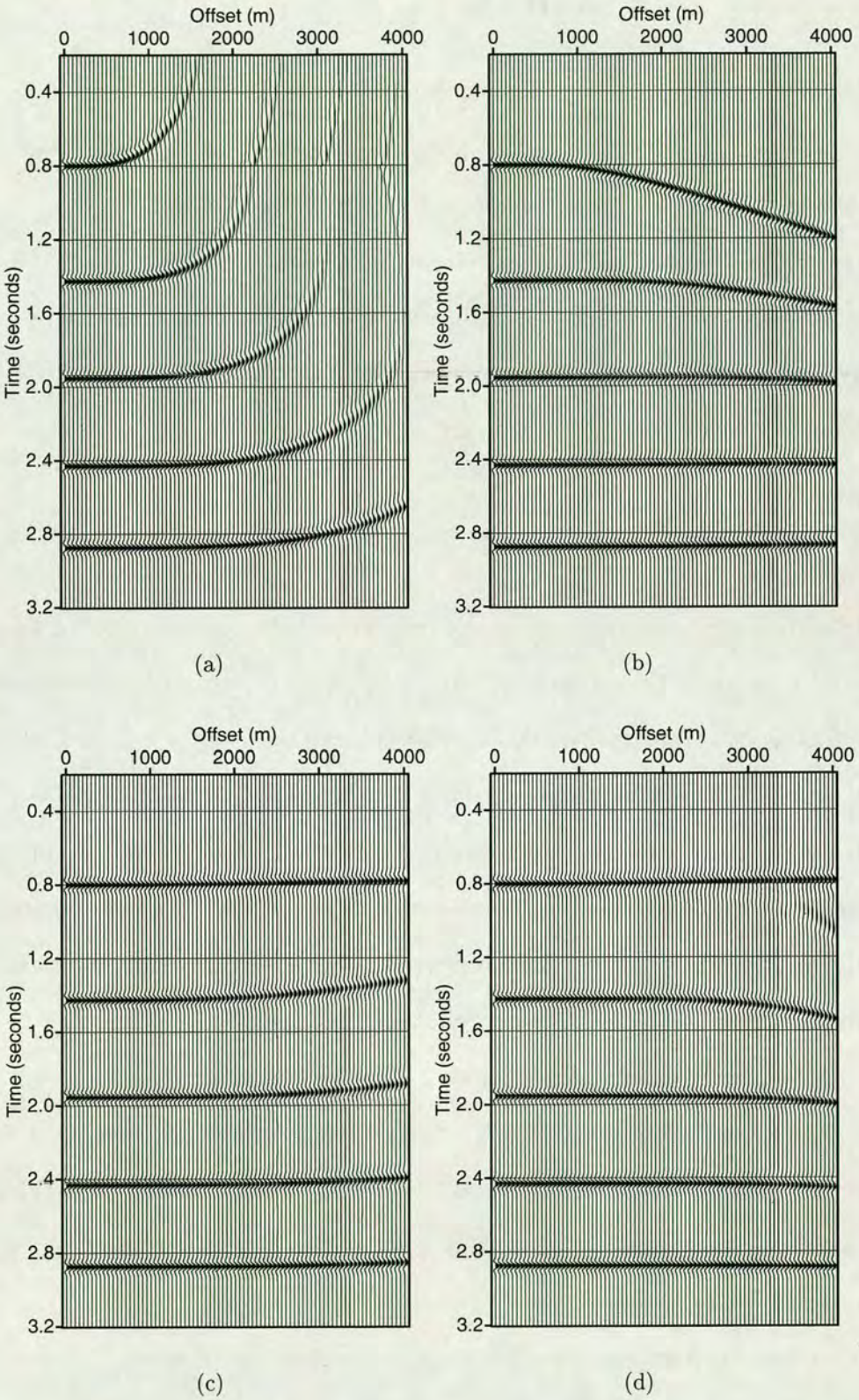

Figure 5.12: Converted wave moveout corrections using (a) hyperbolic equation (2.9), (b) three-term Taylor series (5.2), (c) DSR equation (5.24) without vertical inhomogeneous correction, and (d) DSR equation (5.25) with fourth-order vertical inhomogeneous correction.

5.8 Field data example

A field data example is shown here to demonstrate the accuracy and efficiency of non-hyperbolic velocity analysis and moveout correction using DSR equations, in comparison with the hyperbolic or the three-term Taylor equations.

Figure 5.13 shows a CCP gather of inline horizontal component at CCP location 1100. The seismogram is plotted with first break muting, automatic gain control (AGC) with a time gate of 1000ms, and a bandpass filter of 8-12.5-60-80 Hz. The data show relatively good signal-to-noise ratio.

5.8.1 Velocity analysis

Non-hyperbolic velocity analysis using equation (5.2) has been compared with conventional velocity analysis using hyperbolic equation (2.9). A background velocity ratio of 2.5 is used for non-hyperbolic velocity analysis.

Figure 5.14 shows the semblance spectra of hyperbolic velocity analysis (Taner and Koehler, 1969), and Figure 5.15 those for the non-hyperbolic counterparts. For these two methods, offset-to-depth ratios of 1.0 and 1.5 are used to check the sensitivity of spectra to the offsets involved. The picked velocity functions from hyperbolic (thin lines) and non-hyperbolic analysis (thick lines) using offset-to-depth of 1.0 are superimposed on all the spectra diagrams for comparison.

It is can be seen from spectra with offset-to-depth ratio of 1.0, that the difference between the hyperbolic and non-hyperbolic results can be about 2-3% (Table 5.3). The difference may seem trivial at first glance. However, when considering V_{c2} is used not only for moveout correction, but also for properly positioning the conversion points for imaging purposes, the situation can get more complicated. The conversion points are mainly determined by effective velocity ratio γ_{eff}, which can be calculated from V_{c2}, V_{p2} and γ_0. A 3% error in V_{c2} can propagate into a 20% error in γ_{eff}, as

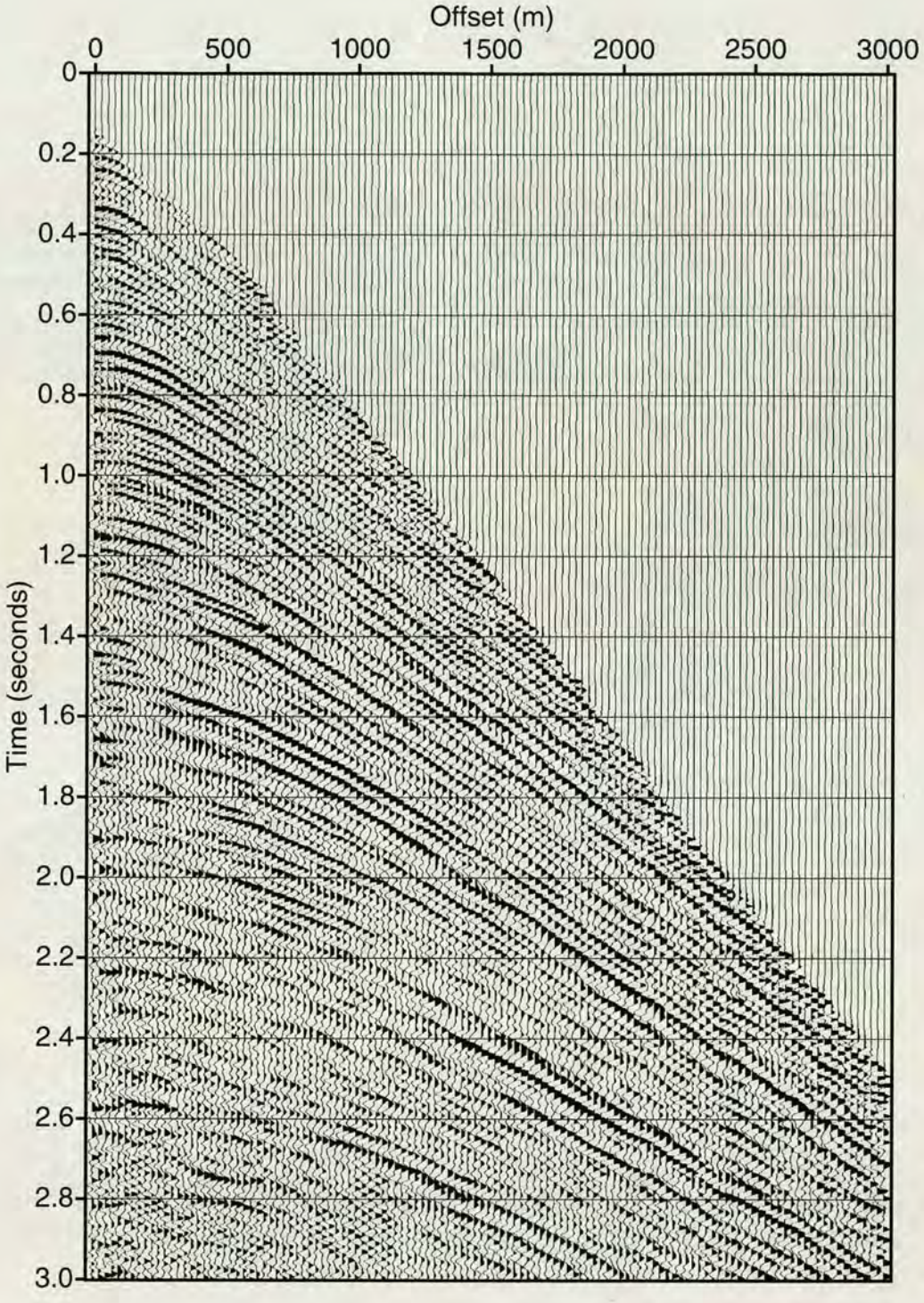

Figure 5.13: Inline horizontal component data (converted wave) at CCP 1100. The seismogram is plotted with first break muting, automatic gain control (AGC) with gate of 1000ms, and a bandpass filter of 8-12.5-60-80 hertz.

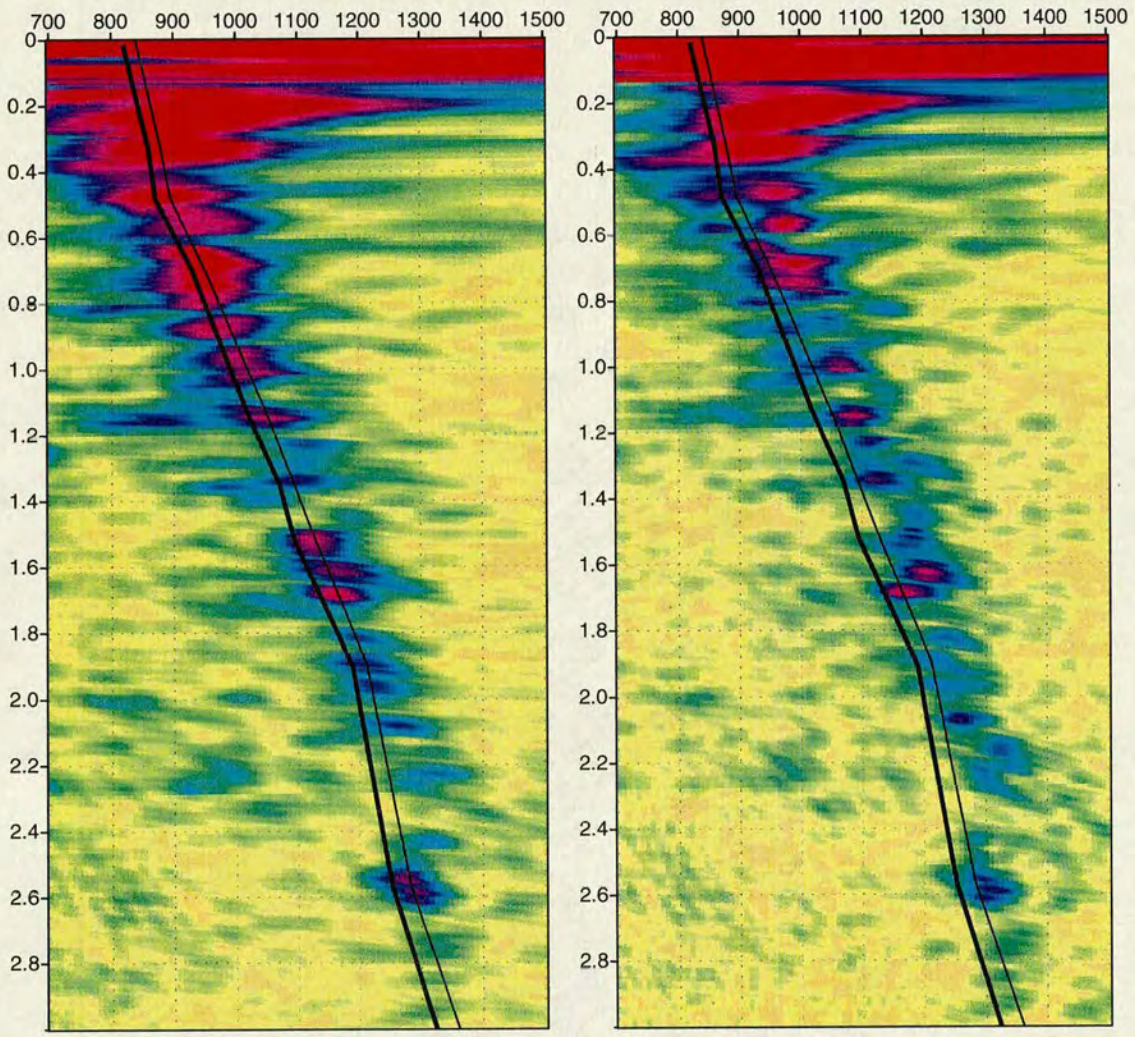

Figure 5.14: Hyperbolic velocity analyses with offset-to-depth ratios of (a) 1.0 (b) 1.5. The thin line shows the picked velocity curve from Figure 5.14a, while the thick line shows the corresponding curve from Figure 5.15a for comparison.

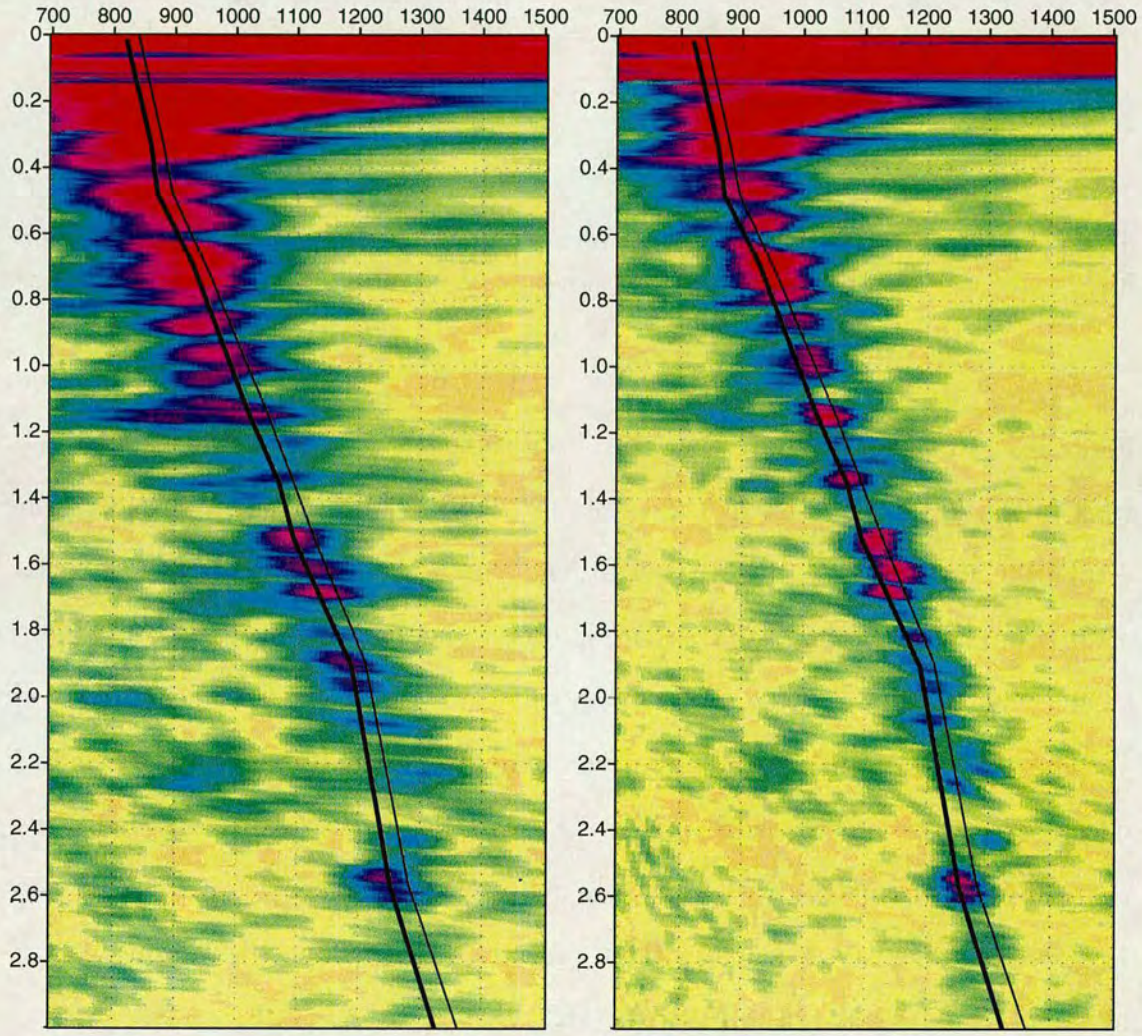

(a) (b)

Figure 5.15: Non-hyperbolic velocity analyses with offset-to-depth ratios of (a) 1.0 (b) 1.5. The thin line shows the picked velocity curve from Figure 5.14a, while the thick line shows the corresponding curve from Figure 5.15a for comparison.

seen in Table 5.3, and as demonstrated also by Figure 5.8. This error can generate an error of several hundred meters in positioning of the conversion points at large offsets.

No.	t_{c0} (ms)	V_{p2} (m/s)	γ_0	Hyperbolic		Non-hyperbolic	
				V_{c2}(m/s)	γ_{eff}	V_{c2}(m/s)	γ_{eff}
1	1531	1920	3.33	1127	2.03	1098	2.40
2	2064	2020	3.21	1252	1.62	1206	2.00
3	2574	2058	3.14	1275	1.70	1240	1.99
4	3310	2113	2.93	1349	1.66	1317	1.90

Table 5.3: Some picked V_{c2} from hyperbolic (Figure 5.14) and non-hyperbolic (Figure 5.15) velocity analysis, and their corresponding V_{p2} and γ_0.

As far as the resolution of the velocity spectrum is concerned, it is clear from Figures 5.14b and 5.15b that the ability to resolve the estimated velocity increases with increasing offset used in the analysis. However, the errors from hyperbolic estimation increase dramatically, resulting in more than 5% errors. In contrast, errors from non-hyperbolic analysis are limited to just 1-2%, which is acceptable for velocity analysis purposes.

The other advantage in the use of non-hyperbolic velocity analysis using longer offset data is to improve the resolution of velocity analysis for some events whose near offset reflections are rather weak. Such events, for example the reflections at 1.35 seconds and 2.06 seconds in Figure 5.13, are better focused when using non-hyperbolic analysis shown in Figure 5.15b.

The four NMO methods discussed in the previous section are applied to the data. As expected, hyperbolic NMO gives a poor result, and extensive muting has to be done before the converted wave stack (Figures 5.16a). Both the three-term Taylor series expansion (5.2) and the DSR equation (5.24) without layering correction give reasonably good results (Figures 5.16b and 5.16c). However, none of these three methods can flatten the reflection events at far offsets. By including the layering effects with equation (5.25), nearly all the events are correctly flattened (Figure

5.16d).

5.9 Discussion and conclusions

From Table 5.3, it can be seen that there are large differences between the average vertical velocity ratio γ_0 and the effective velocity ratio γ_{eff} due to layering. Using a Dix-like inversion procedure, one can obtain the interval velocity ratios. The dif-

No.	t_{c0}(ms)	V_{p2}(m/s)	γ_0	V_{c2}(m/s)	γ_{eff}	$V_{p2}^{(k)}$(m/s)	$V_c^{(k)}$(m/s)	$\gamma_0^{(k)}$	$\gamma_2^{(k)}$	$\gamma_{eff}^{(k)}$
1	1531	1920	3.33	1098	2.40					
2	2064	2020	3.21	1206	2.00	2258	1473	2.90	2.10	1.52
3	2574	2058	3.14	1240	1.99	2193	1369	2.86	2.38	1.98
4	3310	2113	2.93	1317	1.90	2260	1556	2.33	2.01	1.73

Table 5.4: Interval velocities $V_{p2}^{(k)}$, $V_c^{(k)}$ and velocity ratios $\gamma_0^{(k)}$, $\gamma_2^{(k)}$ by Dix-like inversion from Table 5.3.

ference between various interval velocity ratios is still very big. This demonstrates that strong anisotropy, or TIV anisotropy, to be exact, is present in the data, which is the main topic discussed in the next Chapter. The moveout of converted waves in a TIV medium can no longer be represented by equation (5.5) even for the homogeneous case. Fourth or higher order approximation has to be derived for long offsets. The fourth-order moveout correction of equation (5.25) for vertically inhomogeneous isotropic media, can be seen as a special case of anisotropic approximation.

Equation (5.5) shows that converted wave moveouts are determined by moveout velocity V_c and γ. V_c dominates moveout at near offsets, and the influence of γ affects only moveout at large offsets. An intuitive approach is to use converted wave traveltime for determining both parameters. This may be possible for the homogeneous isotropic case with large offset data available, when offset-to-depth ratio is larger than 1.5, as indicated by Figure 5.8. However, for the more realistic vertically inhomogeneous case, existing moveout approximations can not give sufficient

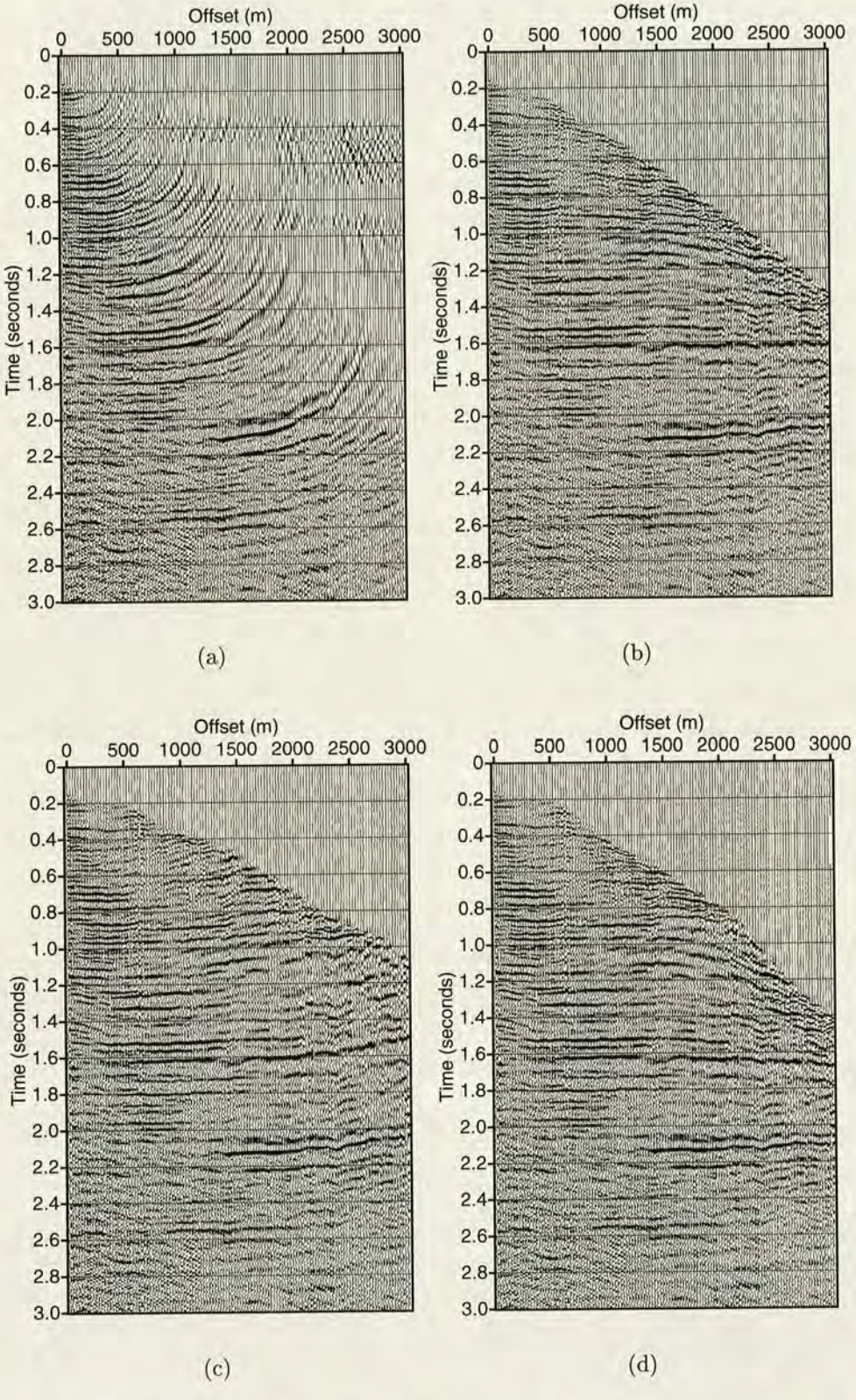

Figure 5.16: Comparison of different converted waved moveout correction methods: (a) hyperbolic; (b) three-term Taylor expansion; (c) DSR equation without vertical inhomogeneity correction and (d) DSR equation with vertical inhomogeneity correction.

accuracy beyond an offset-to-depth ratio of 1.5, and various velocity ratios are also involved as well which complicates the inversion procedure. In this case, velocity ratio can only be obtained from joint *P-P* and *P-S* moveout analysis.

It is interesting to note that, unlike pure-mode or other waves with symmetrical raypaths, converted wave velocities may exhibit diodic effects, which mean that moveout velocities for positive and negative offsets are different (Thomsen, 1999).This occurs whenever there is lateral variation in velocity (Figure 5.17). For

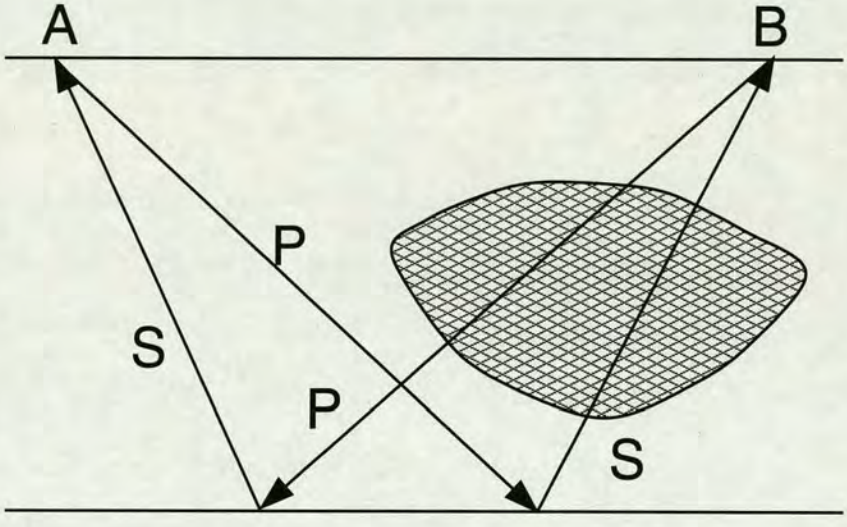

Figure 5.17: Diodic velocity occurs for converted waves whenever there is lateral variation in velocity (after Thomsen, 1999).

example, the presence of a gas cloud (Berg *et al.*, 1994) can decrease *P*-wave velocity, while shear wave velocity remains almost unaffected. The asymmetric raypath causes different *P*-wave velocity for opposite offsets, thus resulting in different converted wave moveout velocities. The diodic velocity requires special attention in data processing. In 2D surveys, there are easy ways to sidestep this problem. A simple procedure is to process positive and negative offsets separately, before final stack. However, in the 3D case, Thomsen (1999) pointed out that the problem is far from trivial, and requires a vector solution.

Another important aspect of seafloor converted-wave processing is static correc-

tions. These can be very much larger for shear-wave than for P-wave. The P-wave velocity tends to vary less near the seafloor since it is to some extent controlled by the fluid velocity except hard rocks. In contrast, shear-wave velocity can change fairly large from location to location, depending on the composition of seafloor sediments, such as mud or boulder clay (Riedel and Theilen, 2001). The main problem is to obtain the shear statics (receiver statics), which is commonly two to ten times greater than the P-wave statics for the same location (Tatham and McCormack, 1991). Conventional residual statics algorithms often fail for very large statics. The common practice for converted-wave receiver statics is to apply a common-receiver-stack approach (Harrison, 1992; Cary and Eaton, 1993). However, the method can only resolve the short-wavelength statics. For long-wavelength statics, near-surface shear-wave velocity can be obtained from some dispersive interface waves (Bohlen *et al.*, 1999; Muyzert, 2000), or from AVO analysis of seafloor reflections (Amundsen and Reitan, 1995b; Riedel and Theilen, 2001).

In summary, the accuracy of conventional hyperbolic velocity analysis for converted waves has been investigated. It shows that large errors can be caused by non-hyperbolic moveout at non-zero offsets. Hyperbolic velocity analysis for converted waves is particularly sensitive to the offset range used in the data analysis, and the error can be as large as 5%. These errors in velocity analysis will be amplified into velocity ratio estimation for CCP binning and moveout correction purposes. To overcome this problem, new equations based on non-hyperbolic analysis are introduced. A non-hyperbolic moveout equation with background γ can be used to perform velocity analysis over the intermediate offset ranges up to offset-depth ratio of 1.5. This reduces the error to less than 1% in velocity analysis. Double-square-root (DSR) approximation for converted waves has also been proposed for high accuracy moveout correction. The equations can handle vertical inhomogeneity as well. Applying DSR equation to field data shows that there is strong TIV anisotropy

present in the data, which is the main topic in the following chapter.

Converted wave moveout equations based on a three-term Taylor series expansion (Thomsen, 1999) have been extensively studied. I have found that there is an error in the A_4 coefficient of the traveltime equation in Thomsen's paper. With the correct coefficient, the three-term Taylor series expansion also performs reasonably well.

Chapter 6

Converted-wave analysis in media with polar anisotropy

6.1 Introduction

One of the main problems in processing converted-wave (C-wave) data from 4C marine surveys is the wide occurrence of polar anisotropy (transverse isotropy with a vertical symmetry axis, TIV) in marine sediments. The presence of polar anisotropy causes mis-positioning of reflectors during time and depth migration, and may also give misleading results in AVO modelling. Thus both conventional seismic interpretation and subtle lithology and fluid prediction are affected if the presence of anisotropy is ignored. Over recent years, various methods have been presented for quantifying polar anisotropy and compensating for its effects using either P-waves (Alkhalifah and Tsvankin, 1995), or C-waves (Seriff and Sriram, 1991; Yuan and Li, 1998), or both (Tsvankin and Thomsen, 1994; Li and Yuan, 1999a; Li and Yuan, 1999b).

For C-wave propagation, the presence of TIV anisotropy affects both the moveout and the conversion point position. On one hand, it is known that TIV has stronger

influence on SV-waves than on P-waves (Tsvankin and Thomsen, 1994). On the other hand, neglecting TIV will cause severe lateral smearing in stack section (Klie, 2000; Gaiser and Jackson, 2000).

In the previous chapter, I focused on converted-wave velocity analysis in isotropic media. Here I discuss the extension of the analysis methods into media with polar anisotropy. I also extend the conversion point approximation to polar anisotropy. I start with the parameterization of polar anisotropy, then discuss its effects on velocity estimation. This is followed by the anisotropic analysis methods.

6.2 TI parameters

Polar anisotropy, or TIV can either be intrinsic due to microscopic particle alignments such as in many types of shales (Winterstein and Paulsson, 1990), or be induced by fine layering such as in a sedimentary sequence (Backus, 1962) as shown in Figure 6.1. Five elastic constants are often required to describe polar anisotropy:

$$\mathbf{C} = \begin{bmatrix} C_{11} & C_{11}-2C_{66} & C_{13} & 0 & 0 & 0 \\ & C_{11} & C_{13} & 0 & 0 & 0 \\ & & C_{33} & 0 & 0 & 0 \\ & & & C_{44} & 0 & 0 \\ & & & & C_{44} & 0 \\ & & & & & C_{66} \end{bmatrix} \tag{6.1}$$

For traveltime analysis, it is often more convenient to use the so-called Thomsen (1986) parameters. The parameters are defined in terms of elastic constants:

$$\varepsilon \equiv \frac{C_{11}-C_{33}}{2C_{33}}, \tag{6.2}$$

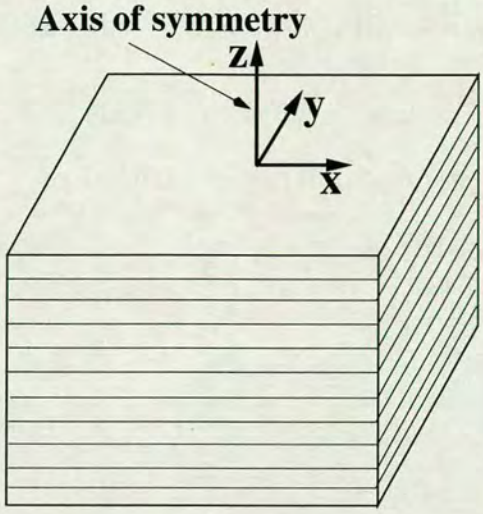

Figure 6.1: Model of a TIV material induced by fine layering.

$$\gamma' \equiv \frac{C_{66} - C_{44}}{2C_{44}}, \tag{6.3}$$

$$\delta \equiv \frac{(C_{13} + C_{44})^2 - (C_{33} - C_{44})^2}{2C_{33}(C_{33} - C_{44})}, \tag{6.4}$$

$$V_{p0} = \sqrt{C_{33}/\rho}, \tag{6.5}$$

and

$$V_{s0} = \sqrt{C_{44}/\rho} \tag{6.6}$$

where V_{p0} is the vertical P-wave velocity, V_{s0} is the SV-wave vertical velocity, ε measures the amount of P-wave anisotropy, γ' measures the amount of S-wave anisotropy, and δ relates to the shape of the wavefront; its physical significance is less obvious than the other parameters (Thomsen 1986). Note that in Thomsen's original notation γ instead of γ' is used for describing the amount of shear-wave anisotropy. However, in our context, γ is used for velocity ratio. Also only four Thomsen parameters are responsible for P-, SV- and C-wave propagation in TIV media, and these are V_{p0}, V_{s0} and the anisotropic parameters ε and δ. Thus Thomsen parameter

γ' will not be used, and γ will always be referred to as velocity ratio.

For velocity and traveltime analysis, two other anisotropic parameters σ and η, are also found to be very useful. They are defined as

$$\sigma = \frac{V_{p0}^2}{V_{s0}^2}(\varepsilon - \delta), \tag{6.7}$$

and

$$\eta = \frac{\varepsilon - \delta}{1 + 2\delta}. \tag{6.8}$$

If $\delta > -0.5$ (see equation (6.9)), σ and η will have the same sign, and are related to each other by

$$\eta = \frac{\sigma}{\gamma_0^2\,(1 + 2\delta)}.$$

Note that, most physical materials obey the inequality $\delta > -0.5$ (Thomsen 1986).

With the above parameterization, the following relationship can be established between the various velocities and anisotropic parameters (Thomsen 1986):

$$V_{p2} = V_{p0}\sqrt{1 + 2\delta}, \tag{6.9}$$

$$V_{s2} = V_{s0}\sqrt{1 + 2\sigma}, \tag{6.10}$$

and

$$\gamma_2 = \frac{V_{p2}}{V_{s2}} = \gamma_0 \frac{1 + 2\delta}{1 + 2\sigma}, \tag{6.11}$$

where V_{p2} and V_{s2} are P- and SV-wave stacking (rms) velocities, respectively, and γ_2 is the ratio between them. Thus one can see that δ is related to the difference between the P-wave vertical and stacking velocity, and we refer to it as the P-wave processing anisotropy. Similarly, we refer to σ as the SV-wave processing anisotropy. η is related to the difference between the moveout velocity V_{p2} and horizontal velocity

v_{ph} (Alkhalifah and Tsvankin, 1995) as

$$v_{ph} = V_{p2}\sqrt{1+2\eta}. \tag{6.12}$$

Since for elliptical anisotropy the moveout velocity equals the horizontal velocity (Levin, 1978), η is thus a parameter measuring the deviation of the medium from elliptical anisotropy, and is referred to as an anellipticity parameter.

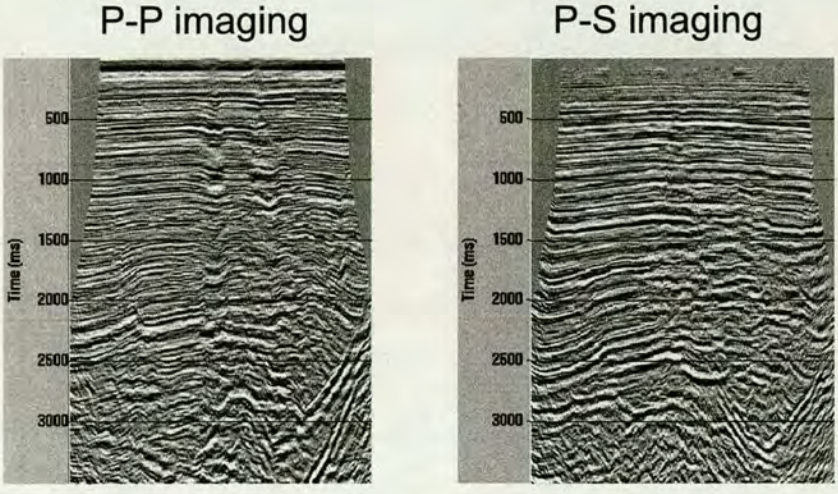

(a) (b)

Figure 6.2: Isotropically migrated (a) P-wave and (b) C-wave sections from Nolte *et al.* (1999). The C-wave section is displayed in P-wave traveltime. The horizons in the C-wave section appear at later times than their corresponding horizons in the P-wave section due to anisotropy assuming that errors γ_0 are small.

For depth processing, substantial positioning errors will arise for horizons in the C-wave section if anisotropy is ignored. For positive η or σ, the stacking velocity ratio γ_2 will be smaller than the vertical velocity ratio γ_0. Thus as the C-wave section was converted to P-wave time for joint P- and C-wave analysis, the horizons in the C-wave section will appear deeper than those in the P-wave section since $t_{p0} = t_{c0}/(1+\gamma_0)$ when ignoring anisotropy. Figure 6.2 illustrates this problem. Note that the original imaging was performed by the authors in depth domain using isotropic algorithms. After converting both P- and C-wave sections into P-wave

time using velocity ratio from isotropic migration velocity analysis, there is a mistie between P- and C-wave sections.

6.3 Accuracy and limitation of isotropic method

Before I present the anisotropic analysis methods, let us examine how accurate the isotropic method will be, and what parameters we can obtain from the C-wave data using isotropic methods despite the presence of anisotropy.

The isotropic method (Thomsen, 1999) is based on the short-spread approximation. There are two areas that it concerns: moveout and conversion point position, as I have discussed in the last chapter. The short-spread moveout is governed by C-wave moveout velocity V_{c2}, and the conversion point of short-spread is controlled by effective velocity ratio γ_{eff}.

The moveout velocity of C-wave in TIV media is given by Tsvankin and Thomsen (1994) as

$$V_{c2}^2 = \frac{V_{p2}^2 + \gamma_0 V_{s2}^2}{1+\gamma_0}, \tag{6.13}$$

where γ_0 is the traveltime ratio between the one-way down-going P-wave and the up-going S-wave, which equals the vertical velocity ratio, and V_{p2} and V_{s2} are the short-spread moveout velocities of P- and S- waves in horizontally-layered anisotropic media. V_{p2} and V_{s2} are defined by (Hake *et al.*, 1984; Tsvankin and Thomsen, 1994)

$$V_{p2}^2 = \frac{1}{t_{p0}} \sum_{i=1}^{n} v_{p2i}^2 \Delta t_{pi}\,, \text{ and} \tag{6.14}$$

$$V_{s2}^2 = \frac{1}{t_{s0}} \sum_{i=1}^{n} v_{s2i}^2 \Delta t_{pi}, \tag{6.15}$$

where v_{p2i} and v_{s2i} are the interval moveout velocities defined by equations (6.9) and

(6.10).

As for effective γ_{eff} , Thomsen (1999) has shown that it has the same form in a layered anisotropic medium as in a layered isotropic medium. Because equation (6.13) also has the same form in isotropic media, the isotropic code might be used for time processing of seismic data in anisotropic media.

Here, I study the accuracy of the isotropic method. Table 6.1 shows three TIV materials documented by Thomsen (1986). These materials have been widely used in literatures of TIV studies (Seriff and Sriram, 1991; Levin, 1992; Tsvankin and Thomsen, 1994). The reflector depth of the modelling is 500 meters. Although this is a single-layered model, its conversion points and moveouts are calculated using equations for isotropic layered media, as suggested by (Thomsen, 1999).

Material	V_{p0}(m/s)	V_{s0}(m/s)	ε	δ
Dog Creek shale	1875	826	0.225	0.100
Pierre shale	2202	969	0.015	0.060
Taylor sandstone	3368	1829	0.110	-0.035

Table 6.1: Modelling parameters of three layers with TIV anisotropy. The parameters are from Thomsen (1986).

First I check the accuracy of conversion point position x_c. The isotropic approximation results calculated from equations (5.12) and (5.18) are compared with exact solution from ray-tracing. Three parameters are used to calculate conversion points: effective velocity ratio γ_{eff} , vertical velocity ratio γ_0 and C-wave moveout velocity V_{c2}. Figure 6.3 shows the accuracy of conversion point position in single-layered anisotropic medium using the isotropic method. It can be seen that error in conversion point is very large. For Dog Creek shale (dotted line), when x/z is larger than 1, the relative error $|x_c^{(exact)} - x_c^{(approx)}|/x$ is over 4%. For a typical offset of 3000 meters, this represents a lateral shift of 120 meters. At offset-to-depth ratio of 2.0, the error can be more than 8%, which is comparable with the asymptotic approximation. If the limit for a good x_c approximation is 1% (for example, 20 meter

error for an offset of 2000 meters), the isotropic approximation is only accurate up to offset-to-depth ratio of 0.4, within which the reflectivity of converted wave is still very low. Similar results are found from two other TIV materials: Taylor sandstone and Pierre shale. Note that Dog Creek shale and Taylor sandstone have positive σ values, whilst Pierre shale has a negative σ. The difference causes different types of error (positive or negative) in the conversion point approximation.

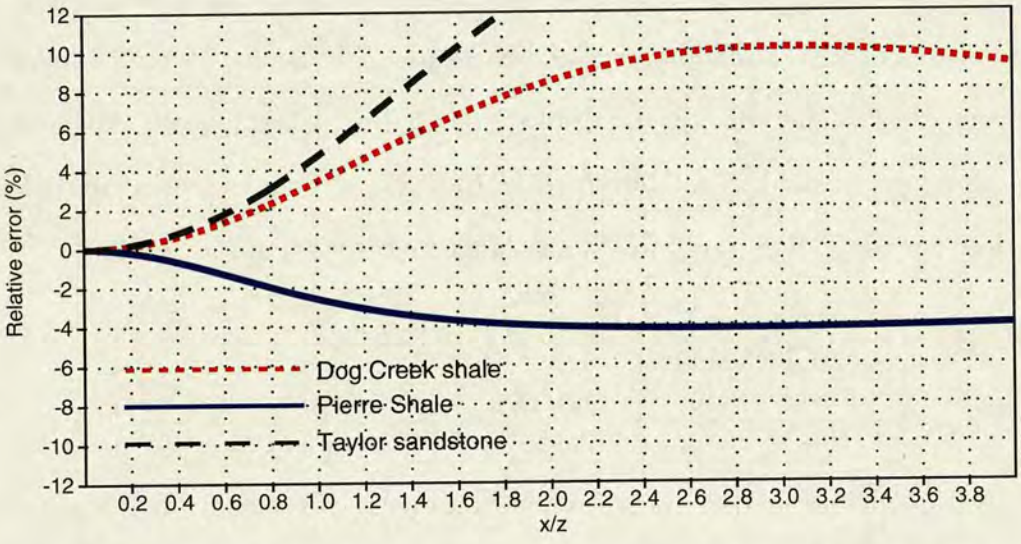

Figure 6.3: Accuracy of conversion point position in single-layered anisotropic medium using isotropic method. The horizontal axis is the offset-to-depth ratio, and vertical axis is normalized error of conversion points $\left(x_c^{(exact)} - x_c^{(approx)}\right)/x$. Three lines show the conversion point error compared with ray-tracing in different TIV materials: Dog Creek shale (dotted-line), Pierre shale (solid-line) and Taylor sandstone (dashed-line).

Secondly, I check the accuracy of moveout approximation using isotropic code. Based on the same model parameters as Table 6.1, Figure 6.4 demonstrates the accuracy of C-wave moveout approximation in a single-layered anisotropic medium using the isotropic method [equation (5.24)]. Unlike isotropic approximation of conversion point position, the isotropic approximation for moveout performs relatively well within offset-to-depth ratio of 1.0. Large errors can be seen at far offsets.

Note that, in the above analysis, I have assumed that there are no errors in the

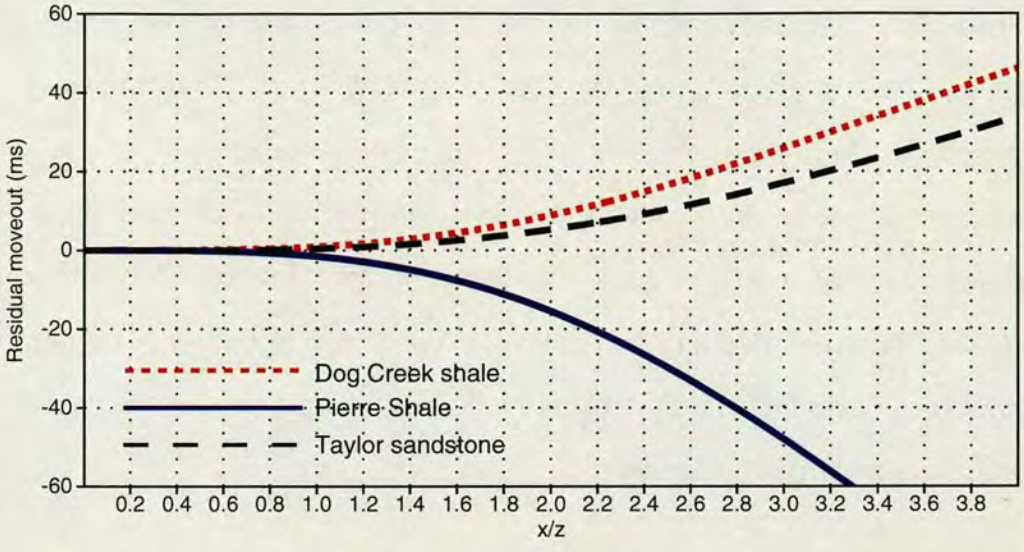

Figure 6.4: Accuracy of C-wave moveout in a single-layered anisotropic medium using the isotropic method. The horizontal axis is the offset-to-depth ratio, and the vertical axis is the residual moveout. Three lines show residual moveout in different TIV media: Dog Creek shale (dotted-line), Pierre shale (solid-line) and Taylor sandstone (dashed-line).

anisotropic parameters themselves. This is fine for the above analysis which aims to examine the accuracy of the isotropic assumption. In practice, there are often errors in the estimation of the anisotropic parameters either from laboratory measurements or from seismic data. Wang (2001) discussed the accuracy of anisotropic parameters measured from laboratory; Li and Yuan (2001) discussed accuracy and sensitivity of anisotropic parameters from 4C seismic data.

In summary, ignoring anisotropy and using the effective velocity ratio and the vertical velocity ratio, the isotropic conversion point equation can be accurate only up to an offset-to-depth ratio of 0.4. Considering that converted wave energy is small at near offset, the effective velocity ratio γ_{eff} for C-wave stacking is actually not so ***effective*** for a moderate degree of anisotropy.

On the other hand, the isotropic moveout equation is accurate up to 1.0. This implies we can use the same methods to determine V_c as in Chapter 5. Once V_c is determined, with known V_P and γ_0, the effective velocity ratio γ_{eff} can be de-

termined from the data. However, for imaging purposes, accurate conversion point positioning requires anisotropy estimation in order to stack C-wave data of mid-to-long offsets. In other words, mid-to-long offset data are necessary to determine anisotropic parameters from C-wave moveout. In modern 4C surveys, long offset data up to an offset-to-depth ratio of 3.0 are common. Furthermore, for joint P- and C-wave interpretation and for depth imaging, it is also necessary to determine the anisotropic parameters. For this more accurate travel time equations suitable for mid-to-long offset are necessary.

6.4 Converted waves in a single-layered TIV medium

First, I start with single-layered TIV medium in search of a more accurate approximation for conversion point and moveout.

6.4.1 Determination of the conversion point

Following Thomsen (1999), the Taylor expansion of conversion point offset, x_c, is derived in Appendix D as

$$x_c = x\left(c_0 + \frac{c_2 x^2}{1 + c_3 x^2}\right), \tag{6.16}$$

where

$$c_0 = \frac{\gamma_{eff}}{1+\gamma_{eff}}, \quad c_3 = \frac{c_2}{1-c_0}, \tag{6.17}$$

$$c_2 = \frac{\gamma_{eff}\left(1+\gamma_0\right)}{2t_{c0}^2 V_c^2 \gamma_0 \left(1+\gamma_{eff}\right)^3}\left(\gamma_0\gamma_{eff} - 1 + 8\left(\gamma_0 + \gamma_{eff}\right)\gamma_{eff}\eta\right). \tag{6.18}$$

Among the three coefficients, c_0 and c_3 are the same as Thomsen (1999), whilst c_2 is different and more accurate. The term, $8\left(\gamma_0 + \gamma_{eff}\right)\gamma_{eff}\eta$ in equation (6.18) shows the influence of anisotropy which was neglected by Thomsen (1999). Here, I choose

η, which is the measurement of P-wave anisotropy, as the parameter to describe the influence of TIV on converted waves. Another option is to use σ, which is the measurement of the S-wave anisotropy. I prefer η because I find that the influence of P-wave anisotropy is stronger than that of S-wave anisotropy, especially in the more realistic multi-layered case discussed in the following sections.

The accuracy of equations (6.16)-(6.18) is tested by comparing the approximation with ray tracing. I use the three TIV materials in Table 6.1. Relative errors of conversion point offsets x_c using equations (6.16)-(6.18) are shown in Figure 6.5. Among these three materials, two with positive σs or ηs (Dog Creek shale: σ=0.644; Taylor sandstone: σ=0.494) show that equations (6.16)-(6.18) are accurate up to offset-to-depth ratio of 2.5, and the relative error $\left|x_c^{(exact)} - x_c^{(approximation)}\right| / x$ is well within 1%. These results are comparable with the x_c approximation in an isotropic medium (Figure 5.1). For Pierre shale, which has a negative σ or η (σ=-0.232), the approximation is accurate to $x/z = 1.0$. It is still far more accurate than the isotropic approximation shown in Figure 6.3.

Nevertheless, the Pierre shale example still shows that negative σ or η makes the conversion point in a TIV medium deviate greatly from its isotropic counterpart. This has also been observed in the shear-wave moveout approximation by Tsvankin and Thomsen (1994). For S-wave, this is because its moveout velocity is much slower than its vertical velocity, particularly when σ is close to -0.5. For converted waves, it causes relatively larger γ_{eff} which makes the anisotropic term in equation (6.18) more prominent than its isotropic counterpart.

6.4.2 Moveout: Taylor series expansion

The traditional methods for quantifying polar anisotropy and compensating for its effects are based on the extension of the isotropic Taylor series equation. Seriff

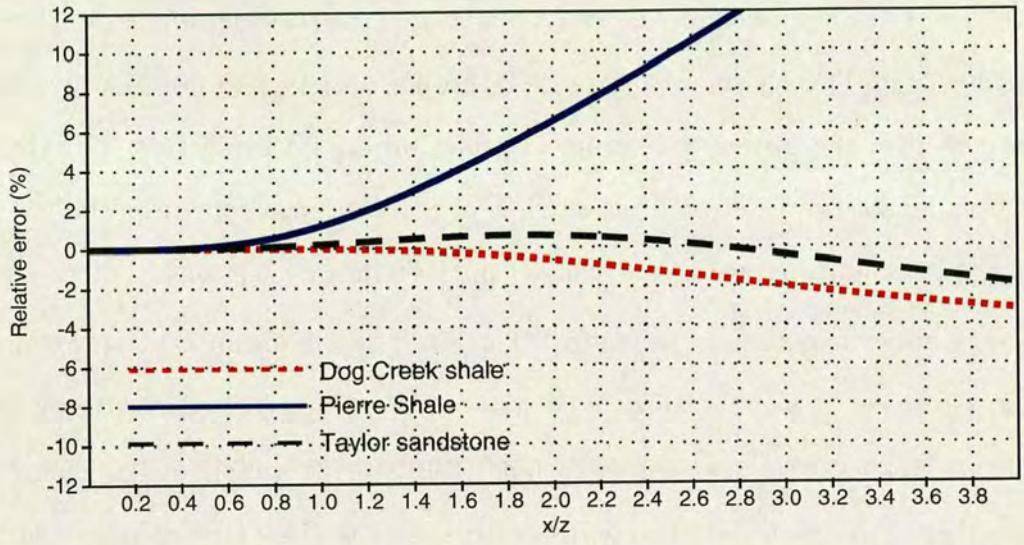

Figure 6.5: Relative errors of conversion point offsets x_c using equations (6.16)-(6.18) in an anisotropic single-layered medium. The relative errors are calculated by $\left(x_c^{(exact)} - x_c^{(approximation)}\right)/x$, where $x_c^{(exact)}$ is the exact conversion point offset calculated from ray tracing. Three curves indicate different materials: Dog Creek shale (dotted line), Pierre shale (solid line) and Taylor sandstone (dashed line), respectively. Note that the horizontal axis is the offset-to-depth ratio.

and Sriram (1991) first discussed this problem based on hyperbolic approximation. The non-hyperbolic equation of three-term Taylor series expansion of a C-wave moveout in multi-layered media was presented by Tsvankin and Thomsen (1994). That equation is very complicated. For a single-layered medium, Thomsen (1999) gave a simplified form as

$$t_c^2 = t_{c0}^2 + A_2 x^2 + \frac{A_4 x^4}{1 + A_5 x^2}, \tag{6.19}$$

where

$$\frac{1}{A_2} = V_{c2}^2 = \frac{V_{p2}^2}{1+\gamma_0} + \frac{\gamma_0 V_{s2}^2}{1+\gamma_0}; \tag{6.20}$$

$$A_4 = \frac{-A_2^2}{4t_{c0}^2\gamma_0(1+\gamma_{eff})^2}\left[(\gamma_0\gamma_{eff}-1)^2 + 8\left(\gamma_0^2-1\right)\gamma_{eff}^2\eta\right]; \tag{6.21}$$

$$A_5 = \frac{A_4}{1/V_{ph}^2 - A_2}, \tag{6.22}$$

where V_{ph} is the horizontal P-wave velocity. Note that Thomsen (1999) did not give a detailed derivation of equation (6.21). In Appendix E, a detailed derivation is given.

It is also important to point out that the original Thomsen's moveout equation was not correct. Its A_4 coefficient had an error.

Equation (6.19) can be accurate up to offset-to-depth ratio of 2.0 for all three TIV materials discussed above (Figure 6.6). The approximation for Pierre shale (negative η) is slightly worse than those for Dog Creek shale and Taylor sandstone (positive η).

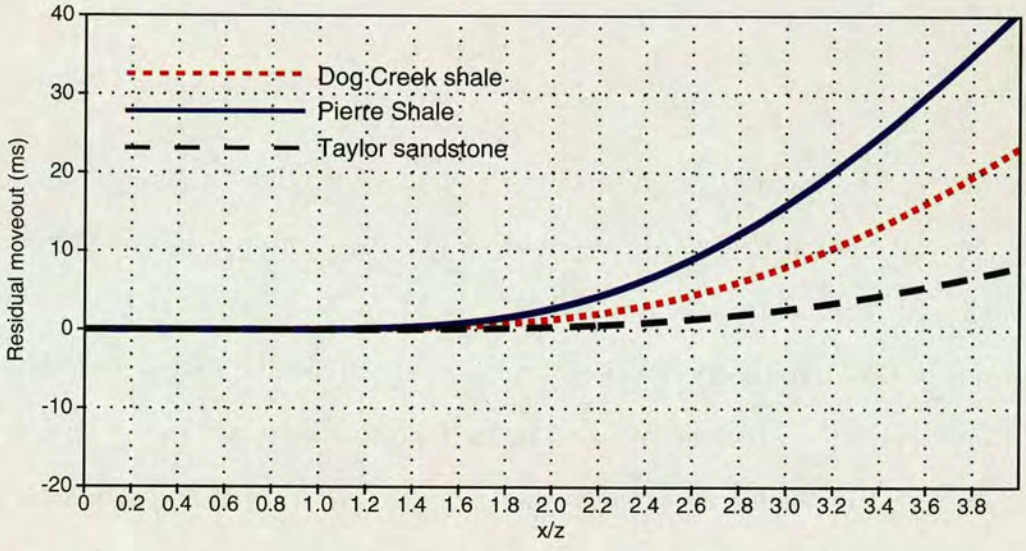

Figure 6.6: The traveltime difference (residual moveout) between the exact traveltime and the three-term Taylor series expansion (6.19) for a C-wave from a TIV medium. The parameters of the three TIV materials are listed in Table 6.1. Dog Creek shale and Taylor sandstone show $\eta > 0$, whilst Pierre shale shows $\eta < 0$.

6.4.3 Moveout: double-square-root (DSR) approximation

Using the traveltime equations for single wave modes (Tsvankin and Thomsen, 1994), the travel time t_c for a single layered TIV medium can be derived as (see Appendices B and C for more details of the derivation),

$$t_c = t_p + t_s = \sqrt{t_{p0}^2 + \frac{x_c^2}{V_{p2}^2} - \frac{2\eta x_c^4}{V_{p2}^2\left(t_{p0}^2 V_{p2}^2 + (1+2\eta)x_c^2\right)}} + \sqrt{t_{s0}^2 + \frac{(x-x_c)^2}{V_{s2}^2} + \frac{2\zeta(x-x_c)^4}{V_{s2}^2\left(t_{s0}^2 V_{s2}^2 + (x-x_c)^2\right)}}, \tag{6.23}$$

where

$$\zeta = \gamma_{eff}^2 \eta, \tag{6.24}$$

$$t_{p0} = \frac{1}{1+\gamma_0} t_{c0},$$

and

$$t_{s0} = \frac{\gamma_0}{1+\gamma_0} t_{c0}.$$

Here, in order to simplify the moveout equation, I introduce a new parameter ζ, which governs the fourth-order moveout at middle-to-far offset for S-S moveout (see Appendix C), similar to η introduced by Alkhalifah and Tsvankin (1995). More importantly, the simplification makes it possible to extend the moveout equation to multi-layered media, which is discussed in the following section. On the other hand, equation (6.23) depends on the conversion point x_c, which can be calculated from equations (6.16)-(6.18).

Equation (6.23) contains four independent parameters: γ_0, V_{p2}, V_{s2} and η, noting ζ is related to η through equation (6.24). Note that η, σ and ζ have the same sign, either positive and negative, in a single-layered TIV medium.

The accuracy of equation (6.23) is tested by synthetic modelling. Figure 6.7 shows the residual moveout between the exact traveltime and the DSR approximation. The same three materials discussed before are used here as well. For materials with positive σ (or ζ), Dog Creek shale and Taylor sandstone, the DSR equation performs very well, and its accuracy is even beyond offset-to-depth ratio of 4.0.

However, there is slight overcorrection starting from x/z of 1.4. For Pierre shale with negative σ or ζ, its accuracy is limited to x/z of 1.5. It is expected that the conversion point approximation does not perform well for negative ζ, thus the moveout errors calculated by the DSR equation are mainly due to this factor.

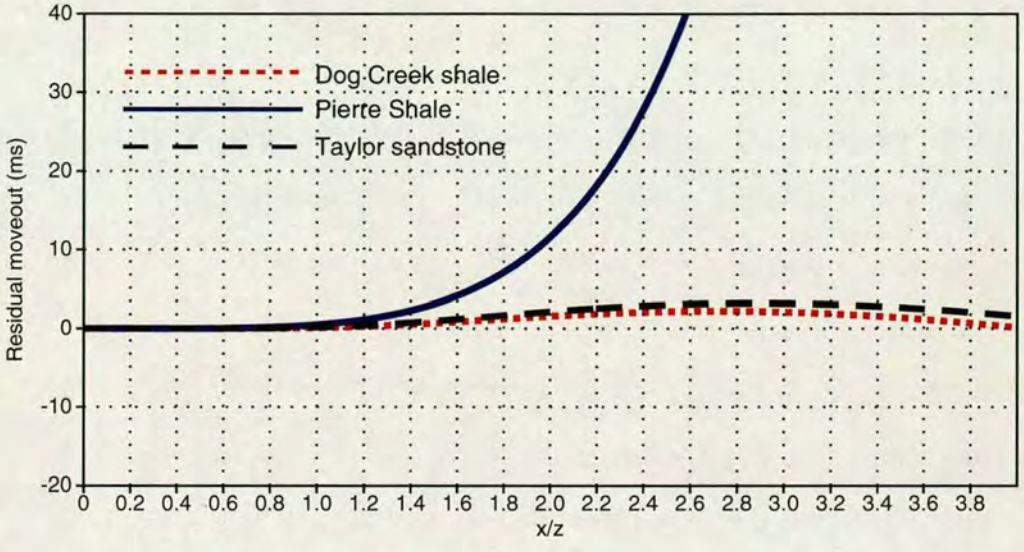

Figure 6.7: The traveltime difference (residual moveout) between the exact traveltime and the DSR approximation (equation (6.23)) for a C-wave from a TIV medium. The parameters of the three TIV materials are listed in Table 6.1. Dog Creek shale and Taylor sandstone show $\sigma > 0$, whilst Pierre shale shows $\sigma < 0$.

6.4.4 Parameter dependency

From equations (6.16), (6.19) and (6.23), it is clear that both conversion point offset and moveout of C-wave are dependent on the vertical velocity ratio γ_0. In order to obtain the vertical velocity ratio, several authors suggested the use of P- and P-S correlation (Sena and Toksöz, 1993; Tsvankin and Thomsen, 1995; Gaiser, 1996). Thomsen (1998) elaborated this further: First a stacked C-wave section is obtained using the two-term Taylor series expansion for short offsets, then the C-wave section is correlated with the P-wave section to obtain the vertical velocity ratio, and afterwards other types of processing such as anisotropy estimation, or

depth conversion may follow. Obviously the success of this procedure is highly dependent on the correlation results. Unfortunately P- and C-wave correlation is known to be a major issue in joint P- and C-wave processing and interpretation.

Therefore, in combining P- and C-wave data, without requiring prior information about depth and velocities, I would like to address three questions. 1) *What* additional parameters can we obtain from C-wave data with the intermediate spread? 2) *How* can we invert the S-stacking velocity in the case when the vertical velocity ratio is unknown? 3) Are the vertical velocities really undetectable?

To answer the *what* and *how* questions, let us assume that V_{p2} and η are known from processing P-waves which are almost always acquired in modern surveys, and also note that V_{c2} and γ_2 or γ_{eff} are usually the parameters waiting to be determined. Thus the main parameter concerned is the vertical velocity ratio γ_0. Variation of γ_0 affects both t_c and the conversion point x_c, and variation of x_c in turn affects t_c through equation (6.7).

Let us consider how a small variation in γ_0 will affect the conversion point x_c and the travel time t_c by keeping other parameters the same.

First examine x_c. Differentiating equation (6.16) with respect to γ_0, and ignoring the higher-order term (the term with 8η) in c_2 of equation (6.18), with some manipulations, gives

$$\frac{\Delta x_c}{x_c} = \frac{-1}{1+\gamma_{eff}} \frac{\Delta \gamma_0}{\gamma_0} \left[1 - \frac{c^*(1-c_0-c^*)}{c_0(1-c_0)}(3\gamma_{eff}-1) - \frac{(c^*)^2}{(1-c_0)^2} \right] \frac{c_0 x}{x_c}, \qquad (6.25)$$

where

$$c^* = \frac{c_2 x^2}{1+c_3 x^2}.$$

The higher order terms (the terms of the inverse of $(1-c_0)$ and $(1-c_0)^2$ within the big bracket) have opposite sign to the first order term (the asymptotic term). Also note that $(1+\gamma_{eff})$ is normal larger than 2.0, so it can be seen that the error

propagation into x_c due to γ_0 will be minimized, and x_c will be relatively insensitive to γ_0 variations. To verify this, I perturb γ_0 with 5%, 10% and 15% variations, and calculate the corresponding variation in conversion-point distance (Δx_c) for Dog Creek shale (Figure 6.8a) with reflector depth of 1000m. For up to 15% variation, the maximum variation in x_c is less than 15m. The conversion point at short offsets ($x/z < 3.0$) is more sensitive to γ_0 variation than those at far offsets ($x/z > 4.0$). However, as a whole, the effects are small. This also holds for other anisotropic materials such as the Pierre Shale.

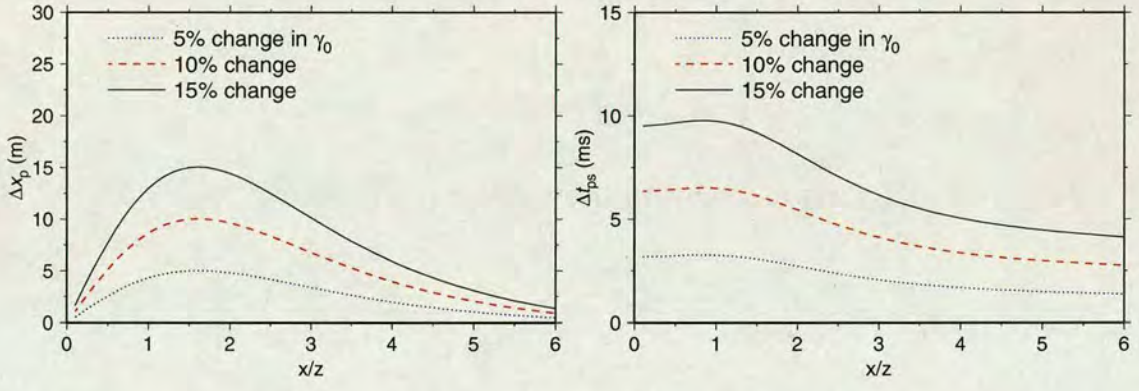

(a) (b)

Figure 6.8: Variation of (a) x_c and (b) t_c with the vertical velocity ratio γ_0. γ_0 is perturbated by 5% (dotted lines), 10% (dashed lines) and 15% changes (solid lines) for C-wave reflection in a single layer of Dog Creek shale with depth of 1000 meters.

Now examine t_c. Differentiating equation (6.23) on both sides, and ignoring the quartic terms inside the square-root of t_p and t_s, gives

$$\frac{\Delta t_c}{t_c} = \frac{\Delta t_p}{t_c} + \frac{\Delta t_s}{t_c}, \tag{6.26}$$

where

$$\Delta t_p = \frac{-1}{(1+\gamma_0)^3}\frac{t_{c0}^2}{t_c}\Delta\gamma_0 + \frac{x_c^2}{t_c V_{p2}^2}\frac{\Delta x_c}{x_c},$$

$$\Delta t_s = \frac{\gamma_0}{(1+\gamma_0)^3}\frac{t_{c0}^2}{t_c}\Delta\gamma_0 - \frac{x_c(x-x_c)}{t_c V_{s2}^2}\frac{\Delta x_c}{x_c}. \tag{6.27}$$

Equation (6.27) shows that variations of t_p and t_s due to γ_0 have opposite signs, which will result in a reduction in the variations of t_c due to γ_0. Thus the C-wave travel time t_c may be relatively insensitive to the variation of γ_0. This may also be explained intuitively as below. Suppose that the t_c curve is decomposed as the sum of two curves: t_p and t_s. If an error in γ_0 reduces the one-wave zero-offset P-wave time t_{p0}, this approximates to a shift of the t_p upwards, whilst the same error in γ_0 will increase the one-wave zero-offset SV-wave time t_{s0}, and this approximates to a shift of the t_s curve downwards. As a result, the sum of these two shifted curves may give a curve similar to the original t_c curve.

To quantify the variation, substituting equation (6.27) into equation (6.26), gives

$$\frac{\Delta t_c}{t_c} = \frac{\gamma_0(\gamma_0-1)}{(1+\gamma_0)^3}\frac{t_{c0}^2}{t_c^2}\frac{\Delta\gamma_0}{\gamma_0} + \frac{1}{t_c^2}\left(\frac{x_c^2}{V_{p2}^2} - \frac{x_c(x-x_c)}{V_{s2}^2}\right)\frac{\Delta x_c}{x_c}. \tag{6.28}$$

Equations (6.25) and (6.28) allow a quantitative analysis of the relative variation of t_c due to γ_0 variation. Similarly, as in Figure 6.8a, I calculate the travel time variation (Δt_c) due to the variations in γ_0 for the Dog Creek shale (Figure 6.8b). The maximum variation for 15% changes in γ_0 happens at the near offsets and is less than 10ms. As the offset increases, the sensitivity decreases. Again, overall effects are small.

Although the overall sensitivity of the C-wave data to the variation of the vertical velocity ratio γ_0 is low, the above analysis reveals that the data at near offsets are most sensitive to the variations in γ_0, and the data at far offsets are least sensitive. This explains why the problem of vertical velocity inversion remains highly ambiguous even if far-offset non-hyperbolic terms are included for inversion, as demonstrated by Tsvankin and Thomsen (1995). The only way to obtain the vertical

velocity information is to utilize the near-offset information, if this is possible.

Figures 6.9 and 6.10 provide another numerical confirmation, where we assume known V_{p2} and η and directly invert γ_0 and γ_2 (the stacking velocity ratio). Synthetic modelling (Figure 6.9) is generated by ray tracing for all three TIV materials discussed above, Dog Creek shale, Pierre shale and Taylor sandstone. The reflector depth is 1000 meters, the maximum offset is 3000 meters, and a 30 Hz Ricker's wavelet is used here. For inversion, I also use ray tracing to calculate synthetic x_c and t_c for each pair of γ_0 and γ_2, in order to evaluate the parameter dependency more accurately. The traces are stacked for semblance analysis as shown in Figure 6.10b.

For Dog Creek shale (Figure 6.10a), a relatively good resolution for γ_2 (1.5-1.8) is achieved, whilst the resolution for γ_0 (1.8-3.0) is very poor, although double scanning over γ_0 and γ_2 does invert correct values. For Pierre shale, (Figure 6.10b), the resolution for γ_0 (2.0-26) is relatively better than that for γ_2 (2.5-5.0). For Taylor sandstone, there is almost no resolution for γ_0, although the resolution for γ_2 is better (1.2-1.4). Note that different scales for γ_0 and γ_2 are used to highlight the resolution problems.

Also note that both Dog Creek shale and Taylor sandstone have positive σ, and Pierre shale has negative σ. Because most published TIV materials (Thomsen, 1986; Vernik and Liu, 1997), show positive σ, one can expect that the resolution of γ_0 will be worse than that of γ_2.

Nevertheless, all three materials studied above show poor resolution for determining γ_0 and γ_2 simultaneously. These results indicate that γ_0 may be hard, if not impossible, to obtain from C-wave moveout inversion.

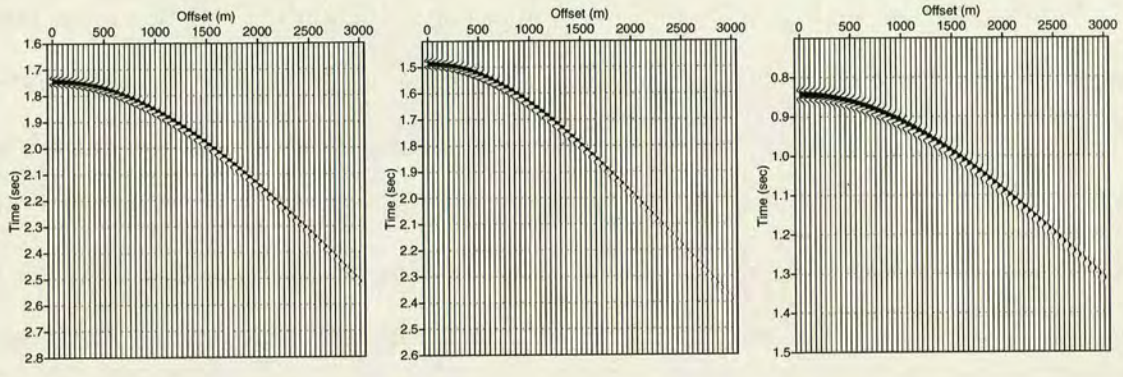

(a) (b) (c)

Figure 6.9: Synthetic modelling of three TIV materials: (a) Dog Creek shale, (b) Pierre shale, and (c) Taylor sandstone .

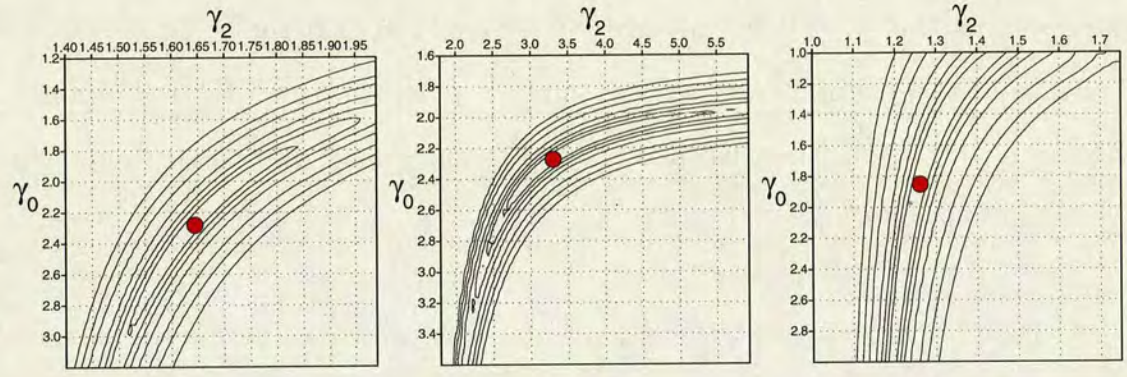

(a) (b) (c)

Figure 6.10: Semblance analysis for γ_0 and γ_2 with prior information about V_{p2} and η. The red dots are expected values of γ_0 and γ_2. (a) Dog Creek shale (V_{p2}=2054m/s, η=0.1042), (b) Pierre shale (V_{p2}=2330m/s, η=0.0402), and (c) Taylor sandstone (V_{p2}=3248m/s and η=0.156). Note that different scales are used to highlight the resolution problems.

6.4.5 Anisotropic velocity analysis

From the above analysis, I have demonstrated that the influence of vertical velocity ratio γ_0 on the C-wave moveout is very weak. The vertical velocity ratio γ_0 has to be obtained from independent measurements, for example, from well-log or from cross-correlation of $P-P$ and $P-S$ stack sections. If V_{p2} and γ_0 are known, can we obtain the other two parameters in order to invert all four TIV parameters from the C-wave moveout ?

Using V_{p2} and γ_0 as prior information, I perform double scanning of V_{c2} and η for all three materials discussed above. I use the Taylor series expansion equation (6.19) owing to its slightly better approximation up to offset-to-depth range of 2.0. Figure 6.11 shows the semblance analysis of V_{c2} and η. The red dots are the exact values calculated from the models. From the contour plots of semblance analysis, it can be seen that there is almost no error for V_{c2}, but small errors are found for η (about 0.01 - 0.02). Overall, the inversion results are satisfactory.

As far as the issue of resolution is concerned, Pierre shale (Figure 6.11b) has the highest resolution, Taylor sandstone (Figure 6.11b) has lowest resolution, and the resolution of Dog Creek shale is somewhere in between. This is expected from the isotropic approximation discussed above (Figure 6.4), where the residual moveout of Pierre shale is largest and Taylor sandstone is smallest. In fact, for fixed offset-to-depth range and primary frequency of the wavelet, the resolution of η is determined by $(\gamma_0^2 - 1)\,\gamma_{eff}^2$ as suggested from equation (6.21). The larger the values of γ_0 and γ_{eff}, the higher is the resolution of η. In our examples, the values of $(\gamma_0^2 - 1)\,\gamma_{eff}^2$ for Taylor sandstone, Dog Creek shale and Pierre shale are 0.986, 3.87 and 146.3, respectively. The Taylor sandstone has a very small value, owing to its γ_{eff} of only about 0.864, but the Pierre shale has a very high value of γ_{eff}, 4.76. For typical OBC surveys reported in the literature (Thomsen, 1999), γ_0 is around 3.0 whilst

γ_{eff} is about 2.0, and the value of $(\gamma_0^2 - 1)\,\gamma_{eff}^2$ is 32, which should give a very good resolution of η. Nevertheless, even for small values of $(\gamma_0^2 - 1)\,\gamma_{eff}^2$, such as the Taylor sandstone here, the resolution of η is still acceptable for a reasonably good interpretation.

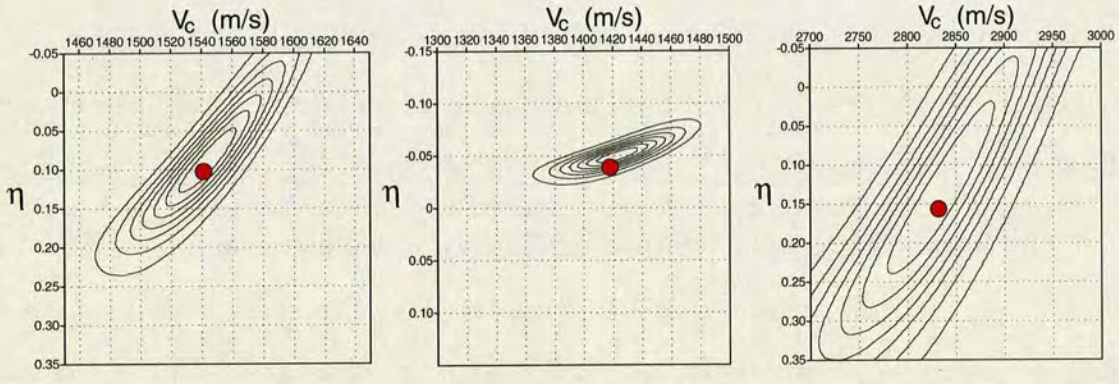

(a) (b) (c)

Figure 6.11: Semblance analysis for V_{c2} and η with prior information about V_{p2} and γ_0 for given t_{c0}, using the three-term Taylor-series expansion. The red dots are expected values of V_{c2} and σ. (a) Dog Creek shale (V_{p2}=2054m/s and γ_0=2.27), (b) Pierre shale (V_{p2}=2330m/s and γ_0=2.272), and (c) Taylor sandstone (V_{p2}=3248m/s and γ_0=1.841).

6.5 Converted waves in multi-layered TIV media

Here, I extend the equations for conversion point and moveout into a more realistic case: horizontally multi-layered TI media.

6.5.1 Conversion point

The Taylor series expansion of conversion point offset x_c in multi-layered TIV media, is derived in Appendix D as

$$x_c = x\left(c_0 + \frac{c_2 x^2}{1 + c_3 x^2}\right), \tag{6.29}$$

where

$$c_0 = \frac{\gamma_{eff}}{1+\gamma_{eff}}, \quad c_3 = \frac{c_2}{1-c_0}, \tag{6.30}$$

$$c_2 = \frac{\gamma_{eff}\left(1+\gamma_0\right)}{2t_{c0}^2 V_{c2}^2 \gamma_0 \left(1+\gamma_{eff}\right)^3}\left(\gamma_0\gamma_{eff} - 1 + 8\left(\eta_{eff}\gamma_0\gamma_{eff} + \zeta_{eff}\right)\right). \tag{6.31}$$

η_{eff} is the effective anisotropic parameter for P-wave in multi-layered media, introduced by Alkhalifah (1997) as

$$\eta_{eff} = \frac{1}{8t_{p0}V_{p2}^4}\left(\sum_{i=1}^{n} v_{p2i}^4\left(1+8\eta_i\right)\Delta t_{p0i} - t_{p0}V_{p2}^4\right), \tag{6.32}$$

η_i is the interval anisotropic parameter for the i-th layer, as defined by equation (6.8), ζ_{eff} is the effective anisotropic parameter for SV-wave in multi-layered media, defined as

$$\zeta_{eff} = \frac{1}{8t_{s0}V_{s2}^4}\left(t_{s0}V_{s2}^4 - \sum_{i=1}^{n}\Delta t_{s0i}v_{s2i}^4\left(1-8\zeta_i\right)\right), \tag{6.33}$$

and ζ_i is the anisotropic parameter for the i-the layer defined by equation (6.24). The detailed derivation of ζ_{eff} can be found in Appendix C. For a single-layered medium, η_{eff} and ζ_{eff} will reduce to η and ζ, respectively.

The accuracy of equations (6.29)-(6.33) is tested by numerical modelling. Table 6.2 shows the parameters of a three-layer model. Each layer has a thickness of 500 meters. The conversion points calculated by equations(6.29)-(6.33) are shown in Figure 6.12. The relative error is below 2%, which is slightly bigger that its isotropic multi-layer (see Figures 5.3 and 5.4) and anisotropic single-layer counterparts (see Figure 6.5). Note that the above test is merely a proof of concept. To gain more

No.	Material	v_{p0i}	v_{s0i}	ε_i	δ_i	V_{c2}	η_{eff}	ζ_{eff}
1	Dog Creek shale	1875	826	0.225	0.100	1541	0.104	0.154
2	Limestone shale	3306	1819	0.134	0.000	2047	0.187	0.130
3	Taylor sandstone	3368	1829	0.110	-0.035	2264	0.187	0.119

Table 6.2: Modelling parameters of three layers with TIV anisotropy. The parameters are from Thomsen (1986).

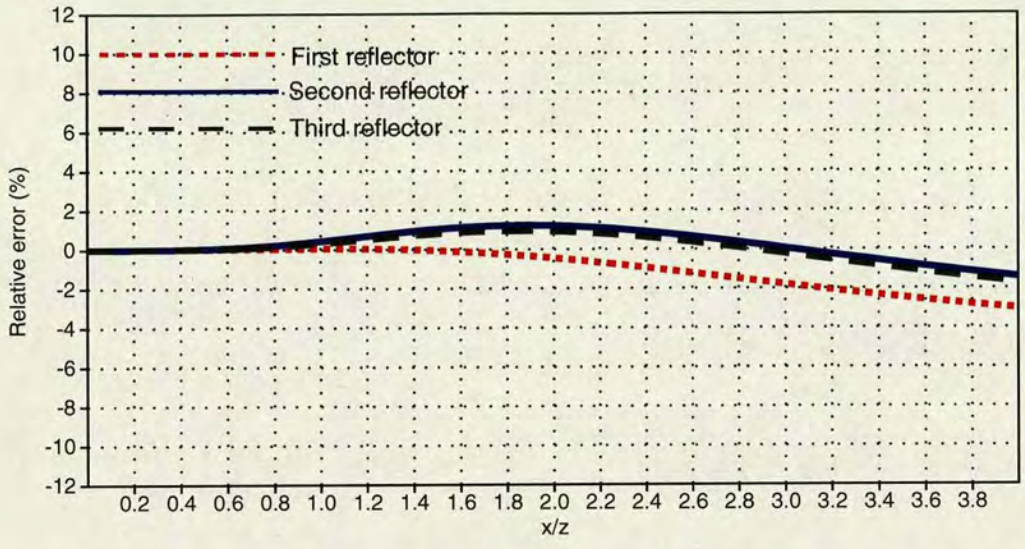

Figure 6.12: Accuracy of conversion point approximation (equations (6.29)-(6.33)). The horizontal axis is the offset-to-depth ratio, and the vertical axis is the normalized error of conversion points $\left(x_c^{(exact)} - x_c^{(approx)}\right)/x$. The modelling parameters are in Table 6.2. The dotted line is from first reflector, the solid line from second reflector and the dashed line from the third reflector.

insights into the C-wave behaviour, more tests are required to examine 1) the effects of varying layer thickness, 2) the effects of varying impedance contrast, and 3) effects of layers with negative σ values, etc.

6.5.2 Moveout: Taylor series expansion

The Taylor series expansion for the converted-wave moveout in multi-layered TIV media is derived in Appendix E as

$$t_c^2 = t_{c0}^2 + \frac{x^2}{V_{c2}^2} + \frac{A_4 x^4}{1 + A_5 x^2}, \tag{6.34}$$

where

$$A_4 = -\frac{\left(\gamma_0\gamma_{eff} - 1\right)^2 + 8\left(1+\gamma_0\right)\left(\eta_{eff}\gamma_0\gamma_{eff}^2 - \zeta_{eff}\right)}{4t_{c0}^2 V_{c2}^4 \gamma_0 \left(1+\gamma_{eff}\right)^2}. \tag{6.35}$$

Figure 6.13 shows the accuracy of equations (6.34)-(6.35) using the same model in Table 6.2. The moveouts calculated by equations (6.34)-(6.35) are compared with

those calculated by ray-tracing. It can be seen that the approximation works very well up to x/z of 2.4.

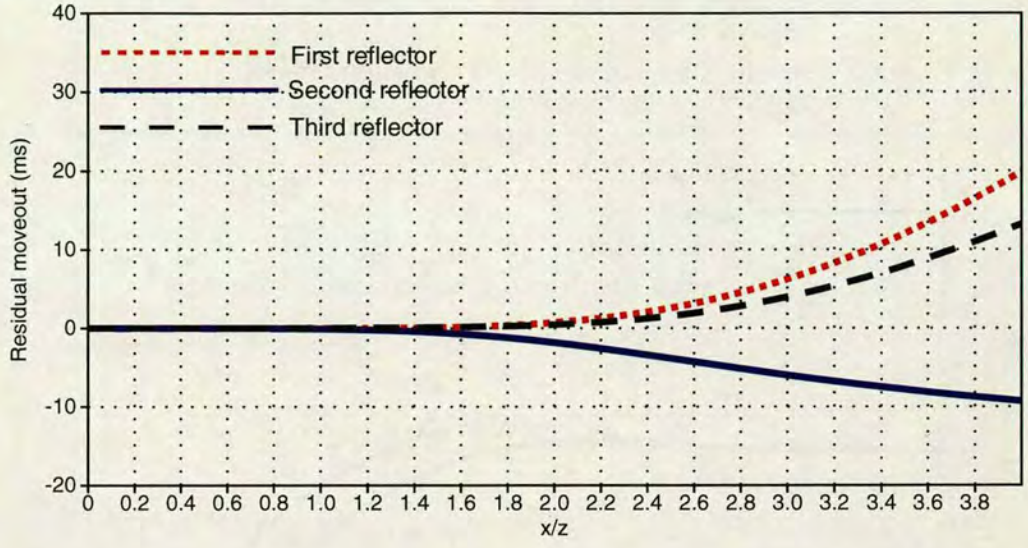

Figure 6.13: Accuracy of moveout approximation (equations (6.34)-(6.35)). The horizontal axis is the offset-to-depth ratio, and the vertical axis is the residual moveout compared with exact moveout from ray tracing. The modelling parameters are in Table 6.2. The dotted line is from first reflector, the solid line from second reflector and the dashed line from the third reflector.

6.5.3 Moveout: double -square-root (DSR) approximation

Using the traveltime equations for single wave modes (Tsvankin and Thomsen 1994), the travel time t_c for layered TI media can be derived as (see Appendices B and C for more details of the derivation),

$$\begin{aligned} t_c = t_p + t_s &= \sqrt{t_{p0}^2 + \frac{x_c^2}{V_{p2}^2} - \frac{2\eta_{eff} x_c^4}{V_{p2}^2\left(t_{p0}^2 V_{p2}^2 + (1+2\eta_{eff})x_c^2\right)}} \\ &+ \sqrt{t_{s0}^2 + \frac{(x-x_c)^2}{V_{s2}^2} + \frac{2\zeta_{eff}(x-x_c)^4}{V_{s2}^2\left(t_{s0}^2 V_{s2}^2 + (x-x_c)^2\right)}}, \end{aligned} \tag{6.36}$$

where conversion point x_c can be calculated using equations (6.29)-(6.33).

Figure 6.14 shows the accuracy of equation (6.36) using the model in Table 6.2. The moveouts calculated using the DSR equation are compared with those from ray-tracing. It can be seen that the approximation works well up to x/z of 2.0. Thus its accuracy is slightly less than that of equation (6.34).

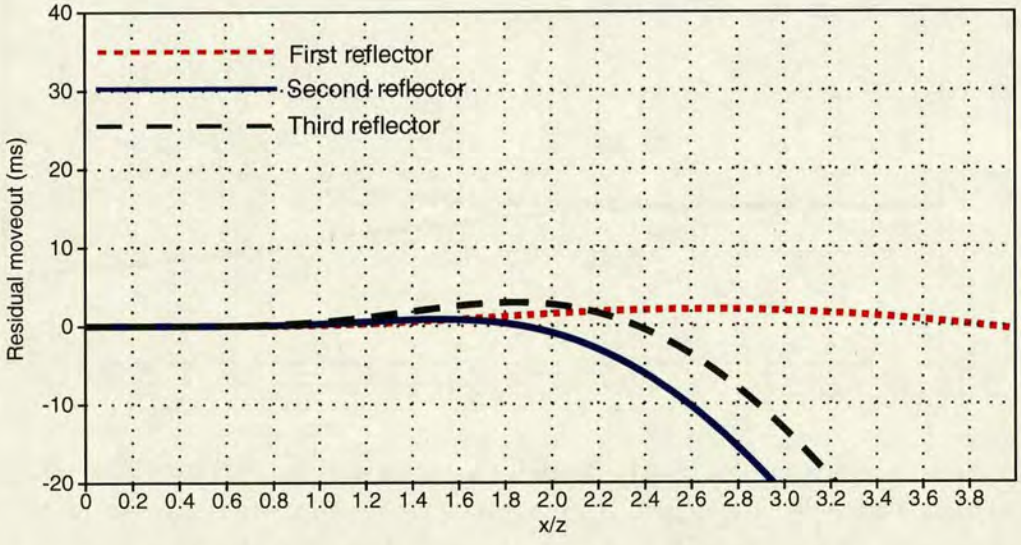

Figure 6.14: Accuracy of moveout approximation (equation (6.36)). The horizontal axis is the offset-to-depth ratio, and the vertical axis is the residual moveout compared with exact moveout from ray tracing. The modelling parameters are in Table 6.2. The dotted line is from first reflector, the solid line from second reflector and the dashed line from the third reflector.

6.5.4 Influence of anisotropy on converted waves

TIV influences the converted wave both on its conversion point and its moveout. This influence comes from two sources, P-wave anisotropy indicated by η or η_{eff}, and S-wave anisotropy indicated by ζ or ζ_{eff}.

First, I evaluate the influence of P- and S-wave anisotropy separately, in order to determine which one is dominant.

For a single-layered medium, I list the P- and S-wave anisotropy effects of three materials, Dog Creek shale, Pierre shale and Taylor sandstone in Table 6.3. The anisotropy effect can be found from equations (6.31)-(6.35) in terms corresponding

to P- and S-wave respectively. It is seen that the influence of P-wave anisotropy is generally stronger than that of S-wave, for conversion point and for moveout. The only exception is conversion point x_c in Pierre shale, where the influence of S-wave anisotropy is stronger. However, even for this case, P-wave anisotropy has stronger influence on moveout t_c. Note that Pierre shale has negative σ, which is relatively rare in published materials (Thomsen, 1986; Vernik and Liu, 1997).

Material	x_c - equation(6.31)		t_c - equation (6.35)	
	$\eta\gamma_0\gamma_{eff}$	ζ	$\eta\gamma_0\gamma_{eff}^2$	ζ
Dog Creek shale	0.282	0.154	0.335	0.154
Pierre shale	-0.434	-0.932	-2.06	-0.932
Taylor sandstone	0.248	0.113	0.214	0.113

Table 6.3: Influence of P- and S-wave anisotropy on converted wave in single-layered medium.

In multi-layered media, η and ζ are replaced by η_{eff} and ζ_{eff}. From their definitions in equations (6.32)-(6.33), both η_{eff}, and ζ_{eff} are influenced by the layering effect and the interval anisotropy. However, from the definition of η_{eff}, the layering effect and interval η_i reinforce each other, and thus η_{eff} generally gets bigger when the reflector gets deeper. This is demonstrated by the synthetic model in Table 6.2, in which, by contrast, for ζ_{eff}, the layering effect and interval ζ cancel each other, causing decreasing ζ_{eff} for increasing reflector depth (Table 6.2).

From the two reasons discussed above, I can safely conclude that P-wave anisotropy has the stronger influence on converted waves, particularly in moveout.

Secondly, I explain why polar anisotropy has a stronger influence on conversion point than on moveout as demonstrated in section 6.3.

Let us compare the difference between the anisotropic and isotropic approximations based on equations (6.31)-(6.35). By ignoring terms with c_3 and A_5 in

equations (6.31)-(6.35), the difference between $x_c^{(aniso)}$ and $x_c^{(iso)}$ can be written as,

$$x_c^{(aniso)} - x_c^{(iso)} \approx \frac{4\gamma_{eff}\left(1+\gamma_0\right)\left(\eta_{eff}\gamma_0\gamma_{eff}+\zeta_{eff}\right)}{t_{c0}^2 V_{c2}^2 \gamma_0 \left(1+\gamma_{eff}\right)^3} x^3 \tag{6.37}$$

and the difference between $t_c^{(aniso)}$ and $t_c^{(iso)}$ as,

$$t_c^{(aniso)} - t_c^{(iso)} \approx -\frac{4\left(1+\gamma_0\right)\left(\eta_{eff}\gamma_0\gamma_{eff}^2-\zeta_{eff}\right)}{t_{c0}^2 V_{c2}^4 \gamma_0 \left(1+\gamma_{eff}\right)^2} x^4. \tag{6.38}$$

From these two expressions, it is clear that anisotropy begins to influence the conversion point from the cubic term whilst it is the quartic term in the moveout calculation. Since lower-order (cubic) terms can be significant in near offsets, ignoring anisotropy in the calculation of conversion point position can cause serious lateral smearing in the stack of converted waves. Moreover, P-wave anisotropy (η_{eff}) and S-wave anisotropy (ζ_{eff}) reinforce each other in determining conversion points (equation (6.37)), whilst they cancel each other in equation (6.38). This further causes anisotropy to have a stronger influence on x_c and a weaker influence on t_c.

6.5.5 Anisotropic velocity analysis

As we know, four parameters are required in order to determine the conversion point and moveout of converted waves in TIV media. However, equations (6.31), (6.35) and (6.36) rely on five parameters: V_{c2}, γ_{eff}, γ_0, η_{eff} and ζ_{eff}. Obviously, there is parameter redundancy.

For a single layered TIV medium, there is a direct relation between η and ζ. However, for multi-layered media, layering makes the relation between η_{eff} and ζ_{eff} very complex, and there is no direct relation between them. η_{eff} is the measurement of vertical variation of interval v_{p2i} and η_i, whilst ζ_{eff} is the measurement of vertical variation of interval v_{s2i} and ζ_i. However, when V_{c2}, γ_0 and V_{p2} (or γ_{eff}) are known,

one can obtain ζ_{eff} from η_{eff} by Dix-type layer stripping similar to the case of calculating interval velocities from rms velocities.

The dependence of converted wave moveout on η_{eff} therefore makes it inappropriate to apply the velocity analysis method used for a single layer medium in the more realistic multi-layered case. It seems that the only information one can get from converted wave alone is short-spread moveout velocity V_{c2}. However, if we can get additional information about TIV anisotropy from converted waves, it will give the seismic processor more confidence in processing.

Similarly to Alkhalifah (1997) for P-waves in TIV media, I use a double-scan semblance analysis to determine the C-wave moveout velocity and anisotropy parameters for a given event. A combined parameter χ_{eff} is used for this purpose,

$$\chi_{eff} = \eta_{eff}\gamma_0\gamma_{eff}^2 - \zeta_{eff}, \tag{6.39}$$

which is the total influence of TIV and layering on the C-wave moveout signature. In these formulations, the C-wave moveout is controlled by four parameters, V_{c2}, γ_0, γ_{eff} and χ_{eff}, whereas the P-wave moveout signature is controlled by only two parameters V_{p2} and η_{eff}. For a single TIV layer, one can obtain

$$\chi = \eta\left(\gamma_0 - 1\right)\gamma_{eff}. \tag{6.40}$$

Substituting equation (6.39) into equation (6.35), I obtain a further simplified A_4 for C-wave moveout as

$$A_4 = -\frac{\left(\gamma_0\gamma_{eff} - 1\right)^2 + 8\left(1 + \gamma_0\right)\chi_{eff}}{4t_{c0}^2 V_{c2}^4 \gamma_0 \left(1 + \gamma_{eff}\right)^2}. \tag{6.41}$$

Equation (6.41) makes anisotropy velocity analysis using converted wave in layered media possible. Assume that γ_0 can be obtained by correlating P- and C-wave

stacked or migrated sections, then γ_{eff} can be obtained from

$$\gamma_{eff} = \frac{V_{p2}^2}{V_{c2}^2 (1+\gamma_0) - V_{p2}^2} \tag{6.42}$$

where the P-wave moveout velocity V_{p2} can be determined from P-wave data. Thus equations (6.34) and (6.41) can be used for double scanning to determine V_{c2} and χ_{eff}. Assumptions also have to be made to constrain the P-wave horizontal velocity V_{ph}. In a layered medium, the definition of horizontal velocity is uncertain. Empirically, I find that,

$$V_{ph} = V_{p2}\sqrt{1+2\eta} \approx V_{p2}\sqrt{1+\frac{2\chi_{eff}}{(\gamma_0-1)\,\gamma_{eff}^2}},$$

is a good approximation for moveout analysis, although it is only strictly valid for a single TIV layer.

Figure 6.15a shows the synthetic modelling data for the model in Table 6.2. Figures 6.15b, 6.15c and 6.15d are semblance analyses of V_{c2} and χ_{eff} , using V_{p2} and γ_0 as prior information. The offset range used for semblance analysis is limited to offset-to-depth ratio of 2.0. The resolution of both V_{c2} and χ_{eff} is reasonably good although not very high.

6.5.6 Moveout correction

Once all the parameters, V_{c2}, γ_{eff}, γ_0 and χ_{eff}, are determined, converted wave moveout can be corrected using non-hyperbolic equations. Here, I use Taylor series expansion equations (6.34)-(6.35) due to their slightly higher accuracy than the DSR equation in TIV media.

First I start with the isotropic method. Figure 6.16a shows NMO using only two parameters V_{c2} and γ_{eff}, by letting $\gamma_{eff} = \gamma_0$ and ignoring anisotropic parameters in

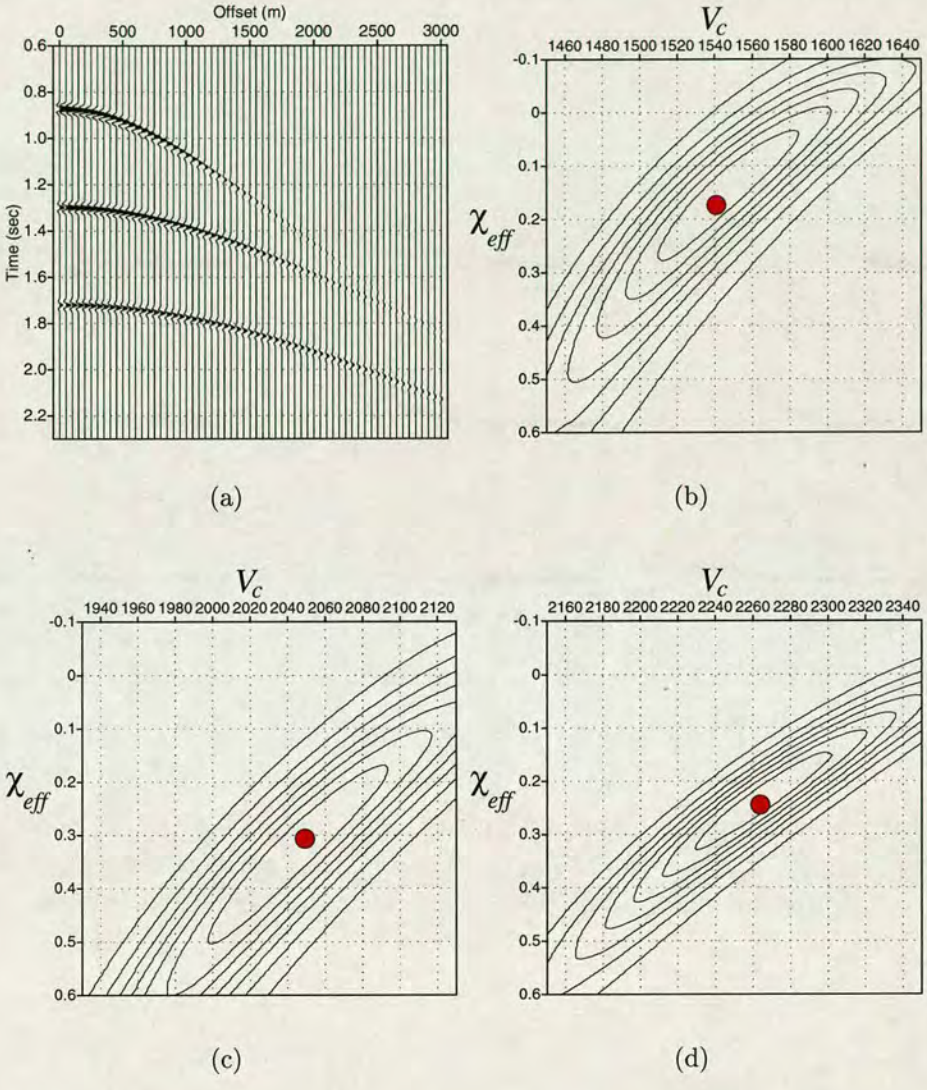

Figure 6.15: Semblance analysis for V_{c2} and χ_{eff} with prior information about V_{p2} and γ_0 for given t_{c0}, using three term Taylor expansion equation (6.34). The circles are expected values of V_{c2} and χ_{eff}. (a) Synthetic seismogram from ray tracing. Semblance analysis of (b) first reflector, (c) second reflector and (d) third reflector.

equation (6.35). It can be seen that its accuracy is limited to an offset-to-depth ratio of less than 1. If we use three parameters V_{c2}, γ_{eff} and γ_0, a small improvement can be achieved (Figure 6.16b). A dramatic improvement can be seen in Figure 6.16c, which uses all four parameters. It is accurate to and offset-to-depth ratio of well beyond 2.

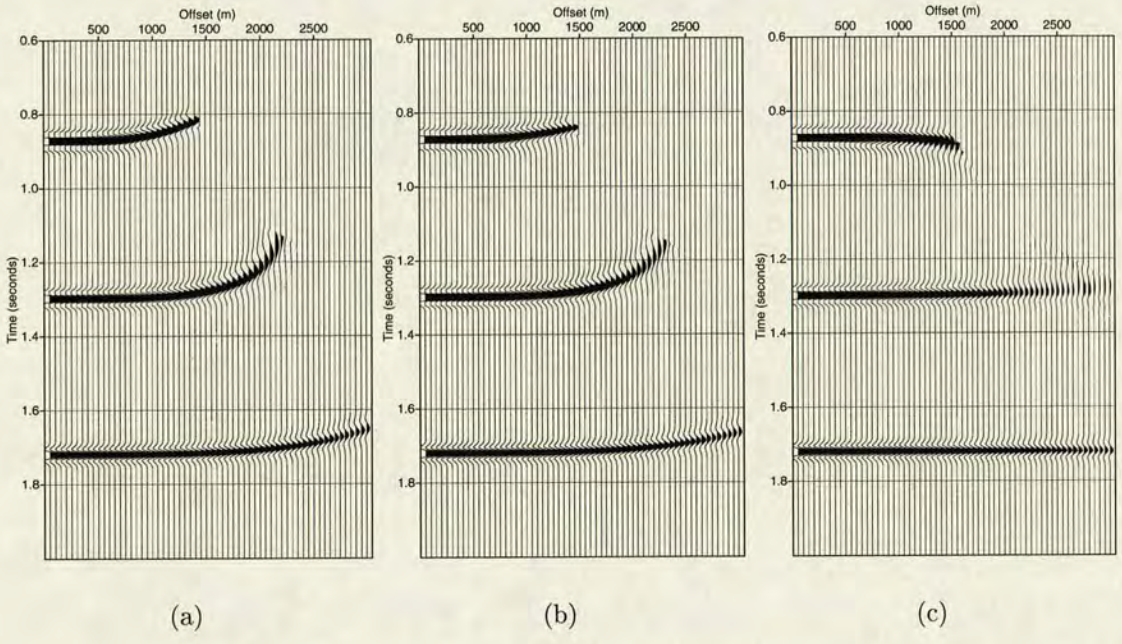

Figure 6.16: Moveout corrections of Figure 6.15a using (a) V_{c2} and γ_{eff} only, (b) V_{c2}, γ_{eff} and γ_0 and (c) V_{c2}, γ_{eff}, γ_0 and η_{eff} . The moveout correction is based on Taylor series expansion equations (6.34)-(6.35). Note that data is muted to offset-to-depth ratio of 3.0.

6.6 Discussion and conclusions

In this chapter, I have focused on the estimation of anisotropic parameters using converted-wave moveout data. However, since the anisotropy has a stronger influence on the conversion point than on the moveout, a more reliable method of anisotropy analysis could be based on searching for the conversion point and on binning analysis. The isotropic counterpart of the method has been presented by some

authors (Audebert *et al.*, 1999; Bagaini *et al.*, 1999). If x_c, V_{c2} and γ_0 are known, equations (6.29)-(6.31) may be used for estimating the effective velocity ratio γ_{eff} and anisotropic parameters with the improved accuracy. V_{c2} can be determined from short-spread C-wave velocity analysis, and γ_0 from a coarse correlation of P- and C-wave stacked sections. At certain locations with distinct geological features, such as at a fault plane, or the crest of an anticline, the conversion-point offset x_c can be obtained by comparing the positive with negative common-offset gathers. The effective velocity ratio γ_{eff} and residual anisotropic term $\eta_{eff}\gamma_0\gamma_{eff} + \zeta_{eff}$ may then be recovered from equations (6.29)-(6.31) by inversion. Compared with moveout analysis, this method does not require prior knowledge of the P-wave stacking velocity V_{p2}.

For isotropically layered media, η_{eff} and ζ_{eff} are not equal to zero due to the layering effect. They have the forms

$$\eta_{eff} = \frac{1}{8t_{p0}V_{p2}^4}\left(\sum_{i=1}^{n} v_{p2i}^4 \Delta t_{p0i} - t_{p0}V_{p2}^4\right), \tag{6.43}$$

and

$$\zeta_{eff} = \frac{1}{8t_{s0}V_{s2}^4}\left(t_{s0}V_{s2}^4 - \sum_{i=1}^{n} \Delta t_{s0i} v_{s2i}^4\right). \tag{6.44}$$

This means that even if the media are isotropic, the appropriate method of data processing still requires consideration of the anisotropic effect, when there is a vertical velocity gradient. Alkhalifah (1997) showed that effective anisotropy introduced by smooth velocity gradient is small at all times, comparing with typical TIV media such as Taylor sandstone or Dog Creek shale.

In this chapter, I presented two types of moveout equations for converted waves: Taylor series expansion and double-square-root (DSR) equation. It appears that the Taylor series expansion performs slightly better than the DSR equation. Thus, for velocity analysis and moveout correction purposes, the Taylor series expansion is

preferred. However, the DSR equation has its merits as well. Owing to its separated forms for P- and S- wave paths, it can be used to implement prestack Kirchhoff time migration (Li and Druzhinin, 2000). In the presence of dipping reflectors, the anisotropy velocity analysis should be performed in common imaging gathers after prestack time migration.

This chapter only discusses polar or TIV anisotropy. However, the real earth also shows azimuthal anisotropy to some extent. If this is the case, handling azimuthal anisotropy is necessary. This includes consideration of shear-wave splitting (Chapter 7), and azimuthal velocity variation. This chapter also only discusses horizontally layered media. The presence of a dipping layer will make the anisotropic effects more pronounced. In fact, it is more important to account for the anisotropic effects in media with dipping layers than with horizontal layers, and again this is a subject of future development.

In summary, I have investigated the accuracy of the isotropic method for processing converted wave data in the presence of TIV anisotropy. It is found that TIV has a much stronger influence on the conversion point position than on the moveout of converted waves. The effective velocity ratio γ_{eff} alone is not sufficient in determining the conversion point. New equations have been derived for conversion point and moveout approximation, both for single- and multi-layered media. An error in the moveout equation in Thomsen's (1999) paper has been pointed out. New parameters ζ and χ are introduced to handle TIV anisotropy for C-waves in a single-layered medium, and their effective parameters ζ_{eff} and χ_{eff} for C-waves in multi-layered media. A C-wave anisotropic velocity analysis has been proposed to estimate C-wave anisotropy. Anisotropic moveout correction can greatly improve the flattening of the events of C-waves.

Chapter 7

Analysis of azimuthal anisotropy

7.1 Introduction

It is generally believed that shear wave splitting in the earth crust is caused by stress-induced fractures with various fluid contents (Crampin and Lovell, 1991). When a shear wave travels in a fractured or azimuthally anisotropic medium, it is split into two components with orthogonal or nearly orthogonal polarizations, and with different speeds. For near vertical propagations in a medium with a single fracture system, the polarization of the fast shear wave is parallel to the fracture direction, and that of the slow shear wave perpendicular to it. Shear wave splitting is more pronounced when multiple fracture systems exist. However, Liu *et al.* (1993) found that the aggregate polarization of the fast shear waves is in the average fracture direction weighted by the fracture density, if two or more sets of vertical parallel fractures are combined with a conjugate angle of less than about 50°.

A rotation-based analysis can obtain information such as fracture strike and time delay using seismic data recorded by vector sensors. The earliest rotation analysis for azimuthal anisotropy utilizes two orthogonal shear wave sources and two orthogonal geophones (Alford, 1986; Thomsen, 1988; Li and Crampin, 1993). This is often

called four-component tensor rotation. Tensor rotation can give a robust solution for determining the fracture strike and time delay. However, a shear wave source is relatively expensive and difficult to deploy especially in the marine environment. In recent years, industry has been more interested in acquiring marine shear waves by OBC survey. The shear waves acquired are more likely to be *P-S* type mode-converted shear waves, in which conversions occur at deep reflectors.

When a *P-S* conversion occurs at a reflector and the medium above the reflector is azimuthally anisotropic, the converted shear wave splits into a fast and a slow shear wave. This chapter focuses on fracture detection using converted-waves in both 2D and 3D 4C OBC data.

7.2 Rotation analysis for 2D acquisition

7.2.1 Theory

As we know, the tensor rotation algorithms, like Alford's rotation, require two orthogonal horizontal sources. In the absence of two orthogonal sources, the algorithms have to rely on two-component (2C) vector analysis. Harrison (1992) first presented a 2C vector rotation algorithm based on crosscorrelation and autocorrelations of two traces. The method was later further developed by Fang (1998). Here we reformulate Fang's method and discuss its limitations.

Figure 7.1 shows a map view of shear wave splitting when an up-going converted shear wave travels in a vertically fractured medium. The principal direction of fracture forms an oblique angle θ with the survey line. The orientation of the three component geophone forms a right-handed coordinate system: radial component R is the inline horizontal, transverse component T crossline horizontal and vertical component V upwards. The polarization of the fast split shear wave S_1 is parallel

to the fracture direction, and that of the slow shear wave S_2 perpendicular to it. To process the split shear waves, it is common to assume that the two split shear waves have the same waveform separated by a time delay of Δt when recorded by three-component geophones at the surface. Thus

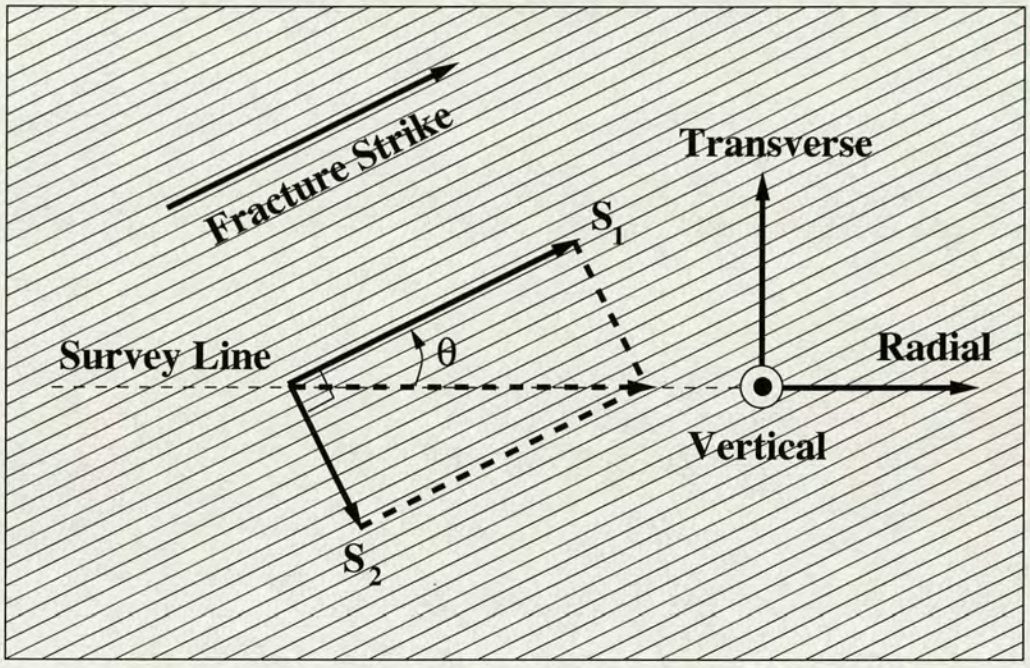

Figure 7.1: Map view of shear wave splitting when an up-going converted shear wave travels in a vertically fractured medium.

$$\begin{bmatrix} S_1(t) \\ S_2(t) \end{bmatrix} = \begin{bmatrix} S(t)\cos\theta \\ -S(t-\Delta t)\sin\theta \end{bmatrix} \tag{7.1}$$

The wavefields recorded by the radial and transverse components would be

$$\begin{aligned} \begin{bmatrix} R(t) \\ T(t) \end{bmatrix} &= \begin{bmatrix} \cos\theta & -\sin\theta \\ \sin\theta & \cos\theta \end{bmatrix} \begin{bmatrix} S_1(t) \\ S_2(t) \end{bmatrix} \\ &= \begin{bmatrix} \cos^2\theta & \sin^2\theta \\ \sin\theta\cos\theta & -\sin\theta\cos\theta \end{bmatrix} \begin{bmatrix} S(t) \\ S(t-\Delta t) \end{bmatrix} + \begin{bmatrix} N_R(t) \\ N_T(t) \end{bmatrix}, \end{aligned} \tag{7.2}$$

where $N_R(t)$ and $N_T(t)$ are the noise components in the radial and transverse direc-

tions. Transforming into the frequency domain, one can obtain

$$\begin{bmatrix} R(\omega) \\ T(\omega) \end{bmatrix} = \begin{bmatrix} \cos^2\theta & \sin^2\theta \\ \sin\theta\cos\theta & -\sin\theta\cos\theta \end{bmatrix} \begin{bmatrix} S(\omega) \\ S(\omega)\, e^{-i\omega\Delta t} \end{bmatrix} + \begin{bmatrix} N_R(\omega) \\ N_T(\omega) \end{bmatrix}.$$

By eliminating $S(\omega)$, one can get

$$(R(\omega) - N_R(\omega)) \sin\theta\cos\theta \left(1 - e^{-i\omega\Delta t}\right) = (T(\omega) - N_T(\omega)) \left(\cos^2\theta + \sin^2\theta e^{-i\omega\Delta t}\right),$$

or, in the time domain,

$$\begin{aligned} E(\theta, \Delta t, t) &= \left(R(t)\sin\theta\cos\theta - T(t)\cos^2\theta\right) \\ &\quad - \left(R(t-\Delta t)\sin\theta\cos\theta + T(t-\Delta t)\sin^2\theta\right) \\ &= \left(N_R(t)\sin\theta\cos\theta - N_T(t)\cos^2\theta\right) \\ &\quad - \left(N_R(t-\Delta t)\sin\theta\cos\theta + N_T(t-\Delta t)\sin^2\theta\right). \end{aligned} \tag{7.3}$$

Ignoring the noise terms,

$$E(\theta, \Delta t, t) = 0.$$

Equation (7.3) forms the basis for 2C vector rotation analysis. One can perform double scanning over the rotation angle θ and time delay Δt, and the objective function $F(\theta, \Delta t)$ is to minimize the summed $E(\theta, \Delta t, t)$ as

$$F(\theta, \Delta t) = \left(\sum_{k=0}^{n} E(\theta, \Delta t, t_k)^p\right)^{1/p} \tag{7.4}$$

for a time-window length with n samples.

7.2.2 Application to zero-offset synthetic S-wave data

Figure 7.2 shows the input synthetic zero-offset S-wave data for 2C rotation analysis. The first trace is the radial and the second trace the transverse component. The fracture strike is designed as 30° counterclock-wise from the survey direction. We check four scenarios with different time delays: (a) 4ms, (b) 8ms, (c) 12ms, and (d) 20ms. A zero-phase Ricker wavelet with primary frequency of 15 Hz is used. The input traces in Figure 7.2 have been rotated into the direction of the fracture strike (Figure 7.3), where two shear waves are supposed to be separated. The first trace is the fast shear wave and the second trace the slow shear wave.

The synthetic data in Figure 7.2 have been analysed using 2C rotation as suggested from Equations (7.3) and (7.4). Double scanning over rotation angle θ and time delay Δt is performed as shown in Figure 7.4. The scanning is looking for a minimum value (in red). As we can see, the ability of double scanning to solve rotation angle θ and time delay Δt depends on the time delay. When Δt=4ms, the resolution in Figure 7.4a is rather limited. Increasing Δt gives better resolution (Figures 7.4b , 7.4c and 7.4d).

Unlike tensor rotation analysis which uses two orthogonal sources, vector (2C) rotation analysis is not robust when the fracture strike is nearly parallel or perpendicular to the survey direction (Thomsen, 1988; Harrison, 1992). This is simply because one of the split shear waves is very weak. Figure 7.5 shows synthetic data for checking robustness of 2C rotation analysis. These scenarios are used: (a) $\theta = 0°$, Δt=8ms; (b) $\theta = 5°$, Δt=8ms, (c) $\theta = 5°$, Δt=20ms, and (d) same as (c) but with 5% Gaussian noise. The fast and slow shear waves are shown in Figure 7.6. Scanning results for θ and Δ are shown in Figure 7.7. It can be seen that in the first two cases, there is no resolution. In the third case, it seems possible to interpret the result. However, with a small perturbation of 5% Gaussian noise, the result becomes

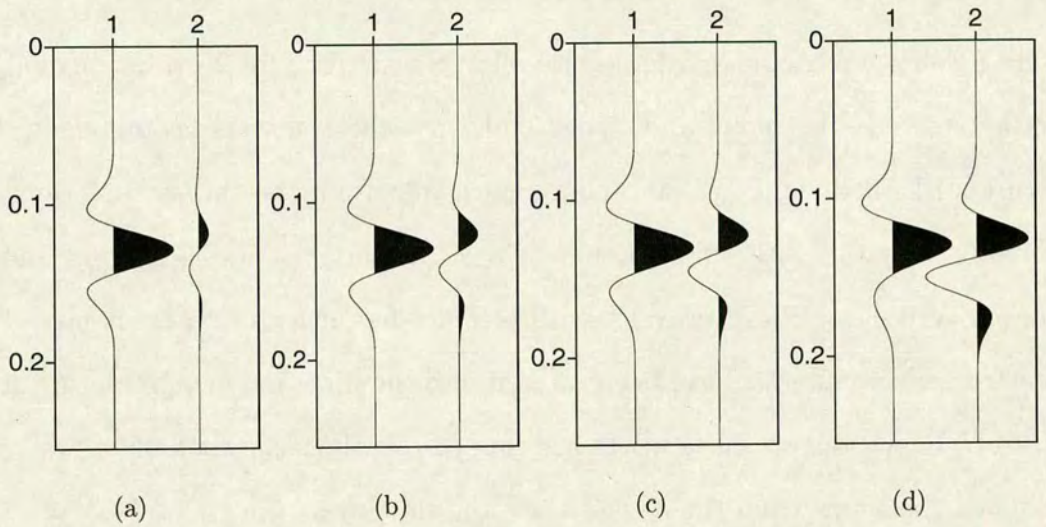

Figure 7.2: Input synthetic data for 2C rotation analysis. The first trace is radial component and the second trace transverse component. All four diagrams have fracture strike at 30° counterclockwise from the survey line, whilst their time delays are different: (a) 4ms, (b) 8ms, (c) 12ms, and (d) 20ms. A zero-phase Ricker wavelet with primary frequency of 15 hertz is used.

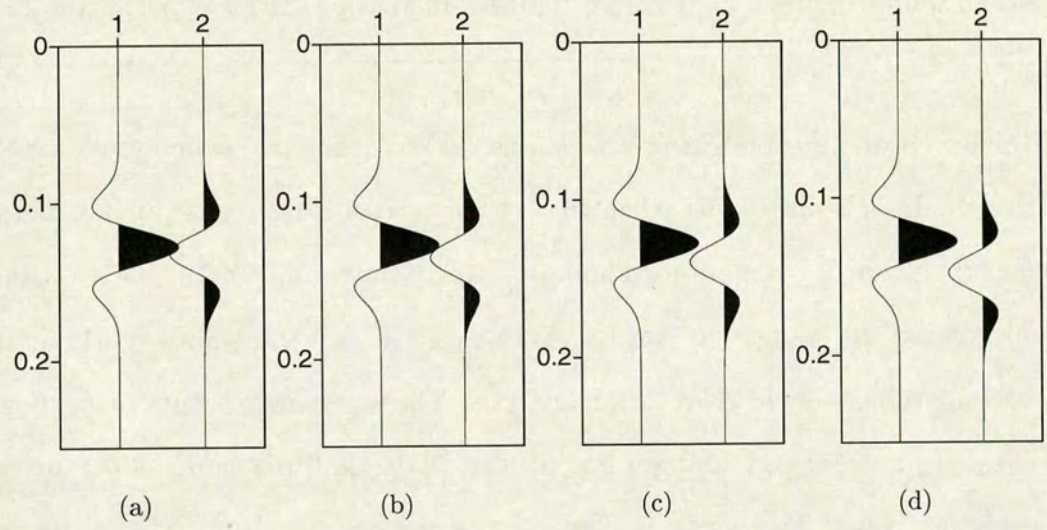

Figure 7.3: Rotated synthetic data from Figure 7.2. The first trace is fast shear wave and the second trace slow shear wave. Time delays : (a) 4ms, (b) 8ms, (c) 12ms, and (d) 20ms.

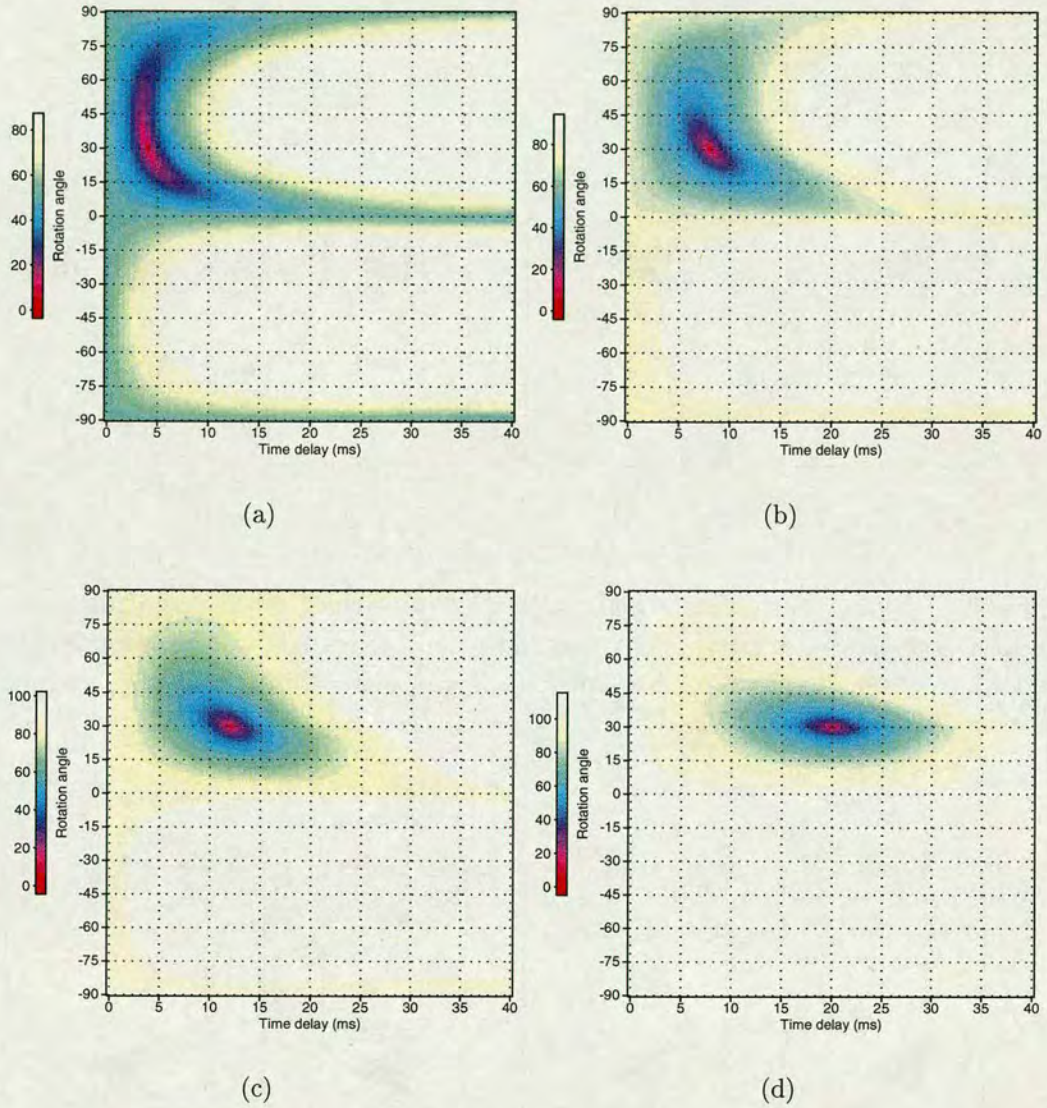

Figure 7.4: 2C rotation analysis for input synthetic data in Figure 7.2. Double scanning over rotation angle θ and time delay Δt is performed using the objective function as defined in equation (7.4). The scanning is looking for a minimum value (in red). Time delays : (a) 4ms, (b) 8ms, (c) 12ms, and (d) 20ms.

unstable. For the general case, in order to perform 2C rotation analysis, the survey line should be at least 10° away from the principal fracture-strike direction in the survey area.

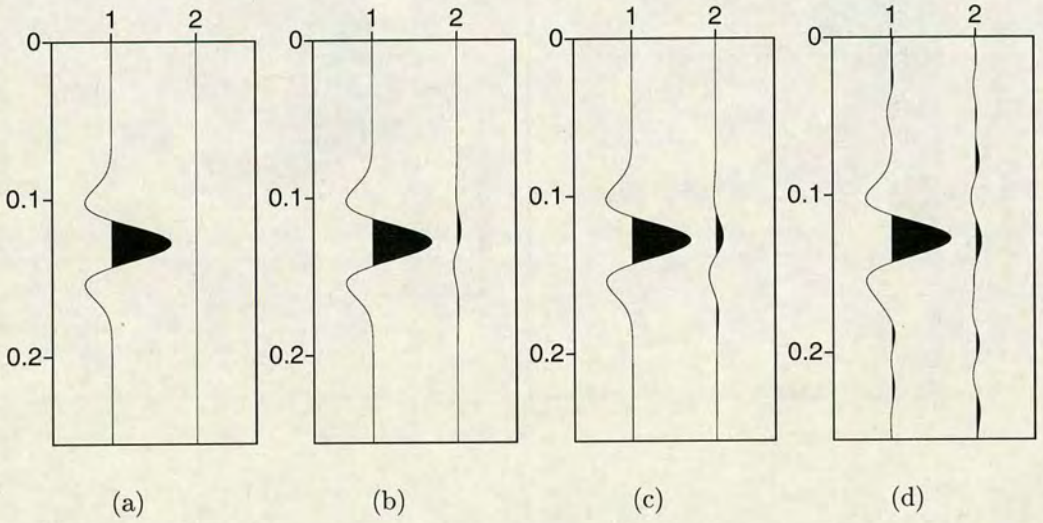

Figure 7.5: Input synthetic data for checking robustness of 2C rotation analysis. The first trace is radial component and the second trace transverse component. (a) $\theta = 0°$, Δt=8ms; (b) $\theta = 5°$, Δt=8ms, (c) $\theta = 5°$, Δt=20ms, and (d) same as (c) but with 5% Gaussian noise.

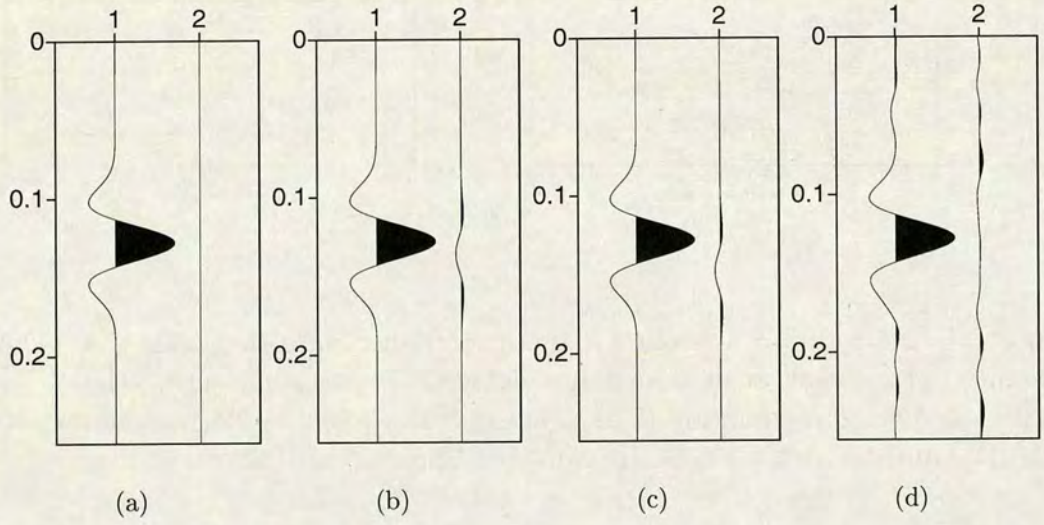

Figure 7.6: Rotated synthetic data from Figure 7.5. The first trace is fast shear wave and the second trace slow shear wave.

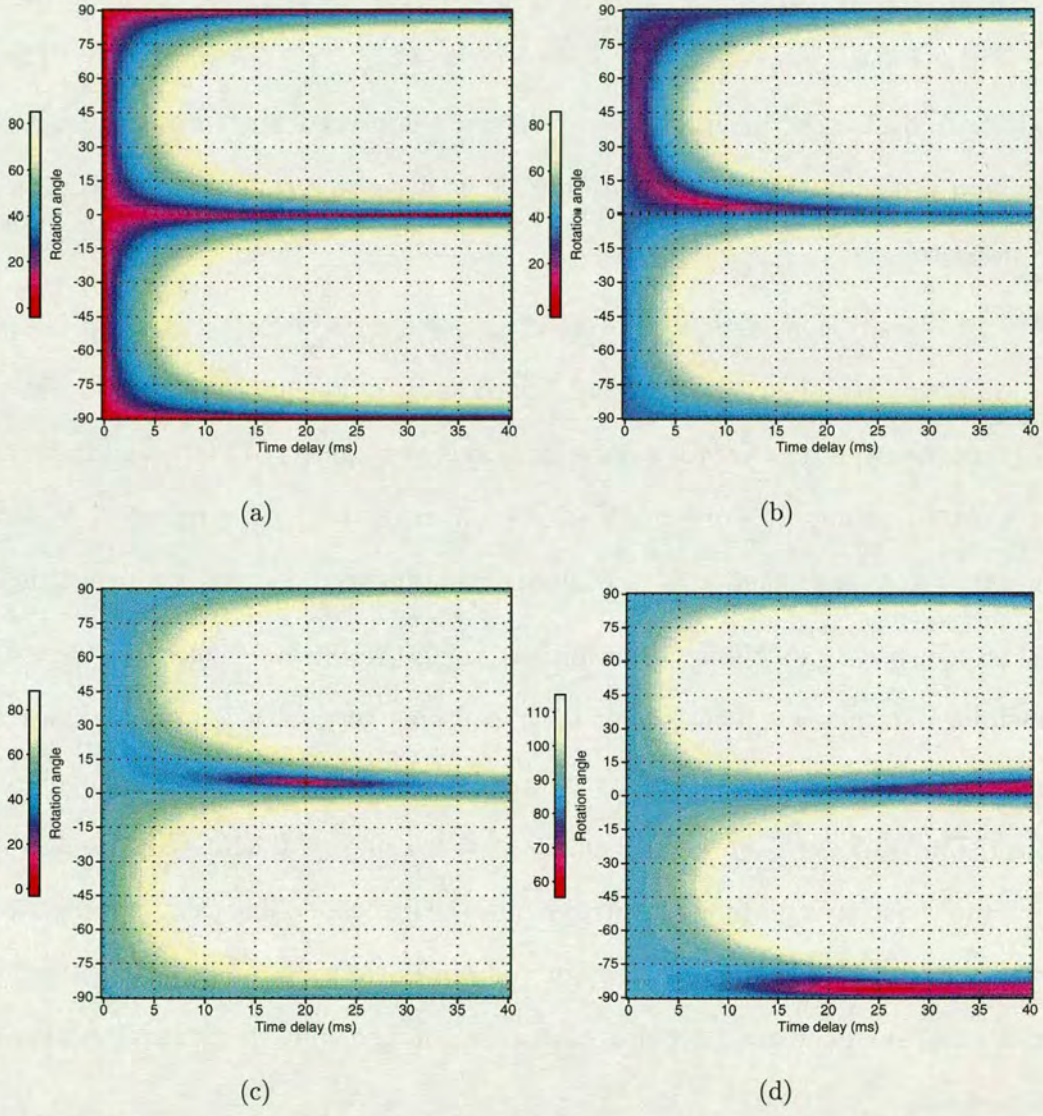

Figure 7.7: 2C rotation analysis for input synthetic data in Figure 7.5.

7.2.3 Application to post-stack converted-wave data

The rotation analysis algorithms, such as the tensor rotation of Alford (1986), or the 2C vector rotation discussed above, require that shear waves propagate vertically in a vertically fractured medium. However, in a horizontally layered medium, there is no effective reflection of converted shear waves at zero or near zero offsets. The 2C rotation analysis thus inevitably involves using non-vertically incident shear wave data, and typically stacked seismic data. It is necessary to analyse the validity of this practice.

Two cases are considered: 1) a set of parallel vertical fractures in an isotropic material, 2) a set of parallel vertical fractures in a TIV material. The first case shows transverse isotropy with a horizontal axis of symmetry (TIH), and the second shows orthorhombic anisotropy which is more realistic. The purpose of including TIV anisotropy in modelling is to evaluate its influence on shear wave splitting.

The synthetic modelling is performed using ANISEIS. Figure 7.8 shows the modelling parameters. The second layer contains vertical fractures with fracture strike 30° north of east. Its velocity parameters are from those of Dog Creek Shale (V_{p0}=1875m/s, V_{s0} =826m/s, ε = 0.225, δ = 0.1 and γ=0.345) (Thomsen, 1986), which shows relatively strong anisotropy. For the first modelling case, the anisotropic parameters of Dog Creek Shale are ignored. In both cases, a crack density of 0.04 is used, and the expected time delay between the two split shear waves is about 15 milliseconds.

First, I consider the isotropic material with vertical fractures. Figure 7.9 is the ANISEIS modelling result. The analysed event (labeled as $\grave{P}\grave{P}\acute{S}\acute{S}$ in Figure 7.9) is the C-wave converted from the bottom of the second layer at two-way C-wave time of 2.33 seconds. The event is NMO-corrected, and stacked according to different offset ranges. The stacked traces are performed by 2C rotation analysis.

Isotropic overburden V_p=1733m/s V_s=500m/s Δz=700m
Fractured layer θ=30° V_{p0}=1875m/s V_{s0}=826m/s Δz=300m
Isotropic halfspace V_p=2000m/s V_s=1000m/s

Figure 7.8: Three layer model for 2C rotation analysis from post-stack data.

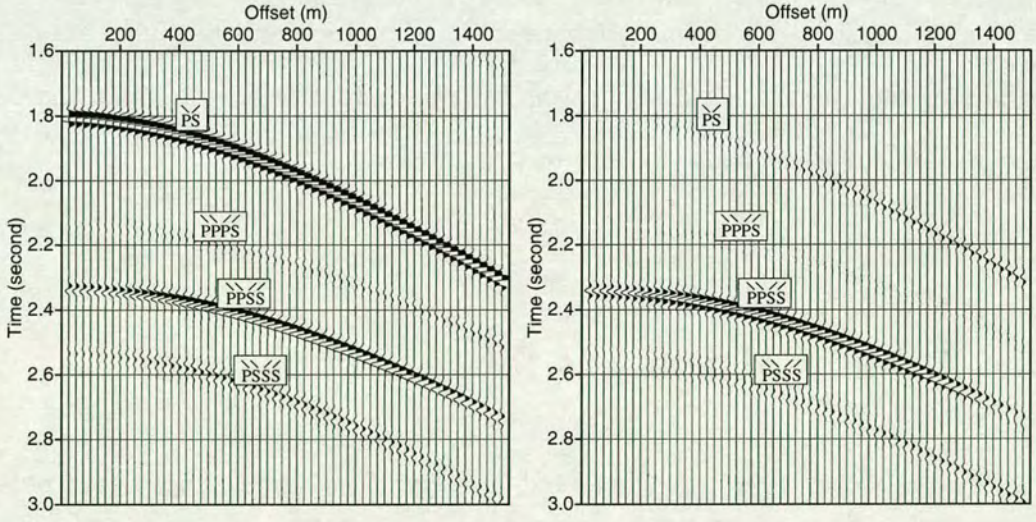

Figure 7.9: Synthetic modelling for the model in Figure 7.8, whose second layer is vertically-fractured in isotropic material. (a) Radial component, (b) Transverse component. The fracture strike is 30° north of east.

The picked rotation angle and time delay are shown in Figures 7.10a and 7.10b, respectively, and two examples of double scanning results for offsets 500m and 1000m are shown in Figures 7.10c and 7.10d. It is clear that far-offset data used for stacking generally cause the focusing of the double scanning to deviate from the desired values. However, the error in rotation angle is less than 3° and that in time delay is less than 1.5 milliseconds, even when the offset range for stack is up to offset-to-depth of 1.5. These errors are generally acceptable.

Now consider the influence of TIV anisotropy on the 2C rotation analysis. Figure 7.11 shows the synthetic modelling of shear wave splitting in TIV material (Dog Creek Shale) with vertically aligned fractures. The picked rotation angle and time delay are shown in Figures 7.12a and 7.12b, respectively, and two examples of double scanning results for offsets 500m and 1000m are shown in Figures 7.12c and 7.12d. At near offset, TIV anisotropy does not have much influence on the rotation analysis. However, increasing the offset range used for the stack substantially affects the accuracy of the analysis. In order to obtain the desired result, the offset-to-depth ratio for data stack has to be limited to 0.5.

7.3 Azimuthal analysis for 3D acquisition

For 3D surveys, Li (1998) demonstrated from synthetic modelling that a polarity reversal and amplitude dimming will occur in the azimuthal gathers of the transverse components. The azimuth at which the phenomenon occurs indicates the fracture strike. From equation (7.2), by ignoring the noise terms,

$$\begin{aligned} T(t,\theta) &= 0 \text{ for } \theta = 0, \text{ or } \pi/2 \\ T(t,\theta) &= -T(t,-\theta). \end{aligned}$$

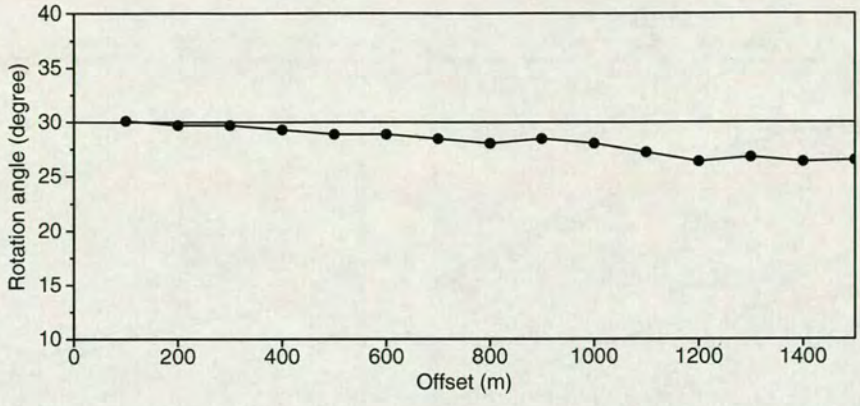

(a)

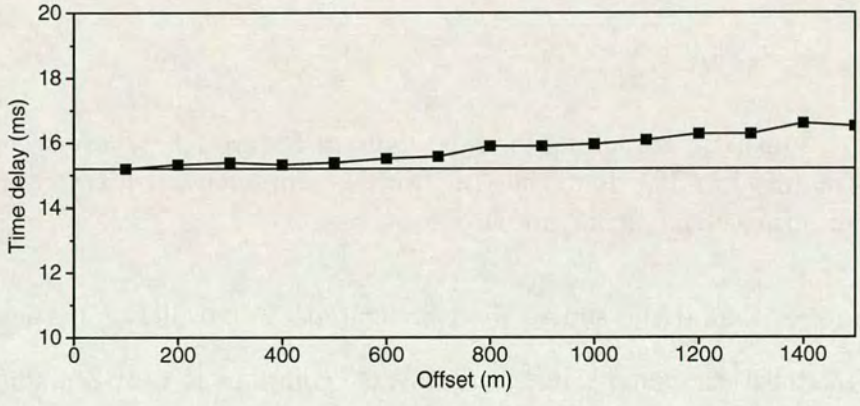

(b)

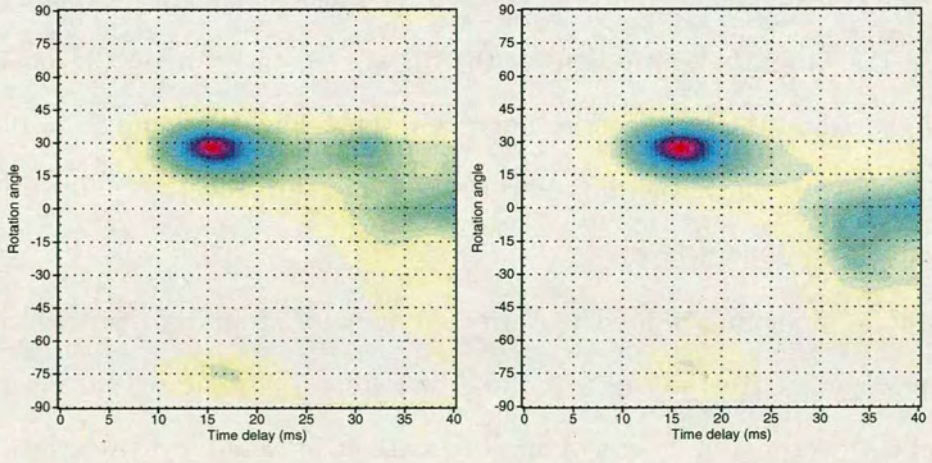

(c) (d)

Figure 7.10: 2C rotation analysis of Figure 7.9: picked rotation angle (a) and time delay (b) for different offset range, and double scanning results from stacked data up to offset of 500m (c) and 1000m (d).

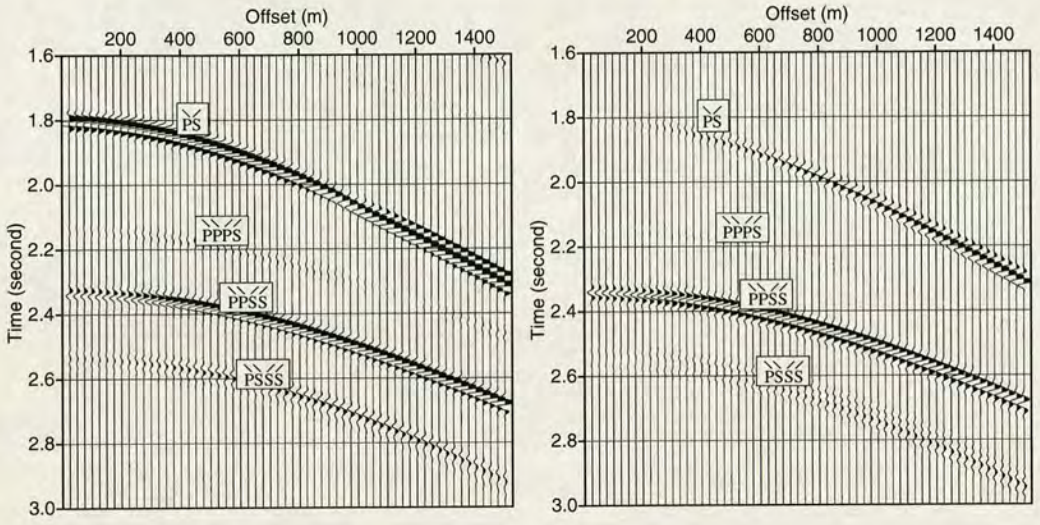

Figure 7.11: Synthetic modelling for the model in Figure 7.8, whose second layer is vertically-fractured in TIV material. (a) Radial component, (b) Transverse component. The fracture strike is 30° north of east.

This implies that if the source-receiver azimuth is parallel or perpendicular to the fracture strike, the energy in the transverse component vanishes, and the wave forms show a polarity reversal.

Thus, a two-stage procedure can be used for anisotropy analysis. The first stage is to use the azimuthal gathers from the 3D survey to estimate the polarization azimuth, based on the two criteria: polarity reversal and minimum amplitude. The second stage is to rotate the data into the fast and slow shear wave directions and to determine the time delays.

Synthetic modelling is used to verify the azimuthal analysis procedures. The model parameters are the same as those of Figure 7.8. The second layer is TIV material with vertical fractures. Azimuthal gathers of radial and transverse components are shown in Figure 7.13. In this model, the geophones are located around the source with constant offset of 500m. The arrows at the top indicate the fracture-strike direction, which is 30° north of east. The shear wave reflection from the

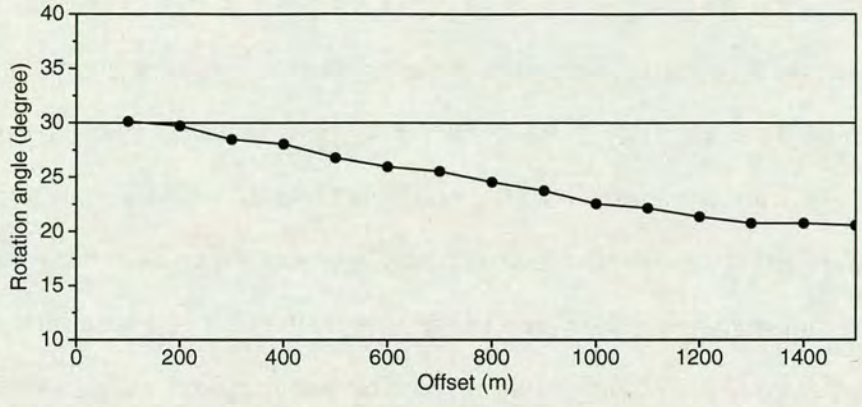

(a)

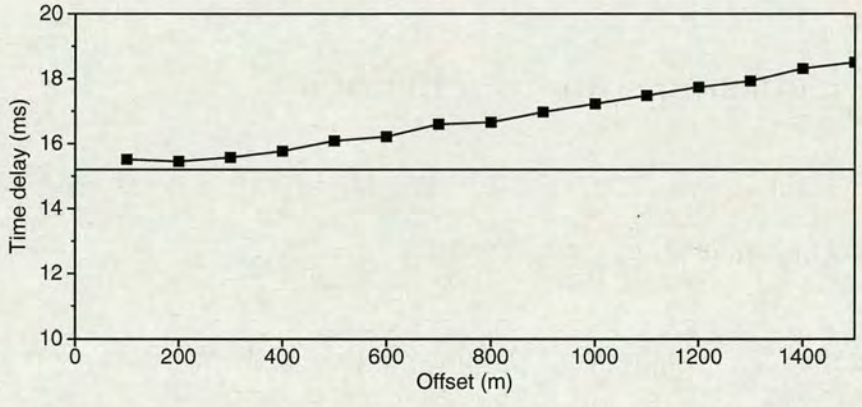

(b)

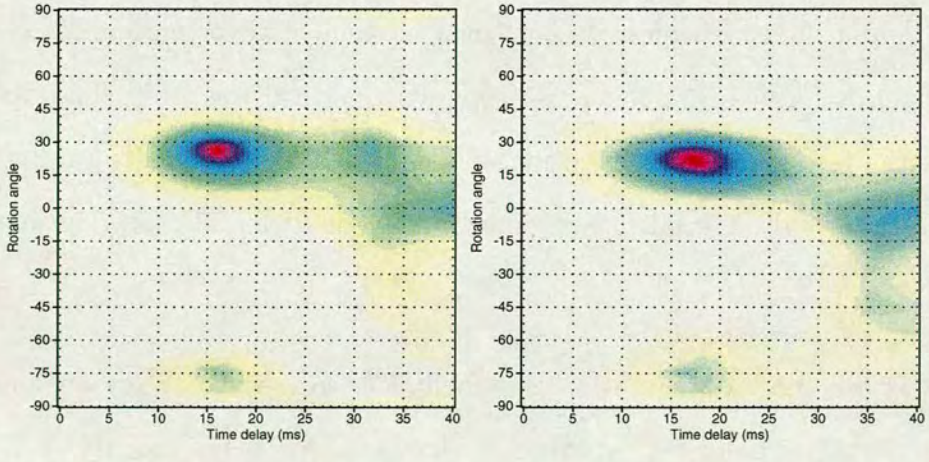

(c) (d)

Figure 7.12: 2C rotation analysis of Figure 7.11: picked rotation angle (a) and time delay (b) for different offset range, and double scanning results from stacked data up to offset of 500m (c) and 1000m (d).

bottom of the second layer is the third event labelled as $\grave{P}\grave{P}\acute{S}\acute{S}$. In the transverse component, it can be seen clearly that polarity reversal happens every 90° when the source-receiver line direction is either parallel or perpendicular to the fracture-strike direction. The amplitude of the radial component also has some dim points. However, they are due to transition between the fast and slow shear wave modes, and do not have polarity reversals. Once the fracture direction is determined, the radial and transverse components are rotated into the fast and slow shear waves as shown in Figure 7.14.

7.4 Discussion and conclusions

The 2C rotation analysis is straight-forward, however, it is necessary to discuss the conditions which make this analysis valid.

1. Equation (7.1) implies that the polarization of the fast shear wave is parallel to the strike of fractures as shown as Figure 7.1, and that the converted shear waves on the interface can be orthogonally decomposed. However, Wild and Crampin (1991) suggested that, in a medium with orthorhombic symmetry which is formed by polar anisotropy with vertical fractures, the polarization of the fast shear wave is no longer wholly parallel to the fracture strike. In practice, only a small offset range can be used for 2C rotation analysis as shown by Figure 7.12.

2. It is a common assumption that before a shear-wave enters an anisotropic medium, its polarization does not change. This is not exactly true at non-normal incident angle. In Figures 7.9 and 7.11, the converted wave from the top of the fractured layer (at time 1.8 seconds) does introduce a small amount of energy into the transverse component.

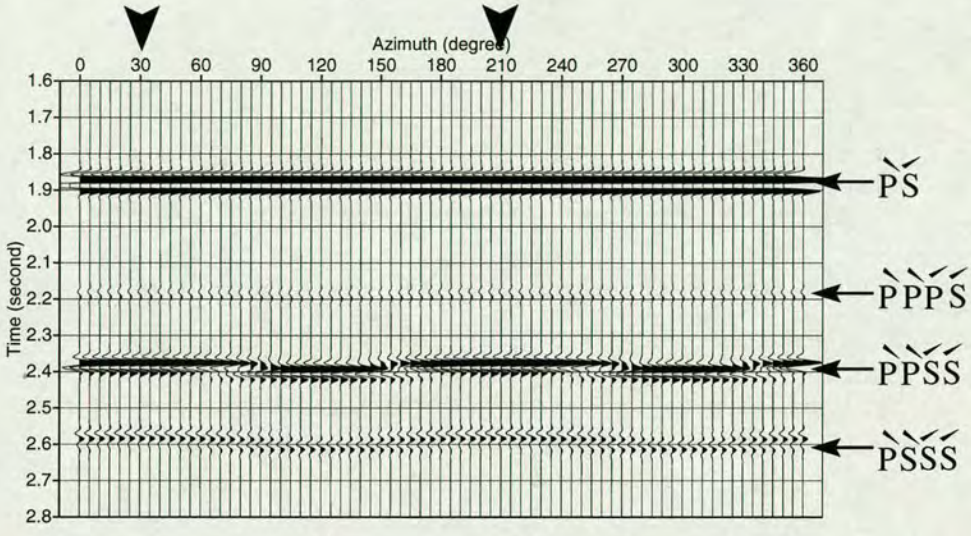

(a)

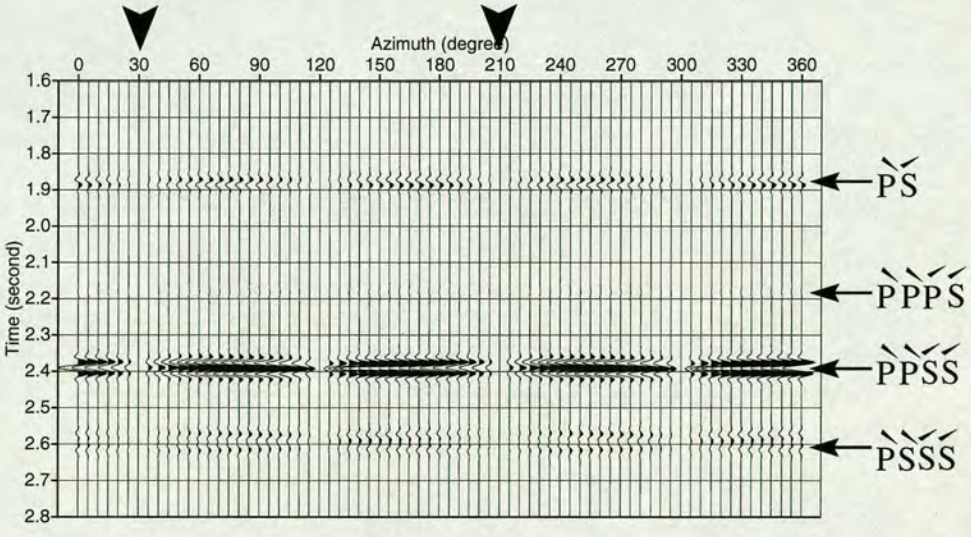

(b)

Figure 7.13: Azimuthal gathers of (a) radial and (b) transverse components, calculated from the model in Figure 7.8. The geophones are located around the source with constant offset of 500m. The arrows at the top indicate the fracture-strike direction, the arrows at the right are for the events with different raypaths.

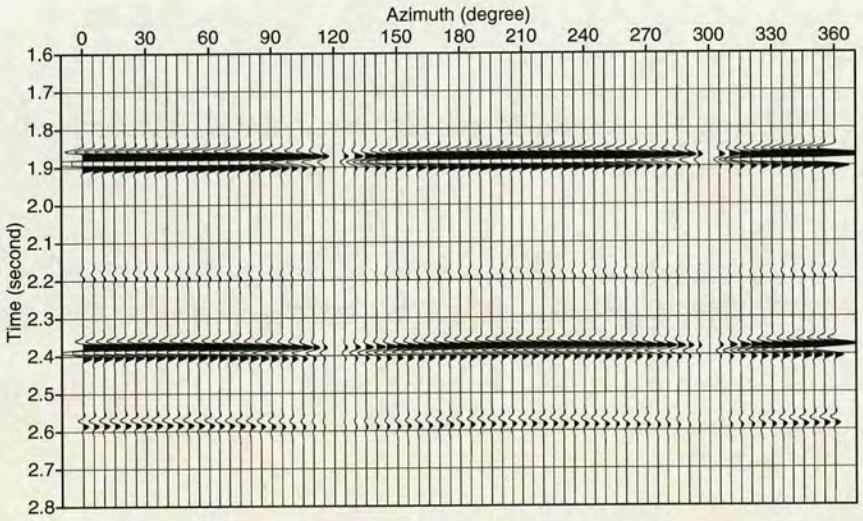

(a)

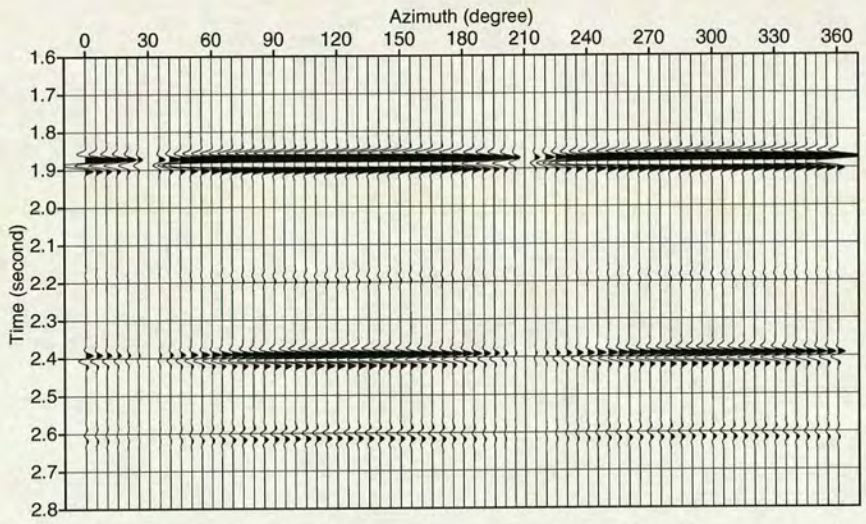

(b)

Figure 7.14: Separated (a) S_1 (fast shear wave) and (b) S_2 (slow shear wave) components from the synthetic data shown in Figure 7.13.

3. The wavelets of two split shear waves are identical. This is not true in the general case since the attenuation for the fast shear wave may be different from that for the slow shear wave. (Thomsen, 1999; Gaiser, 2000).

4. The contribution of noise and other irrelevant signals is negligible or constant in the rotation analysis. This depends on noise or signal types and the length of the time window used for summation.

Furthermore, the presence of TIV anisotropy can make the 2C rotation analysis less reliable. However, polarity reversal in an azimuthal gather does not suffer from the distortion caused by TIV. Thus, in theory, polarity reversal should give a more robust estimation of fracture direction than by the 2C vector rotation method. In field data practice, this depends on many other factors, such as vector fidelity of the geophone sensors, the signal-to-noise ratio of the data, etc.

From Figure 7.13, it can be seen that the geophone responses of converted wave from the bottom of the second layer are complicated by shear wave splitting. One can expect that a full azimuthal stack or migration may cause the energy of the fast and slow shear waves to cancel each other. On the contrary, stack or migration image will be enhanced from processing of the separated fast and slow shear wave data as indicated by Figure 7.14.

In summary, the 2C vector rotation analysis algorithm has been implemented, and its assumptions and limitations have been discussed through synthetic data analysis. Although the 2C rotation analysis requires normal incident shear wave data, the synthetic analysis shows that it is generally acceptable to use post-stack data instead. The presence of TIV anisotropy can degrade the accuracy of 2C rotation analysis, and a limited offset range should be used. In a 3D dataset, polarity reversal in the transverse component can be used for identification of fracture direction, which is independent of TIV anisotropy.

Chapter 8

Case study : Guillemot, The North Sea

8.1 Introduction

The Guillemot 4C survey was one of the earliest 4C OBC experiments. The Guillemot field is located in the west wing of the East Central Graben in the North Sea. There is a mild geological structure in the area with gentle dips.

The sediments in the area are mainly shales or shaly sandstones, thus the presence of polar anisotropy (or TIV anisotropy) is expected in this area. Shale can also exhibit some degrees of azimuthal anisotropy if there are vertical or tilted cracks presented in the rockmass. Winterstein and Paulsson (1990) have observed both horizontal and vertical shear-wave splitting or birefringence in shale. Horizontal shear-wave splitting is a phenomenon of polar anisotropy, which is introduced mainly by microscopic particle alignments. Vertical shear-wave splitting is caused by vertical microcracks parallel to the direction of the maximum stress and perpendicular to the minimum stress (Crampin and Atkinson, 1986). Liu *et al.* (2000) have found two dominant vertical fracture sets in both outcrops and the subsurface in the Antrim

Shale. The two nearly orthogonal fracture sets are developed under the regional stresses.

In this chapter, I apply the methods developed in the previous chapters to process the Guillemont 4C seismic data, and I study the presence of both polar and azimuthal anisotropy.

8.2 Data acquisition

In November 1996, Shell Exploration and Production (UK) acquired four lines of 4C seismic data in the North Sea. The dataset comprises three kilometres of full fold data recorded by the Geco-Prakla drop-drag cable. Figure 8.1 shows the outline of

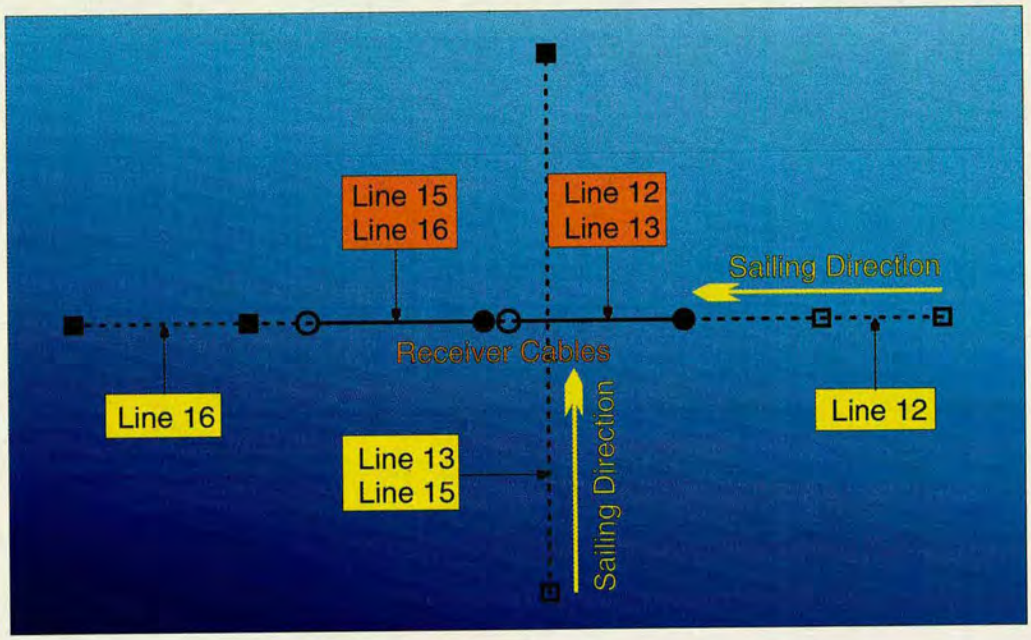

Figure 8.1: The outline of the survey geometry. Receiver locations are shown by the solid lines with circles, and the shot locations by the dashed lines with squares. The open objects (circles and squares) indicate the starting positions, and the filled ones are the ending positions.

the survey geometry. The water depth in the survey area ranges from 88.3 to 90.5 metres, so the seabed can be considered to be more or less flat. The cable length

is 1.5 kilometres. The geophones and hydrophones were planted east-west on the seabed, while the shooting vessel travelled westward and northward, sequentially. After Lines 12 and 13 were acquired, the receivers were replanted at the western end for Lines 15 and 16. Therefore, Lines 12 and 16 constitute a conventional 2-D survey, Lines 13 and 15 are a cross-spread survey. The original purpose of the cross-spread survey was to check the sensitivity of the inline and crossline horizontal geophones, although the cross-spread data have been used to understand the azimuthal anisotropy in this area as well. The airgun source interval for the whole survey is about 25 metres. There are 300 receiver channels. The hydrophones, vertical geophones and cross-line horizontal geophones each used 60 channels with a spacing of 25 metres, while the in-line horizontal geophones have 120 channels with a spacing of 12.5 metres. The double spatial sampling of the inline horizontal component was designed to avoid spatial aliasing due to slow shear-wave velocity, although it is considered unnecessary nowadays as the primary frequency of shear waves is rather low compared with that of P- waves.

Table 8.1 shows the acquisition parameters. Figures 8.2 and 8.3 show some typical shot and receiver gathers, respectively. The overall quality of this data set is excellent. The data recorded on the two horizontal components are dominated by low velocity shear waves, whilst the vertical component has both P-wave and shear-waves, which is an indicator of geophone energy leakage from the inline horizontal component to the vertical component as discussed in Chapter 3. This is due to the problem of the present acquisition implementation, which has been gradually improved through the later designs of OBC acquisition systems. A match filter can be applied to suppress most of these leaked energy.

Location:	UK 21/2, Guillemot Field
Acqusition date:	16/11/1996 - 17/11/1996
Cable laying direction:	0.00°
Number of receiver groups:	300 (PXYZ - 60/120/60/60)
Cable length:	1500 m
Number of cables:	1
Group interval:	25 m (PYZ) 12.5m (X)
Air gun volume:	3397 cu. in.
SP interval:	25 m
Recording length:	10.24 sec
Sampling rate:	2ms
Filter:	Low 3hz/18db
	High 180hz/70db
Recording format:	SEG-D 8015
Navigation format:	UKOOA-90

Table 8.1: Acquisition parameters of the Guillemot 4C suvey.

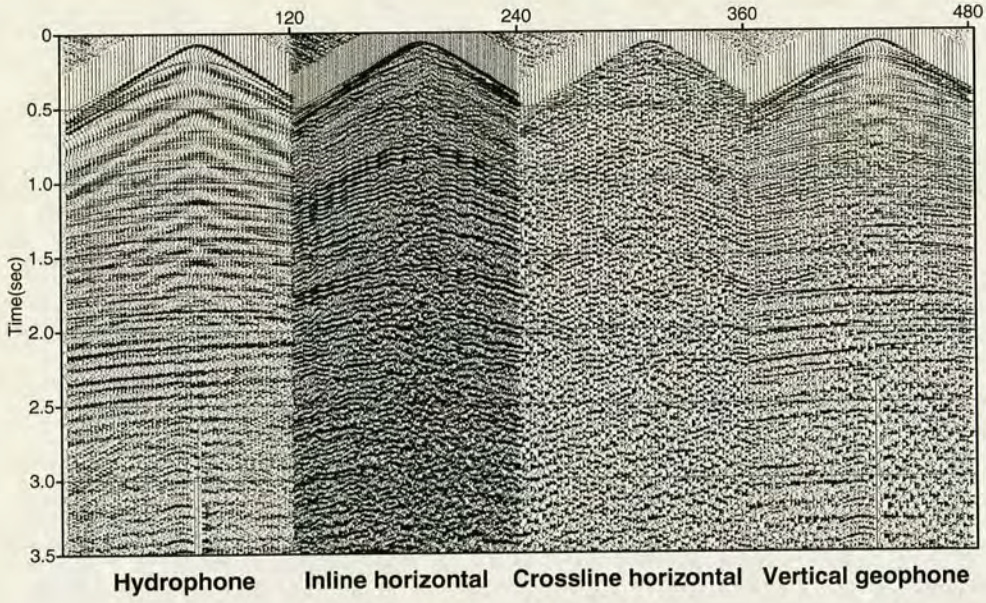

Figure 8.2: A common shot gather (FFID 510) from line 16. Note that AGC with gate 1000ms is applied for display purposes.

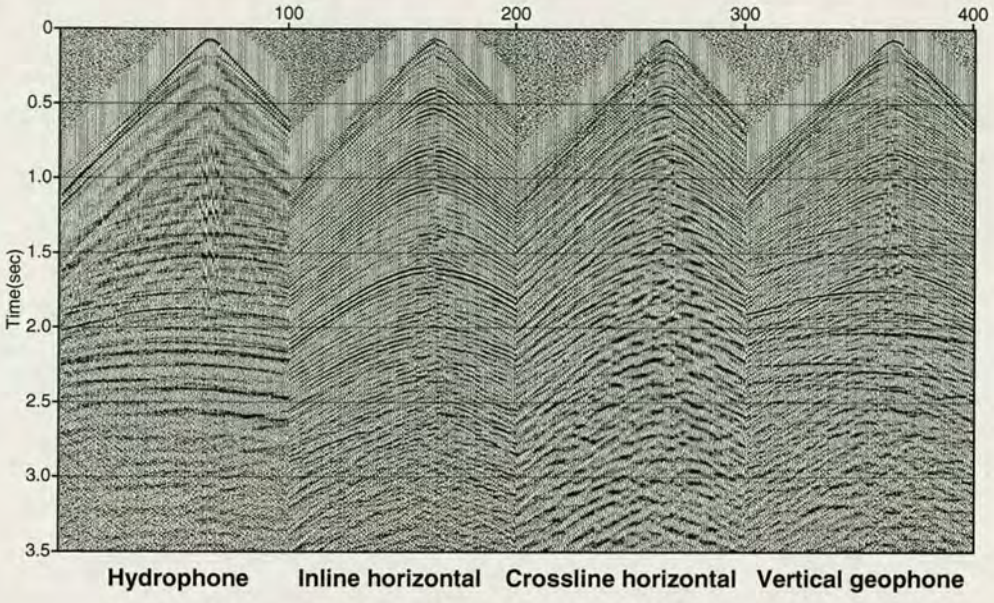

Figure 8.3: A common receiver gather (receiver channel 2) from line 16. Note that AGC with gate 1000ms is applied for display purposes.

8.3 Data processing and analysis of polar anisotropy

8.3.1 P-P data processing

The P-P data were processed using the flow shown in Figure 8.4. Due to the cancelling effect of source- and receiver-side water-column reverberations as discussed in Chapter 3, no dual sensor (hydrophone and vertical geophone) summation is applied. Only the vertical component is processed. After loading UKOOA-90 navigation data to the demultiplexed SEG-D data, true amplitude recovery and some trace editing are applied. An elevation statics is applied to lower the source to the sea-floor, which is about 90 meters below the sea surface. An unusual processing step here is match filter to remove the shear-wave energy in the vertical geophone, by using inline geophone data as reference signal (see Chaper 3). The inline geophone data used have gone through the same preprocessing.

Figure 8.5 shows the stack section of the vertical geophone data after velocity

analysis and normal moveout correction. Finally, the stack section is migrated with a phase-shift migration algorithm. (Figure 8.6). In our geometry definition, the CDP number is decreasing from west to east (Figure 8.1). Thus for easy comparison, the CDP number is decreasing from left to right as well in these figures. This plotting convention is applied to all sections in this chapter.

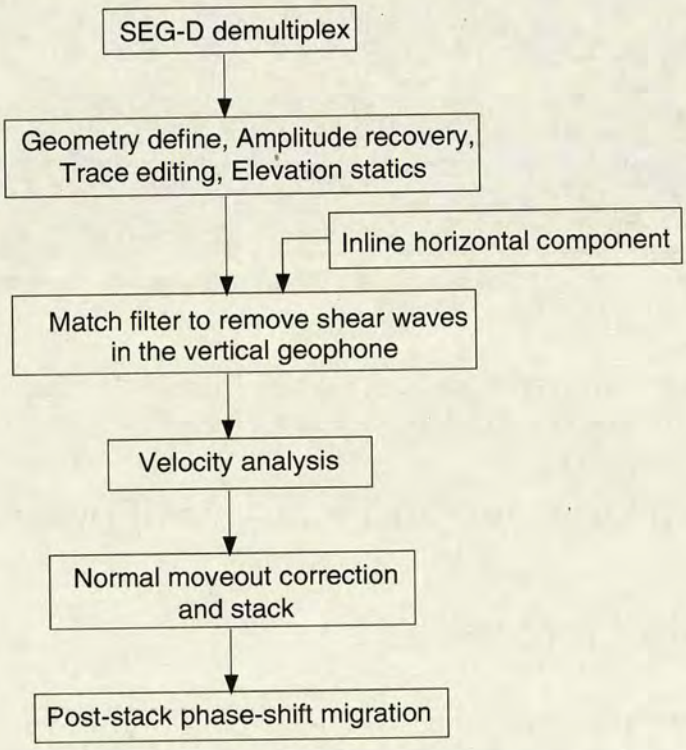

Figure 8.4: Processing flowchart for vertical component data.

8.3.2 Converted-wave data processing

Figure 8.7 shows the processing flowchart for the horizontal components. After SEG-D demultiplex, geometry definition, amplitude recovery, trace editing and elevation statics, the two horizontal components were rotated into radial and transverse components. Geophone re-orientation was not applied here, as we found that the geophone orientation is rather good in Chapter 4. The following processing is mainly focused on the radial component.

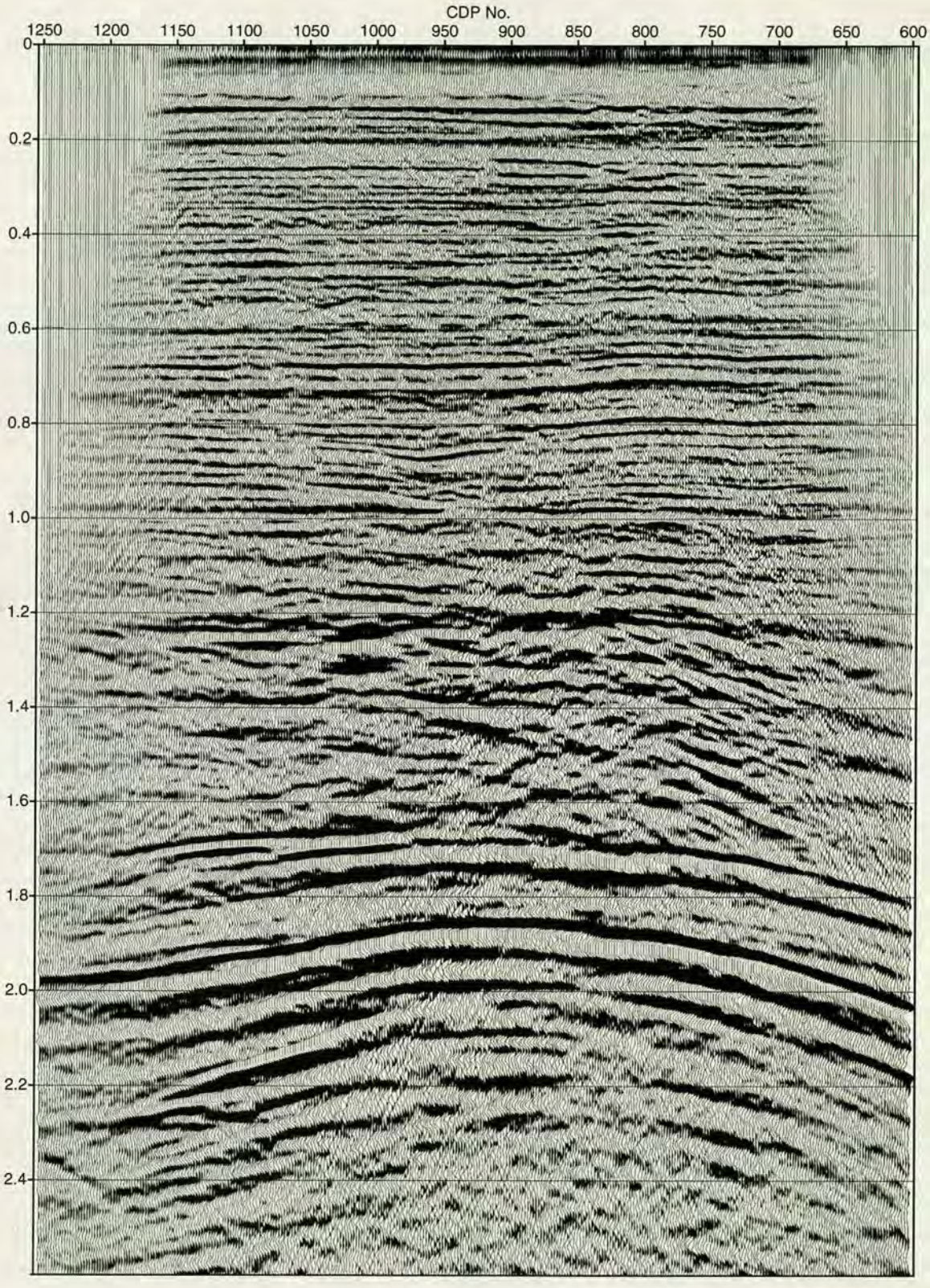

Figure 8.5: Stack section of the vertical geophone data.

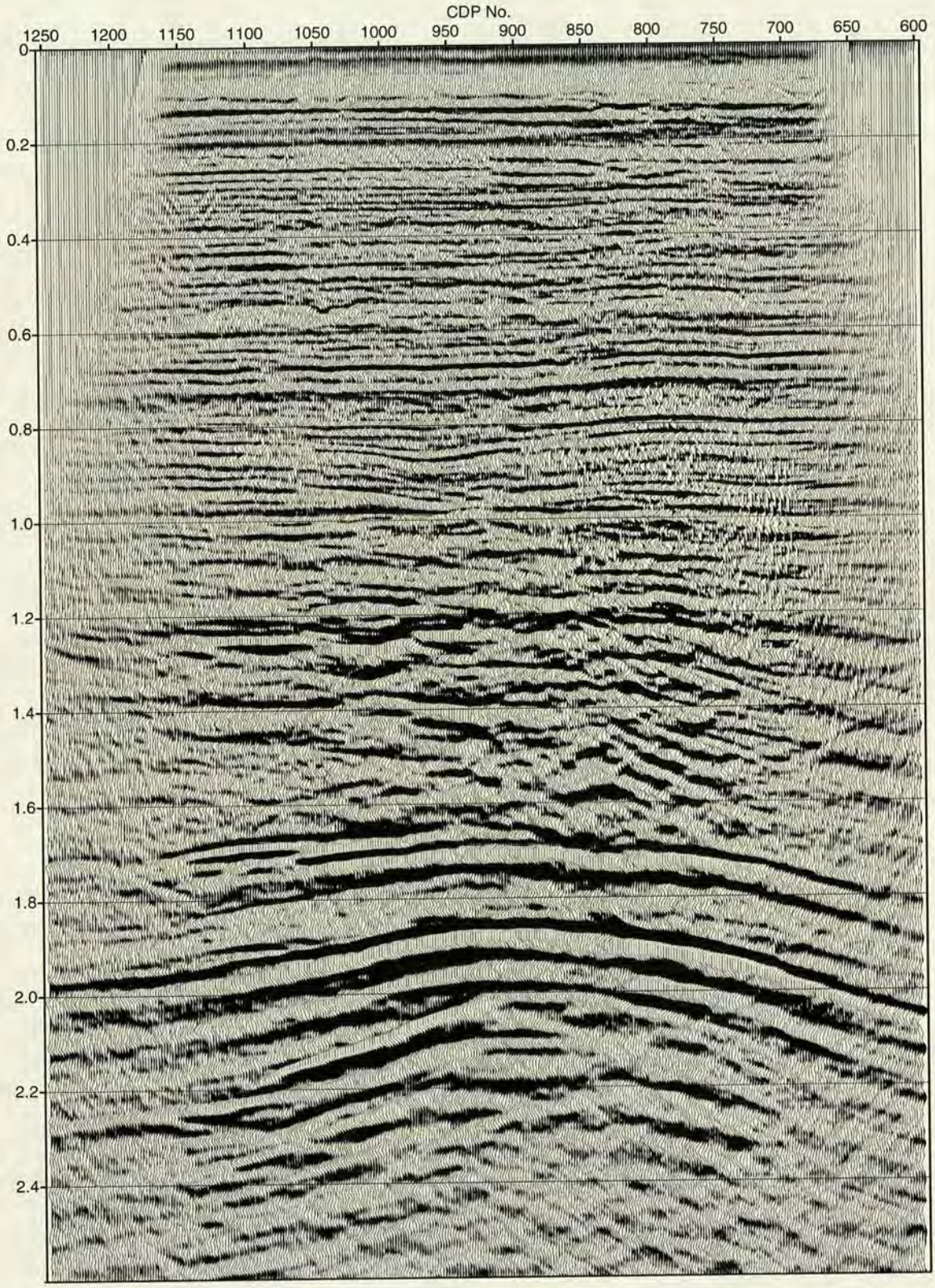

Figure 8.6: Migrated section of the vertical geophone data.

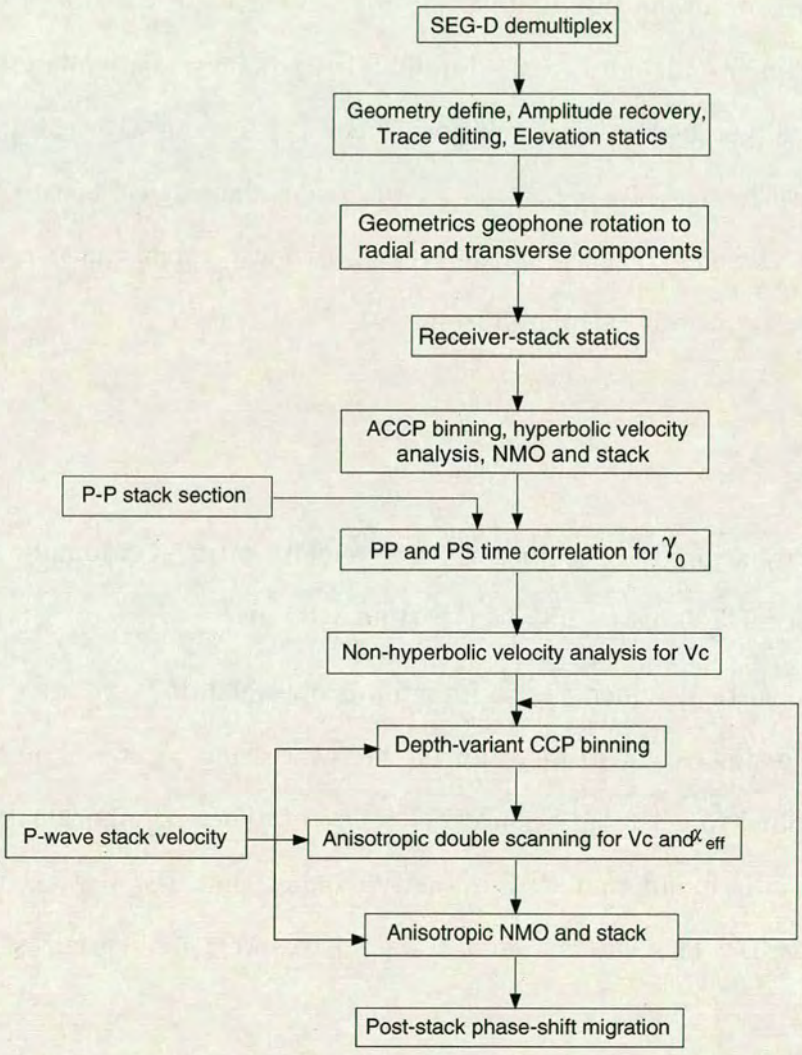

Figure 8.7: Processing flowchart for the horizontal components.

As we have pointed out before, the converted-wave data are severely affected by the receiver-side statics (see Chapter 3). Using the receiver-stack technique (Harrison, 1992), we removed short-period receiver statics (Figure 8.8).

After receiver static correction, a brute-stack sequence is applied to the radial component to obtain an initial stack in order to correlate with the P-P stack section. This sequence includes ACCP binning, hyperbolic velocity analysis, and NMO stack. Figure 8.9 shows the correlation of the P-P events with the P-S events. I have managed to correlate six events based on some geological features such as the syncline at CDP 960. By picking the vertical two-way travel times, t_{p0} and t_{c0}, the vertical velocity ratio is calculated from

$$\gamma_0 = \frac{2t_{c0}}{t_{p0}} - 1.$$

From the correlation, the obtained vertical velocity ratio γ_0 gradually changes from 4.43 at P-S time 760 ms to 2.85 to P-S time 3400 ms.

Once the vertical velocity ratio function is obtained, P-P stacking velocity from P-wave processing can be utlilized for further processing. A non-hyperbolic V_c analysis was applied to get more accurate V_c function. Then γ_{eff} is calculated from V_c, V_p and γ_0. It is found that γ_{eff} is vastly smaller than the vertical velocity ratio (see Chapter 5). This shows that the data is severely influenced by layering and anisotropy.

As we have found in Chapter 6, the layering and anisotropy have significant influence on both conversion point and moveout. Appropriate processing should take them into account. The conventional DMO processing for converted waves (Harrison, 1992) can only handle homogeneous isotropic model, where γ_{eff} equals γ_0. Therefore, it is not appropriate to be applied here. Instead, we applied a depth-variant CCP binning procedure. The procedure can be applied to both NMO-

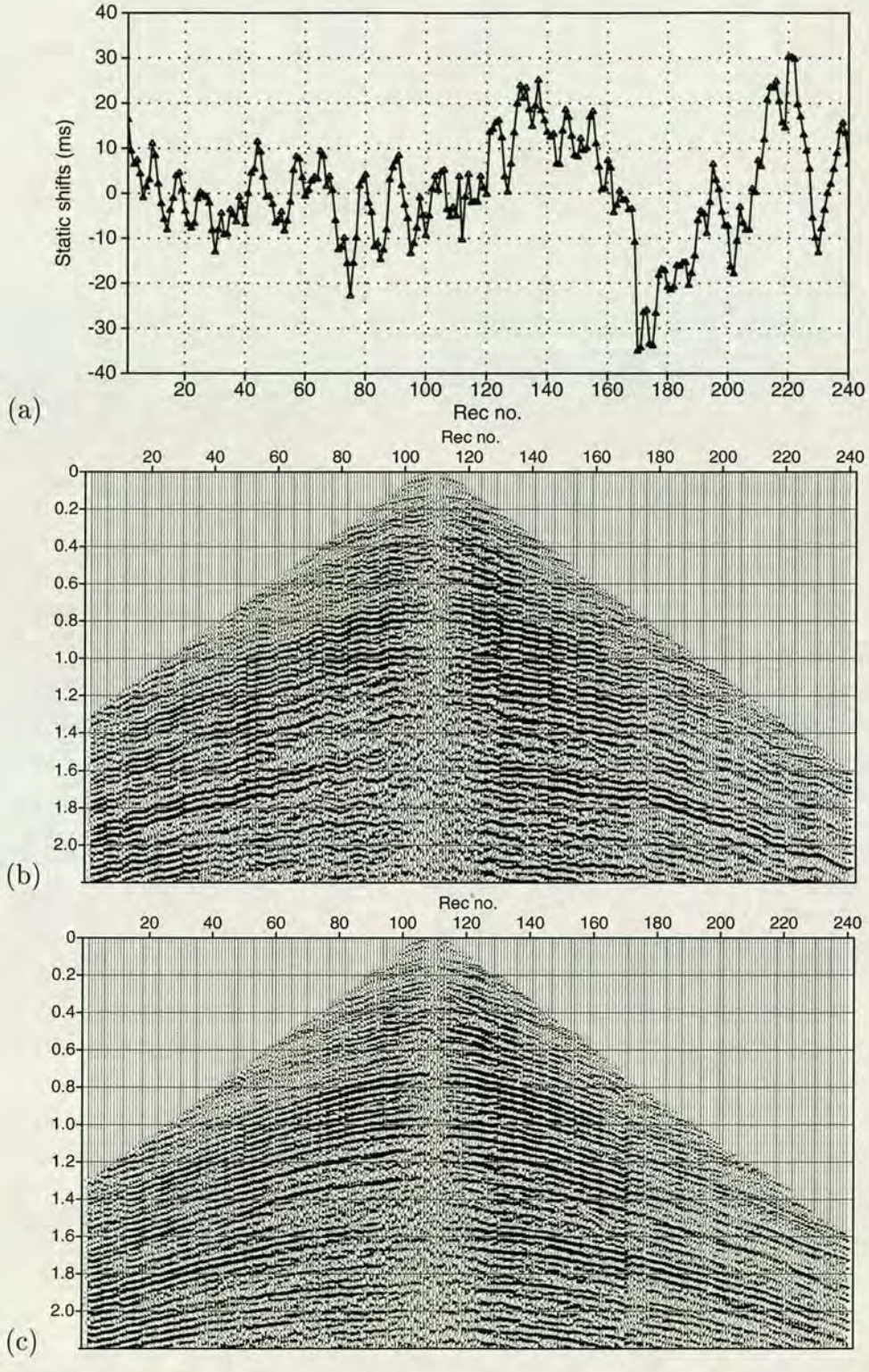

Figure 8.8: Receiver statics correction by receiver stack. (a) receiver static shifts; a shot gather before (b) and after (c) receiver static correction.

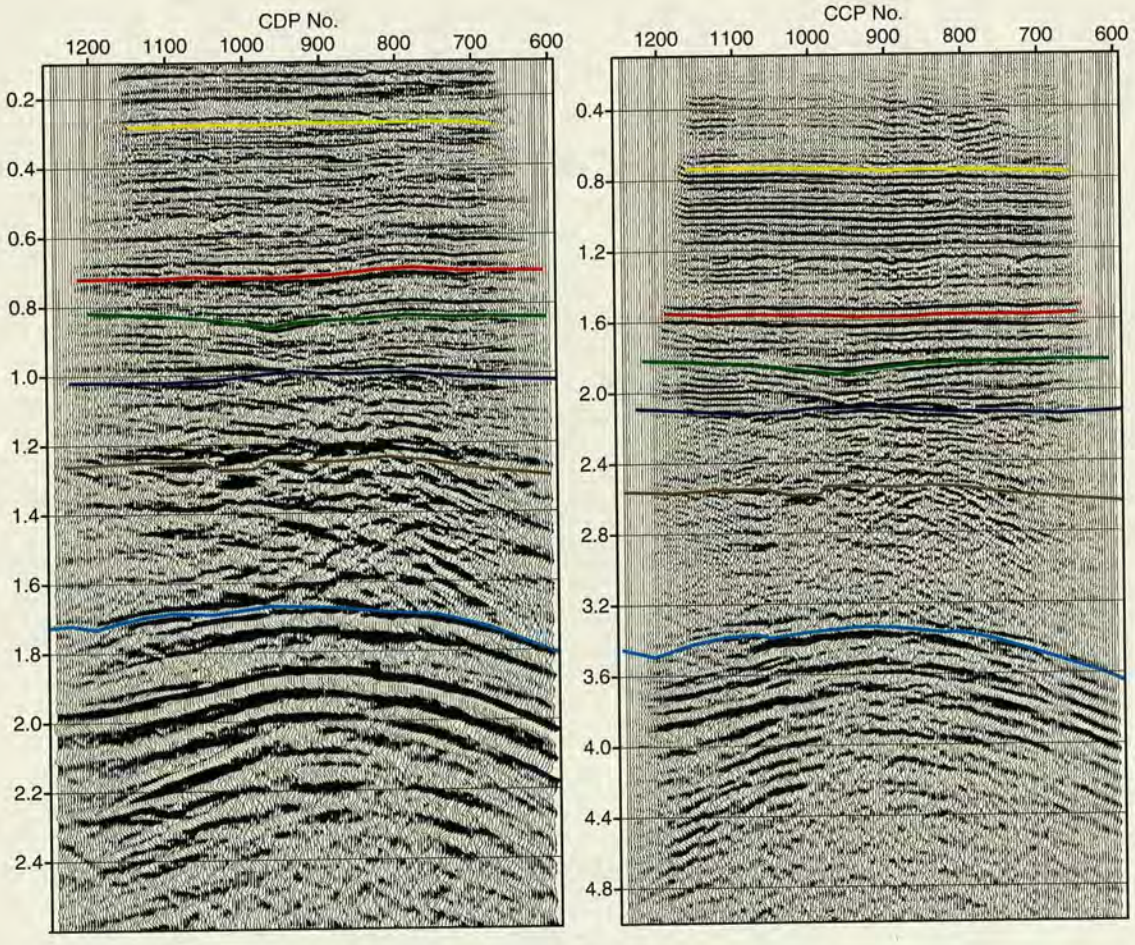

(a) (b)

Figure 8.9: Correlation of P-P and P-S stack sections. Note that except for the first three events, correlation of the other events is very difficult and not unique.

corrected and non-NMO-corrected data. The procedure considers the influence of both layering and anisotropy. It is equivalent to a zero-dip DMO for converted waves.

After depth-variant CCP binning, an anisotropic velocity analysis (see Chapter 6) is carried out on CCP gahters to quantify the degree of anisotropy. Figure 8.10 shows a super gather at CCP 900 stacked from 21 CCP points. Figure 8.11 shows the semblance analysis for V_{c2} and effective anisotropy parameter χ_{eff} . Among five events displayed, two shallow events at 1300ms and 1600ms have the best resolution for V_{c2} and χ_{eff}, due to large offset-to-depth ratio coverage. The following two events at 2100ms and 2670ms show relatively good resolution. The resolution of χ_{eff} for the last event at 3330ms is not very good. In general, the χ_{eff} varies between 0 and 0.4 with a trend increasing with time.

Using the results from the semblance analysis, an anisotropic moveout correction is applied to the super CCP gather (Figure 8.12a). It can be seen that anisotropic moveout correction works very well for near to far offsets. To demonstrate the influence of effective anisotropy parameter χ_{eff}, an isotropic moveout correction by ignoring χ_{eff}, is also shown in Figure 8.12b. If anisotropy is ignored, the over-correction is very significant at far offsets.

Once the anisotropic parameters are determined, the data are binned using depth-variant algorithm again, and an anisotropic moveout correction is applied. Figure 8.13 is the final stack section for the radial component. Finally a phase-shift poststack migration is applied to obtain Figure 8.14.

Comparing ~~with~~ P-wave sections (Figures 8.5-8.6) with PS-wave sections (Figures 8.13-8.14), it can been seen that P-waves can penetrate deeper than P-S waves, however, they suffer from relatively low signal-to-noise ratio. The P-S section has a high signal-to-noise ratio, however, its frequency band is rather limited due to its ringy wavelet. P-P and P-S stack sections share some similar geological features,

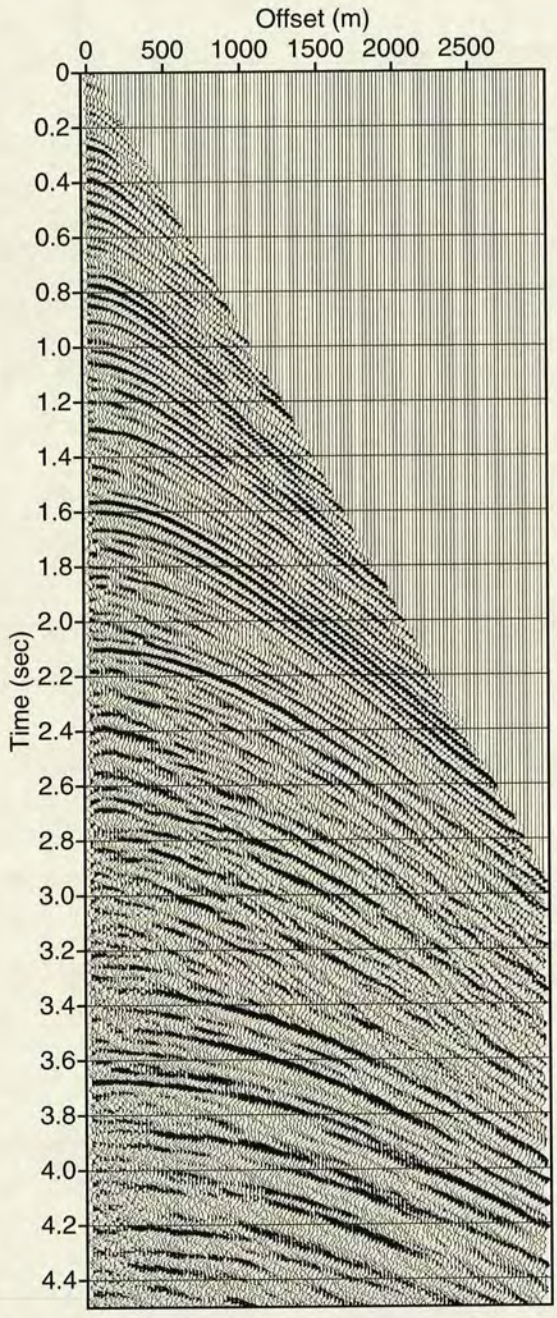

Figure 8.10: A super gather at CCP 900.

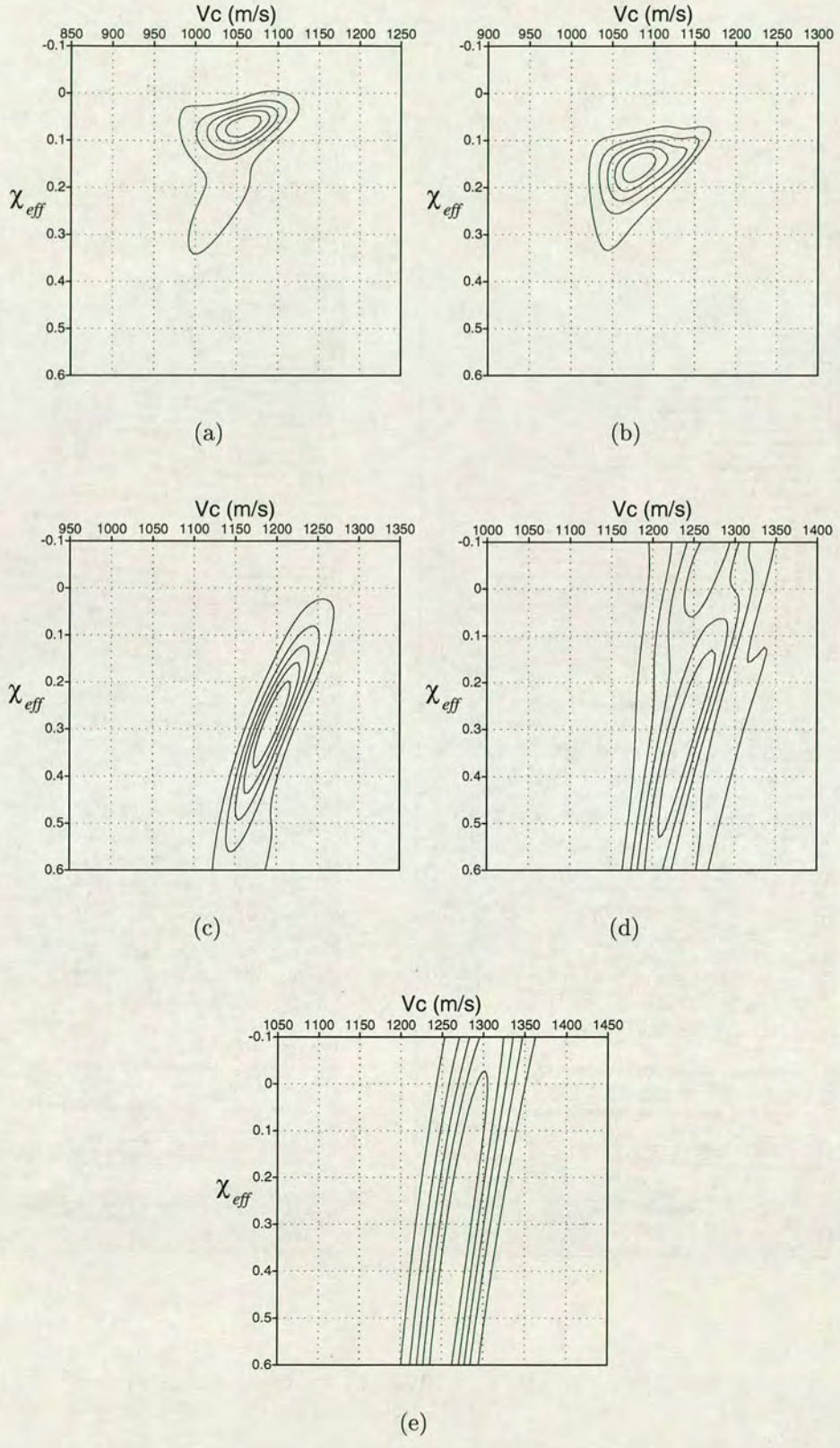

Figure 8.11: Semblance analysis of the field data in Figure 8.10 for V_{c2} and χ_{eff} using prior information for V_{p2} and γ_0. Events (a) 1300ms, (b) 1600ms, (c) 2100ms, (d) 2670ms and (e) 3330ms.

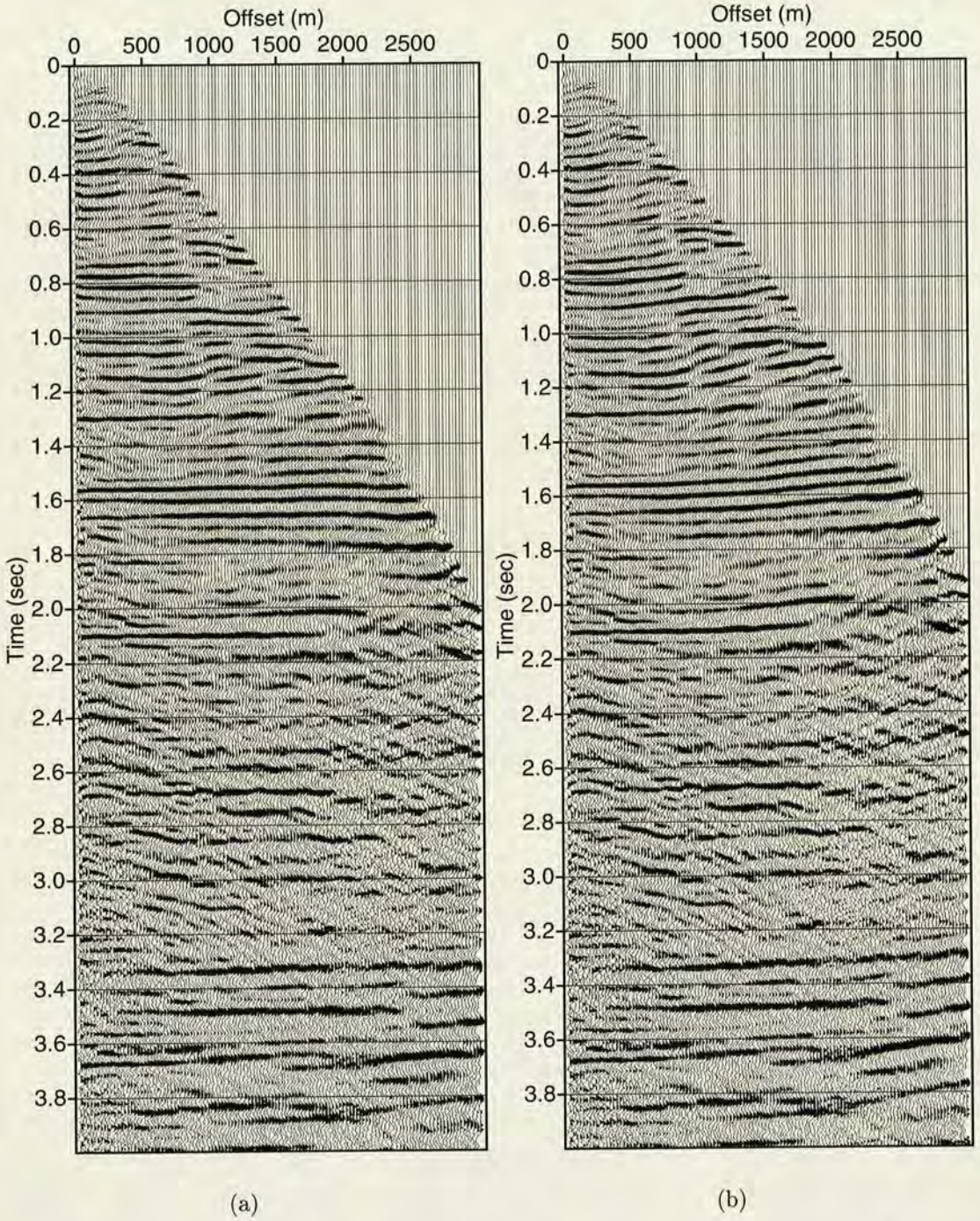

Figure 8.12: Anisotropic (a) and isotropic (b) moveout correction of field data in Figure 8.10.

such as the syncline at CDP 970 (at about 860 ms for *P-P* and about 1850 ms for *P-S*).

8.4 Analysis of azimuthal anisotropy

8.4.1 Analysis from the inline 2D shooting

The energy in the transverse component is very week. However, in order to investigate the presence or absence of azimuthal anisotropy, the transverse component has also been processed. The processing flow and processing parameters are the same as those applied to the radial component in order to make the stack sections comparable. Note that in all of the processing, only deterministic processing routines are used, and I avoid the use of any statistical processing routines such as deconvolution, and amplitude balance. The stack sections of transverse component is shown in Figure 8.15.

Two shear-wave sections, Figures 8.13 and 8.15, are highly comparable, with similar geological features. It is also noticeable that there is a dim area from CDP 1000 to CDP 1200 at time above 2.5 seconds in the transverse stack section. For other areas, there are good correlations in two sections. There are three possible reasons for the coherent energy in the transverse stack section:

1. Mis-orientation of horizontal geophones - this possibility has been eliminated from our geophone orientation analysis;

2. Off-plane reflections - for this case, the events in two horizontal phones should have the same traveltime, theoretically;

3. Azimuthal anisotropy - split fast and slow shear-waves are recorded by two horizontal geophones.

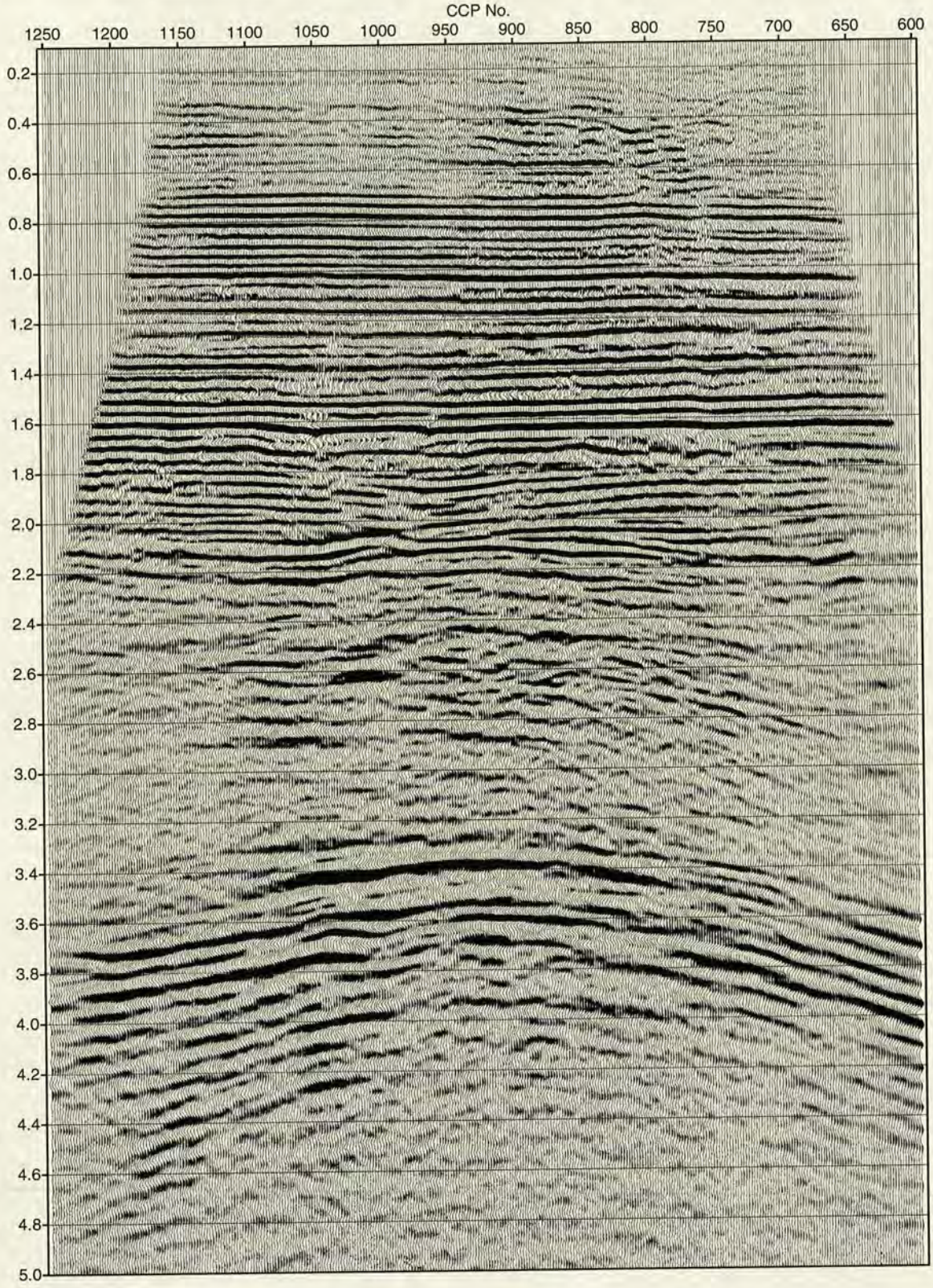

Figure 8.13: Stack section of radial component using anisotropic binning and move-out correction.

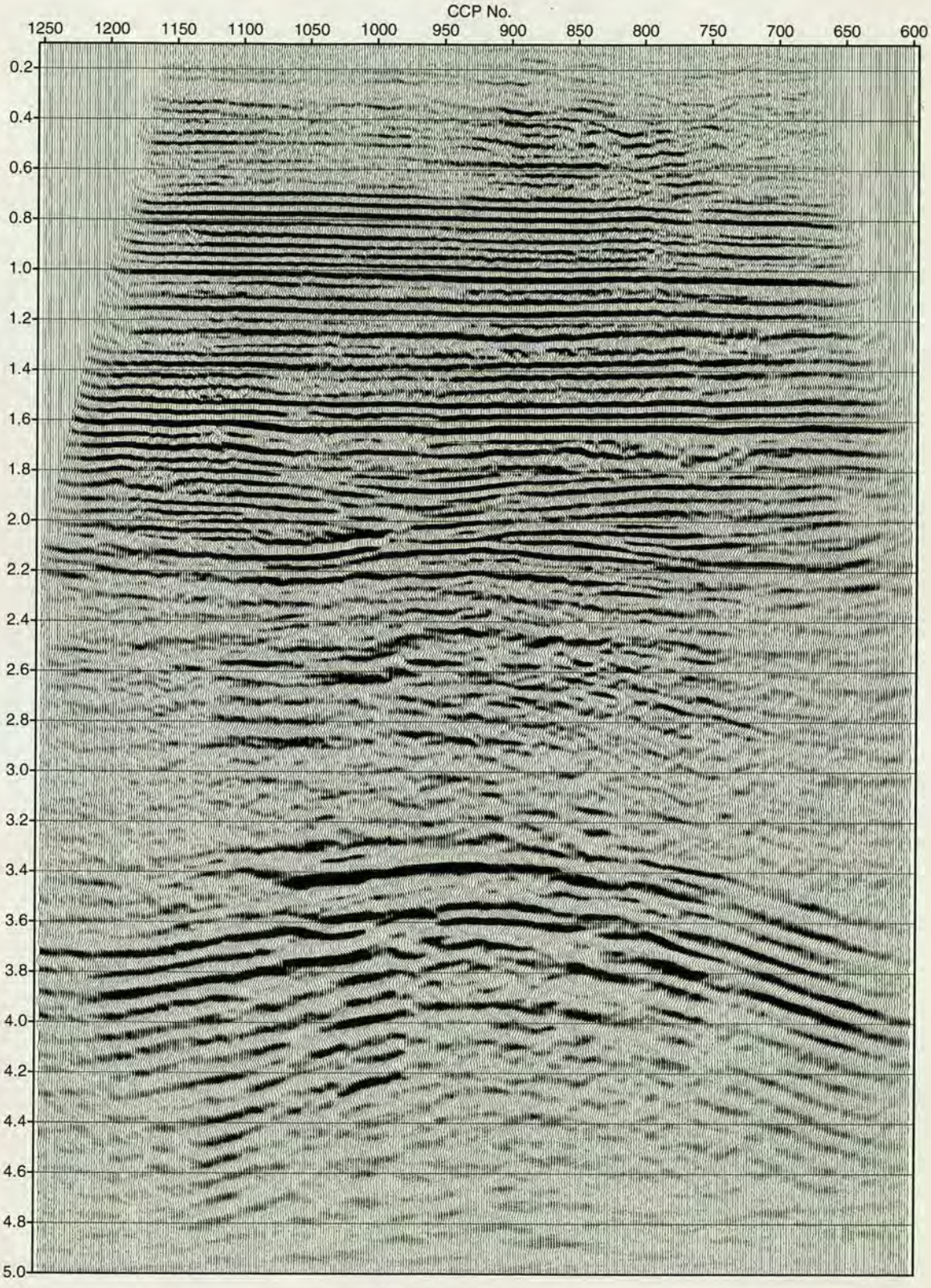

Figure 8.14: Post-stack migrated section of Figure 8.13.

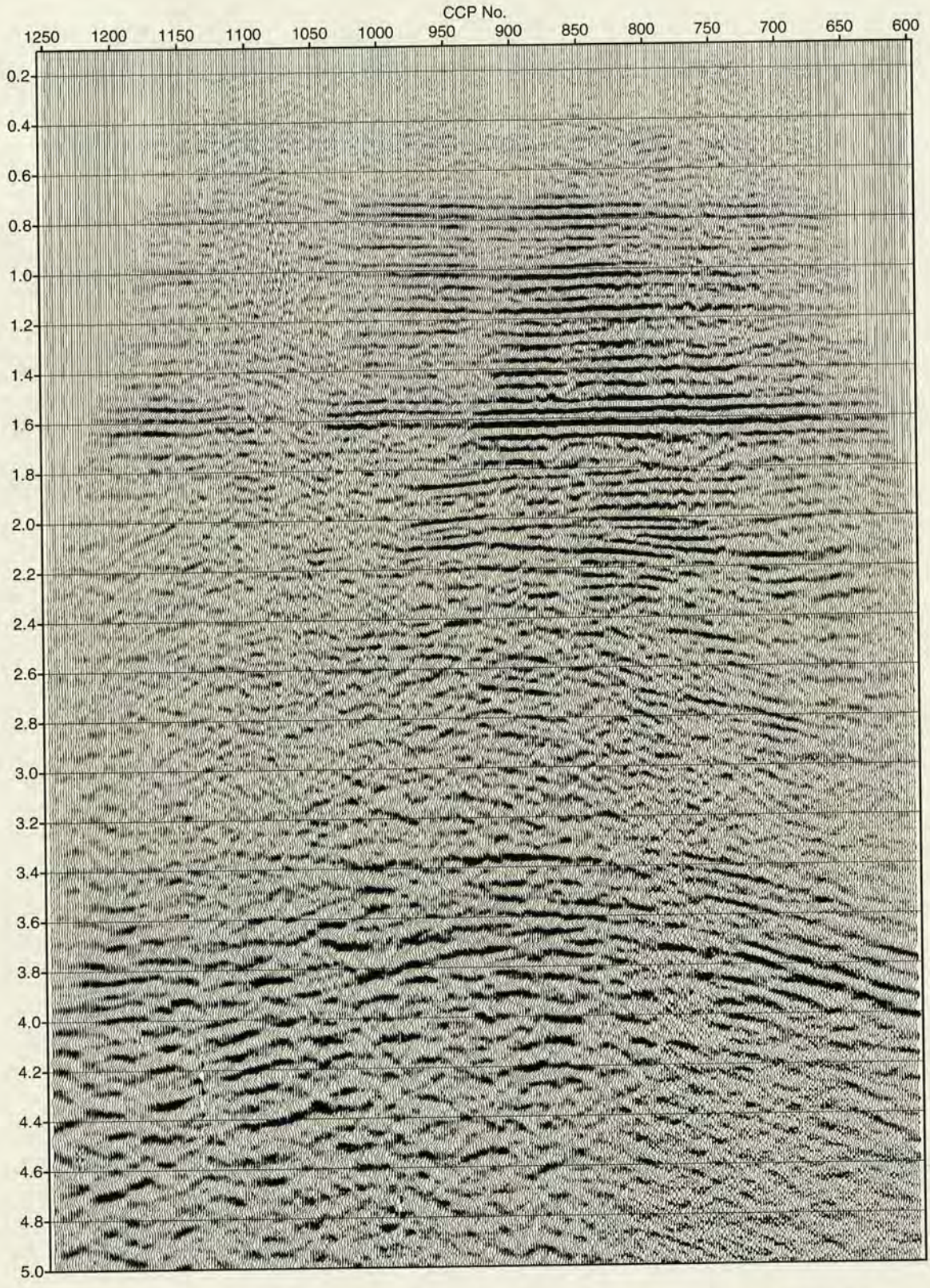

Figure 8.15: Final S-wave stack section from the transverse component.

However, careful comparison of corresponding events in two horizontal sections for the two horizontal components, reveals that there are time delays between them. The events in the transverse component are generally faster than those of the radial component. Thus we can safely conclude that there is shear-wave splitting in the data caused by azimuthal anisotropy. Although we still cannot eliminate the possibility of off-plane reflection, the dim reflection area between CDP 1000 and 1200 suggests that its influence is quite small if it exists. For reason of simplification, we assume that the energy in the crossline stack section is due to azimuthal anisotropy.

After identifying that azimuthal anisotropy is present in the data, the next step is to quantify the strength of anisotropy and to find the fracture direction in the survey area. The 2C rotation analysis discussed in Chapter 7 has been applied to the Guillemot field data. The double scanning over rotation angle θ and time delay Δt is performed on three different time windows: (1) 600-1400 ms; (2) 1400-2200 ms; and (3) 3200-4400 ms in *P-S* stack sections (Figures 8.13and 196). Figures 8.16 and 8.17 show the picked rotation angle and time delay, respectively, and some example plots of rotation analysis at CDPs 800, 900, 1000, 1100 are shown in Figures 8.18, 8.19, and 8.20 for three different time windows, respectively. The analysis is performed for every 10 CDPs.

From Figure 8.16, it is clear that the fracture direction in the survey area varies both vertically and laterally. For reflections in time window 600-1400 ms, the fracture direction gradually changes from east-west in the west to about 20° south of east in the east; for 1400-2200 ms, it changes to 30° south of east; and for 3200-4400 ms, about 40° south of east. Although there are some fluctuations among the CDPs, this overall trend remains.

As far as the time delay is concerned, for the first time window, it is about 6-7 ms, and for the second time window, it is about 10 ms, and in the last time window, two split shear waves have a time delay of 18 ms. Considering that vertical two-

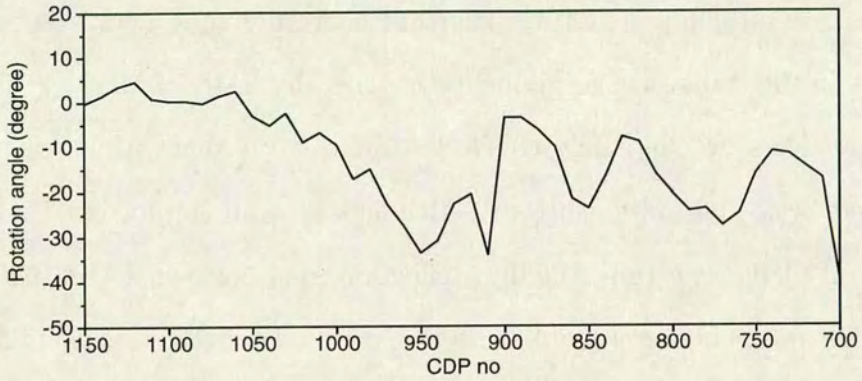

(a)

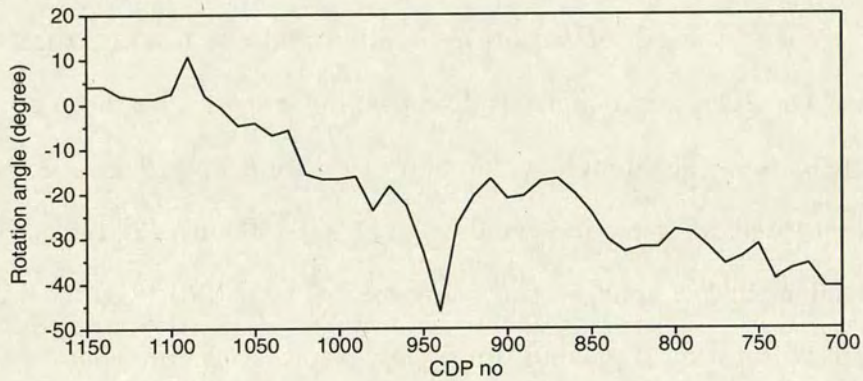

(b)

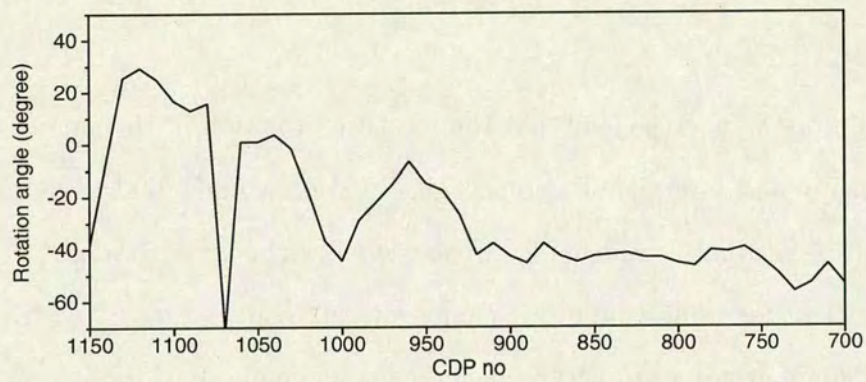

(c)

Figure 8.16: Picked rotation angle θ from 2C rotation analysis. The analysis is made for every 10 CDPs for different time windows: (a) 600-1400 ms; (b) 1400-2200 ms and (c) 3200 - 4400 ms.

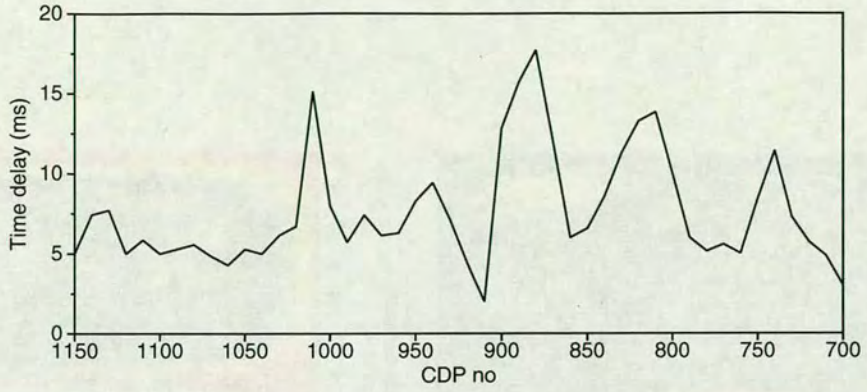

(a)

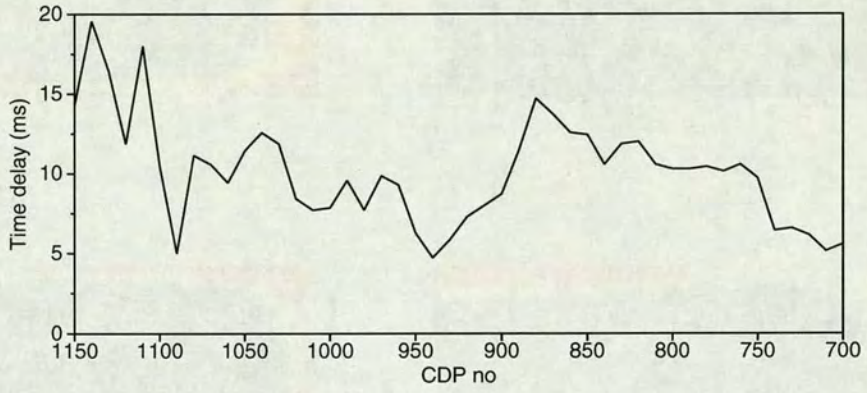

(b)

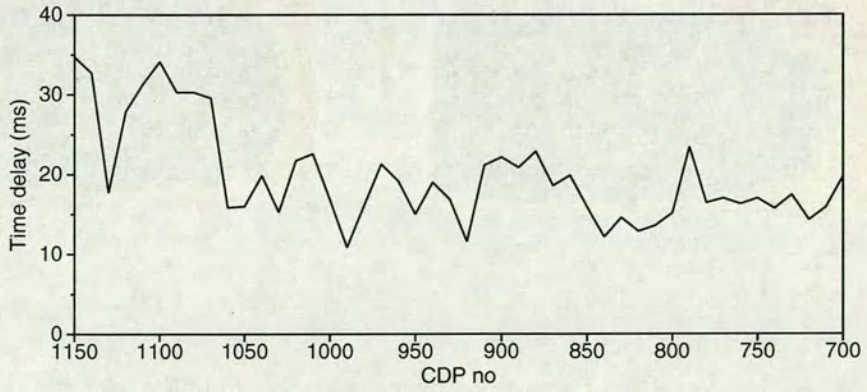

(c)

Figure 8.17: Picked time delay Δt from 2C rotation analysis. The analysis is made for every 10 CDPs for different time windows: (a) 600-1400 ms; (b) 1400-2200 ms and (c) 3200 - 4400 ms.

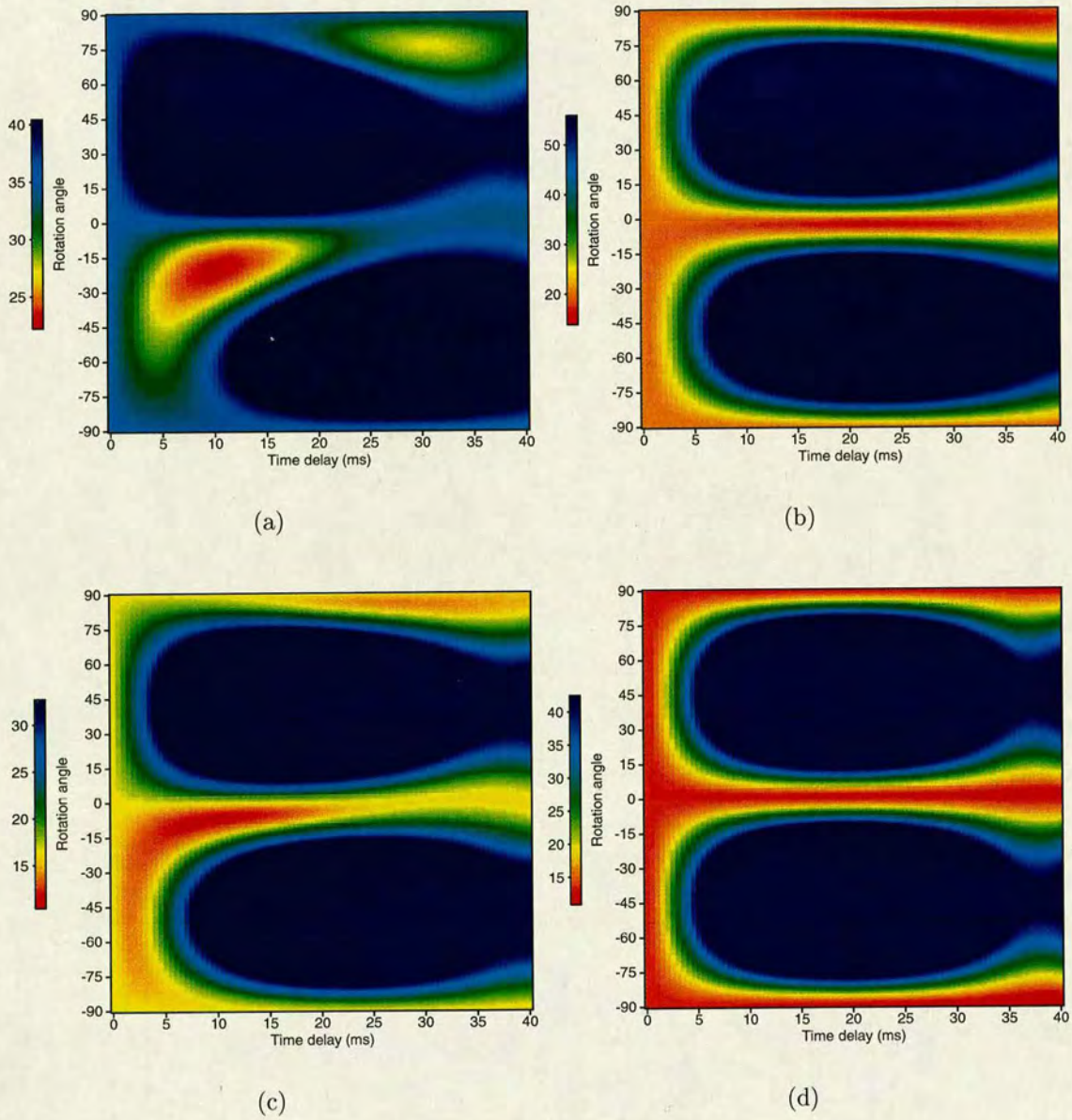

Figure 8.18: Example plots of scanning over rotation angle θ and time delay Δt for time window 600-1400 ms (Figures 8.16a and 8.17a). (a) CDP 800, (b) CDP 900, (c) CDP 1000, (d) CDP 1100.

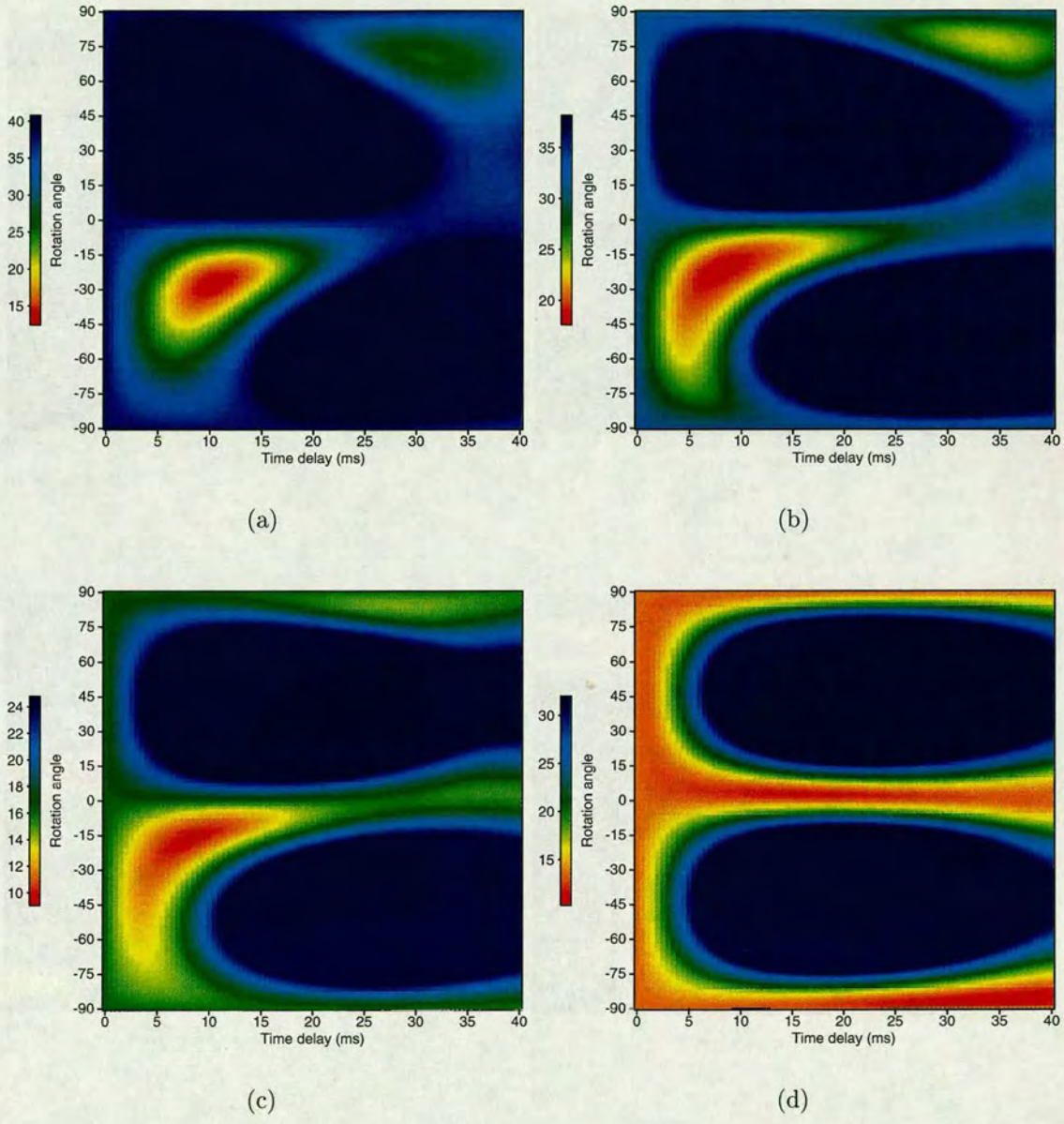

Figure 8.19: Example plots of scanning over rotation angle θ and time delay Δt for time window 1400-2200 ms (Figures 8.16b and 8.17b). (a) CDP 800, (b) CDP 900, (c) CDP 1000, (d) CDP 1100.

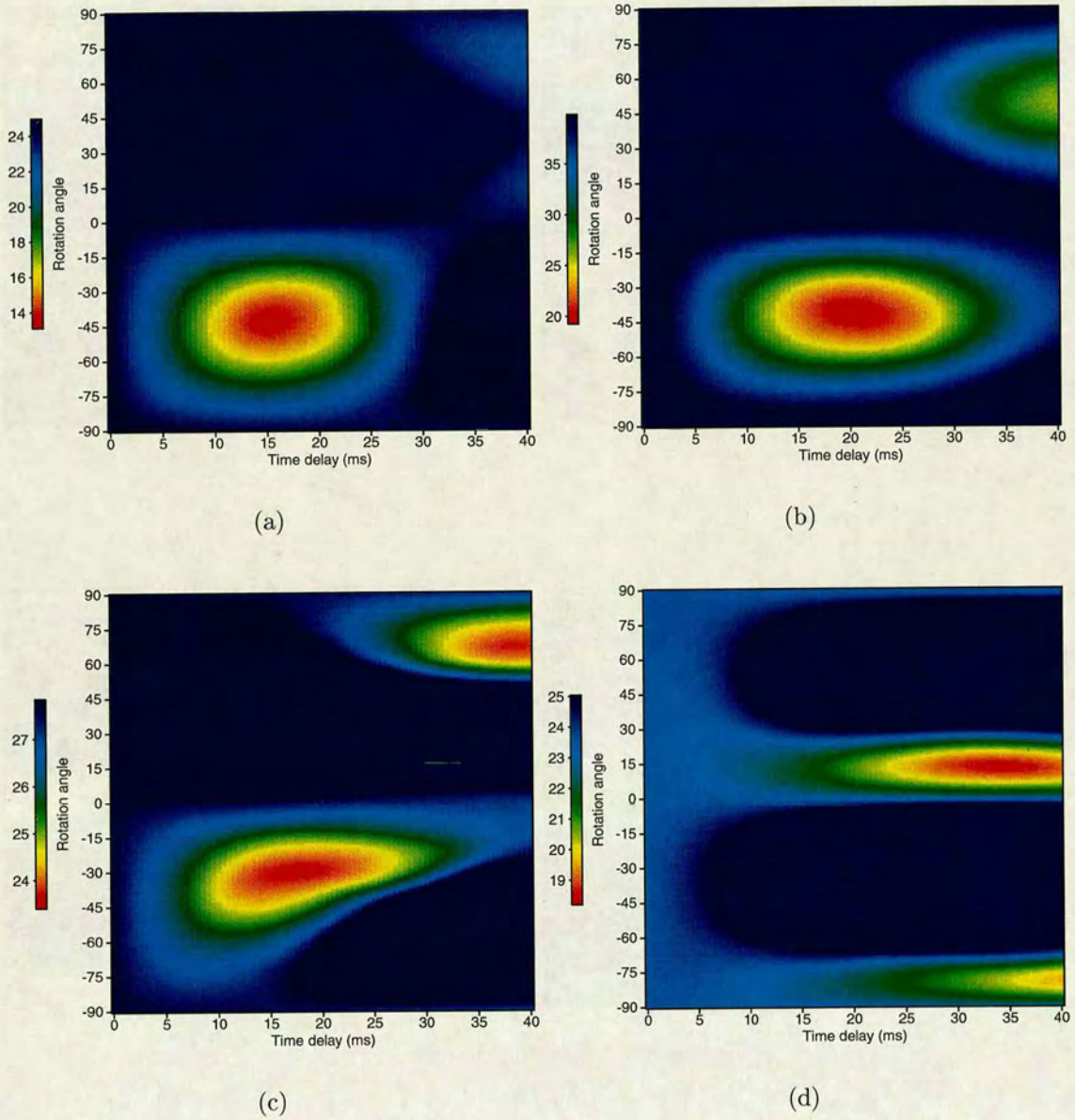

Figure 8.20: Example plots of scanning over rotation angle θ and time delay Δt for time window 3200-4400 ms (Figures 8.16c and 8.17c). (a) CDP 800, (b) CDP 900, (c) CDP 1000, (d) CDP 1100.

way traveltimes are about 1000, 1800, and 3800 ms for these three time windows, respectively, and the overall vertical velocity ratio V_p/V_s is about 3 in the survey area, the time delays represent 0.6% - 1% shear wave anisotropy.

8.4.2 Analysis from the cross-spread shooting

The above analysis is based on the stacked data, on the assumption of vertical wave propagation in a vertically fractured medium. We can also use pre-stack data from different azimuths, which is available from a cross-spread survey. Li (1998) demonstrated from synthetic modelling that a polarity reversal and amplitude dimming will occur in the azimuthal gathers of the transverse components. The azimuth at which the phenomenon occurs indicates the fracture direction.

Figure 8.21 shows some receiver gathers of the rotated horizontal components from the cross-spread survey (Figure 8.1). The transverse component is in the upper panel and the radial component in the lower panel. The horizontal axis is shooting azimuths counterclockwise from the east. In order to check polarity reversal easily, hyperbolic NMO corrections are applied with a constant velocity. Receiver channel 6 (Figure 8.21a) is located at the west of the survey, where the fracture direction is east-west as indicated by 2C rotation analysis. It can be seen clearly that polarity reversal in the transverse component is indeed in this direction. At other locations (Figures 8.21b, 8.21c and 8.21d), we are still able to observe that the polarity reversals move to the southeast (negative azimuthal angles) as indicated by dim spots. However, the dim spots also exist in other directions. Moreover, the locations of the dim spots vary substantially even in the successive receiver channels, (comparing Figures 8.21c, 8.21d, 8.21e and 8.21f).

Therefore, fracture direction cannot be reliably determined from the cross-spread data in this survey. The following are possible reasons.

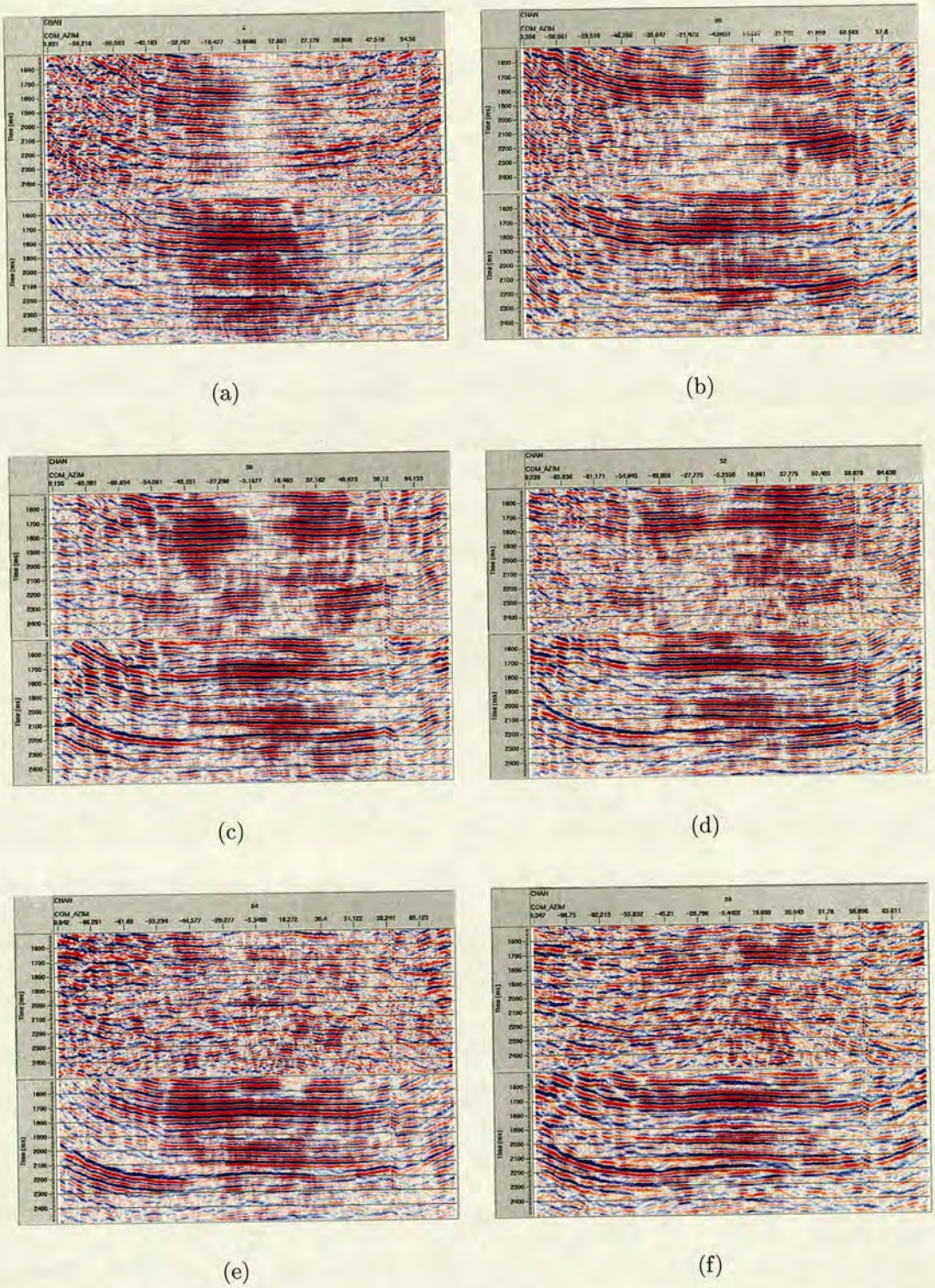

Figure 8.21: Some receiver gathers of the rotated horizontal components from cross-spread survey (Figure 8.1). The transverse component is in the upper panel and the radial component in the lower panel. The receiver channel numbers are (a) 6, (b) 20, (c) 50, (d) 52, (e) 54 and (f) 56. The horizontal axis is shooting azimuths counterclockwise from the east. Hyperbolic NMO corrections are applied.

1. Coupling and vector fidelity of two horizontal phones are not very good . The problem of vector fidelity certainly exists as shown by significant changes of signal characteristics recorded in adjacent receivers (Figure 8.21). This problem also implies that even the post-stack 2C rotation analysis should be treated with caution.

2. The shear waves are reflected from different reflection points. A proper analysis should be based on CCP azimuthal gathers. however, it is not possible for a single-fold cross-spread survey.

3. In the survey area, the fracture direction and density vary both laterally and vertically as indicated from previous 2C rotation analysis.

4. The strong polar anisotropy in the region also affects the polarization patterns of split shear waves substantially (Wild and Crampin, 1991).

8.4.3 Discussion and Conclusions

The presence of polar anisotropy in the Guillemot data has a significant influence on the determination of both conversion point and moveout. It is inappropiate to apply Harrison's DMO which was developed for homogeneous insotropic media. Instead, we applied a depth-variant-binning technique as the geological structure in the survey area is very mild. However, a DMO algorithm for polar anisotropy would be more desirable for a complex geological structure.

In summary, we have carried out a detailed processing of Guillemot 4C data taking into account both polar and azimuthal anisotropy. From the velocity analysis, the data show strong TIV anisotropy. A double scanning semblance analysis has been applied to the data to evaluate the strength of TIV anisotropy. An anisotropic moveout correction can flatten the data from near to far offset. Comparing *P-P* and

P-S sections , it can been seen that *P*-waves can penetrate deeper than *P-S* waves, however, they suffer from relative low signal-to-noise ratio. The *P-S* section has a high signal-to-noise ratio, however, its frequency band is rather limited due to its ringy wavelet.

The processing results of the radial and transverse components data from the Guillemot data have shown that the Guillemot field is azimuthally anisotropic to some extent. On the assumption that the azimuthal anisotropy is caused by a single set of vertical fractures, we carried out a detailed analysis to quantify the fracture direction and the intensity of anisotropy, using both conventional 2D and cross-spread survey data. It shows that the fracture direction and time delay vary both laterally and vertically. In the west of the survey line, the fracture direction is about parallel to the survey direction in an east-west direction. It rotates gradually to about 40° south of east at the east of the survey line. The azimuthal anisotropy is likely caused by aligned fractures in the overburden and the estimated orientation agrees with the regional stress direction (Floris Strijbos of Shell Expro, personal communication). The time delays between the two split shear waves represent 0.6% - 1% shear wave anisotropy. The cross-spread survey data are also used to verify the fracture direction, using polarity reversal from the azimuthal transverse component gathers. The results generally agree with those by 2C rotation analysis, however, the method is not as robust as 2C rotation analysis.

Chapter 9

Conclusions and future work

As an emerging technology, there exist a lot of gaps in 4C seismic acquisition, processing and interpretation. To further the development of this technology, I have examined and modelled the characteristics of 4C seismic data, reviewed the basic theory of converted-wave processing, and developed new kinematic theories for converted-waves propagating in anisotropic, inhomogeneous media. I have also applied these new methods to field 4C data from the North Sea. This Chapter summarizes the main results and also gives recommendations for further work in this important subject.

9.1 Thesis conclusions

Processing converted waves with asymmetric raypaths is an essential part of 4C seismic data processing (Chapter 2). The conventional converted-wave processing includes CCP binning, velocity analysis, DMO and post-stack migration. Asymptotic binning combined with hyperbolic velocity analysis can be used to generate an initial stack section, which is good for the estimation of processing parameters. To overcome CCP binning periodicity, it is necessary to increase the binning width.

However, asymptotic binning can introduce lateral smearing for the shallow events. Although true CCP binning can reduce the lateral smearing, it cannot image the dipping events properly, which makes it less desirable in the presence of structure. To overcome this, DMO binning is recommended.

From the study of 4C data characteristics (Chapter 3), I have found: 1) the water-column reverberations in the vertical geophone are much weaker than those in the hydrophone, because of the different sensor responses to the source- and receiver-side multiples; 2) the presence of a low shear-wave velocity gradient in the seabed prohibits P-to-S conversion, and this implies that most shear-waves recorded in 4C data are converted at deep reflectors; 3) due to the sensor design used, there was a shear-wave energy leakage from the inline horizontal geophone to the vertical geophone, resulting in geophone coupling problem. I have also studied the problem of sensor orientation and presented geophone orientation algorithms for both gimballed and non-gimballed geophone systems (Chapter 4).

Velocity analysis is an important step in seismic data processing (Chapter 5). For converted waves, the hyperbolic velocity analysis can introduce 3-5% errors to the velocity field even for noise-free synthetic data due to the asymmetric raypath and the non-hyperbolic moveout behaviours. Hyperbolic velocity analysis for converted waves is also particularly sensitive to the offset range used in the analysis. These errors in velocity analysis will be amplified into velocity ratio estimation for CCP binning and moveout correction purposes. To overcome this problem, a non-hyperbolic moveout equation with a background γ can be used to perform velocity analysis over the intermediate offset ranges up to offset-depth ratio of 1.5. This reduces the error to less than 1% in velocity analysis. I have also proposed a double-square-root (DSR) approximation for performing high-accuracy converted-wave moveout correction. Re-derivation of the converted wave moveout equations based on a three-term Taylor expansion (Thomsen, 1999) shows that there is an

error in the A_4 coefficient of the traveltime equation in Thomsen's paper. With the correct coefficient, the three term Taylor series expansion also performs reasonably well.

The presence of polar anisotropy (transverse isotropy with a vertical axis of symmetry, TIV) severely affects converted-wave data processing (Chapter 6). The effective velocity ratio γ_{eff} alone is not sufficient to compensate for the anisotropic effects on both the conversion point and the moveout. New parameters ζ and χ (or their corresponding effective parameters ζ_{eff} and χ_{eff}) are introduced to describe converted-wave propagation in layered TIV media, and new equations have been derived for both the conversion point and the moveout using these new parameters. The new equations are accurate for intermediate-to-far offset with an offset-to-depth ratio of 2.0. The equations for the conversion-point offset are derived by the Taylor series expansion method, and those for converted-wave moveout are derived by both the Taylor-expansion method and by a double-square-root (DSR) approach.

From the Taylor-expansion, the converted-wave moveout is controlled by four parameters. These are the vertical and effective velocity ratios γ_0 and γ_{eff}, the converted-wave stacking velocity V_{c2} and the converted-wave anisotropic coefficient χ_{eff}. However, from the DSR equation, the moveout is controlled by five parameters. These are vertical velocity ratio γ_0, P- and S-wave stacking velocities V_{p2} and V_{s2}, and P- and S-wave anisotropic coefficients η_{eff} and ζ_{eff}. Among the five parameters, only four of them are independent. For a single TIV layer, the relationships are: $\zeta = \gamma_{eff}^2 \eta$, and $\chi = \eta(\gamma_0 - 1)\gamma_{eff}$.

Therefore, the Taylor series expansion can be used for parameter estimation and moveout correction, and the DSR equation can be used for anisotropic pre-stack time migration. Based on the Taylor-series expansion, a double-scanning procedure has been proposed to determine the converted-wave stacking velocity and the anisotropic parameters. Anisotropy moveout correction can greatly improve the flattening of

the converted-wave events. From these new developments, it is also observed that TIV anisotropy has a stronger influence on the conversion point offset than on the moveout.

Estimating azimuthal anisotropy using shear-wave splitting analysis plays an important role in seismic detection of natural fractures (Chapter 7). To help the study of shear-wave splitting using 4C seismic data, I have developed a 2C vector rotation algorithm for extracting the polarizations of the fast split shear-wave and the time delays between the two split shear-waves. Although the 2C rotation analysis requires normal incident shear wave data, the synthetic analysis shows that it is generally acceptable to use post-stack data instead. The presence of TIV anisotropy can degrade the accuracy of 2C rotation analysis, and a limited offset range should be used. In a 3D dataset, polarity reversals in the transverse component can be used for the identification of the fracture direction, and it is independent of TIV anisotropy.

To verify the methodology, I have carried out a detailed processing of the Guillemot 4C data taking into account both polar and azimuthal anisotropy. From the velocity analysis, the data show the presence of strong TIV anisotropy. A double-scanning semblance analysis has been applied to the data to evaluate the strength of TIV anisotropy. An anisotropic moveout correction can flatten the data from near to far offset. The processing results of the radial and transverse components data from the Guillemot data have shown that the Guillemot field is azimuthally anisotropic to some extent. The time delays between the two split shear waves represent 0.6% - 1% shear wave anisotropy.

9.2 Future work

In Chapter 3, I have found that converted-wave from the horizontal components also exhibits some multiples, mostly related to the source-side water-column reverberations. The conventional dual-sensor summation technique cannot be applied to remove this type of multiple. This is an area which has the potential to enhance converted-wave imaging.

The layering and TIV anisotropy have a significant influence both on the conversion point and the moveout of converted waves. This makes it undesirable to apply the conventional DMO algorithms developed for homogeneous and isotropic media. More work is needed to develop a converted-wave DMO algorithm for layered anisotropic media.

An alternative for DMO in TIV media is to perform a prestack time migration. The DSR equation for TIV media developed in Chapter 6 can serve this purpose. However, further work is necessary to establish an effective workflow for parameter estimation and data processing, particularly for 3D 4C OBC data.

Currently, converted-wave imaging serves only as a compliment to P-wave imaging, such as in areas with gas cloud or weaker impedence contrast, where P-waves fail to produce a coherent image. The full potential of converted-wave has not been realized. I believe that converted-waves will play a big role in prestack depth imaging. Without additional information, such as well-logs, P-wave alone cannot estimate the vertical velocity, which is essential for time-to-depth conversion. Joint P-wave and converted-wave analysis can provide complete parameters for anisotropic prestack depth imaging. Furthermore, converted-waves can contribute significantly to fluid and lithology prediction, and this area is certainly worthy of further studies.

About anisotropy parameter estimation, I have found that TIV has a more significant influence on conversion point than converted-wave moveout. Hence, it is

very likely that estimation of anisotropy from the conversion-point offset is more robust than from the moveout. Unlike P-waves, which has a symmetric raypath, the asymmetric raypath of converted-wave may be give us a way to estimate the conversion-point offset from negative and positive offset sections. Once the conversion point offsets are obtained, an inversion procedure can be carried out to estimate the anisotropic parameters.

Appendix A

Polarization analysis

As shown in Figure A.1, the direction of a polarization vector $[a(t),\ b(t)]^T$ is often

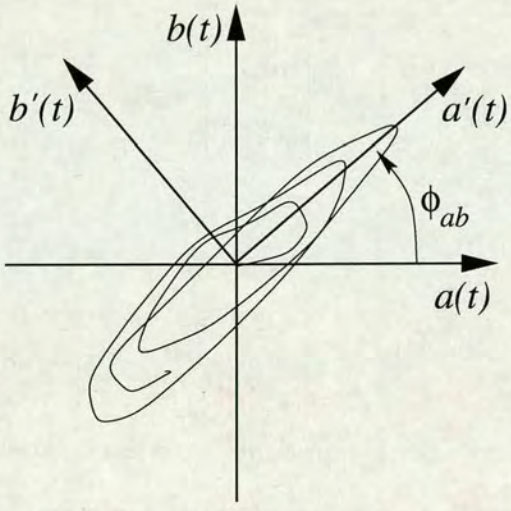

Figure A.1: Concepts of polarization analysis: polarization vector $[a(t),\ b(t)]^T$, its major polarization axes $[a'(t),\ b'(t)]^T$, and polarization angle ϕ_{ab}.

defined as the direction of the major axis of the polarization trajectory. Supposing ϕ_{ab} be the angle between the major axis $a'(t)$ and $a(t)$ (Figure A.1), then ϕ_{ab} is often referred to as the polarization direction, or polarization angle. ϕ_{ab} can be determined from the covariance matrix of vector $[a(t),\ b(t)]^T$ using eigen analysis. The covariance matrix of vector $[a(t),\ b(t)]^T$can be defined as:

$$\begin{bmatrix} \sum_t a^2(t) & \sum_t b(t)a(t) \\ \sum_t a(t)b(t) & \sum_t b^2(t) \end{bmatrix} \tag{A-1}$$

and ϕ_{ab} satisfies:

$$\phi_{ab} = \frac{1}{2} \arctan \left(\frac{2 \sum_t a(t)b(t)}{\sum_t a^2(t) - \sum_t b^2(t)} \right). \tag{A-2}$$

ϕ_{ab} is the Jacobi rotation angle which minimizes the off-diagonal elements in the covariance matrix (A-1). Jacobi rotation is equivalent to rotating the axes $a(t)$ and $b(t)$ into the major and minor polarization axes $a'(t)$ and $b'(t)$ (Figure A.1a). If we rotate a geophone vector, as shown in Figure A.1a, the un-rotated and rotated polarization vectors are then given by:

$$\begin{bmatrix} a(t) \\ b(t) \end{bmatrix} = \mathbf{R}^T(\phi_{ab}) \begin{bmatrix} a'(t) \\ b'(t) \end{bmatrix} = \mathbf{R}(-\phi_{ab}) \begin{bmatrix} a'(t) \\ b'(t) \end{bmatrix} \tag{A-3}$$

where

$$\mathbf{R}(\alpha) = \begin{bmatrix} \cos\alpha & \sin\alpha \\ -\sin\alpha & \cos\alpha \end{bmatrix} \tag{A-4}$$

is a 2-D rotation matrix, and T represents matrix transposition. Here in defining the rotation matrix, we follow the convention that in a right-hand coordinate system and looking towards the origin, a counter-clockwise rotation is a positive rotation. As shown in Figure A.1a, the rotation in equation (A-3) maximizes one of the coordinates $a'(t)$ and minimizes the other $b'(t)$.

Appendix B

P-P reflection moveout for TIV

The three-term Taylor series expansion of P-P reflection moveout for a single-layered TIV is derived by Tsvankin and Thomsen (1994):

$$t_p^2 = t_{p0}^2 + \frac{x^2}{V_{p2}^2} + \frac{A_4 x^4}{1 + A_5 x^2} \tag{B-1}$$

where

$$A_4 = \frac{-2(\varepsilon - \delta)}{t_{p0}^2 V_{p0}^4} \frac{1 + \frac{2\delta}{1 - V_{s0}^2/V_{p0}^2}}{(1 + 2\delta)^4} \tag{B-2}$$

and

$$A_5 = \frac{A_4}{\frac{1}{V_{ph}^2} - \frac{1}{V_{p2}^2}}, \tag{B-3}$$

where V_{ph} is P-wave horizontal velocity in TIV medium.

Note that coefficient A_4 shows that the moveout of P-wave is depended all four parameters of TIV medium. Tsvankin (1995) found that the influence of vertical shear-wave velocity V_{s0} is negligible in computation of P-wave moveout. Based on this fact, Alkhalifah and Tsvankin (1995) derived a simplified P-wave moveout equation by ignoring V_{s0}:

$$t_p^2 = t_{p0}^2 + \frac{x^2}{V_{p2}^2} - \frac{2\eta x^4}{V_{p2}^2\left(t_{p0}^2 V_{p2}^2 + (1+2\eta)\,x^2\right)} \tag{B-4}$$

where t_{p0} is two-way P-wave vertical traveltime and η is P-wave anisotropy moveout parameter defined as

$$\eta = \frac{\varepsilon - \delta}{1 + 2\delta}. \tag{B-5}$$

For multi-layered TIV media, equation (B-4) continues to hold, with η being replaced by an effective parameter (Alkhalifah, 1997)

$$\eta_{eff} = \frac{1}{8 t_{p0} V_{p2}^4}\left(\sum_{i=1}^{n} v_{p2i}^4\,(1+8\eta_i)\,\Delta t_{p0i} - t_{p0} V_{p2}^4\right) \tag{B-6}$$

Appendix C

SV- reflection moveout for TIV

The three-term Taylor series expansion of *SV*-*SV* reflection moveout for a single-layered TIV is also derived by Tsvankin and Thomsen (1994):

$$t_s^2 = t_{s0}^2 + \frac{x^2}{V_{s2}^2} + \frac{B_4 x^4}{1 + B_5 x^2} \tag{C-1}$$

where

$$B_4 = \frac{2\sigma}{t_{s0}^2 V_{s0}^4} \frac{1 + \frac{2\delta}{1 - V_{s0}^2/V_{p0}^2}}{(1+2\sigma)^4} = \frac{2\sigma}{t_{s0}^2 V_{s2}^4} \frac{1 + \frac{2\delta}{1 - V_{s0}^2/V_{p0}^2}}{(1+2\sigma)^2} \tag{C-2}$$

and

$$B_5 = \frac{B_4}{\frac{1}{V_{sh}^2} - \frac{1}{V_{s2}^2}}, \tag{C-3}$$

where V_{sh} is *SV*-wave horizontal velocity in TIV medium.

Note that quartic coefficient B_4 shows that the moveout of *SV*-wave is also depended all four parameters of TIV medium. In order to simplify equation (C-2), we introduce a new parameter

$$\zeta = \frac{\sigma}{(1+2\sigma)^2} \left(1 + \frac{2\delta}{1 - V_{s0}^2/V_{p0}^2} \right). \tag{C-4}$$

Thus

$$B_4 = \frac{2\zeta}{t_{s0}^2 V_{s2}^4}. \tag{C-5}$$

However, the defination of new introdued parameter ζ is too complicated. We find the influence of V_{s0}/V_{p0} in SV-wave moveout at middle-to-far offset is negligible, as Alkhalifah and Tsvankin (1995) found for P-wave. Hence further simplification can be made as

$$\zeta = \frac{\sigma\left(1+2\delta\right)}{\left(1+2\sigma\right)^2}. \tag{C-6}$$

Substituting the following equations

$$\sigma = \gamma_0^2\left(\varepsilon - \delta\right),$$

$$\frac{\gamma_{eff}}{\gamma_0} = \frac{1+2\delta}{1+2\sigma}$$

for converted-wave, and

$$\eta = \frac{\varepsilon - \delta}{1+2\delta}$$

for P-wave, the defination of ζ becomes a very simple form as

$$\zeta = \gamma_{eff}^2 \eta. \tag{C-7}$$

The accuracy of ζ simplification is tested by synthetic modelling (Figure C.1). Two TIV materials are used: Taylor sandstone and Dog Creek shale. The dotted lines are using ζ defined from equation (C-4), while the dashed lines are using ζ defined from equation (C-7). The difference between two curves are very small. Therefore, throughout this thesis, the olny simplied form of ζ is used.

Unlike P-wave, the moveout approximation for SV-wave is less accurate. It is only accruate within offset-to-depth ratio of 1.5, as obsevered by Tsvankin and

Thomsen (1994).

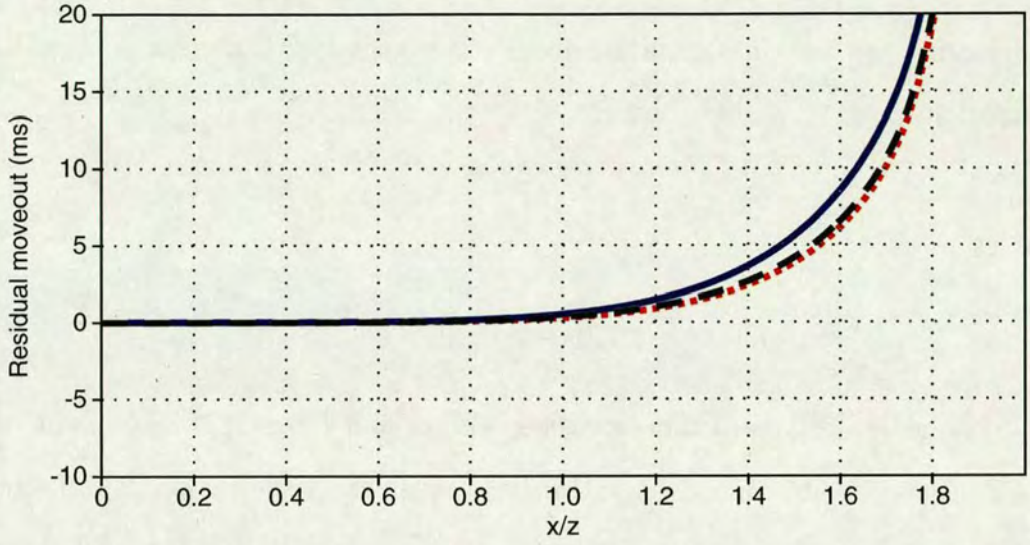

(a)

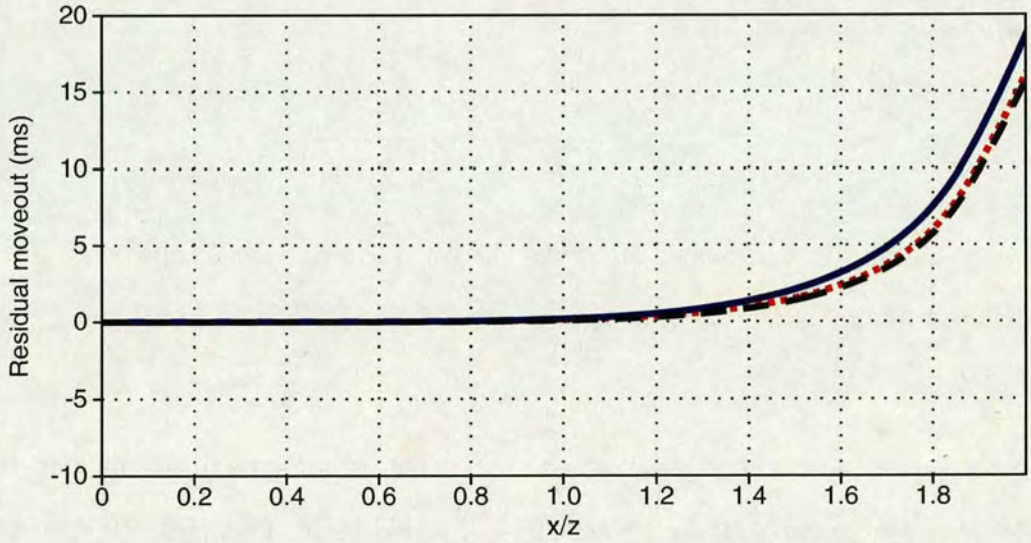

(b)

Figure C.1: Accuracy of SV-wave moveout approximation. Materials used: (a) Taylor sandstone ($V_{p0} = 3368$m/s, $V_{s0} = 1829$m/s, $\varepsilon = 0.110$ and $\delta = -0.035$; (b) Dog Creek shale ($V_{p0} = 1875$m/s, $V_{s0} = 826$m/s, $\varepsilon = 0.225$ and $\delta = 0.100$. The dotted lines use equations (C-3) and (C-4), the dahsed lines use equations (C-3) and (C-7), and the solid lines use equations (C-8) and (C-7).

Now we discuss parameter B_5. It requires an additional parameter V_{sh}, SV-wave

horizontal velocity, which equals to vertical velocity in a single-layered TIV medium. For surface surveys, vertical velocity is often unknown. In order to eliminate this requirement, further approximation for B_5 is neccesary. Under weak anisotropy assumption ($\sigma \ll 1$), we have

$$\zeta \approx \sigma,$$

and

$$B_5 \approx \frac{1}{t_{s0}^2 V_{s2}^2}. \tag{C-8}$$

For published materials (Thomsen, 1986; Vernik and Liu, 1997), the assumption, $\sigma \ll 1$, usually is not a good one. However, considering the reason of introducing coefficient B_5 in equation (C-1) is to make t_s^2 increase with offset as x^2 instead of x^2 (Tsvankin and Thomsen, 1994), relatively large error in B_5 is acceptable. Thus equation (C-1) becomes

$$t_s^2 = t_{s0}^2 + \frac{x^2}{V_{s2}^2} + \frac{2\zeta x^4}{V_{s2}^2 \left(t_{s0}^2 V_{s2}^2 + x^2\right)}. \tag{C-9}$$

The simplication by coefficient B_5 make the SV-wave moveout approximation less accurate although satisfactory, as shown in solid lines in Figure C.1.

Now we consider the multi-layered case. The exact quartic coefficient B_4 of Taylor series expansion (Hake *et al.*, 1984; Tsvankin and Thomsen, 1994) is given by

$$\begin{aligned} B_4 &= \frac{t_{s0}^2 V_{s2}^4 - t_{s0} \sum_{i=1}^{n} \Delta t_{s0i} v_{s2i}^4 \left(1 - \frac{8\sigma_i}{(1+2\sigma_i)^2}\left(1 + \frac{2\delta_i}{1 - v_{s0i}^2/v_{p0i}^2}\right)\right)}{4 t_{s0}^4 V_{s2}^8} \\ &= \frac{t_{s0}^2 V_{s2}^4 - t_{s0} \sum_{i=1}^{n} \Delta t_{s0i} v_{s2i}^4 \left(1 - 8\zeta_i\right)}{4 t_{s0}^4 V_{s2}^8}. \end{aligned} \tag{C-10}$$

Similar to the effective P-wave anisotropic paramter η_{eff} for multi-layered media,

we introcuce a new effective paramter ζ_{eff} for SV-wave in layered media

$$B_4 = \frac{2\zeta_{eff}}{t_{s0}^2 V_{s2}^4} \tag{C-11}$$

to make the B_4 in same form as that in equation (C-5). Substituting equation (C-11) into equation (C-10), with straight-forward manipulation, results in

$$\zeta_{eff} = \frac{1}{8t_{s0}V_{s2}^4}\left(t_{s0}V_{s2}^4 - \sum_{i=1}^{n}\Delta t_{s0i}v_{s2i}^4\left(1-8\zeta_i\right)\right). \tag{C-12}$$

Therefore SV-wave moveout in multi-layered media can be approximated an equation which takes same form as that for single-layered medium:

$$t_s^2 = t_{s0}^2 + \frac{x^2}{V_{s2}^2} + \frac{2\zeta_{eff}x^4}{V_{s2}^2\left(t_{s0}^2V_{s2}^2 + x^2\right)} \tag{C-13}$$

Appendix D

Conversion point offset in layered anisotropic media

D.1 General derivation of convertion point in layered anisotopic media

Here, I generalize the results of Thomsen (1999) and derive Taylor series coefficients for conversion point offset in layered transverse isotropic media.

Consider a horizontally-layered medium, as shown in Figure D.1, with each layer homogeneous and transverse isotropic. v_{pi}, w_{pi} are interval P-wave phase and group velocities, v_{si} and w_{si} are their S-wave counterparts, and Δz_i is layer thickness of the ith layer. θ_{pi} and θ_{si} are the angles between group or ray velocities and vertical axis. x_p is the conversion point offset from source, and x_s is the corresponding offset to the receiver of the shear wave path.

The total offset of the ray path x is

$$x = x_p + x_s \tag{D-1}$$

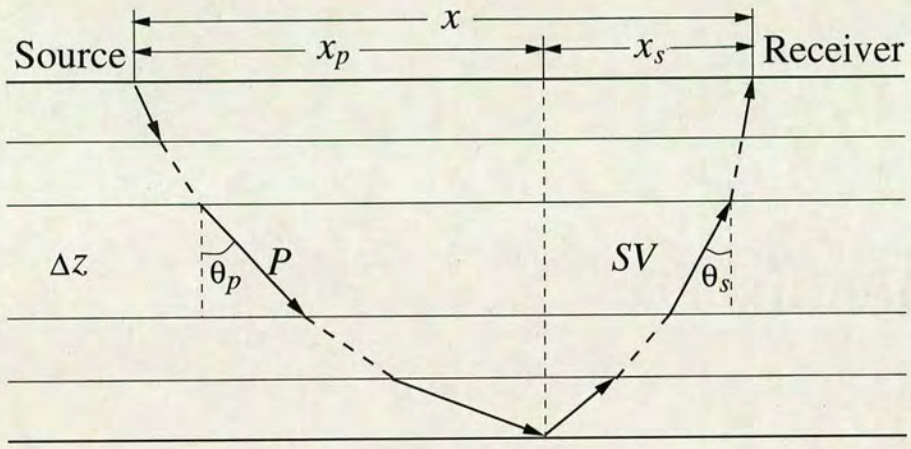

Figure D.1: Geometry of a ray of converted wave in horizontal layered transverse isotropic media.

with

$$x_p = \sum_{i=1}^{n} \Delta x_{pi} = p \sum_{i=1}^{n} U_{pi} \Delta t_{pi}, \tag{D-2}$$

$$x_s = \sum_{i=1}^{n} \Delta x_{si} = p \sum_{i=1}^{n} U_{si} \Delta t_{si} \tag{D-3}$$

and

$$U_i = \frac{w_{1i}}{p}. \tag{D-4}$$

Here, p is the horizontal component of slowness vector (the ray parameter, dt/dx) for the ray emerging at offset x, Δt_i is the oblique one-way traveltime in the ith layer. w_1 is the horizontal component of the group velocity vector. The subscripts $_p$ and $_s$ indicates the terms related with P- or S- wave paths.

Because x_p is an odd function of x, Taylor series expansion of the conversion point offset x_p at total offset x can be written as

$$x_p = \lim_{x \to 0} \sum_{k=0}^{\infty} c_{2k} x^{2k+1} = \lim_{p \to 0} \sum_{k=0}^{\infty} c_{2k} x^{2k+1} \tag{D-5}$$

with

$$c_{2k} = \frac{1}{(2k+1)!} \frac{d^{2k+1} x_p}{dx^{2k+1}}.$$

When $k = 0$,

$$c_0 = \lim_{p\to 0} \frac{dx_p}{dx} = \lim_{p\to 0} \frac{dx_p}{dp}\frac{dp}{dx}. \tag{D-6}$$

From equations (D-1)-(D-3),

$$\frac{dx_p}{dp}\frac{dp}{dx} = \frac{\sum_{i=1}^{n} U_{pi}\Delta t_{pi} + p\frac{d}{dp}\left(\sum_{i=1}^{n} U_{pi}\Delta t_{pi}\right)}{\sum_{i=1}^{n} U_{pi}\Delta t_{pi} + p\frac{d}{dp}\left(\sum_{i=1}^{n} U_{pi}\Delta t_{pi}\right) + \sum_{i=1}^{n} U_{si}\Delta t_{si} + p\frac{d}{dp}\left(\sum_{i=1}^{n} U_{si}\Delta t_{si}\right)}. \tag{D-7}$$

In equation (D-7),

$$p\frac{d}{dp}\left(\sum_{i=1}^{n} U_{pi}\Delta t_{pi}\right) = p\sum_{i=1}^{n}\frac{dU_{pi}}{dp}\Delta t_{pi} + p\sum_{i=1}^{n} U_{pi}\frac{d\Delta t_{pi}}{dp}. \tag{D-8}$$

Because

$$\Delta x_{pi} = pU_{pi}\Delta t_{pi}$$

and

$$\frac{d\Delta t_{pi}}{d\Delta x_{pi}} = p,$$

we have

$$\frac{d\Delta t_{pi}}{dp} = \frac{d\Delta t_{pi}}{d\Delta x_{pi}}\frac{d\Delta x_{pi}}{dp} = pU_{pi}\Delta t_{pi}. \tag{D-9}$$

Substituting equation (D-9) into equation (D-8), we obtain

$$p\frac{d}{dp}\left(\sum_{i=1}^{n} U_{pi}\Delta t_{pi}\right) = p\sum_{i=1}^{n}\frac{dU_{pi}}{dp}\Delta t_{pi} + p^2\sum_{i=1}^{n} U_{pi}^2\Delta t_{pi}. \tag{D-10}$$

In a same manner , we have

$$p\frac{d}{dp}\left(\sum_{i=1}^{n} U_{si}\Delta t_{si}\right) = p\sum_{i=1}^{n}\frac{dU_{si}}{dp}\Delta t_{si} + p^2\sum_{i=1}^{n} U_{si}^2\Delta t_{si}. \tag{D-11}$$

In the context of TIV medium, Tsvankin and Thomsen (1994) have given that

$$\lim_{p\to 0} U_{pi} = v_{p2i}^2 = v_{p0i}^2 \left(1 + 2\delta_i\right), \tag{D-12}$$

$$\lim_{p\to 0} U_{si} = v_{s2i}^2 = v_{s2i}^2 \left(1 + 2\sigma_i\right), \tag{D-13}$$

$$\lim_{p\to 0} \frac{1}{p}\frac{dU_{pi}}{dp} = \lim_{p\to 0} \frac{d^2U_{pi}}{dp^2} = 8v_{p0i}^4 \left(\varepsilon_i - \delta_i\right)\left(1 + \frac{2\delta_i}{1 - \frac{v_{s0i}^2}{v_{p0i}^2}}\right), \tag{D-14}$$

and

$$\lim_{p\to 0} \frac{1}{p}\frac{dU_{si}}{dp} = \lim_{p\to 0} \frac{d^2U_{si}}{dp^2} = -8v_{s0i}^4 \sigma_i \left(1 + \frac{2\delta_i}{1 - \frac{v_{s0i}^2}{v_{p0i}^2}}\right). \tag{D-15}$$

Here, V_0 is the vertical velocity and V_n is the short-spread moveout velocity. ε and δ are dimensionless parameters introduced by Thomsen (1986). They are defined through elastic moduli as

$$\varepsilon = \frac{C_{11} - C_{33}}{2C_{33}} \tag{D-16}$$

and

$$\delta = \frac{\left(C_{13} + C_{44}\right)^2 - \left(C_{33} - C_{44}\right)^2}{2C_{33}\left(C_{33} - C_{44}\right)}. \tag{D-17}$$

Substituting equations (D-12)-(D-15) into equation (D-6), and taking the limit of ray parameter p for zero, we get

$$\begin{aligned} c_0 &= \lim_{p\to 0} \frac{dx_p}{dp}\frac{dp}{dx} = \frac{\sum_{i=1}^n U_{pi}\Delta t_{pi}}{\sum_{i=1}^n U_{pi}\Delta t_{pi} + \sum_{i=1}^n U_{si}\Delta t_{si}} \\ &= \frac{\sum_{i=1}^n v_{p2i}^2\Delta t_{pi}}{\sum_{i=1}^n v_{p2i}^2\Delta t_{pi} + \sum_{i=1}^n v_{s2i}^2\Delta t_{si}} \\ &= \frac{V_{p2}^2 t_{p0}}{V_{p2}^2 t_{p0} + V_{s2}^2 t_{s0}} \\ &= \frac{\gamma_2^2}{\gamma_2^2 + \gamma_0} = \frac{\gamma_{eff}}{1 + \gamma_{eff}}. \end{aligned} \tag{D-18}$$

where t_{p0} and t_{s0} are one-way P- and S- wave vertical travel times. V_{p2}, V_{s2} are the

RMS moveout velocity of P- and S-waves defined by

$$V_{p2} = \sqrt{\frac{\sum_{i=1}^{n} v_{p2i}^2 \Delta t_{p0i}}{\sum_{i=1}^{n} \Delta t_{p0i}}} \quad \text{and} \quad V_{s2} = \sqrt{\frac{\sum_{i=1}^{n} v_{s2i}^2 \Delta t_{s0}}{\sum_{i=1}^{n} \Delta t_{s0i}}}$$

and γ_2 is their ratio V_{p2}/V_{s2}. γ_0 is average velocity ratio, and γ_{eff} is the effective velocity ratio defined by (Thomsen) as

$$\gamma_{eff} = \gamma_2^2/\gamma_0.$$

Equation (D-18) agrees with the results given by Thomsen (1999).

When $k = 1$,

$$c_2 = \frac{1}{6} \lim_{p \to 0} \frac{d^3 x_p}{dx^3}.$$

By differentiating equation (D-7) with regard to p, after some tedious algebraic manipulation, one can get

$$\begin{aligned} \frac{d^3 x_p}{dx^3} &= \frac{d}{dp}\left(\frac{d}{dp}\left(\frac{dx_p}{dp}\frac{dp}{dx}\right)\frac{dp}{dx}\right)\frac{dp}{dx} \\ &= \frac{(e_p + pf_p + e_s + pf_s)\left(3\left(e_s g_p - e_p g_s\right) + p\frac{d}{dp}\left(e_s g_p - e_p g_s\right) + \frac{d}{dp}\left(p^2\left(f_s g_p - f_p g_s\right)\right)\right)}{\left(e_p + pf_p + e_s + pf_s\right)^5} \\ &\quad - \frac{3\left(2f_p + pg_p + 2f_s + pg_s\right)\left(2\left(e_s f_p - e_p f_s\right) + p\left(e_s g_p - e_p g_s\right) + p^2\left(f_s g_p - f_p g_s\right)\right)}{\left(e_p + pf_p + e_s + pf_s\right)^5} \end{aligned} \tag{D-19}$$

where

$$e = \sum_{i=0}^{n} U_i \Delta t_i,$$

$$f = \frac{de}{dp} = \frac{d}{dp}\sum_{i=0}^{n} U_i \Delta t_i = \sum_{i=0}^{n} \frac{dU_i}{dp}\Delta t_i + p\sum_{i=0}^{n} U_i^2 \Delta t_i$$

and

$$\begin{aligned} g &= \frac{df}{dp} = \frac{d^2}{dp^2}\sum_{i=0}^{n} U_i \Delta t_i \\ &= \sum_{i=0}^{n} U_i^2 \Delta t_i + \sum_{i=0}^{n} \frac{d^2 U_i}{dp^2}\Delta t_i + 3p\sum U_i \frac{dU_i}{dp}\Delta t_i + p^2 \sum U_i^3 \Delta t_i. \end{aligned}$$

From equations (D-12) - (D-15), by taking limit of p to zero, one can get

$$\lim_{p\to 0} e_p = \sum_{i=0}^{n} v_{p2i}^2 \Delta t_{p0i} = V_{p2}^2 t_{p0}, \tag{D-20}$$

$$\lim_{p\to 0} e_s = \sum_{i=0}^{n} v_{s2i}^2 \Delta t_{s0i} = V_{s2}^2 t_{s0}, \tag{D-21}$$

$$\lim_{p\to 0} f_p = \lim_{p\to 0} f_s = 0, \tag{D-22}$$

$$\begin{aligned} \lim_{p\to 0} g_p &= \lim_{p\to 0}\sum_{i=0}^{n} U_{pi}^2 \Delta t_{pi} + \lim_{p\to 0}\sum_{i=0}^{n} \frac{d^2 U_{pi}}{dp^2}\Delta t_{pi} \\ &= \sum_{i=0}^{n} v_{p2i}^4 \Delta t_{p0i} + \sum_{i=0}^{n} 8 v_{p0i}^4 (\varepsilon_i - \delta_i)\left(1 + \frac{2\delta_i}{1 - \frac{v_{s0i}^2}{v_{p0i}^2}}\right)\Delta t_{p0i} \end{aligned} \tag{D-23}$$

and

$$\begin{aligned} \lim_{p\to 0} g_s &= \lim_{p\to 0}\sum_{i=0}^{n} U_{si}^2 \Delta t_{si} + \lim_{p\to 0}\sum_{i=0}^{n} \frac{d^2 U_{si}}{dp^2}\Delta t_{si} \\ &= \sum_{i=0}^{n} v_{s2i}^4 \Delta t_{s0i} - \sum_{i=0}^{n} 8 v_{s0i}^4 \sigma_i \left(1 + \frac{2\delta_i}{1 - \frac{v_{s0i}^2}{v_{p0i}^2}}\right)\Delta t_{s0i}. \end{aligned} \tag{D-24}$$

Substituting equations (D-20) - (D-24) into equation (D-19), the c_2 term of Taylor series expansion of conversion point in layered TIV medium has the form

$$c_2 = \frac{1}{6}\lim_{p\to 0}\frac{d^3 x_p}{dx^3} = \lim_{p\to 0}\frac{(e_s g_p - e_p g_s)}{2\left(e_p + e_s\right)^4}$$

$$= \frac{1}{2}\frac{V_{s2}^2 t_{s0}\sum_{i=0}^{n}\left(\Delta t_{p0i} v_{p0i}^4\left((1+2\delta_i)^2+8(\varepsilon_i-\delta_i)\left(1+\frac{2\delta_i}{1-\frac{v_{s0i}^2}{v_{p0i}^2}}\right)\right)\right)}{\left(V_{pn2}^2 t_{p0}+V_{sn2}^2 t_{s0}\right)^4}$$
$$-\frac{1}{2}\frac{-V_{p2}^2 t_{p0}\sum_{i=0}^{n}\left(\Delta t_{s0i} V_{s0i}^4\left((1+2\sigma_i)^2-8\sigma_i\left(1+\frac{2\delta_i}{1-\frac{v_{s0i}^2}{v_{p0i}^2}}\right)\right)\right)}{\left(V_{p2}^2 t_{p0}+V_{s2}^2 t_{s0}\right)^4}. \quad \text{(D-25)}$$

Although equation (D-25) is the exact expression for coefficient c_2, it is not convenient for calculation of conversion point. Its simpler approximation can be derived by using effective parameters η_{eff} and ζ_{eff} defined by equations (B-6) and (C-12), respectively.

Subsitituting equations (B-5), (B-6), (C-7), and (C-12) into D-25, with some manipulation, gives

$$c_2 = \frac{\gamma_{eff}(1+\gamma_0)}{2t_{c0}^2 V_{c2}^2 \gamma_0 (1+\gamma_{eff})^3}\left(\gamma_0\gamma_{eff}-1+8\left(\eta_{eff}\gamma_0\gamma_{eff}+\zeta_{eff}\right)\right). \quad \text{(D-26)}$$

D.2 Special cases

D.2.1 Single-layered isotropic case

For single-layered isotropic medium, let $\gamma = \gamma_{eff}$, and anisotropic paramters zero, one can obtain

$$c_0 = \frac{\gamma}{1+\gamma} \quad \text{(D-27)}$$

and

$$c_2 = \frac{\gamma-1}{2V_c^2 t_{c0}^2 (\gamma+1)}.$$

This agrees with the results of Thomsen (1999).

D.2.2 Multi-layered isotropic case

For multi-layered isotropic media, the parameters η_{eff} and ζ_{eff} become

$$\eta_{eff} = \frac{1}{8t_{p0}V_{p2}^4}\left(\sum_{i=0}^{n} v_{pi}^4 \Delta t_{p0i} - t_{p0}V_{p2}^4\right) \tag{D-28}$$

and

$$\zeta_{eff} = \frac{-1}{8t_{s0}V_{s2}^4}\left(\sum_{i=0}^{n} v_{si}^4 \Delta t_{s0i} - t_{s0}V_{s2}^4\right) \tag{D-29}$$

which control the residual layering effects on P- ans S-waves, respectively. Ignoring these residual effects leads to,

$$c_2 = \frac{\gamma_{eff}}{2\gamma_0 V_{c2}^2 t_{c0}^2}\frac{(\gamma_{eff}\gamma_0 - 1)(1+\gamma_0)}{(1+\gamma_{eff})^3}, \tag{D-30}$$

which has the same form as the expressions given by Thomsen (1999).

D.2.3 Single-layered anisotropic case

In single-layered TIV medium, by letting $\eta_{eff} = \eta$ and $\zeta_{eff} = \zeta = \gamma_{eff}^2\eta$, c_2 term becomes

$$c_2 = \frac{\gamma_{eff}(1+\gamma_0)}{2t_{c0}^2 V_{c2}^2 \gamma_0 (1+\gamma_{eff})^3}\left(\gamma_0\gamma_{eff} - 1 + 8(\gamma_0 + \gamma_{eff})\gamma_{eff}\eta\right). \tag{D-31}$$

Appendix E

P-SV reflection moveout for TIV

E.1 Taylor series expansion

First, we start from the three-term Taylor series expansion approximation. The three-term Taylor series expansion of *P-SV* reflection moveout for a single-layered TIV is derived by Tsvankin and Thomsen (1994):

$$t_c^2 = t_{c0}^2 + \frac{x^2}{V_{c2}^2} + \frac{A_4 x^4}{1 + A_5 x^2} \tag{E-1}$$

where

$$A_4 = \frac{t_{c0} V_{c2}^4 - \left(\sum_{i=1}^{n} \left(H_{pi} + v_{p2i}^4\right) \Delta t_{p0i} + \sum_{i=1}^{n} \left(H_{si} + v_{s2i}^4\right) \Delta t_{s0i}\right)}{4 t_{c0}^3 V_{c2}^8}, \tag{E-2}$$

$$H_{pi} = 8 v_{p0i}^4 \left(\varepsilon_i - \delta_i\right) \left(1 + \frac{2\delta_i}{1 - 1/\gamma_{0i}^2}\right) \tag{E-3}$$

and

$$H_{si} = -8 v_{s0i}^4 \sigma_i \left(1 + \frac{2\delta_i}{1 - 1/\gamma_{0i}^2}\right). \tag{E-4}$$

Using the parameters η and ζ defined by equations (B-5) and (C-7), and ignoring the influence of vertical shear-wave velocity, we obtain

$$H_{pi} = 8v_{p2i}^4\eta_i \tag{E-5}$$

and

$$H_{si} = -8v_{s2i}^4\zeta_i \tag{E-6}$$

For multi-layered TIV media, from effective parameters η_{eff} defined by equation (B-6), and ζ_{eff} by equation (C-12) we can obtain

$$\sum_{i=1}^{n}\left(H_{pi}+v_{p2i}^4\right)\Delta t_{p0i} = \left(1+8\eta_{eff}\right)t_{p0}V_{p2}^4. \tag{E-7}$$

and

$$\sum_{i=1}^{n}\left(H_{si}+v_{s2i}^4\right)\Delta t_{s0i} = \left(1-8\zeta_{eff}\right)t_{s0}V_{s2}^4. \tag{E-8}$$

Substituting equations (E-7)-(E-8) into (E-2), gives

$$A_4 = \frac{t_{c0}V_{c2}^4-\left(\left(1+8\eta_{eff}\right)t_{p0}V_{p2}^4+\left(1-8\zeta_{eff}\right)t_{s0}V_{s2}^4\right)}{4t_{c0}^3V_{c2}^8}. \tag{E-9}$$

Replacing V_{p2} and V_{s2} with V_{c2}, and t_{p0} and t_{s0} with t_{c0}, we can obtain

$$A_4 = -\frac{\left(\gamma_0\gamma_{eff}-1\right)^2+8\left(1+\gamma_0\right)\left(\eta_{eff}\gamma_0\gamma_{eff}^2-\zeta_{eff}\right)}{4t_{c0}^2V_{c2}^4\gamma_0\left(1+\gamma_{eff}\right)^2}. \tag{E-10}$$

E.2 Double-square-root approximation

The double-square-root (DSR) approximation can be obtained using *P-P* approximation (see Appendix B) for *P*-leg of converted-wave, and *SV-SV* approximation (see Appendix C) for *S*-leg, while the conversion points can be determined by equa-

tion (D-26) or by other methods such as ray tracing.

References

Alfaraj, M., 1993, Transformation to zero offset for mode-converted waves: Ph.D. thesis, Colorado School of Mines.

Alford, R. M., 1986, Shear data in the presence of azimuthal anisotropy: Dilley, Texas: 56th Annual Internat. Mtg., Soc. Expl. Geophys., Expanded Abstracts, S9.6.

Alkhalifah, T., and Tsvankin, I., 1995, Velocity analysis for transversely isotropic media: Geophysics, **60**, 1550–1566.

Alkhalifah, T., 1997, Velocity analysis using nonhyperbolic moveout in transversely isotropic media: Geophysics, **62**, 1839–1854.

Amundsen, L., and Reitan, A., 1995a, Decomposition of multicomponent sea-floor data into upgoing and downgoing $P-$ and $S-$waves: Geophysics, **60**, 563–572.

—— 1995b, Estimation of sea-floor wave velocities and density from pressure and particle velocity by AVO analysis: Geophysics, **60**, 1575–1578.

Audebert, F., Granger, P. Y., and Herrenschmidt, A., 1999, CCP-Scan technique: True common conversion point sorting and converted wave velocity analysis solved by PP and PS pre-stack depth migration: 69th Annual Internat. Mtg., Soc. Expl. Geophys., Expanded Abstracts, 1186–1189.

Backus, G. E., 1962, Long-wave elastic anisotropy produced by horizontal layering: Journ. Geophys. Res., **67**, 4427–4440.

Bagaini, C., Bale, R., Caprioli, P., and Ronen, S., 1999, Converted wave binning analysis: in search of γ: 69th Annual Internat. Mtg., Soc. Expl. Geophys., Expanded Abstracts, 703–706.

Barr, F. J., and Sanders, J. I., 1989, Attenuation of water-column reverberation using pressure and velocity detectors in a water-bottom cable: 59th Annual Internat. Mtg., Soc. Expl. Geophys., Expanded Abstracts, 653–656.

Barr, F. J., Paffenholz, J., and Rabson, W., 1996, The dual-sensor ocean-bottom cable method: Comparative geophysical attributes, quantitative geophone coupling analysis and other recent advances: 66th Annual Internat. Mtg., Soc. Expl. Geophys., Expanded Abstracts, 21–23.

Barr, F. J., 1997, Dual-sensor OBC technology: The Leading Edge, **16**, 45–51.

Beasley, C., and Lynn, W., 1992, The zero-velocity layer: Migration from irregular surfaces: Geophysics, **57**, 1435–1443.

Beasley, C. J., Chambers, R., Workman, R., and Meister, L., 1996, Repeatability of 3-D ocean bottom cable seismic surveys: 66th Annual Internat. Mtg., Soc. Expl. Geophys., Expanded Abstracts, 1–4.

Berg, E., Svenning, B., and Martin, J., 1994, SUMIC: multicomponent sea-bottom seismic surveying in the North Sea – data interpretation and applications: 64th Annual Internat. Mtg., Soc. Expl. Geophys., Expanded Abstracts, 477–480.

Berteussen, K. A., Fromyr, E., Rokkan, A., Langhammer, J., and Strand, C., 1997, Acquisition of multi-component data by 'Dragged Array': 59th EAGE Conference, Expanded Abstracts, B021.

Bevc, D., 1995, Imaging under rugged topography and complex velocity structure: Ph.D. thesis, Stanford University.

Beydoun, W. B., 1984, Seismic tool - formation coupling in boreholes, *in* Toksöz, M. N., and Stewart, R. R., Eds., Vertical Seismic Profiling - Part B: Advanced Concepts: Geophysical Press, 80–86.

Bohlen, T., Klein, G., Duveneck, E., Milkereit, B., and Franke, D., 1999, Analysis of dispersive seismic waves in submarine permafrost: 61st EAGE Conference, Expanded Abstracts, 6037.

Bole, J., Zinn, N., and Stupel, M., 1999, Seismic detector positioning in a 4D/4C OBC survey using bother acoustics and first breaks: First Break, **17**, 305–309.

Brink, M., Granger, P. Y., Manin, M., and Spitz, S., 1996, Seismic methodologies for a 3 components sea floor geophone experiment on a potential flat spot in the Vøring basin: 58th EAEG Conference, Expanded Abstracts, B020.

Caldwell, J., 1999, Marine multicomponent seismic-acquisition technologies: Proceedings of Offshore Technology Conference, OCT 10981.

Cary, P. W., and Eaton, D. W. S., 1993, A simple method for resolving large converted-wave ($P - SV$) statics: Geophysics, **58**, 429–433.

Crampin, S., and Atkinson, B. K., 1986, Microcracks in the earth's crust: First Break, **3**, 16–20.

Crampin, S., and Lovell, J. H., 1991, A decade of shear-wave splitting in the Earth's crust: what does it mean? what use can we make of it? and what should we do next?: Geophys. J. Int., **107**, 387–407.

Crampin, S., and Radovich, B., 1982, Interpretation of synthetic common-depth-point gathers for a single anisotropic layer: Geophysics, **47**, 323–335.

Crampin, S., Booth, D. C., Evans, R., Peacock, S., and Fletch, J. B., 1986, Estimating the internal structure of reservoirs with shear-wave VSPs: The Leading Edge, **5**, 35–39.

Crampin, S., 1966, Higher modes of seismic surface waves: propagation in Eurasia: Bulletin of the Seismological Society of America, **56**, 1227–1239.

Crampin, S., 1981, A review of wave motion in anisotropic and cracked elastic media: Wave Motion, **3**, 343–391.

Crampin, S., 1985, Evaluation of anisotropy by shear-wave splitting: Geophysics, **50**, 142–152.

Deregowski, S. M., and Rocca, F., 1981, Geometrical optics and wave theory of constant offset sections in layered media: Geophys. Prosp., **29**, 374–406.

DiSiena, J. P., Gaiser, J. E., and Corrigan, D., 1984, Horizontal components and shear wave analysis of three-component VSP data, *in* Toksöz, M. N., and Stewart, R. R., Eds., Vertical Seismic Profiling - Part B: Advanced Concepts: Geophysical Press, 177–188.

Dragoset, B., and Barr, F. J., 1994, Ocean-bottom cable dual-sensor scaling: 64th Annual Internat. Mtg., Soc. Expl. Geophys., Expanded Abstracts, 857–860.

Dunn, D. A., Biat, B. N. M., and Johns, M. V., 1986, Physical properties data, deep sea drilling project: Init. Reports Deep Sea Drill Proj., **93**, 445–464.

Eaton, D. W. S., and Lawton, D. C., 1992, $P - SV$ stacking charts and binning periodicity (short note): Geophysics, **57**, 745–748.

Eaton, D. W. S., Slotboom, R. T., Stewart, R. R., and Lawton, D. C., 1990, Depth-variant converted-wave stacking: 60th Annual Internat. Mtg., Soc. Expl. Geophys., Expanded Abstracts, 1107–1110.

Eaton, D. W. S., Stewart, R. R., and Harrison, M. P., 1991, The fresnel zone for $P - SV$ waves: Geophysics, **56**, 360–364.

Esmersoy, C., 1984, Polarization analysis, rotation and velocity estimation in three component VSP, *in* Toksöz, M. N., and Stewart, R. R., Eds., Vertical Seismic Profiling - Part B: Advanced Concepts: Geophysical Press, 236–255.

Fang, K., 1998, Pseudo-spectral modelling of cracked anisotropic media and rotation of multicomponent shear-wave data: Master's thesis, The University of Calgary.

Frasier, C., and Winterstein, D., 1990, Analysis of conventional and converted mode reflections at Putah Sink, California using three-component data: Geophysics, **55**, 646–659.

Fromm, G., Krey, T., and Wiest, B., 1985, Static and dynamic corrections, seismic shear waves:, *in* Handbook of geophysical exploration Geophysical Press, 15a, 191–225.

Gaiser, J., and Jackson, A., 2000, Accuracy and limitations of $P - S$ wave conversion-point computations: How effective is η_{eff}?: 70th Annual Internat. Mtg., Soc. Expl. Geophys., Expanded Abstracts, 1138–1141.

Gaiser, J. E., Fulp, T. J., Petermann, S., and Karner, G. M., 1984, Three-component vertical seismic profiles: Geophone-sonde stability: 54th Annual Internat. Mtg., Soc. Expl. Geophys., Expanded Abstracts, BHG2.6.

Gaiser, J. E., 1996, Multicomponent V_p/V_s correlation analysis: Geophysics, **61**, 1137–1149.

Gaiser, J. E., 1998, Compensating OBC data for variations in geophone coupling: 68th Annual Internat. Mtg., Soc. Expl. Geophys., Expanded Abstracts, 1429–1432.

Gaiser, J. E., 2000, 3D $PS-$wave data - unraveling shearwave birefringence for fracture detection: 62nd EAGE Conference, Expanded Abstracts, C–15.

Granli, J. R., Arntsen, B., Sollid, A., and Hilde, E., 1999, Imaging through gas-filled sediments using marine shear-wave data: Geophysics, **64**.

Hake, H., Helbig, K., and Mesdag, C. S., 1984, Three-term taylor series for $t^2 - x^2$-curves of $P-$ and $S-$waves over layered transversely isotropic ground: Geophysical Prospecting, **32**, 828–850.

Hale, D., 1984, Dip-moveout by Fourier transform: Geophysics, **49**, 741–757.

Hale, D., 1991, A nonaliased integral method for dip moveout: Geophysics, **56**, 795–805.

Hardage, B. A., 1983, Vertical Seismic Profiling - Part A: Principles: Geophysical Press.

Harrison, M. P., 1992, Processing of $P - SV$ surface-seismic data: anisotropy analysis, dip moveout and migration: Ph.D. thesis, The University of Calgary.

Herrenschmidt, A., Granger, P.-Y., Audebert, F., Gerea, C., Etienne, G., Stopin, A., Alerini, M., Lebegat, S., Lambare, G., Berthet, A. P., Nebieridze, S., and Boelle, J.-L., 2001, Comparison of different strategies for velocity model building and imaging of PP and PS real data: The Leading Edge, 984–995.

Jakubowicz, H., 1990, A simple efficient method of dip-moveout correction: Geophysical Prospecting, **38**, 221–245.

Judson, D. R., Schultz, P. S., and Sherwood, J. W. C., 1978, Equalizing the stacking velocities of dipping events via develish: 48th Annual Internat. Mtg., Soc. Expl. Geophys., Expanded Abstracts.

Kim, N. W., and Seriff, A. J., 1992, Marine $PSSP$ reflections with a bottom velocity transition zone: Geophysics, **57**, 161–170.

Klie, H., 2000, An efficient and accurate conversion point formula for anisotropic CCP stacking: 70th Annual Internat. Mtg., Soc. Expl. Geophys., Expanded Abstracts, 1134–1137.

Krey, T., and Helbig, K., 1956, A theorem concerning anisotropy of stratified media and its significance for reflection seismics: Geophysical Prospecting, **4**, 294–302.

Kristiansen, P., 1998, Analysing the quality of multi-component seabed data: Petex 98, Petroleum Exploration Society, Expanded Abstracts.

Levin, F. K., 1978, The reflection, refraction, and diffraction of waves in media with an elliptical velocity dependence: Geophysics, 528–537.

Levin, F. K., 1992, P-wave anisotropy of pierre shale (short note): Geophysics, **57**, 1346–1347.

Li, X.-Y., and Crampin, S., 1993, Linear-transform techniques for processing shear-wave anisotropy in four-component seismic data: Geophysics, **58**, 240–256.

Li, X.-Y., and Druzhinin, A., 2000, A practical approach to $P-SV$ prestack time migration and velocity analysis for transverse isotropy: 70th Annual Internat. Mtg., Soc. Expl. Geophys., Expanded Abstracts, 1142–1145.

Li, X.-Y., and Yuan, J., 1999a, Anisotropic velocity analysis for 4C seismic data: a case study: 69th Annual Internat. Mtg., Soc. Expl. Geophys., Expanded Abstracts, 732–735.

—— 1999b, Converted-wave moveout and parameter estimation for transverse isotropy: 61st EAGE Conference, Expanded Abstracts, **I**, 4–35.

—— 1999c, Geophone orientation and coupling in three-component sea-floor data: a case study: Geophysical Prospecting, **47**, 995–1013.

Li, X.-Y. and Yuan, J., 2001, Accuracy and sensitivity analysis for estimating anisotropic parameters from 4C seismic data: 71sth Annual Internat. Mtg., Soc. Expl. Geophys., Expanded Abstracts, **II**, 869-872.

Li, J., Atlan, S., Sanders, J., Zhu, X., and Brzostowski, M., 1999, Processing issues with orienting ocean bottom multicomponent receivers: 61st EAGE Conference, Expanded Abstracts, P063.

Li, X.-Y., 1997, Fractured reservoir delineation using multicomponent seismic data: Geophysical Prospecting, **45**, 39–64.

Li, X.-Y., 1998, Fracture detection using azimuthal $P-$wave moveout from orthogonal seismic survey lines: 68th Annual Internat. Mtg., Soc. Expl. Geophys., Expanded Abstracts, 2056–2059.

Li, X.-Y., 1999, Fracture detection using azimuthal variation of $P-$wave moveout from orthogonal seismic survey lines: Geophysics, **64**, 1193–1201.

Liu, E., Crampin, S., Queen, J. H., and Rizer, W. D., 1993, Behaviour of shear waves in rocks with two sets of parallel cracks: Geophys. J. Int., **113**, 509–517.

Liu, E., Queen, J. H., and Cox, V. D., 2000, Anisotropy and attenuation of crosshole channel waves from the Antrim Shale gas play, Michigan Basin: Journal of Applied Geophysics, **44**, 47–61.

Lynn, H. B., and Thomsen, L. A., 1986, Reflection shear-wave data along the principal axes of azimuthal anisotropy: 56th Annual Internat. Mtg., Soc. Expl. Geophys., Expanded Abstracts, 473–476.

MacLeod, M. K., Hanson, R. A., Hadley, M. J., Reynolds, K. J., Lumley, D., McHugo, S., and Probert, A., 1999, The Alba field OBC seismic survey: 61st EAGE Conference, Expanded Abstracts, 6–25.

Mallick, S., Craft, K., Meister, L., and Chambers, R., 1998, Determination of the principle direction of azimuthal anisotropy from $P-$wave seismic data: Geophysics, **63**, 692–706.

Meunier, J., Huguet, F., and Michel, J. M., 1997, Determining acquisition parameters for time lapse seismic recording: 59th EAGE Conference, Expanded Abstracts, B042.

Meunier, J., Chameau, J., Bijou, J., and Maida, J., 1998, 4C sea bottom receiver evaluation: 60th EAGE Conference, Expanded Abstracts, 2–03.

Muyzert, E., 2000, Scholte wave velocity inversion for a near surface S-velocity model and PS-statics: 70th Annual Internat. Mtg., Soc. Expl. Geophys., Expanded Abstracts, 1197–1200.

Nolte, B., Bishop, K., and Sukup, D., 1999, Anisotropic prestack depth migration of converted-wave data from the Gulf of Mexico: 69th Annual Internat. Mtg., Soc. Expl. Geophys., Expanded Abstracts, 691–694.

Pettenati-Auziere, C., Debouvry, C., and Berg, E., 1997, Node-based sea-bottom seismic, a new way to reservoir management: 67th Annual Internat. Mtg., Soc. Expl. Geophys., Expanded Abstracts, 71–74.

Postma, G., 1955, Wave propagation in stratified medium: Geophysics, **20**, 780–806.

Riedel, M., and Theilen, F., 2001, AVO investigations of shallow marine sediments: Geophysical Prospecting, **49**, 198–212.

Samson, C., Barton, P. J., and Karwatowski, J., 1995, Imaging beneath an opaque basaltic layer using densely sampled wide-angle OBS data: Geophys. Prosp., **43**, 509–527.

Sena, A. G., and Toksöz, M. N., 1993, Kirchhoff migration and velocity analysis for converted and nonconverted waves in anisotropic media: Geophysics, **58**, 265–276.

Sena, A. G., 1991, Seismic traveltime equations for azimuthally anisotropic and isotropic media: Estimation of interval elastic properties: Geophysics, **56**, 2090–2101.

Seriff, A., and Sriram, K., 1991, $P-SV$ reflection moveouts for transversely isotropic media with a vertical symmetry axis: Geophysics, **56**, 1271–1274.

Sheriff, R. R., and Geldart, L. P., 1995, Exploration seismology: Cambridge University Press, second edition.

Soubaras, R., 1998, Multiple attenuation and $P-S$ decomposition of multicomponent ocean-bottom data: 68th Annual Internat. Mtg., Soc. Expl. Geophys., Expanded Abstracts, 1336–1339.

Stewart, R. R., 1991, Rapid map and inversion of $P-SV$ waves (short note): Geophysics, **56**, 859–862.

Stolt, R. H., 1978, Migration by Fourier transform: Geophysics, **43**, 23–48.

Taner, M. T., and Koehler, F., 1969, Velocity spectra - Digital computer derivation and applications of velocity functions: Geophysics, **34**, 859–881.

Tatham, R. H., and Goolsbee, D. V., 1984, Separation of $S-$wave and $P-$wave reflections offshore western Florida: Geophysics, **49**, 493–508.

Tatham, R. H., and McCormack, M. D., 1991, Multicomponent seismology in petroleum exploration: Soc. Expl. Geophys.

Tatham, R. H., and Stoffa, P. L., 1976, V_p/V_s - A potential hydrocarbon indicator: Geophysics, **41**, 837–849.

Taylor, D. B., 1991, Aniseis II manual: Available to licencees of ANISEIS from Applied Geophysical Software Inc., Houston.

Tessmer, G., and Behle, A., 1988, Common reflection point data-stacking for converted-waves: Geophysical Prospecting, **36**, 671–688.

Tessmer, G., Krajewski, P., Fertig, J., and Behle, A., 1990, Processing of $PS-$reflection data applying a common conversion-point stacking technique: Geophysical Prospecting, **38**, 267–286.

Theilen, F., Ayres, A., and Lange, G., 1997, Physical properties of near surface marine sediments: 59th EAGE Conference, Expanded Abstracts, P064.

Thomsen, L. A., Barkved, O., Haggard, B., Kommedal, J., and Rosland, B., 1997, Converted-wave imaging of Valhall reservoir: 59th EAGE Conference, Expanded Abstracts, B048.

Thomsen, L., 1986, Weak elastic anisotropy: Geophysics, **51**, 1954–1966.

Thomsen, L., 1988, Reflection seismology over azimuthally anisotropic media Geophysics, **53**, 304–313.

Thomsen, L., 1998, Converted-wave reflection seismology over anisotropic, inhomogeneous media: 68th Annual Internat. Mtg., Soc. Expl. Geophys., Expanded Abstracts, **II**, 2048–2051.

Thomsen, L., 1999, Converted-wave reflection seismology over inhomogenous, anisotropic media: Geophysics, **64**, 678–690.

Tsvankin, I., and Thomsen, L., 1994, Nonhyperbolic reflection moveout in anisotropic media: Geophysics, **59**, 1290–1304.

Tsvankin, I., and Thomsen, L., 1995, Inversion of reflection traveltimes for transverse isotropy.: Geophysics, **60**, 1095–1107.

Tsvankin, I., 1995, Normal moveout from dipping reflectors in anisotropic media: Geophysics, **60**, 268–284.

Vernik, L., and Liu, X., 1997, Velocity anisotropy on shales: A petrophysical study: Geophysics, **62**, 521–532.

Wang, Z., 2001, Seismic anisotropy in sedimentary rocks: 71st Annual Internat. Mtg., Soc. Expl. Geophys., Expanded Abstracts, **II**, 1740-1743.

Wessel, P., and Smith, W., 1995, New version of Generic Mapping Tool released: EOS trans. AGU, **76**, 329.

White, J. E., 1965, Seismic waves radiation, transmission, and attenuation: McGraw-Hill Book Company.

Wild, P., and Crampin, S., 1991, The range of effects of azimuthal isotropy and EDA anisotropy in sedimentary basins: Geophys. J. Int., **107**, 513–529.

Winterstein, D. F., and Paulsson, B. N. P., 1990, Velocity anisotropy in shale determined from crosshole seismic and vertical seismic profile data: Geophysics, **55**, 470–479.

Winterstein, D. F., 1990, Velocity anisotropy terminology for geophysicists: Geophysics, **55**, 1070–1088.

Yilmaz, Ö., 2001, Seismic data analysis: Processing, inversion, and interpretation of seismic data: Society of Exploration Geophysicists.

Yuan, J., and Li, X.-Y., 1998, A new approach for converted-wave moveout in transversely isotropic media: 68th Annual Internat. Mtg., Soc. Expl. Geophys., Expanded Abstracts, **II**, 1495–1498.

Yuan, J., Li, X.-Y., and Taylor, D., 1997, Orientation of non-gimballed three-component geophones in sea-floor data: 59th EAGE Conference, Expanded Abstracts, P041.

Yuan, J., Li, X.-Y., Ziolkowski, A., and Strijbos, F., 1998, Processing 4C sea-floor seismic data: A case example from the North Sea: 68th Annual Internat. Mtg., Soc. Expl. Geophys., Expanded Abstracts, **I**, 714–717.

Zhang, Y., and Robinson, E. A., 1992, Stacking $P - SV$ converted wave data with raypath velocity: 62nd Annual Internat. Mtg., Soc. Expl. Geophys., Expanded Abstracts, 1214–1217.

Zhu, X., Altan, S., and Li, J., 1999, Recent advances in multicomponent processing: The Leading Edge, **18**, 1283–1288.

List of Publications

1. Yuan, J., Li, X.-Y., and Ziolkowski, A., 2001, Converted-wave moveout analysis in layered anisotropic media - a case study: 63rd EAGE Conference, Expanded Abstracts, **I**, L027.

2. Yuan, J., and Li, X.-Y., 2001, $PS-$wave conversion-point equations for layered anisotropic media: 63rd EAGE Conference, Expanded Abstracts, **II**, P112.

3. Li, X.-Y., and Yuan, J., 2001, Converted-wave imaging in the homogeneous, anisotropic media - Part I - parameter estimation: 63rd EAGE Conference, Expanded Abstracts, **II**, P109.

4. Li, X.-Y., Dai, H., and Yuan, J., 2001, Converted-wave imaging in the homogeneous, anisotropic media - Part II - prestack migration: 63rd EAGE Conference, Expanded Abstracts, **II**, P114.

5. Yuan, J., and Li, X.-Y., 2001, $PS-$wave conversion-point equations for layered anisotropic media: 71st Annual Internat. Mtg., Soc. Expl. Geophys., Expanded Abstracts, 157-160.

6. Li, X.-Y., and Yuan, J., 2001, Accuracy and sensitivity analysis for estimating anisotropic parameters from 4C seismic data: 71st Annual Internat. Mtg., Soc. Expl. Geophys., Expanded Abstracts, 869-872.

7. Li, X.-Y., and Yuan, J., 1999, Geophone orientation and coupling in three-component sea-floor data: a case study: Geophysical Prospecting, **47**, no. 6, 995–1013.

8. Li, X.-Y., Yuan, J., Ziolkowski, A., and Strijbos, F., 1999, Estimating Vp/Vs ratio from converted waves - a 4C case example: 61st EAGE Conference, Expanded Abstracts, **II**,P066.

9. Li, X.-Y., and Yuan, J., 1999, Converted-wave moveout and parameter estimation for transverse isotropy: 61st EAGE Conference, Expanded Abstracts, **I**, 4035.

10. Yuan, J., Li, X.-Y., and Ziolkowski, A., 1999, Anisotropy and correlation analysis in North Sea 4-C sea-floor seismic data: 61st EAGE Conference, Expanded Abstracts, **I**, 4033.

11. Li, X.-Y., and Yuan, J., 1999, Anisotropy velocity analysis for 4-C seismic data: a case study: 69th Annual Internat. Mtg., Soc. Expl. Geophys., Expanded Abstracts, 732–735.

12. Yuan, J., Li, X.-Y., Ziolkowski, A., and Strijbos, F., 1998, Processing North Sea 4C sea-floor seismic data: 60th EAGE Conference, Expanded Abstracts, **I**, 03-35.

13. Yuan, J., and Li, X.-Y., 1998, A new approach for converted-wave moveout in transversely isotropic media: 68th Annual Internat. Mtg., Soc. Expl. Geophys., Expanded Abstracts, **II**, 1495–1498.

14. Yuan, J., Li, X.-Y., Ziolkowski, A., and Strijbos, F., 1998, Processing 4C sea-floor seismic data: A case example from the North Sea: 68th Annual Internat. Mtg., Soc. Expl. Geophys., Expanded Abstracts, **I**, 714–717.

15. Yuan, J., Li, X.-Y., and Taylor, D., 1997, Orientation of non-gimballed three-component geophones in sea-floor data: 59th EAGE Conference, Expanded Abstracts, P041.